A NONLINEAR EQUIVALENT FRAME MODEL FOR DISPLACEMENT
BASED ANALYSIS OF UNREINFORCED BRICK MASONRY BUILDINGS

A THESIS SUBMITTED TO
THE GRADUATE SCHOOL OF NATURAL AND APPLIED SCIENCES
OF
MIDDLE EAST TECHNICAL UNIVERSITY

BY

İSMAİL OZAN DEMİREL

IN PARTIAL FULFILLMENT OF THE REQUIREMENTS
FOR
THE DEGREE OF MASTER OF SCIENCE
IN
CIVIL ENGINEERING

DECEMBER 2010

Approval of the thesis:

A NONLINEAR EQUIVALENT FRAME MODEL FOR DISPLACEMENT BASED ANALYSIS OF UNREINFORCED BRICK MASONRY BUILDINGS

submitted by **İSMAİL OZAN DEMİREL** in partial fulfillment of the requirements for the degree of **Master of Science in Civil Engineering Department, Middle East Technical University** by,

Prof. Dr. Canan Özgen   _____
Dean, Graduate School of **Natural and Applied Sciences**

Prof. Dr. Güney Özcebe   _____
Head of Department, **Civil Engineering**

Prof. Dr. Haluk Sucuoğlu   _____
Supervisor, **Civil Engineering Dept., METU**

Examining Committee Members:

Assoc. Prof. Dr. Murat Altuğ Erberik   _____
Civil Engineering Dept., METU

Prof. Dr. Haluk Sucuoğlu   _____
Civil Engineering Dept., METU

Assoc. Prof. Dr. Barış Binici   _____
Civil Engineering Dept., METU

Assoc. Prof. Dr. Ahmet Türer   _____
Civil Engineering Dept., METU

Assoc.Prof. Dr. Hasan Hüsnü Korkmaz   _____
Civil Engineering Dept., Konya University

Date: Dec 17, 2010

I hereby declare that all information in this document has been obtained and presented in accordance with academic rules and ethical conduct. I also declare that, as required by these rules and conduct, I have fully cited and referenced all material and results that are not original to this work.

Name, Last name: İSMAİL OZAN DEMİREL

Signature

ABSTRACT

A NONLINEAR EQUIVALENT FRAME MODEL FOR DISPLACEMENT BASED ANALYSIS OF UNREINFORCED BRICK MASONRY BUILDINGS

Demirel, İsmail Ozan

M.Sc., Department of Civil Engineering

Supervisor: Prof. Dr. Haluk Sucuoğlu

December 2010, 208 pages

Although performance based assessment procedures are mainly developed for reinforced concrete and steel buildings, URM buildings occupy significant portion of building stock in earthquake prone areas of the world as well as in Turkey. Variability of material properties, non-engineered nature of the construction and difficulties in structural analysis of perforated walls make analysis of URM buildings challenging. Despite sophisticated finite element models satisfy the modeling requirements, extensive experimental data for definition of material behavior and high computational resources are needed. Recently, nonlinear equivalent frame models which are developed assigning lumped plastic hinges to isotropic and homogenous equivalent frame elements are used for nonlinear modeling of URM buildings.

The work presented in this thesis is about performance assessment of unreinforced brick masonry buildings in Turkey through nonlinear equivalent frame modeling technique.

Reliability of the proposed model is tested with a reversed cyclic experiment conducted on a full scale, two-story URM building at the University of Pavia and a dynamic shake table test on a half scale, two story URM building at the Ismes Laboratory at Bergamo. Good agreement between numerical and experimental results is found.

Finally, pushover and nonlinear time history analyses of three unreinforced brick masonry buildings which are damaged in 1995 earthquake of Dinar is conducted using the proposed three dimensional nonlinear equivalent model. After displacement demands of the buildings are determined utilizing Turkish Earthquake Code 2007, performance based assessment of the buildings are done.

Keywords: Unreinforced Masonry Buildings, Equivalent Frame Modeling, Pushover Analysis, Nonlinear Time History Analysis, Performance Assessment

ÖZ

TUĞLA YIĞMA YAPILARIN DEPLASMANA BAĞLI ANALİZİ İÇİN DOĞRUSAL OLMAYAN EŞDEĞER ÇERÇEVE MODELİ

Demirel, İsmail Ozan

Yüksek Lisans, İnşaat Mühendisliği Bölümü

Tez Yöneticisi: Prof. Dr. Haluk Sucuoğlu

Aralık 2010, 208 sayfa

Performansa dayalı değerlendirme yöntemleri her ne kadar öncelikle betonarme ve çelik binalar için geliştirilmiş olsa da, yığma yapılar bugün dünyanın depreme eğilimli bir çok bölgesinde ve Türkiye'de yapı stoğunun önemli bir kısmını oluşturmaktadır. Yığma yapıların malzeme özelliklerindeki değişkenlik, mühendis hizmeti görmeden yapılmış oluşları ve boşluklu duvarların yapısal değerlendirilmesindeki güçlükler analiz edilmelerini güçleştirmektedir. Gelişmiş sonlu elemanlar modelleri modelleme ihtiyacını karşılasa da malzeme davranışını tanımlayabilmek için çok sayıda deneysel veri gerekmekte ve çok fazla hesaplama eforu istemektedir. Son dönemlerde eşyönlü ve bağdaşık eşdeğer çubuk elemanlarla oluşturulan yığma bina modellerine yığılı plastik mafsallar atanarak oluşturulan doğrusal olmayan çubuk çerçeve modelleri, yığma yapıların modellenmesinde kullanılmaktadır.

Bu çalışmada Türkiye'de bulunan tuğla yığma yapıların doğrusal olmayan çubuk çerçeve elemanlarla modellenerek performansa bağlı değerlendirilmesi tarif edilmektedir.

Önerilen modelin güvenilirliği Pavia Üniversitesi'nde gerçek boyutlu ve iki katlı bir yığma bina üzerinde gerçekleştirilen döngüsel itme deneyi ve Bergamo'da bulunan İsmes Loratuarı'nda yarı ölçekli ve iki katlı bir yığma bina üzerinde gerçekleştirilen dinamik sarsma tablası deneyiyle karşılaştırılarak sınanmıştır. Deneysel ve sayısal sonuçlar arasında tatmin edici bir uyum gözlemlenmiştir.

Son olarak 1995 Dinar depreminde hasar gören üç adet tuğla yığma binanın statik itme ve zaman tanım alanında doğrusal olmayan dinamik analizleri, doğrusal olmayan eşdeğer çerçeve metoduna göre oluşturulan üç boyutlu bilgisayar modeli kullanılarak yapılmıştır. 2007 Türkiye Deprem Yönetmeliği'ne göre binaların deplasman istemi hesaplandıktan sonra performansa dayalı değerlendirmeleri yapılmıştır.

Anahtar Kelimeler: Tuğla Yığma Yapılar, Eşdeğer Çerçeve Modeli, Statik İtme Analizi, Zaman Tanım Alanında Doğrusal Olmayan Dinamik Analiz, Performansa Dayalı Değerlendirme

To My Big Family

ACKNOWLEDGMENT

TABLE OF CONTENTS

CHAPTERS

LIST OF SYMBOLS / ABBREVATIONS

1B2S = 1 Bay 2 Story

1F = URM wall investigated by Franklin et al. (2001)

1GT = URM wall investigated by Ganz and Thürlimann (1982)

2B2S = 2 Bay 2 Story

2B3S = 2 Bay 3 Story

A = Area of cross section

A_s = Shear area

CP = Collapse prevention

CSB = Case study building

DOF = Degree of freedom

E = Modulus of elasticity

EFM = Equivalent frame method

EI = Flexural rigidity

EQ = Earthquake

FEM = Finite element method

f'_{dt} = Lower bound diagonal tension strength

f_m = Compressive strength of masonry wall

f'_m = Lower bound compressive strength

F_u = Ultimate force

F_y = Yield force

G = Shear modulus

h = Height of the wall

h_{eff}= Effective height of the wall

h_i = Height of spandrels and piers connecting to the wall

I = Moment of inertia of the pier

I_i = Moment of inertia of spandrels and piers connecting to the wall.

IO = Immediate occupancy

ISD = Inter story drift

K = Lateral stiffness

kAG = Shear rigidity

k_f = Lateral flexural stiffness

$K_{fix-fix}$=Elastic lateral stiffness of both ends fixed wall

$K_{fix-free}$=Elastic lateral stiffness of cantilever wall

K_i = Post elastic stiffness

k_s = Lateral shear stiffness

k_t = Total lateral stiffness

λ = Aspect ratio

L = Length of wall

LS = Life safety

M_y = Yield moment

$\emptyset_{1st\ story,max}$ = Maximum first story drift

$\emptyset_{roof,max}$ = Maximum roof drift

P = Axial compressive force on wall

p = Mean compressive stress on wall

PF = Modal participation factor

PO = Pushover

RC = Reinforced concrete

RO = Rigid end offset

S_a = Spectral acceleration

S_d = Spectral displacement

T = Period

t = Thickness of the wall

THA = Time history analysis

u = Lateral roof displacement

u_f = Lateral flexural displacement

u_m = Ultimate displacement

URM = Unreinforced masonry

u_s = Lateral shear displacement

u_t = Total lateral displacement

u_y = Yield displacement

V = Base shear

$V_{b,max}$ = Maximum base shear

V_{bjs} = Bed joint sliding strength

V_{dt} = Diagonal tension strength

V_r = Rocking strength

V_{tc} = Toe crushing strength

V_u = Lateral strength

W = Weight of the building

α = Support condition factor: 0.5 for cantilever wall, 1 for both ends fixed wall

β = Boundary condition parameter

β_s = Rotational spring constant

δu = Ultimate displacement

δy = Yield displacement

ζ = Damping ratio in per cent

η = Mass participation factor

θ_p = Plastic rotation

θ_y = Yield rotation

κ = Shear coefficient

λ = Aspect ratio

λ_i = Aspect ratio of spandrels and piers connecting to the wall.

μ = Internal shear friction coefficient, 0.5 is recommended

ν_{te} = Bed joint shear strength

ξ = Vertical stress distribution coefficient (κ=0.85)

υ = Poisson's ratio

φ_r = Modal amplitude at roof

Living is no joke,

you must live with great seriousness

like a squirrel for example,

I mean expecting nothing except and beyond living,

I mean living must be your whole occupation.

You must take living seriously,

I mean to such an extent that,

for example your arms are tied from your back, your back is on the wall,

or in a laboratory with your white shirt, with your huge eye glasses,

you must be able to die for people,

even for people you have never seen,

although nobody forced you to do this,

although you know that

living is the most real, most beautiful thing.

I mean you must take living so seriously that,

even when you are seventy, you must plant olive trees,

not because you think they will be left to your children,

because you don't believe in death although you are afraid of it

because, I mean, life weighs heavier.

Nazım Hikmet

CHAPTER 1

INTRODUCTION

1.1 An Overview on Masonry Construction

Throughout his fight against challenging actions of the nature, mankind laid pieces of stones on top of each other, building shelters on the purpose of protection and accommodation. Starting from the simplest shelters to modern reinforced masonry buildings, masonry construction has a long history. Although there is a great improvement in utilized material properties and construction techniques, the main idea behind masonry construction is still the same; reproduction of nature for accommodation needs.

Being the only construction alternative, masonry construction dictated the structural and architectural characteristics of structures in the past. Many civilizations are remembered with tremendous masonry structures build in their era. Egyptian pyramids, Greek temples, Roman aqueducts, Ottoman mosques, Gothic cathedrals, Renaissance age structures (see Figure 1.1) are all examples of masonry construction survived as cultural heritages from old civilizations.

Today, URM construction maintains its popularity over many urban areas world-wide. Low cost, durability, widespread geographic availability, low maintenance, thermal insulation, fire protection and easiness to construct make masonry an appealing construction material for residential buildings. Since it requires little technology and skill, masonry buildings are often constructed without an engineering touch.

Together with the inherent uncertainties in material and structural level, high inertial forces proportional to high mass of the structure makes URM buildings vulnerable to earthquakes.
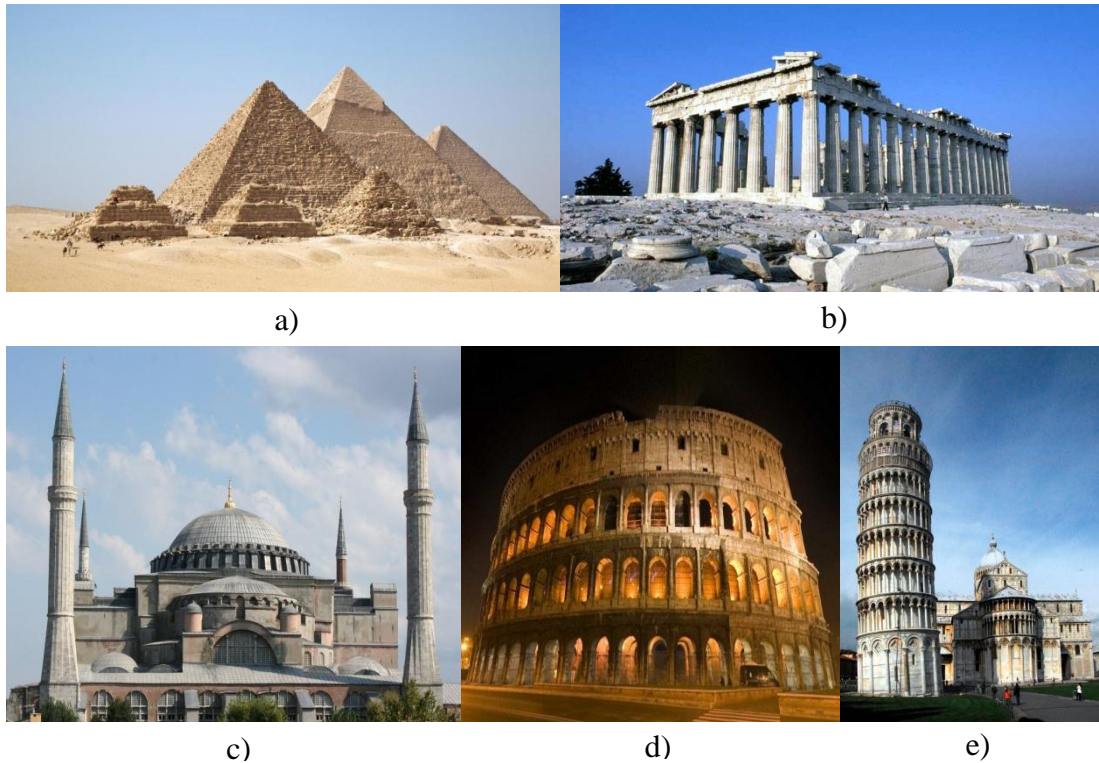
Figure 1.1 Ancient URM Structures a) Great Pyramid of Giza, Egypt b) Greek Temple, Greece c) Hagia Sophia, Turkey d) Coliseum, Italy e) Pisa Tower, Italy

Unfortunately nonlinear response of URM buildings under earthquake induced lateral loads is a challenging task. According to Abrams (2001) despite being the oldest construction material, masonry is still the least understood in terms of strength and deformation characteristics.

As a result, steel and RC have been replacing masonry as a construction material in earthquake prone areas of the world. Instead of using as a construction material, masonry has been mostly used as a non-structural material such as infill of reinforced concrete frames in the last decades (Vasconcelos, 2005). This situation increased the research on masonry as an infill material for reinforced concrete structures (Binici et al., 2007) but also led to limited knowledge of masonry as a construction material. Prior to 1950's, majority of these buildings were designed only for gravity loads without considering the seismic effects. After this period, seismic design principles were introduced into building codes (Erbay, 2007).

Despite all its drawbacks, masonry still has many advantages over RC for low-height residential building construction. Contrary to RC counterparts, masonry buildings save in overall construction time and cost by eliminating the need for expensive formwork, heavy machinery and special equipment for concrete pouring (Akan, 2008).

Also according to comparative analysis conducted by Akan (2008) on a typical three-story residential building (see Figure 1.2), selection of masonry instead of RC as construction material nearly halves the cost.

a)   b)
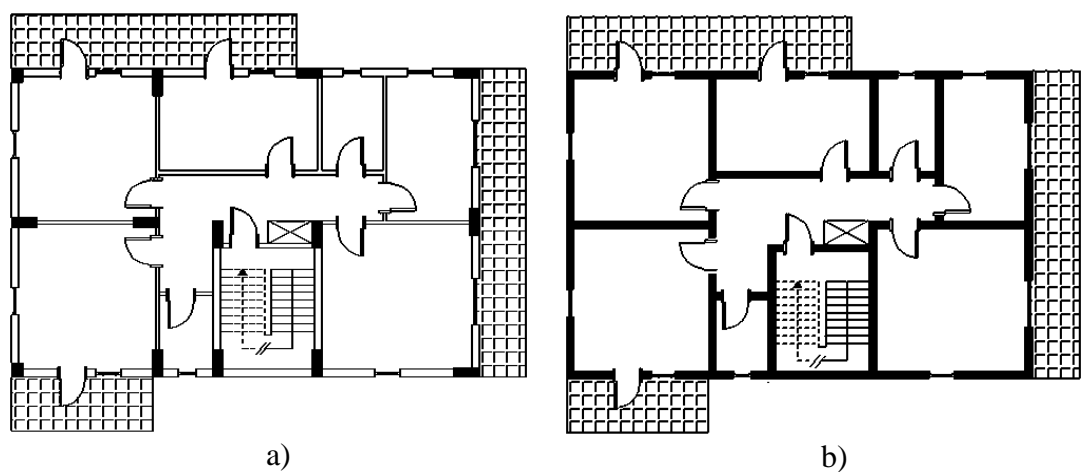
Figure 1.2 Typical Residential Building Designed by Akan (2008) a) RC Structural System b) Masonry Structural System

1.2 Need for Research

Existing URM structures, whether residential buildings or historical structures pose risk in case of seismic disturbances. Neither loss of lives nor loss of cultural heritage due to collapse of URM structures is irreversible. Thus, investigations on conservation of both in case of an earthquake should be conducted.

According to Orduna (2003), earthquakes in 1997 destroyed and damaged more than 200 churches in Italy and earthquake in 1999 destroyed or damaged near 300 ancient churches in Mexico.

Turkey is a rich country considering cultural heritage. A lot of important civilizations lived in Anatolia leaving georgeous masonry structures behind as rich historical heritages (see Figure 1.3). Since historic structures are strong links revealing the cultural evolution of Turkey between past and the present, they should be preserved by means of strengthening against earthquakes.

Iran Bam earthquake of 26 December 2003, Pakistan earthquake of October 2005 and Haiti earthquake of January 2010 are the nearest earthquakes resulting in enormous loss of lives due to the poor performance of URM buildings world-wide.

Likewise, Turkey also suffered from many earthquakes affecting URM building stock in the past. Most recently an earthquake with a magnitude of 6.0 resulted in loss of 42 lives in Elazığ Kovancılar earthquake of March 2010 (Akkar et al., 2010).

According to the report of Housing Development Administration of Turkey, in urban areas 30% of all buildings are the reinforced concrete frame type, 48% are brick masonry or timber framed and 22% are adobe or rubble masonry. In rural areas 82% of the housing stock is masonry of some form (Erdik and Aydınoğlu, 2002).

Since in addition to rich cultural URM heritage, URM construction is also wide spread in Turkey which is an earthquake country, seismic assessment of URM building stock need to be conducted via performance based seismic assessment methods.

Displacement based concepts are used for the purpose of determining the expected performance of a building under an expected seismic action. Due to the prejudgment that masonry is a brittle material with limited deformation capacity, displacement based concepts have been predominantly developed for RC and steel. However, after displacement capacity of masonry is revealed from many experimental tests (FEMA 307, 1999) displacement based analysis of masonry buildings are allowed by many building codes including FEMA 356, Eurocode 8, Italian and Mexican national earthquake codes in the last decade. Also according to Orduna (2004) "application of

modern concepts of mechanics and the development of tools for the structural analysis of ancient masonry constructions have been the topic of very active research mainly in the past decade."

a)

b)

c)

d)
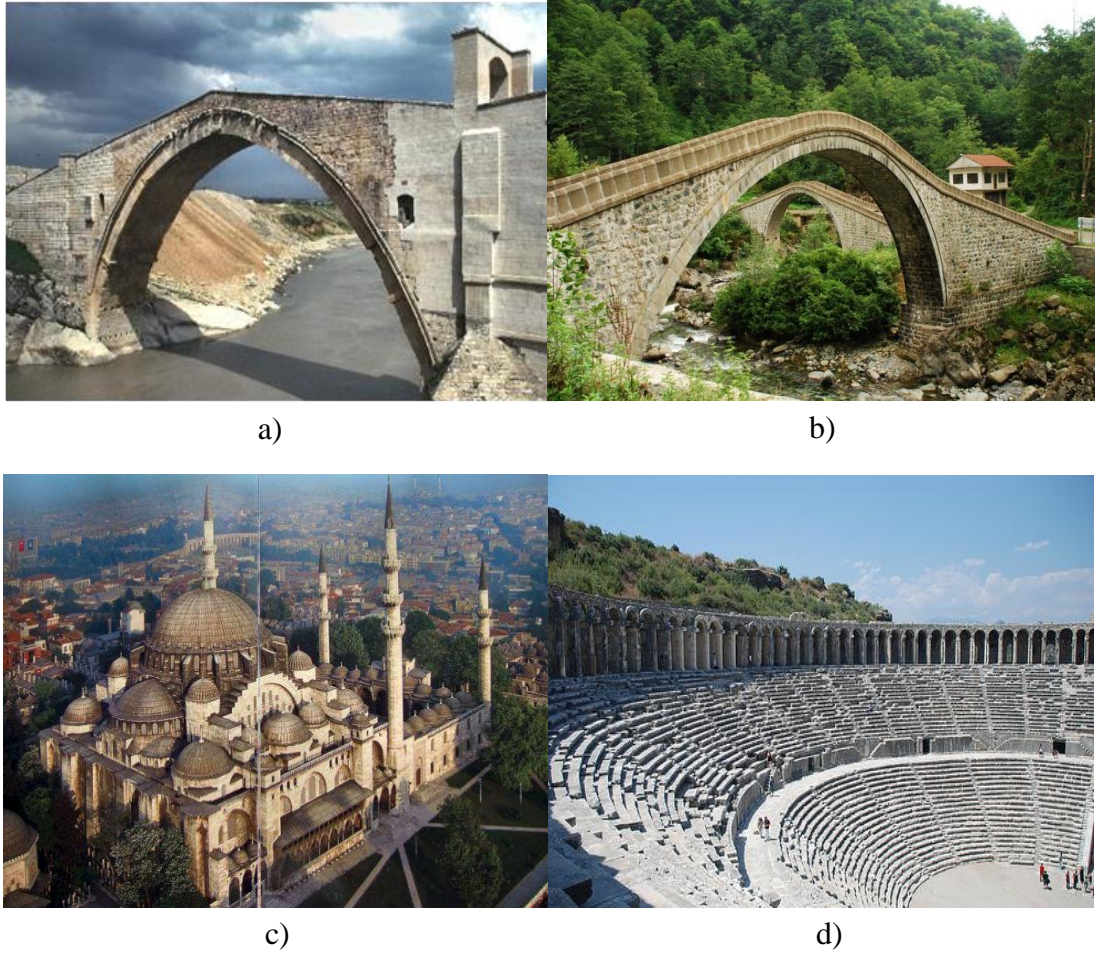
Figure 1.3 Historic URM Heritage of Anatolia a) Malabadi Bridge-Diyarbakır (1140), b) Dual Arch Bridge-Artvin (18th century) c) The Mosque of Soliman-İstanbul (1558) d) Aspendos Theatre-Antalya (2nd century)

1.3 Assumptions Involved in Research

In order to simplify complex nature of masonry for modeling purposes, some assumptions and idealizations have been made throughout the research. Collection of the assumptions and idealizations which are made throughout the dissertation is given in this section. It should be remembered that conclusions achieved as a result of this research is valid only under given assumptions.

1 Although masonry walls which are composed of mortar and brick units show heterogeneous and anisotropic behavior, in case global behavior of the structure is concerned, masonry is idealized as a homogenous and isotropic medium. This assumption is made for elastic stiffness calculations of masonry walls in Chapter 3 and equivalent frame modeling of masonry buildings in Chapter 5.

2 For homogenous and isotropic materials, constitutive relationship is identified by two constants. Namely, modulus of elasticity (E) and poison's ratio (υ). Representative values of these constants for Turkish brick masonry construction practice are taken as 2000 MPa and 0.2 respectively (Aldemir, 2010).

3 Compressive strength of masonry walls is taken as 5 MPa considering typical solid bricks and mortar utilized in Turkey. 5 MPa is also the minimum limit for compressive strength of URM walls in TEC97.

4 It is assumed that although spandrels are prone to early cracking due to low level of axial load on them, ultimate resistance of a masonry building is dictated by pier failure. This assumption is also supported by Calvi et al. (1996) who claim that "final collapse of URM structures is almost always a result of pier failure."

5 Inelastic actions are assumed to take place in piers only. Spandrels are modeled as linear elastic (Belmouden and Lestuzzi, 2007 and Gilmore et al., 2009).

6 Out of plane failure of the walls are not concerned. It is assumed that sufficient precautions such as good connection between walls and the slab is satisfied by means of bond beams, steel anvhors, etc.

7 It is assumed that resistance to lateral loadings is solely provided by in plane walls. Out of plane resistance of the frames are neglected. As analytically and experimentally observed by Yi et al. (2003), the level of this assumption is negligible and effect on total stiffness and strength is around 5-8 %.

8 In Chapter 6, rigid diaphragm action is assumed. Story masses are lumped to center of mass of each floor which is calculated taking weights of the slab and walls into account.

9 The calculations for 3-D masonry building are further simplified by taking into account only one horizontal component of the seismic ground motion and analyzing the structure in each orthogonal direction separately (Tomazevic et al., 2004).

10 Equivalent viscous damping for demand calculations of the masonry buildings according to TEC2007 are taken as 10%.

1.4 Organization of the Thesis

The present dissertation is divided into seven Chapters and four Appendices. Chapters are organized to follow a path going from simple elastic response to complicated plastic response in both component and structural levels.

Chapter 2 is a review of the main concepts and previous investigations on experimental and analytical researches illustrating nonlinear response of URM walls and structures which are essential in implementing displacement based concepts for URM buildings. In the component level, experimental studies and simple analytical formulas illustrating ultimate strength, softening behavior and ultimate drift of URM walls related to four primary failure modes (i.e. rocking, sliding, diagonal tension, toe crushing) are reviewed. In the structural level, nonlinear modeling techniques utilized to simulate nonlinear behavior of URM structures are summarized. Emphasis is given on equivalent frame method which will be further investigated in the upcoming chapters. Finally performance limit states for URM walls and buildings are presented which is also essential for performance assessment of URM buildings.

Chapter 3 deals with elastic response of solid and perforated URM walls. Derivation of analytical equations illustrating elastic lateral stiffness of solid URM walls is

made. Influence of coupling imposed by beams on lateral stiffness of cantilever walls is investigated and an analytical equation is proposed for elastic lateral stiffness of masonry walls coupled with spandrels. A modeling technique, named as equivalent frame method, idealizing perforated URM walls as frame elements such as piers and spandrels is introduced for elastic lateral stiffness calculation of perforated walls. Calibration of the method is made via comparative analyses between finite element model and equivalent frame model.

Chapter 4 introduces a finite element macro model that has been developed by Aldemir (2010) for the simulation of nonlinear response of URM walls. The model is capable of reflecting effects of cracking, estimating damage propagation and ultimate failure mechanism of masonry walls. After properties and assumptions of the model are illustrated, reliability of the model is tested. First, comparison of the equations proposed by Aldemir (Equation 4.1 and 4.2) with simple strength formulas and ultimate drift capacities of URM walls that are proposed by FEMA 356(2000) is made. Second, detailed comparison of the model with the results of two experimental studies is made. Results of the proposed model form the basis for the nonlinear modeling of URM buildings in the following chapters.

Chapter 5 deals with derivation and verification of a nonlinear equivalent frame model proposed for nonlinear static and nonlinear dynamic analyses of URM buildings. Proposed nonlinear model is a combination of equivalent frame model that has been mentioned in Chapter 3 whose nonlinear response of its components is defined according to finite element macro model results mentioned in Chapter 4. Validation of the model is performed by means of two experimental tests. First, cyclic experimental test results of the URM building tested at University of Pavia is compared with pushover analysis results of the proposed model. Second, dynamic experimental test results of the URM building tested at Ismes Laboratory at Bergamo is compared with nonlinear time history analysis results of the proposed model. Additionally, influence of different approaches for the determination of axial load level on URM walls, which is crucial for the determination of hinge characteristics, is investigated. A step by step hand calculation method which takes axial force -

shear force interaction into account is proposed. Steps of the procedure is outlined and demonstrated.

Chapter 6 contains the application of the model developed in the previous chapter to three existing URM buildings located in Dinar, Turkey. Capacity curves of the buildings are derived according to equations proposed by Aldemir and equations proposed by FEMA 356 for comparison. After determination of the capacities utilizing the nonlinear equivalent frame model proposed in Chapter 5, earthquake demand of the buildings under the design earthquake specified in TEC2007 are calculated and performance assessment of the buildings are made according to both assessment of member displacement demands and a simple approach proposed by Tomazevic (2007). Nonlinear time history analyses of the buildings are made and calculated demands according to TEC2007 and nonlinear THA are compared.

Chapter 7 presents the findings and conclusions derived from this study and provides suggestions for future research.

CHAPTER 2

LITERATURE REVIEW

2.1 Nonlinear Response of URM Walls

Nonlinear behavior of masonry walls is highly complicated. Nonlinearity is mainly dependent on cracking and crushing of masonry which is heterogeneous and anisotropic by nature. Depending on the mechanical properties, boundary conditions, axial load level and aspect ratio of the wall, different failure mechanisms are observed. Each failure mechanism possesses its own strength and displacement characteristics. Thus, in order to define the nonlinear behavior of a masonry wall, its failure mode needs to be determined first.

To illustrate the effect of failure mechanism on response, hysteretic behavior of two masonry walls under cyclic load reversals are illustrated in Figure 2.1 (Magenes and Calvi, 1997).

In case of flexural response such as rocking of a pier, response is roughly nonlinear elastic with low hysteretic energy dissipation, considerable displacement capacity and limited strength degradation (see Figure 2.1a). On the other hand, in case of shear dominated response such as diagonal tension failure, nonlinear response is characterized by higher hysteretic energy dissipation, limited displacement capacity, sudden strength and stiffness degradation (see Figure 2.1b).

<center>a)　　　　　　　　　　　　　　b)</center>
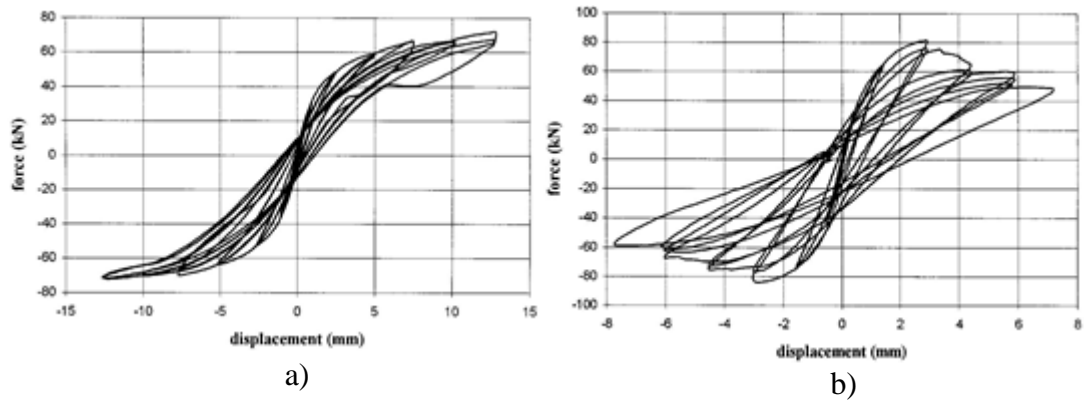
Figure 2.1 Hysteretic Response of Masonry Walls a) Flexure Dominated Response b) Shear Dominated Response (Magenes and Calvi, 1997)

Chapter 2 starts with an investigation on definition and unique characteristics of failure modes of URM walls. Since failure of a URM wall is characterized by strength and ultimate drift, special attention is given on simple strength formulas defined in the literature followed by ultimate drift limit and softening behavior investigation of URM walls under lateral loading. Then, nonlinear modeling techniques utilized for URM is reviewed. Emphasize is given on equivalent frame modeling which will be further investigated in the following chapters. Finally, recent studies on the performance assessment of URM walls and buildings will be summarized.

2.1.1 Failure Modes of URM Walls

Depending on the difficulty in analytical modeling, the knowledge about nonlinear behavior of masonry is mostly extracted from experimental studies. Four primary in-plane failure modes of URM walls such as rocking, bed joint sliding, diagonal tension failure along masonry units or along head and bed joints in a stair stepped fashion and toe crushing (see Figure 2.2) are identified in these experimental works.

However, even four primary discrete failure mechanisms are not sufficient to define inelastic behavior of a masonry wall. Initiation of a failure mechanism might trigger another failure mechanism (TianYi., 2006) or overturning moment due to lateral

<center>11</center>

loads might increase or decrease axial load on the walls of a URM building , turning flexural failure to shear dominated failure (Magenes et al., 1995).
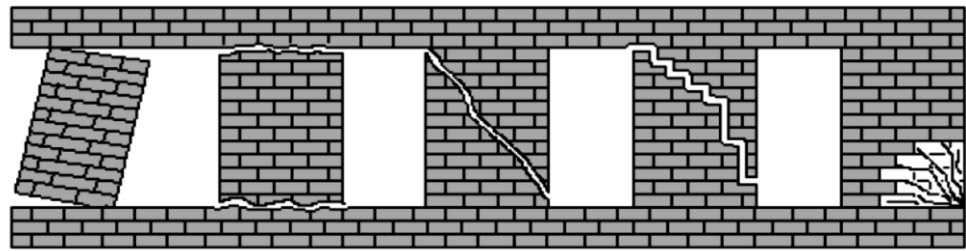
a) Rocking   b) Sliding   c) Diagonal tension   d) Toe crushing

Figure 2.2 Failure Modes of In-plane Masonry Walls (Tianyi, 2006)

As a result, ultimate failure of a pier might be idealized as a combination of four primary modes. According to FEMA 306 "Evaluation of Earthquake Damaged Concrete and Masonry Wall Buildings - Basic Procedure Manual" (1999) in addition to previously mentioned four primary failure modes, coupled failure modes such as: Flexural Cracking / Toe Crushing / Bed Joint Sliding, Flexural Cracking / Toe Crushing, Flexural Cracking / Diagonal Tension are also defined. A summary of experimental studies illustrating combined failure mechanisms are illustrated in FEMA 307 (1999).

The summarized experimental results suggest that aspect ratio and vertical stress are the most important factors in determination of the failure mechanisms of URM walls. Rocking and sliding governs the response under low levels of axial force and high aspect ratio. These failure modes are capable of exhibiting large ultimate drifts. At higher levels of axial force and low aspect ratios, toe-crushing and diagonal tension failures are more common. Although these failure modes are typically assumed to be brittle, if diagonal crack is formed in a stair stepped manner, large displacement capacities have been observed due to the resulting sliding deformations (Franklin L. Moon, 2004).

Definitions and related nonlinear response characteristics of four primary failure modes of URM walls are illustrated below.

2.1.1.1 Rocking

Rocking failure is a flexure dominated mechanism which is distinguished by flexural cracks developing at the bottom and the top of the wall. Under the overturning effect of lateral forces, wall makes a rigid body rotation about the compression zone in the direction of lateral force. Large deformations without significant strength reduction is observed under force reversals since flexural cracks close and uncracked section resist overturning moment in each reversal. While some authors (Tianyi, 2004) conceive rocking as a working condition not as a failure mechanism, a displacement based failure mode with a generalized force deformation relationship is defined for rocking in FEMA 356 (2000). Equation proposed for rocking strength of piers in FEMA 356 is given below:

$$V_r = 0.9\alpha P \frac{L}{h_{eff}} \tag{2.1}$$

Where;

α = Support condition factor; 0.5 for cantilever wall, 1 for both ends fixed wall

P = Axial compressive force on wall

L = Length of wall

h_{eff} = Effective height of wall

2.1.1.2 Shear Sliding along Bed Joints

Bed-joint sliding failure is characterized by either horizontal cracks along bed-joints or stair stepped cracks along bed-joints and head joints. Under the shear force implemented by lateral force, bricks slide on one another producing resistance offered by friction alone between masonry units and mortar. Large deformation without significant strength deterioration is observed and large amount of energy is dissipated due to frictional resistance. Bed-joint sliding is defined as a displacement based failure mechanism in FEMA 356 (2000). Equation proposed for bed-joint sliding strength of URM walls in FEMA 356 is given below:

$$V_{bjs} = 0.5(0.75v_{te} + p)Lt \tag{2.2}$$

Where;

L = Length of wall

t = Thickness of wall

p = Mean compressive stress on wall

v_{te} = Bed joint shear strength (0.75 factor on v_{te} shall not be applied for single wythe masonry walls.)

2.1.1.3 Diagonal Tension

Diagonal tension failure is a shear dominated failure mechanism which is identified by diagonal cracking in the middle of the wall. It is caused by the maximum principle stress (tension) which exceeds the tension strength of masonry. If strong units and weak mortar is utilized cracking takes place through bed and head joints, otherwise diagonal cracks propagate along brick units and mortar. From experimental studies it is found that the cracking that goes through brick units and mortar results in a brittle failure with sudden decrease of strength, whereas second type of cracking exhibits relatively large ultimate drifts. FEMA 356 (2000) does not distinguish between two types of diagonal cracking and defines diagonal tension failure as a force based failure. However it is also observed that cracking going through bed-joints and head-joints resulted in a ductile behavior similar to bed-joint sliding mechanism.

Equation proposed for diagonal tension strength of piers in FEMA 356 is given below:

$$V_{dt} = f'_{dt} A \frac{L}{h_{eff}} \sqrt{1 + \frac{p}{f'_{dt}}} \tag{2.3}$$

Where;

f'_{dt} = lower bound masonry diagonal tension strength

A = Area of cross section

L = Length of the wall

h_{eff} = Effective height of wall

p = Mean compressive stress on wall

2.1.1.4 Toe Crushing

Toe crushing failure is defined as crushing of masonry taking place at the maximum compression zone which is located at the bottom end of the wall. It is usually related with rocking failure. Compressive failure of masonry units results in a sudden decrease in strength and stiffness. Thus, toe crushing is defined to be a force based failure mode in FEMA 356 (2000). Equation proposed for toe crushing strength of piers in FEMA 356 is given below:

$$V_{tc} = \alpha P \frac{L}{h_{eff}} \left(1 - \frac{p}{0.7 f'_m}\right)$$

(2.4)

Where;

α = Support condition factor; 0.5 for cantilever wall, 1 for both ends fixed wall

P = Axial compressive force

L = Length of wall

h_{eff} = Effective height of wall

p = Mean compressive stress on wall

f'_m = Lower bound masonry compressive strength

L/ h_{eff} shall not be taken less than 0.67

2.1.2 Softening Behavior of URM Walls

Lateral stiffness of URM walls degrade with the increase in lateral displacement. Softening of the lateral resistance in URM takes place due to progressive internal crack growth reducing effective area of the wall which resists lateral load. This phenomenon is observed in several experimental studies. While some authors tried to relate post-elastic stiffness degradation to lateral drift, others assume that post-elastic stiffness might be taken as zero for practical purposes.

According to Gürel et al. (2005) elastic lateral stiffness values of the unreinforced masonry columns decrease dramatically with the increase in lateral displacements caused by cracking and second-order effects. P-Δ effects for masonry piers might be ignored since limit states for the ultimate drift of piers are low. However cracking results in significant stiffness drop especially for shear dominant mechanisms.

Based on an experimental study on in-plane loaded full scale masonry walls and half scale confined masonry buildings through shaking table tests, Ruiz García and Alcocer (1998) established a relationship between damage, lateral drift, crack pattern, degradation of lateral strength and stiffness of confined masonry walls (see Figure 2.3). In structural level, they observed that stiffness decays at low drift ratios, even before inclined cracking takes place. They explained this fact by flexural cracking, micro-cracking not visible by naked eye, local loss of mortar bond and adjustment of brick position. They also stated that after first inclined cracking, stiffness decay increased with drift until maximum strength is reached. At larger drift ratios stiffness remained nearly constant (Alcocer et al., 2004).
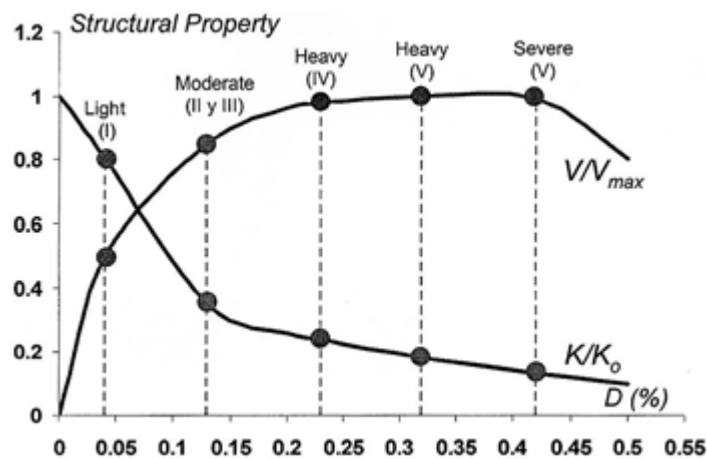
Figure 2.3 Evolution of Damage and Structural Degradation in Confined Masonry Walls Failing under Diagonal Tension (Ruiz-García and Alcocer, 1998)

In Figure 2.3, lateral stiffness (K) corresponding to a particular level of inter-story drift (D) is normalized by initial stiffness (K_o). Similarly, shear force (V) corresponding to a particular level of inter-story drift is normalized by maximum shear strength of masonry wall (V_{max}). Decrease in lateral stiffness starts in the very

first stages of loading, just after the formation of first hairline cracks. After the formation of first diagonal cracking due to diagonal tension, lateral stiffness decreases to 35% of its initial value. Decrease in lateral stiffness and increase in shear force is parabolic until the walls are heavily damaged. Afterwards both shear force and lateral displacement tend to be constant till masonry walls fail at a ultimate drift level of 0.5%.

According to experimental studies made by Tomazevic et al. (1996) it is observed that independent of vertical load and loading history, shape of the stiffness degradation function is constant. The change in stiffness of a pier might be related with lateral displacement using Equation 2.9. Utilizing stiffness degradation parameters proposed by Tomazevic, stiffness degradation functions are drawn for different levels of vertical force on piers (see Figure 2.4).

$$\frac{K}{K_e} = \alpha \left(\frac{d}{d_{Hmax}}\right)^\beta \qquad (2.9)$$

Where;

K = Lateral stiffness

K_e= Secant stiffness evaluated at the occurrence of the first significant cracks

d = lateral displacement

d_{Hmax} = lateral displacement evaluated at maximum resistance

α, β = parameters of stiffness degradation
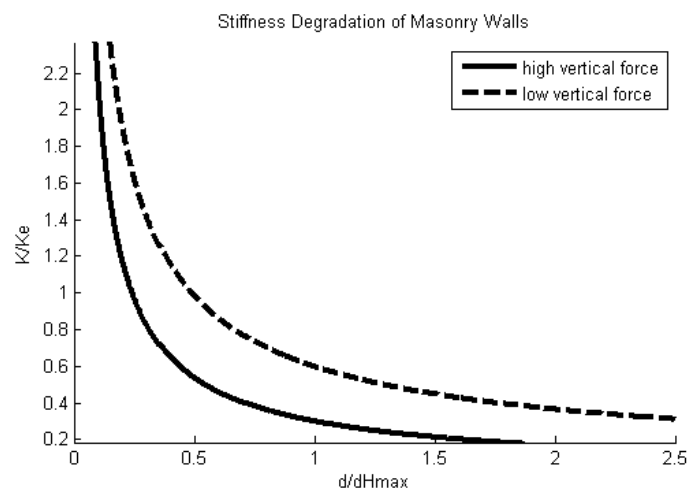
Figure 2.4 Stiffness Degradation Function for Different Levels of Vertical Load, Proposed by Tomazevic et al. (1996)

17

Bosiljkov et al. (2005) investigated the effect of precompression on the stiffness degradation of URM walls. According to an experimental study result", shape of the stiffness degradation curve for cantilever elements depend on the level of precompression (see Figure 2.5). Figure 2.5 also verifies Equation 2.9 in the way that although stiffness degradation function depends on level of precompression, its shape remains unchanged.
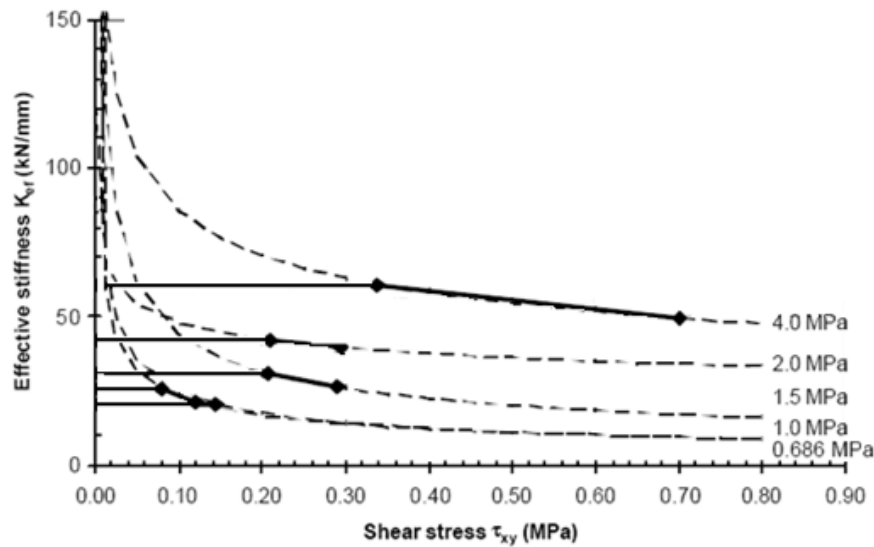
Figure 2.5 Stiffness Degradation vs. Shear Stresses for Different Levels of Precompression, Bosiljkov et al. (2005)

Similar observations were also made by Tian Yi et al (2006). According to the experimental research on a full-scale two-story URM frame which is tested in a quasistatic fashion, it is observed that effective elastic modulus of the masonry decreased rapidly from the initial value of 7 GPa to about 0.9 GPa at a roof displacement of 6.4 mm which corresponds to an inter-story drift of about 0.14% for the first story and about 0.05% for the second story. At this stage only 13% of initial stiffness could be preserved.

The reason why large elastic stiffness of squat masonry walls decreases rapidly, with a small increase in lateral drift, is explained by Anderson and Brzev (2009). They state that the response is initially elastic until cracking takes place. Then there is a large drop in stiffness. This is particularly pronounced after the development of diagonal shear cracks. After a few major cracks develop, the load resistance is taken

over by the diagonal strut mechanism. However, the stiffness drops significantly shortly after the strut mechanism is formed, and can be considered to be zero for most practical purposes.

2.1.3 Ultimate Drift Limit for URM Walls

Ultimate drift limit is an important parameter indicating the deformation capacity of the wall. In force-based approach, member strength is compared with force demand and ultimate drift is not needed. Whereas in displacement-based assessment of structures, structure is pushed into nonlinear range and only members which are capable of accommodating imposed displacement can survive.

Ultimate drift limit for a masonry wall depends on the failure mode of the wall. Flexure dominant failures such as bed joint sliding and rocking results in larger ultimate drifts whereas shear dominant failures such as diagonal tension failure ends up in a brittle failure with smaller ultimate drifts.

Based on the experimental test results collected by FEMA 307 (1999), deformation capacity of URM walls corresponding to different failure mechanisms are illustrated in Table 2.1.

Table 2.1 Ultimate Drift of URM Walls Corresponding to Different Failure Modes (FEMA 307, 1999)

Failure mode	Ultimate drift (%)	Reference
Rocking	0.6 to 1.3	Anthonie (1995), Magenes&Calvi (1995), Costley&Abrams (1996)
Rocking / Toe Crushing	0.8	Abrams&Shah (1992)
Flexural Cracking / Toe Crushing / Bed-joint Sliding	0.8 to 1.3	Manzouri et al. (1995)
Flexural Cracking / Diagonal Tension	0.5 to 0.8	Anthonie (1995), Magenes&Calvi (1992), Magenes&Calvi (1995)
Flexural Cracking / Toe Crushing	0.2 to 0.4	Abrams&Shah (1992), Epperson and Abrams (1989)

According to Magenes and Calvi (1997), pure rocking and bed-joint sliding failure modes are stable and an ultimate displacement limit for these failures has no meaning because other failures like toe crushing and diagonal tension determines the displacement limit before wall fails under pure rocking or sliding. To illustrate, in case of rocking failure, if no other failure mechanism takes place, ultimate displacement can be attained only by a decrease in strength depending on P-Δ effects which may correspond to lateral displacement of 10% of the wall height.

As a result of experimental tests, Magenes and Calvi concluded that, in diagonal shear failure, drift at ultimate state tends to be a uniform number with a mean 0.53% and coefficient of variation of 10% (see Table 2.2).

Table 2.2 Ultimate Drift Associated with Diagonal Shear Failure from Experimental Quasi-static Tests (Magenes and Calvi, 1997)

Wall	h/L	p (MPa)	δ_u/h (%)	δ_u/δ_y
MI1 (+)	1.33	1.12	0.51	4.25
MI2 (-)	1.33	0.68	0.60	2.53
MI3 (+)	2.00	1.24	0.48	3.27
MI3 (-)	2.00	1.24	0.49	4.63
MI4 (+)	2.00	0.69	0.50	1.83
MI4 (-)	2.00	0.69	0.60	2.28
ISP1 (+)	1.35	0.6	0.44	4.54
ISP1 (-)	1.35	0.6	0.54	7.30
ISP3 (+)	1.35	1.08	0.53	6.45
ISP3 (-)	1.35	1.08	0.62	7.55
		mean	0.53	4.46
		c.o.v (%)	10.39	43.94

2.2 Nonlinear Modeling of Masonry

A certain number of methods have been utilized for the study of URM buildings so far. Due to the diversity and high level of complexity inherent to masonry, the approach towards the analytical modeling has led researchers to seek for several constitutive models characterized by different levels of complexity.

From sophisticated finite element micro models to limit analysis approaches, a wide range of numerical methods are available in literature. Equivalent frame models and limit analysis methods are user friendly and require lesser amount of data. However compared to FEM models both of them is limited in terms of simulating distribution of nonlinearity, force redistribution, coupling effect between orthogonal walls, mode of failure prediction and so on.

Although finite element models are the most reliable among all, the best method might be defined as "the method that provides the sought information in a reliable manner, i.e. within an acceptable error, with the least cost" (Oliviera, 2003).

Lourencho (1996) summaries finite element modeling strategies defined in literature depending on the level of refinement used for the structural analysis as below (see Figure 2.6):

• Detailed micro-modeling – requires discrete modeling of mortar, brick units with continuum elements and unit mortar interface with discontinuous elements.

• Simplified micro-modeling – brick units are modeled with continuum elements whereas the behavior of the mortar joints and unit-mortar interface is lumped in discontinuous elements;

• Macro-modeling - units, mortar and unit-mortar interface are smeared out in the continuum.

Each modeling technique starting from the most sophisticated to least will be investigated in detail in the following sections.
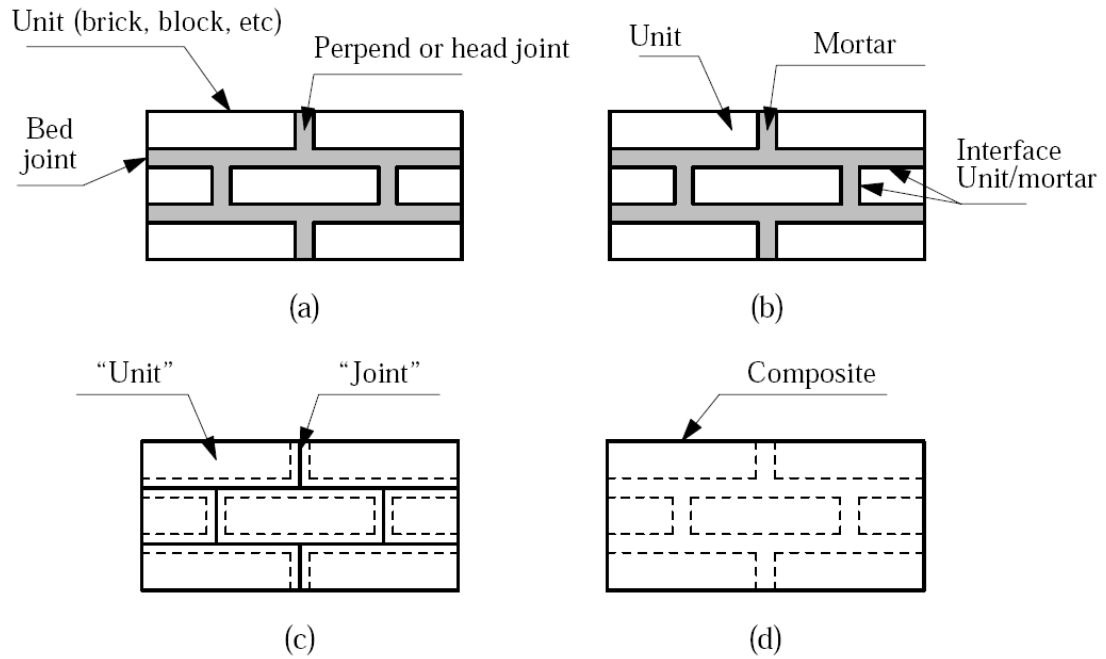
Figure 2.6 Modeling Strategies for Brick Masonry: a) typical masonry sample, b) detailed micro modeling, c) simplified micro-modeling, d) macro-modeling (Lourencho, 1996)

2.2.1 Finite Element Micro-Model

Masonry is a composite material consisting of brick units and mortar joints. In order to reflect the complex nature of the masonry, a complete model should accommodate discrete brick units, mortar joints and the unit-mortar interface whose mechanical properties are different. Finite element micro models represent masonry from the knowledge of mechanical properties of each constituent and the unit mortar interface which require detailed experimental description.

Gathering reliable description of mechanical properties of brick units, mortar joints and interface between them requires massive experimental study due to the diversity inherent to masonry materials and construction practices. According to Lourencho (1996), "the properties of masonry are influenced by a large number of factors, such as material properties of the units and mortar, arrangement of bed and head joints, anisotropy of units, dimension of units, joint width, quality of workmanship, degree of curing, environment and age."

Furthermore finite element micro models require extensive computational facility and complicated failure criterion (Elgawady et al, 2006). As a result finite element micro models are practically applicable to small structural elements in which stress and strain states are heterogeneous.

After studying finite element modeling techniques in detail, Lourencho (1996) concludes that "for large structures, the memory and time requirements become too large and, if a compromise between accuracy and economy is needed, a macro-modeling strategy is likely to be more efficient."

2.2.2 Finite Element Macro-Model

In the modeling of large structural elements, a relation might be defined between average masonry stresses and average masonry strains since neglecting heterogeneous nature of local stress distribution does not have a great influence on global response. Instead of discrete modeling, homogenization of brick units and mortar joints is utilized to generate finite element macro model of masonry.

Compared to micro models, fewer amounts of material parameters which means fewer amounts of experimental work is sufficient for macro model generation. To illustrate, tests on brick units, mortar cubes and small wallets are needed to be conducted to define mechanical properties of masonry constituents and brick mortar interface for micro model generation. Whereas tests conducted on sufficiently large size of composite materials are enough for mechanical property definition of URM walls for macro model generation.

The major drawback of the approach is that under weak mortar strong brick unit combination or vice versa, homogenization of structural properties leads to improper simulation of the local weaknesses of the bricks or the mortar. Moreover some failure modes of masonry such as diagonal tension or sliding in a stair stepped manner could not be caught by macro models.

2.2.3 Equivalent Frame Model

Equivalent frame method is a simple way to conduct nonlinear analyses on URM structures. Least amount of data is required to describe material property among other modeling strategies since homogenous, isotropic material idealization is made. Local nonlinear behavior of each wall is described with nonlinear hinges whose force displacement properties are usually defined from experimental test results.

Being both simple and effective, a wide range of studies to improve the reliability of the EFM is found in the literature. Attempts to simulate nonlinear behavior of URM with equivalent frame models are summarized below:

Gilmore et al. (2009) proposed an equivalent frame model to perform pushover analysis of confined masonry buildings. Structural degradation of confined masonry walls is associated with shear behavior and a rotational shear spring to idealize nonlinear response of masonry walls is proposed. Rotational spring is used to relate shear force on the wall with inter-story drift due to shear deformation. For this purpose hinge is located at the bottom of the wall (see Figure 2.7).
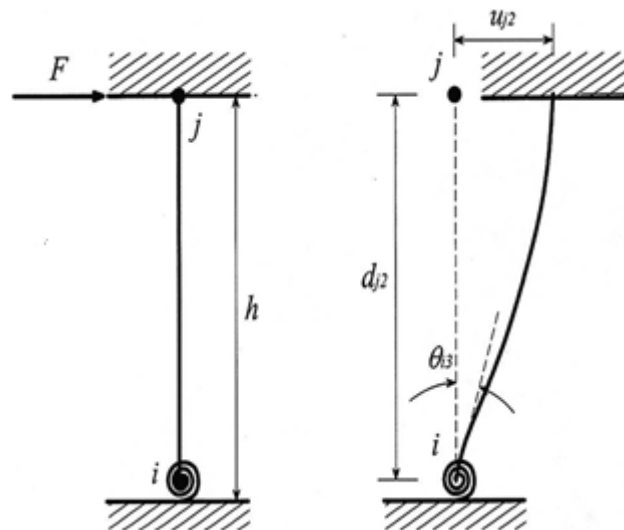
Figure 2.7 Modified Wide Column Model for PO Analysis (Gilmore at al., 2009)

Main limitation of the model is; proposed force-deformation relationship of the springs is independent of aspect ratio and axial load level (see Figure 2.8). It is determined from idealized backbone curve for confined walls which are build using

confined handmade clay brick used in Mexico. As a result, authors give a warning that proposed shear hinge model meant to describe a general state of structural degradation only in the critical story of buildings having similar design and construction practices of Mexico.
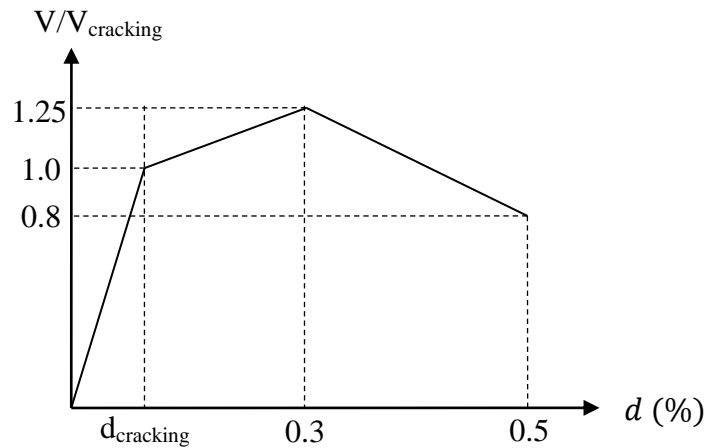
Figure 2.8 Idealized Backbone Curve for Confined Masonry Walls (Gilmore at al., 2009)

Finally a lateral load distribution proportional to modal shape of fundamental mode is used for pushover analysis of a typical confined masonry building in Mexico whose experimental results are satisfactory captured with the proposed computer model.

Kappos et al. (2002) conducted elastic and plastic comparative analyses on two and three dimensional masonry structures aiming to evaluate accuracy of equivalent frame modeling technique. In elastic analyses of a two dimensional perforated wall, equivalent frame and finite element models are formed. Extend of rigid offsets to be employed in equivalent frame model (i.e. full horizontal rigid offsets, full horizontal and vertical rigid offsets and full horizontal and half vertical rigid offsets) and diaphragm constraint are determined as parameters under evaluation. According to analysis results, equivalent frame model with full horizontal and vertical rigid offset yields results closest to finite element model. Also effect of diaphragm constrain is found to be negligible for planar structures whereas crucial for three dimensional structures. For nonlinear analyses finite element model is generated using ANSYS

and equivalent frame model is generated using SAP2000. After proposed model is validated against test data conducted in University of Pavia and Ismes laboratory, EFM is found to be effective and reasonably accurate for nonlinear analysis of masonry buildings.

Salonikios et al. (2003) conducted comparative inelastic analyses on nonlinear equivalent frames and finite element models of 2D masonry frames. Influence of different lateral force distributions on pushover analysis of masonry frames is investigated due to the fact that important fraction of the total mass is distributed along the wall height in masonry buildings which makes it harder to determine load distribution during pushover analyses.

In equivalent frame modeling of masonry elements, flexural and shear hinges are employed together. It is claimed that when an URM building is subjected to earthquake both bending and shear mechanisms are activated and failure will first appear at the location with the smallest strength. Thus, moment-rotation hinges are located at both ends and shear-displacement hinge is located at the mid-span of the element (see Figure 2.9). The constitutive laws of the plastic hinges are defined according to FEMA 273.
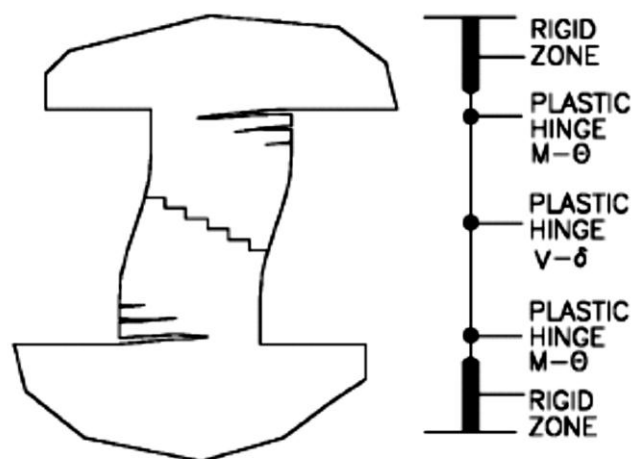
Figure 2.9 Modeling Details for Piers in the Computer Program (Salonikios et al., 2003)

Lateral load distributions imposed on the structure are uniform distribution, inverse triangular distribution and first mode shape distribution. According to analysis results, lateral load distribution does not have an affect on base shear capacity of the structure since ultimate condition is reached by shear failure of all piers in the first storey. Comparing initial stiffnesses under different lateral distribution of lateral loads, higher stiffness under uniform distribution is observed. Although same shear is applied to base story piers for different load distributions, shear force at the upper story piers are higher for inverse rectangular and modal distribution than uniform distribution. Thus a lower roof displacement is observed for uniform distribution of lateral forces.

Pasticier et al. (2007) aimed to utilize SAP2000 for seismic analyses of masonry buildings using EFM. In nonlinear modeling of masonry piers, two rocking hinges at the end of the rigid offsets and one shear hinge at the middle of the pier is used. On the other hand, only one shear hinge was introduced for nonlinear modeling of spandrels. Lateral loads are applied by assuming the inverted triangular distribution. Since SAP2000 does not allow for automatic update of shear strengths due to change in axial load level caused by overturning effect, two different axial load distribution on piers are tested. In the first distribution, axial load on piers are calculated under dead loads only whereas in the second distribution hinge properties are determined under axial load levels calculated by applying dead loads and increasing the lateral loads up to the attainment of the elastic limit of the frame.

According to analysis results, ultimate strength and top displacement are not affected due to different methods to determine axial load distribution on piers. It is stated that main drawback of the SAP2000 which is the impossibility to update the strengths of the piers based on the variation of axial force seem not to be so crucial in pushover analyses on equivalent frames.

Two different distributions of lateral loads (i.e. uniform distribution, inverted triangular distribution) are utilized for pushover analyses. In inverted triangular

distribution the collapse is due to storey mechanism at the second story, while with the uniform distribution mechanism occurred at the base story.

Belmouden and Lestuzzi (2007) come up with and equivalent frame model for seismic analysis of masonry buildings. Unlike other proposed models up to the present, analytical model is based on smeared crack and distributed plasticity approach. Moreover interaction between both axial force-bending moment and axial force-shear force are considered. Inelastic flexural as well as inelastic shear deformations are allowed for piers and spandrels. Translational shear springs are added at the middle of the span and flexural hinges are added at the ends of the span. However since piers and spandrels are discretized into series of slices, nonlinearity is distributed along the length of the spans (see Figure 2.10).
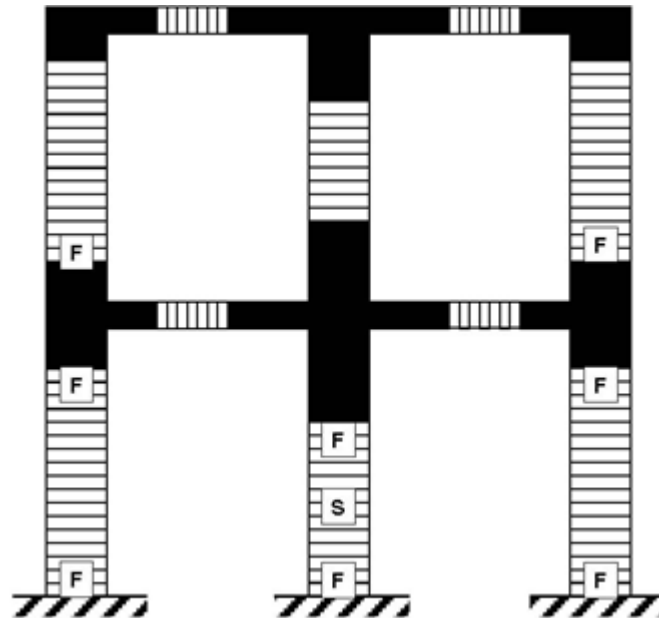
Figure 2.10 Spread Nonlinearity Approach in EFM (Belmouden and Lestuzzi, 2007)

Spandrels which provide coupling to piers are modeled as elastic and the length of the spandrels are taken equal to zero moment length which is updated at each step of the pushover analysis depending on the end moments of the spandrels. Reliability of the model is sustained by comparing model results with experimental results conducted in University of Pavia.

Roca et al. (2005) studied 2D wall panels as equivalent systems of one-dimensional members, namely equivalent frames. Force deformation characteristic of masonry in compression is modeled with Kent and Park model. Axial force-shear force interaction is considered through use of Mohr-Coulomb criterion as biaxial stress envelope. After comparing numerical model with experimental results conducted by D'Asdia in 1972, it is concluded that EFM is capable of predicting failure mechanism and ultimate loading capacity of load-bearing wall masonry systems.

Penelis (2006) developed a method for pushover analysis of URM buildings using EFM. Rotational hinges using lumped plasticity approach are utilized at the ends of structural elements for nonlinear action. Constitutive law of the nonlinear springs is defined by moment rotation curve of each element under constant axial load where rotation is taken as sum of rotation due to flexure and rotation due to shear. Since axial force-bending moment interaction is ignored in material model, axial load level on piers at which hinge properties defined are determined by a linear analysis where in addition to gravity loads and an estimate of lateral load corresponding to base shear capacity is taken into account. Use of vertical rigid offsets is avoided claiming that vertical rigid offsets restrain the extent of cracking unrealistically. Finally model proposed by Penelis is verified with experimental results conducted at the University of Pavia and Ismes laboratory at Bergamo.

Magenes and Fontana (1998) proposed a method named as SAM (simplified analysis of masonry buildings) for simplified non-linear seismic analysis of masonry buildings through equivalent frame idealization of URM walls subjected to in-plane loadings. Constitutive relation of structural members is idealized as elastic-perfectly plastic where shear strength of members are calculated from simple strength equations in literature. A limit to total chord rotation (i.e. flexural rotation plus shear rotation) is assigned as 0.5% for shear failures and 1% for flexural failures. An effective height is used for structural elements in terms of rigid end offsets proposed by Dolce (1989) for the definition of the stiffness matrix in the elastic range. After generation of computer model, parametric analyses are made to determine rigid

offset length. Due to analysis results, full rigid offsets in piers and spandrels prevailed full rigid offset in spandrels only and no rigid offsets at all.

2.2.4 Limit Analysis

Limit analysis is an analysis method especially used to estimate the maximum load that a structure can sustain prior to failure. It is based on the application of the limit theorems of plasticity over possible ultimate mechanisms. In order to consider various possible ultimate mechanisms an iterative solution is required (Roca et al., 2005). It might be regarded as a practical computational tool for failure pattern and ultimate load calculation of URM structures since it only requires a reduced number of material parameters (Oliviera, 2003).

Orduna (2003) applied limit analysis method to URM structures which are modeled as assemblages of rigid blocks connected through joints (see Figure 2.11). Proposed model composed of rigid-perfectly plastic blocks possessing yield surfaces. For critical stress levels on the yield surface, the material becomes plastic and flows normal to the direction of yield surface. In order to apply limit analysis to URM structures some assumptions are made:

- Masonry has no tensile strength.
- Masonry has an infinite compressive strength
- Sliding failure cannot occur
- Failure occur under small displacements
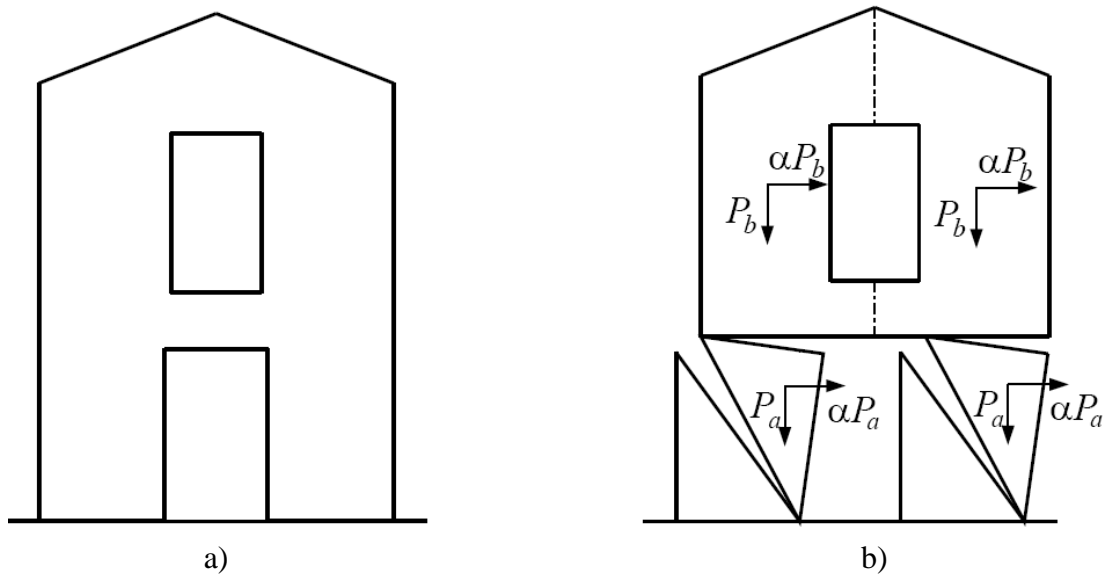
Figure 2.11 Limit Analysis Model for Perforated URM Wall; a) wall, b) failure mechanism (Orduna, 2003)

2.3 Performance Assessment of URM

Performance based assessment of a URM building requires estimation of system damage under a given earthquake demand. According to Tomazevic (2007) structural damage in masonry buildings might be directly related to storey drift and it is independent of type of the masonry. As a result experimental works which relate performance level of URM walls and buildings with lateral drift have a great importance for application of performance based concepts for URM.

2.3.1 Performance Limit States of URM Walls

In order to assess system damage, one has to start from assessment of seismic performance of single structural element (Bosiljkov et al., 2008). Since damage state of a building is directly related to damage of its force resisting members, many researchers investigate the relationship between drift and damage of masonry walls.

Alcocer et al. (2004) conducted drift-controlled cyclic tests on confined masonry walls in order to investigate relationship between lateral drift, wall aspect ratio, wall

vertical stress, type of brick units, type of mortar, reinforcement detailing of confining columns and transverse reinforcement.

According to test results three limit states for masonry piers, namely, serviceability, reparability and safety is identified. Serviceability limit state is associated to onset of masonry inclined cracking, reparability limit state is associated to formation of full inclined cracking and safety limit state is associated to large masonry cracks with a residual width of 5 mm.

Detailed explanation of limit states in relation with crack width and drift angle is illustrated in Table 2.3.

Table 2.3 Performance Criteria for Confined Masonry Structures with Solid Clay Units (Alcocer et al., 2004)

Limit State	Criterion	Residual crack width, mm	Driftt angle, %
Serviceability	Onset of masonry inclined cracking	0.1	0.15
Reparability	Inclined cracking fully formed over masonry wall; hairline cracking into tie-columns; onset of masonry crushing	2	0.25
Safety	Shear strength of wall; wall cracking penetrates into tie-column ends; yielding of tie-column reinforcement due to shearing; onset of tie-column crushing	5	0.4

Four performance levels are defined by Bosiljkov et al (2008) for the performance assessment of URM walls, namely, fully operational, immediate occupancy, life safety and near collapse. In fully operational limit state operation of the building is not disturbed and slight damage occurs. In functional limit state operation of facility continues with minor damage. In life safety limit state, damage is moderate to extensive. In near collapse limit state damage is severe but structural collapse is prevented.

Drift limits on force-displacement curve of masonry walls is identified in order to relate performance states to lateral drift. Crack limit is described by displacement δ_{cr} and resistance H_{cr}. Formation of first flexural cracks which usually corresponds to first change in slope of lateral force-displacement diagram is the identification of crack limit. Shear crack limit which is denoted by displacement δ_{dt} and resistance H_{dt} is identified by occurrence of diagonal shear cracks or horizontal flexural cracks depending on the type of failure. Maximum resistance limit is denoted by δ_{Hmax} and H_{max}. Finally ultimate state is denoted by maximum displacement δ_{max} and corresponding resistance $H_{\delta max}$ (See Figure 2.12).
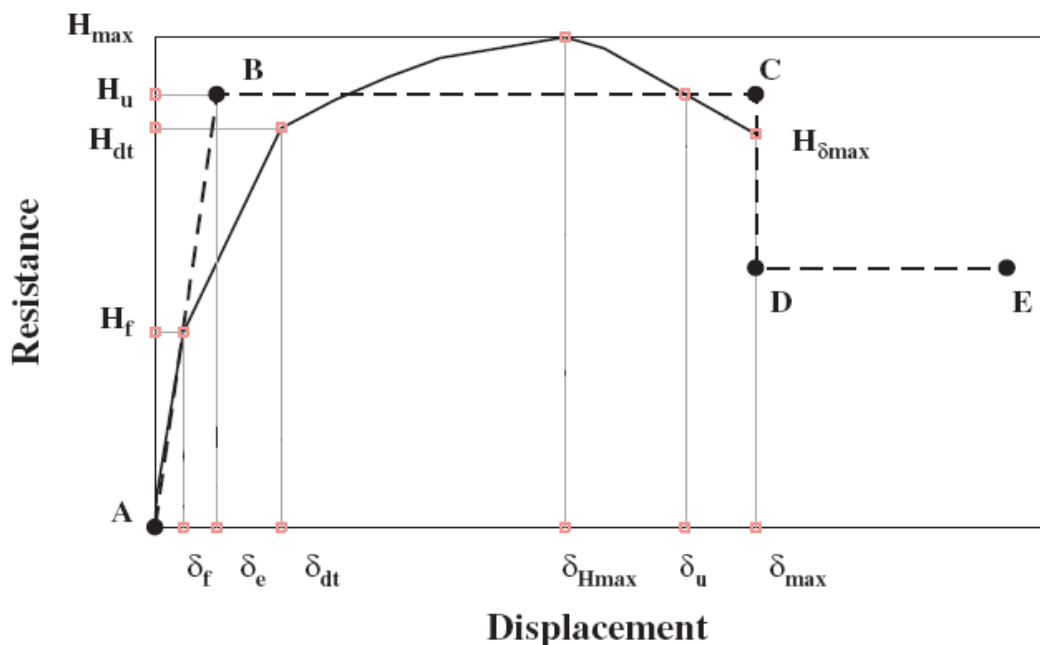
Figure 2.12 Displacement Limits Illustrating Performance Limit States Defined by Bosiljkov et al. (2008) and FEMA 356 (dashed)

According to the laboratory tests made by Bosiljkov et al. (2005) on URM specimens made with various mortar types and different overburden pressures, drifts corresponding to performance levels are shown in Table 2.4. As it is seen on the table, level of axial load determines the failure mechanism, altering deformation capacity of piers. Under low axial load levels flexure dominated failure modes resulted in larger drift values, whereas as axial load level increases shear mechanisms dominate behavior resulting in a brittle, less ductile behavior.

Table 2.4 Performance Drift Limits for URM Cantilever Walls, Bosiljkov et al. (2005)

Failure mode	Precompression	Performance (%)			
		Fully operational	Immediate occupancy	Life safety	Collapse prevention
Sliding failure	1/16 f_m	0.0	-	0.9	1.8
Rocking failure	1/12 f_m	0.0	-	1.8	1.8
Rocking failure	1/8 f_m	0.1	-	1.2	2.5
Diagonal failure	1/6 f_m	0.1	0.5	0.7	0.9
Diagonal failure	1/3 f_m	0.1	0.2	0.5	0.5

In FEMA 356 masonry piers are categorized as force controlled or deformation controlled depending on the failure mechanism of the pier. First a comparison between simple strength equations indicating rocking, sliding, diagonal tension and toe crushing strength are made. Among calculated strengths lowermost prevails the response. If diagonal tension or toe crushing strength overcomes, response is supposed to be force controlled. Otherwise displacement controlled response is assumed with the limit states defined for bed-joint sliding as 0.1%, 0.3%, 0.4% for IO, LS, CP performance levels respectively and for rocking as 0.1%, $0.3h_{eff}/L$%, $0.4h_{eff}/L$% for IO, LS, CP performance levels respectively.

Performance limit states of URM walls defined in literature is summarized in Table 2.5 below:

Table 2.5 Performance Drift Limits for URM Walls

Author	Failure mode	Performance Level (%)		
		IO	LS	CP
FEMA 356 (2000)	Rocking	0.1	$0.3h_{eff}/L$	$0.4h_{eff}/L$
Franklin et al. (2001)		0.1	0.9-1.5	1.2-1.9
Bosiljkov et al. (2008)		0.1	1.2-1.8	1.8-2.5
FEMA 356 (2000)	Sliding	0.1	0.3	0.4
Bosiljkov et al. (2008)		-	0.9	1.8
Alcocer et al. (2004)	Diagonal tension	0.15	0.25	0.4
Bosiljkov et al. (2008)		0.2-0.5	0.5-0.7	0.5-0.9

2.3.2 Performance Limit States of URM Buildings

From force-displacement relationship of components, capacity curve of global structure might be obtained. In order to assess structural performance, limits on global resistance curve should be determined. Several authors investigate the relationship between structural damage and structural performance.

In order to find a correlation between the occurrence of damage, limit states and lateral displacement capacity, Tomazevic (2007) conduct lateral resistance tests on masonry walls and shaking table tests on masonry buildings. He defined four limit states on the capacity curve in order to be used for seismic resistance verification of masonry buildings (see Figure 2.13).

1.   Crack limit state: It is identified by formation of first cracks in the walls. This limit is associated by serviceability limit state of the structure.
2.   Maximum resistance
3.   Design ultimate limit state: Resistance of the system degrades below acceptable level which corresponds to 20% degradation of maximum resistance
4.   Collapse limit state: defined by partial or total collapse of the structure
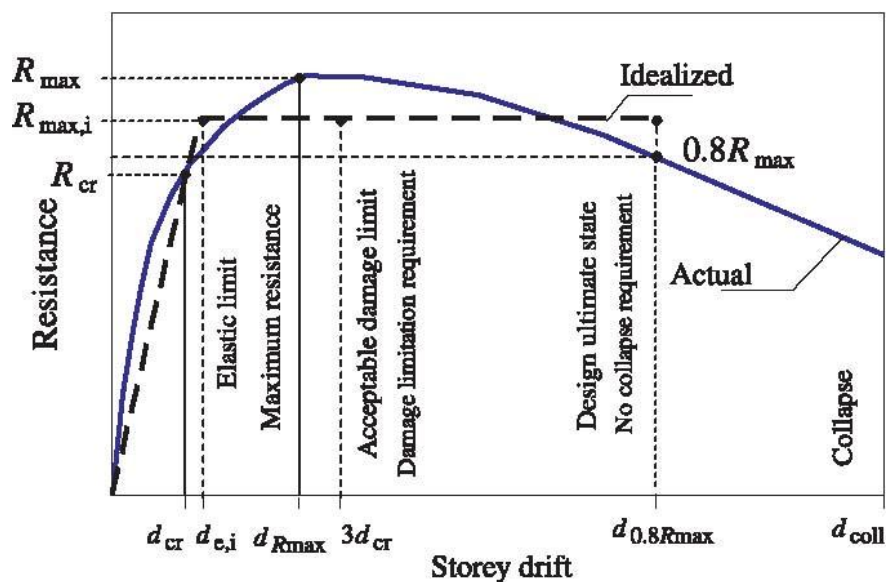
Figure 2.13 Elasto-plastic Idealization and Limit States on the Capacity Curve of URM Buildings (Tomazevic, 2007)

As a result of laboratory tests on confined and URM masonry buildings, Tomazevic propose following story rotation values associated to corresponding limit states for masonry buildings:

Crack limit state = 0.2% - 0.4%

Maximum resistance = 0.3% - 0.6%

Collapse limit state = 2% - 4%

However these numbers are calculated from a set of plain and confined masonry building test results. Since confinement enhances ultimate displacement capacity, collapse limit states for URM buildings will be lower than proposed values. Manipulating drift limits considering only URM building test results, collapse limit state will be reduced to 1% and 2%.

Another effort is made by Calvi (1999) for the evaluation of the vulnerability of different classes of masonry buildings. Starting with definition of limit states that indicate performance levels, Calvi proposed a relation between inter-story drift and the four limit states. Namely,

LS1: No damage. Expected response is linear elastic

LS2: Minor structural damage. The building can be utilized after the earthquake without any need for repair.

LS3: Significant structural damage. The building cannot be used after the earthquake without significant repair

LS4: Collapse. Repairing the building is neither possible nor economical. Beyond this limit total collapse with danger for human life is expected.

Calvi proposed base storey drift values for limit states of masonry buildings:

LS1-LS2 = 0.1%

LS3 = 0.3%

LS4 = 0.5%

In the light of past experimental studies, threshold values utilized by Ömer Onur Erbay (2007) for his analytical study on URM buildings are given below:

Immediate Occupancy = 0.1%

Life Safety = 0.6%

Collapse Prevention = 1%

Total Collapse = 2%

Also in FEMA 356, structural performance levels associated with level of damage is provided in Table C1-3.

Immediate Occupancy = 0.3%

Life Safety = 0.6%

Collapse Prevention = 1%

To sum up performance limit states for masonry buildings are defined in Table 2.6 below.

Table 2.6 Performance Drift Limits for URM Buildings

	Performance Level (%)		
Author	**IO**	**LS**	**CP**
FEMA 356 (2000)	0.3	0.6	1.0
Tomazevic (2007)	0.2-0.4	0.3-0.6	1.0-2.0
Calvi (1999)	0.1	0.3	0.5
Erbay (2007)	0.1	0.6	1.0

CHAPTER 3

LATERAL ELASTIC RESPONSE OF URM WALLS

Resistance of URM buildings to lateral loads such as earthquake and wind load are achieved by in plane walls which are oriented parallel to the direction of the force. In the elastic range where Hooke's law is valid, relation between lateral forces and displacements are determined by lateral stiffness. Elastic lateral stiffness indicates the resistance of a wall to lateral forces, determines overall dynamic behavior and distribution of seismic forces in the structure.

Elastic lateral stiffness of URM walls is a combination of flexural and shear stiffness's which are functions of wall dimensions (see Figure 3.1), boundary conditions and mechanical properties of the wall.
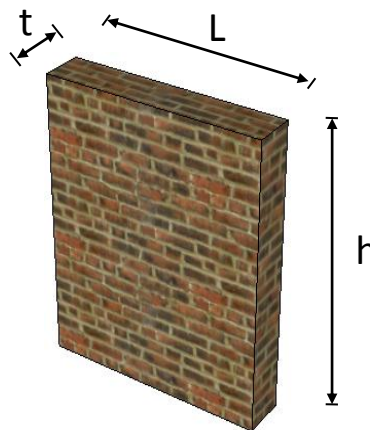
Figure 3.1 Dimensions of a Rectangular Brick URM Wall

Chapter 3 deals with elastic lateral stiffness calculation of solid and perforated URM walls. " and shear mechanisms on total stiffness for extreme boundary conditions (i.e. cantilever wall and both ends fixed wall). Then, total elastic lateral stiffness of a masonry wall coupled with spandrels is derived assuming isotropic and homogenous material behavior.

In section 3.2; a modeling technique which idealizes perforated URM walls as frame elements such as piers and spandrels is presented and it is calibrated by varying effective heights of piers and spandrels. For this purpose, some comparative linear analyses between finite element models derived using ANSYS (2007) and equivalent frame models derived using SAP2000 (2009) for selected frames are conducted. As a result of comparative analyses, the best approach for RO length for masonry piers and spandrels are determined.

3.1 Lateral Stiffness of Solid URM Walls

Lateral stiffness of solid URM walls is composed of shear stiffness and flexural stiffness. Unlike typical one dimensional frame members like beams and columns of a RC or steel frame; contribution of shear is usually dominant in masonry walls. Shear stiffness is related to shear rigidity and height of the wall, whereas flexural stiffness is related to flexural rigidity and height of the wall as well as the boundary conditions of the wall.

Since lateral flexural stiffness depends on the boundary conditions, total lateral stiffness is often calculated for two extreme boundary cases using equation 3.1.

$$k_t = \left(\frac{h^3}{\beta EI} + \frac{h}{\kappa AG}\right)^{-1} \qquad (3.1)$$

Where;

h is the height

β is boundary condition parameter

EI is flexural rigidity

κAG is shear rigidity

The first and the second term inside the parenthesis represent contribution of flexure and shear mechanisms respectively. Boundary condition parameter depends on the rotational restrain on the top of the wall. For cantilever walls (see Figure 3.2a) which are free to rotate and move horizontally at the top, it is equal to 3.This case is appropriate for single story masonry building walls with flexible diaphragm. On the

other hand for both ends fixed walls (see Figure 3.2b) which are free to move horizontally but restrained to rotate at the top, boundary condition parameter is equal to 12. This case is appropriate for walls where restraining effect of slab, lintel beam and the spandrels are dominant.
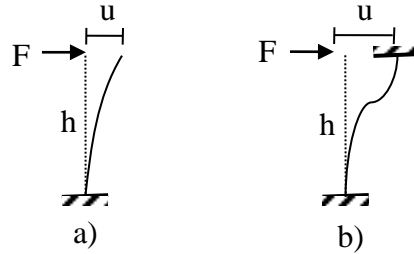
Figure 3.2 Extreme Boundary Conditions of Walls a) Cantilever Boundary Condition b) Both end Fixed Boundary Condition

For masonry walls with rectangular cross sections (see Figure 3.1) below equations hold:

Moment of inertia of wall $(I) = \frac{1}{12} t L^3$

Area of cross section $(A) = Lt$

Aspect ratio of wall $= \frac{h}{L}$

Shear coefficient $(\kappa) = \frac{5}{6}$

Shear modulus $(G) = \frac{E}{2(1+v)}$

When relations above for walls with rectangular cross sections are inserted into Equation 3.1, elastic lateral stiffness for solid rectangular URM walls simplifies to equation below:

$$K_e = \left[\frac{5\beta E t}{60(\lambda)^3 + 12\beta(1+v)(\lambda)} \right] \qquad (3.2)$$

From basic relation between force and displacement of linear systems, lateral displacement due to unit lateral force might be defined below (see Equation 3.3).

$$u_{e=} \frac{1}{K_e} \qquad (3.3)$$

In order to explore the contributions of shear and flexure to total elastic lateral displacement, shear displacement over flexural displacement is plotted in Figure 3.3.
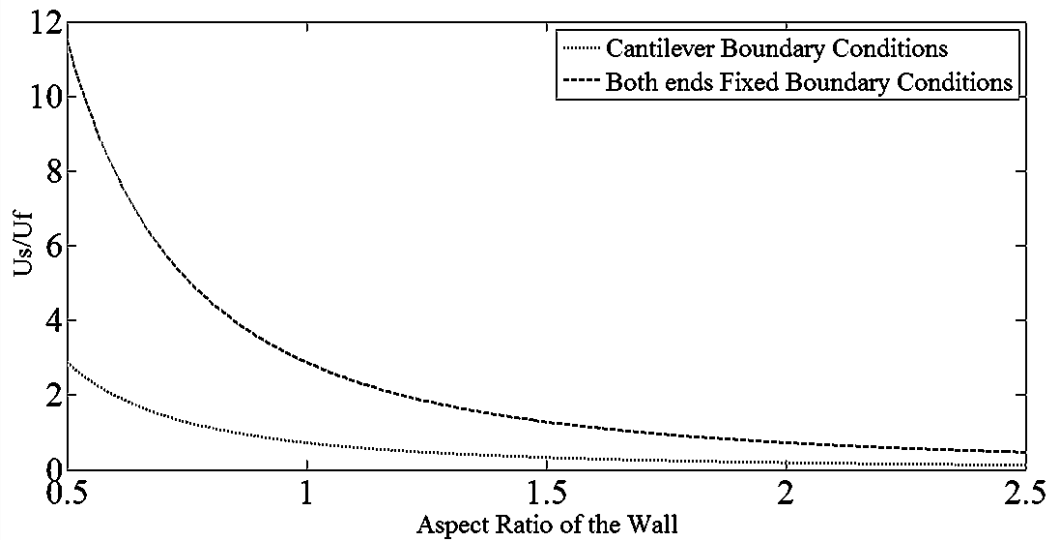
Figure 3.3 Shear Displacement over Flexural Displacement

Another representation of the same information is provided for a better understanding of contribution of shear and flexural displacement to total displacement. Figure 3.4 is drawn for cantilever boundary conditions and Figure 3.5 is drawn for both ends fixed boundary conditions.
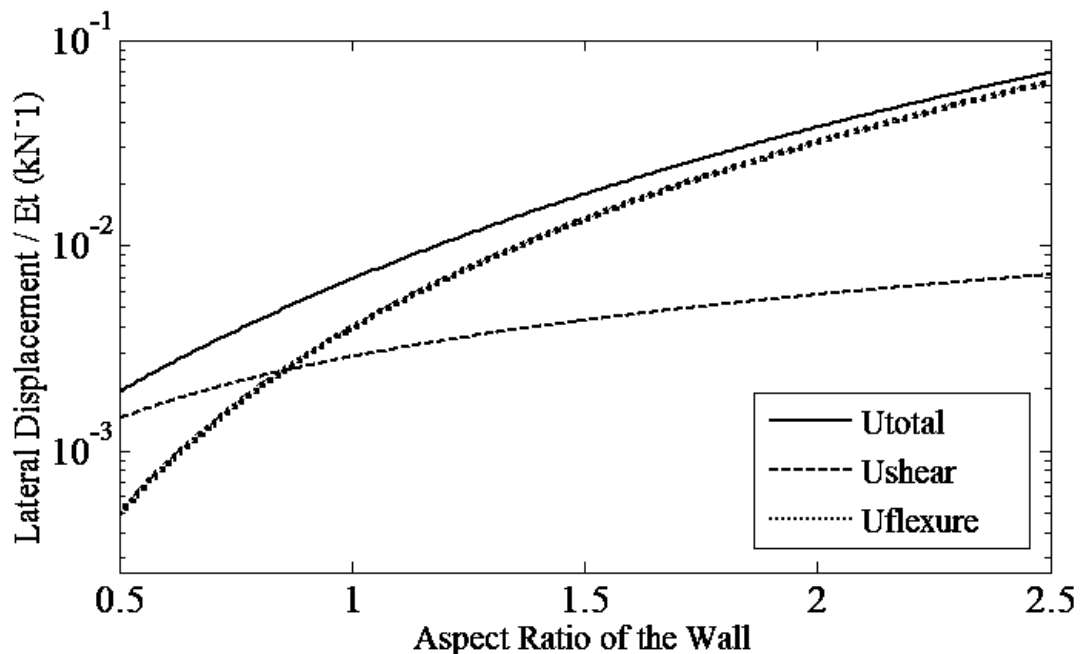
Figure 3.4 Contribution of Shear and Flexure to Total Lateral Displacement for Cantilever Walls
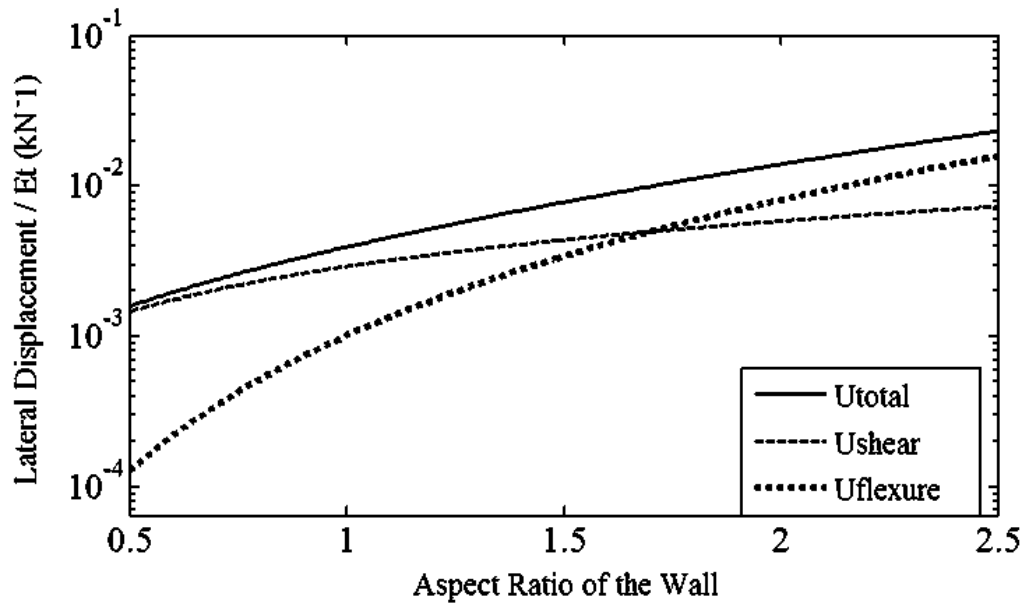
Figure 3.5 Contribution of Shear and Flexure to Total Lateral Displacement for Both ends Fixed Walls

As it is inferred from figures above, both flexural displacement and shear displacement increase with the increase in aspect ratio. However, increase in flexural displacement is cubic whereas increase in shear displacement is linear. As a result, although shear dominates behavior for squat walls, with the increase in aspect ratio, flexure starts to dominate the behavior. Shear displacement is equal to flexural displacement at $\lambda = 0.85$ under cantilever boundary conditions and at $\lambda = 1.7$ under both ends fixed boundary conditions.

Shear stiffness of masonry walls are not affected by boundary conditions whereas flexural stiffness is linearly dependent to boundary condition constant (see Equation 3.1). Boundary condition coefficient (β) depends on the rotational restraints at the tip of the wall. In a masonry frame, rotational restraints of piers are strongly affected by the coupling effect of horizontal elements connecting to piers such as spandrels, rigid slabs and reinforced concrete ring beams. Flexure is dominant for slender piers connected with weak spandrels and flexible slabs since aspect ratio is high and boundaries approach to cantilever type boundary conditions. On the other hand, shear dominates the behavior for short piers connected with strong spandrels and rigid diaphragms since aspect ratio is low and boundaries approach to both end fixed type boundary conditions.

Depending on the coupling effect of spandrels, lateral stiffness of masonry piers change abruptly. In case of weak coupling between piers (see Figure 3.6a), cantilever boundary conditions might be assumed. Nevertheless, in case of strong coupling between walls (see Figure 3.6b), both ends fixed boundary conditions might be assumed.

a)   b)
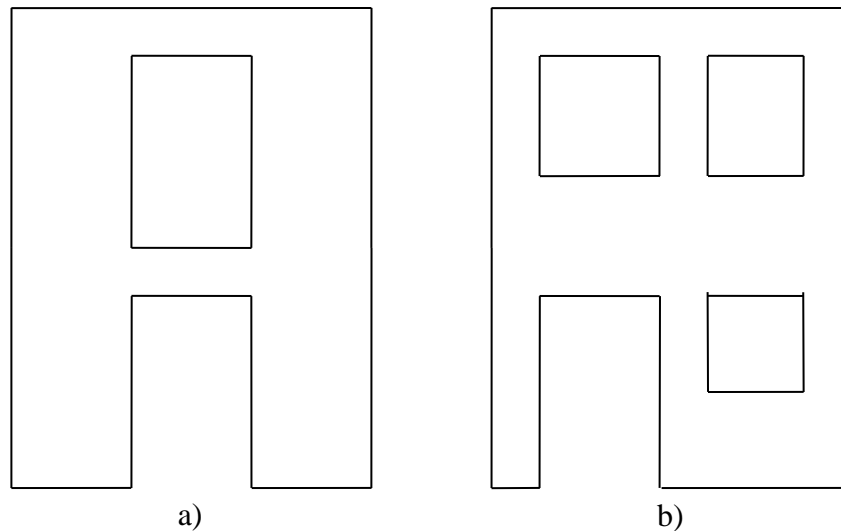
Figure 3.6 a) Weak Coupling Between Masonry Piers due to Poor Spandrels b) Strong Coupling Between Masonry Piers due to Robust Spandrels

So as to reveal the coupling effect of spandrels in detail, a rotational spring simulating rotational restrain of spandrels and upper story piers connecting to the wall might be utilized so that piers belonging to first story of a complex structure are idealized taking spandrel coupling into account (see Figure 3.12). Then, coupling effect of spandrels might be analyzed by identifying influence of spring constant on lateral stiffness.

In order to calculate lateral stiffness of one dimensional frame elements, instead of utilizing Euler-Bernoulli beam theory which assumes that deformations are due to bending only, shear deformations included formulation is preferred (see Figure 3.7) since shear deformations are often significant in lateral deflection of members with low aspect ratios.
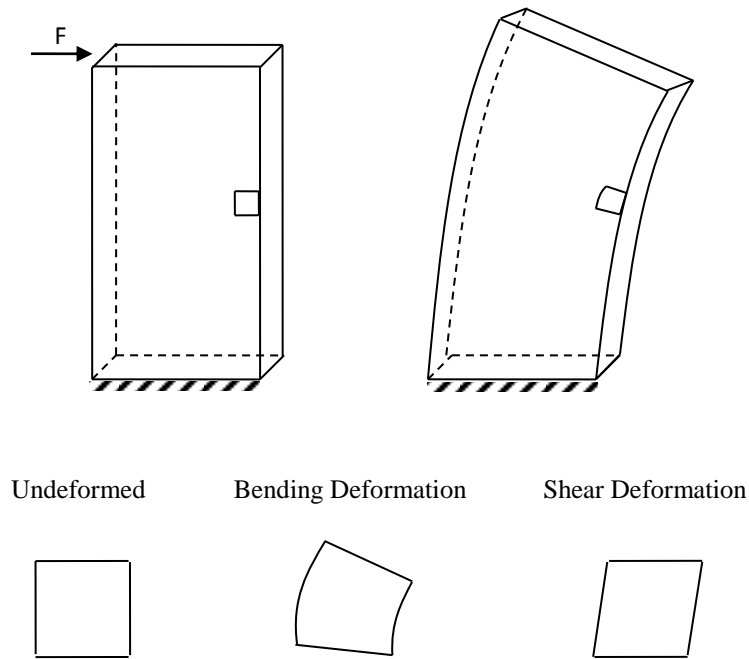
Figure 3.7 Infinitesimal Area on Cantilever Wall Showing Bending and Shear Deformations

As a result frame element stiffness matrix with shearing deformations (see Appendix A) is utilized for calculations. In order to calculate lateral stiffness of a masonry wall with cantilever boundary conditions, in addition to constrained degree of freedoms at the base, DOF in longitudinal direction at the tip is not taken into account since lateral stiffness is not affected by axial deformation.

Stiffness matrix of 2 DOF cantilever wall which is extracted from element stiffness matrix in Appendix A is given in Figure 3.8.
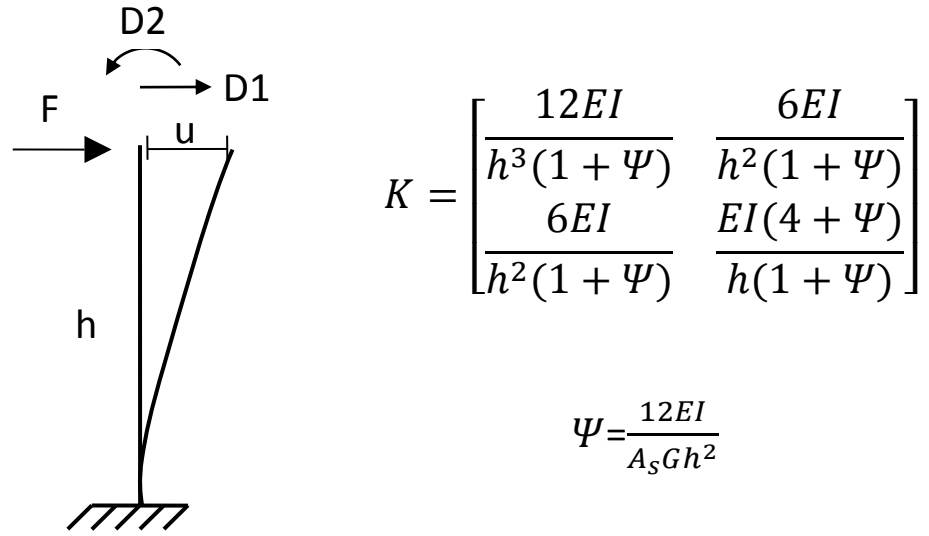
Figure 3.8 Stiffness Matrix of Cantilever Wall with Shearing Deformations Considered

Lateral stiffness of the wall in Figure 3.8 is calculated using static condensation. Application of static condensation is illustrated below:

First equation of equilibrium is written dividing DOF's in two sets: t (translation) and r (rotation). Translational DOF's will be kept and rotational DOF's will be reduced in static condensation process.

$$\begin{bmatrix} k_{tt} & k_{tr} \\ k_{rt} & k_{rr} \end{bmatrix} * \begin{bmatrix} u_t \\ u_r \end{bmatrix} = \begin{bmatrix} F \\ M \end{bmatrix} \tag{3.4}$$

Equation of equilibrium results in these equations:

$$k_{tt}u_t + k_{tr}u_r = F \tag{3.5}$$

$$k_{rt}u_t + k_{rr}u_r = M \tag{3.6}$$

Solving u_r from second equation gives:

$$k_{rt}u_t + k_{rr}u_r = M \ \rightarrow \ u_r = k_{rr}^{-1}(M - k_{rt}u_t) \tag{3.7}$$

Inserting Equation 3.7 into Equation 3.5 results:

$$\{k_{tt} - k_{tr}k_{rr}^{-1}k_{rt}\} * u_r = F - k_{tr}k_{rr}^{-1}M \tag{3.8}$$

Where:

$K^* = k_{tt} - k_{tr}k_{rr}^{-1}k_{rt}$ is named as condensed stiffness matrix,

$F^* = F - k_{tr}k_{rr}^{-1}M$ is named as condensed force vector.

When static condensation is applied to the cantilever wall, lateral stiffness is calculated as:

$$K^* = \frac{12EI}{h^3(1+\Psi)} - \frac{6EI}{h^2(1+\Psi)} \times \left(\frac{EI(4+\Psi)}{h(1+\Psi)}\right)^{-1} \times \frac{6EI}{h^2(1+\Psi)} \tag{3.9}$$

$$K^* = \frac{12EI}{h^3(1+\Psi)}\left[1 - \frac{3}{(4+\Psi)}\right] \tag{3.10}$$

Assuming homogenous, isotropic material properties and rectangular cross section for masonry walls parameter 'Ψ' in above equation simplifies to:

$$\Psi = \frac{12EI}{A_s Gh^2} = \frac{12*E*1/12*t*L^3}{5/6*t*L*0.4*E*t^2} = 3\lambda^{-2} \tag{3.11}$$

Thus, lateral stiffness of a cantilever masonry wall modeled with shear deformations included beam simplifies to Equation 3.12 when Equation 3.11 is inserted into Equation 3.10. Equation 3.12 is also identical to Equation 3.1 when boundary condition parameter (β) is taken as 3.

$$K^* = E*t*\left[\left(\frac{1}{\lambda^3+3\lambda}\right)\left(1 - \frac{3}{(4+3\lambda^{-2})}\right)\right] \tag{3.12}$$

Second extreme boundary condition is both ends fixed wall. Since rotational DOF is fully restrained at the top, stiffness matrix is built for translational DOF only. Boundary conditions and corresponding stiffness matrix with shearing deformations included are provided in Figure 3.9.

$$K = \left[\frac{12EI}{h^3(1+\Psi)} \right]$$

$$\Psi = \frac{12EI}{A_S G h^2}$$
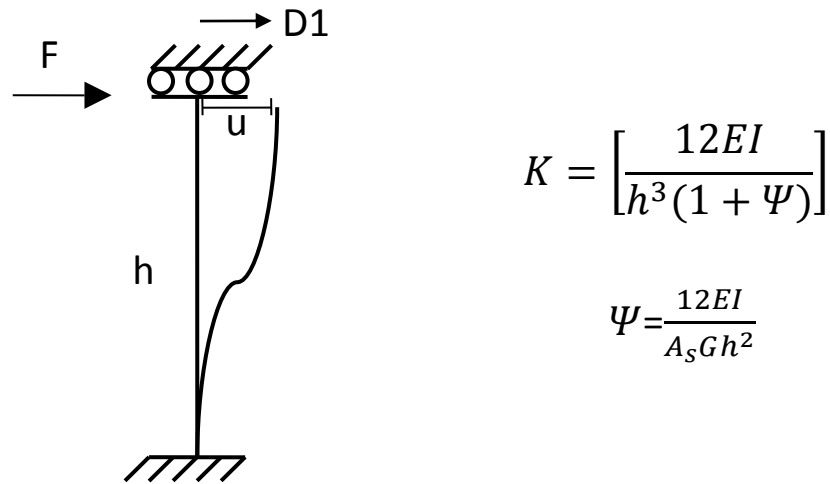
Figure 3.9 Stiffness Matrix of Both ends Fixed Wall with Shearing Deformations Considered

Lateral stiffness of both ends fixed masonry wall modeled with shear deformations included beam simplifies to Equation 3.13 which is also identical to Equation 3.5 when boundary condition parameter (β) is taken as 12.

$$K = \left[\frac{E*t}{(\lambda^3 + 3\lambda)} \right] \tag{3.13}$$

As it is easily identified by looking at Equation 3.12 and Equation 3.13 that elastic lateral stiffness walls depend linearly on modulus of elasticity (E) and thickness (t) of the wall. Contribution of aspect ratio is more complex illustrated in Figure 3.10.
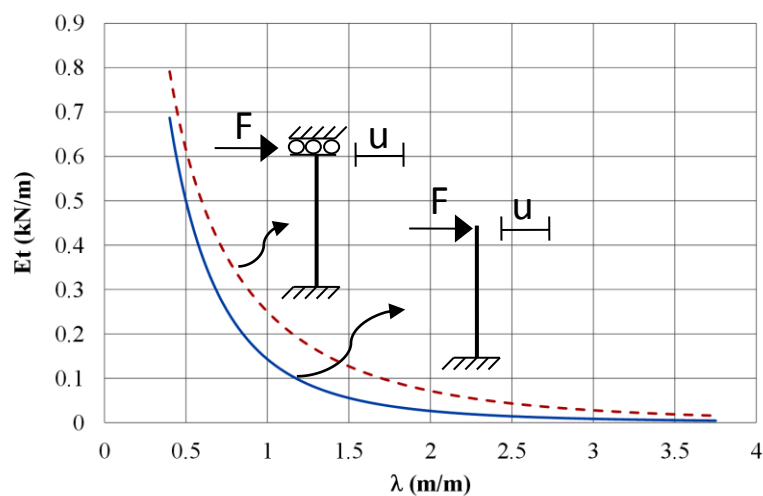
Figure 3.10 Lateral Stiffness versus Aspect Ratio for Different Boundary Conditions

Same information might be illustrated by dividing lateral stiffness of both ends fixed wall to lateral stiffness of cantilever wall for various aspect ratios (see Figure 3.11).
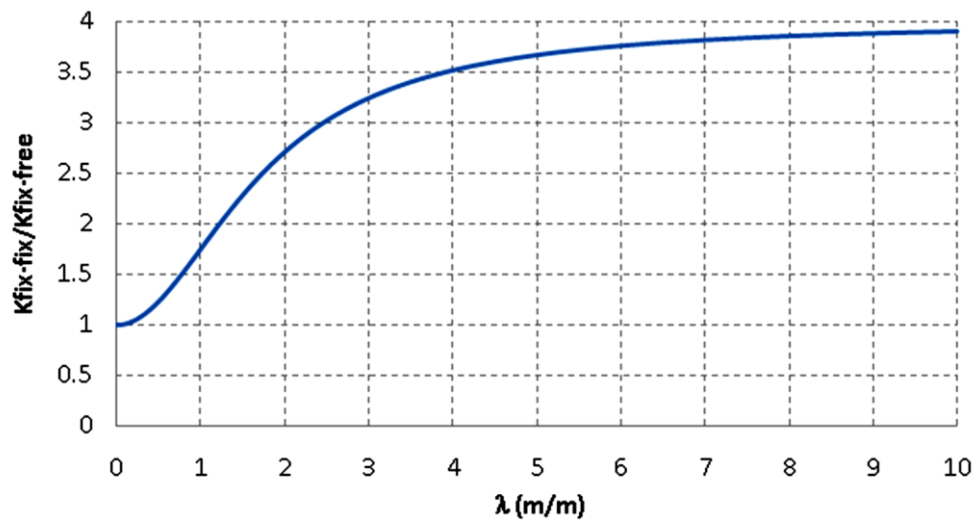
Figure 3.11 Ratio of Elastic Lateral Stiffness of Both ends Fixed Wall to Cantilever Wall

When aspect ratio approaches to zero, influence of boundary conditions on lateral stiffness vanishes (i.e. $K_{fix-fix}/K_{fix-free} = 1$). This is because for squatter walls shear contribution on total stiffness is dominant and it is independent of boundary conditions. On the other hand when aspect ratio approaches to infinity, flexure contribution to total stiffness is dominant and shear contribution vanishes. Thus ratio approaches to 4 which is also ratio of lateral flexural stiffness of both ends fixed wall to lateral flexural stiffness of cantilever wall.

Lateral stiffness of cantilever walls increase as spandrels and upper story walls are connected to the wall. Basically lateral stiffness of rotationally restrained cantilever walls is in between cantilever wall stiffness and both ends fixed wall stiffness. Analytical solution of lateral stiffness of rotationally restrained cantilever beam is illustrated below (see Figure 3.12).
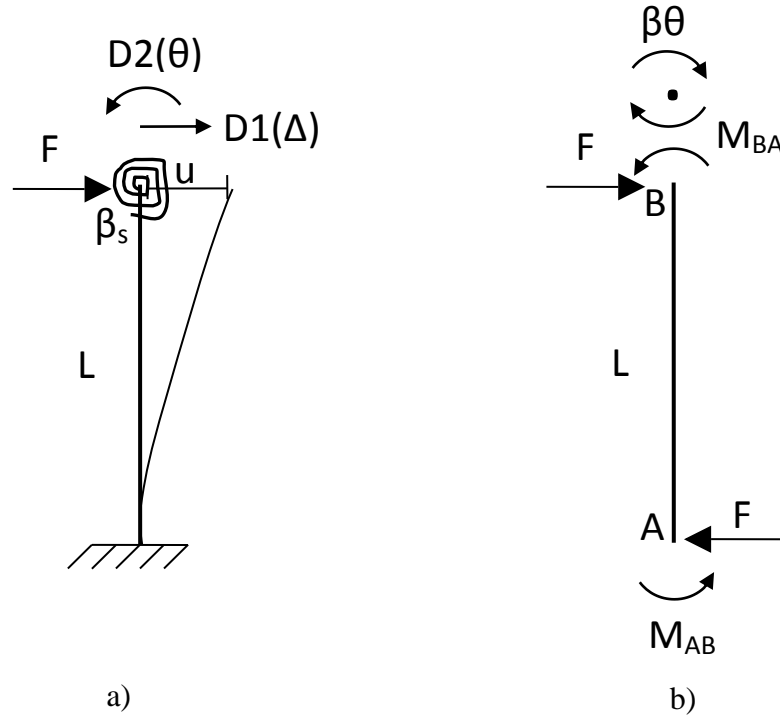
Figure 3.12 a) Idealization of Spandrel Coupling with Rotational Spring b) Free Body Diagram

First, flexural contribution to total stiffness is calculated ignoring shear deformations. Slope deflection method will be employed for this purpose. Then shear contribution to total stiffness will be combined with flexural counterpart forming total stiffness.

Slope deflection equations related to free body diagram in Figure 3.12b is given below:

$$M_{AB} = \frac{2EI}{L}\left(\theta + \frac{3\Delta}{L}\right) \tag{3.14}$$

$$M_{BA} = \frac{2EI}{L}\left(2\theta + \frac{3\Delta}{L}\right) \tag{3.15}$$

Equilibrium equations to solve two unknown in slope deflection equations are:

$$M_{BA} + \beta_S\theta = 0 \tag{3.16}$$

$$M_{BA} + M_{AB} = FL \tag{3.17}$$

Inserting M_{AB} and M_{BA} into equilibrium equations:

$$\left[\frac{4EI}{L} + \beta_S\right]\theta + \frac{6EI}{l^2}\Delta = 0 \tag{3.18}$$

$$\frac{6EI}{L}\theta + \frac{12EI}{L^2}\Delta = FL \tag{3.19}$$

Solving two equations, tip rotation and flexural component of lateral displacement are calculated as below:

$$\theta = -\frac{FL^2}{2(EI+\beta_S L)} \tag{3.20}$$

$$\Delta = \frac{FL^3}{12EI}\left[\frac{4+\frac{\beta_S L}{EI}}{1+\frac{\beta_S L}{EI}}\right] \tag{3.21}$$

Finally lateral flexural stiffness is calculated using linear relation between force and displacement (i.e. $F = \frac{K}{\Delta}$).

$$k_f = \frac{3EI}{L^3}\left[\frac{\left(4+4\frac{\beta_S L}{EI}\right)}{\left(4+\frac{\beta_S L}{EI}\right)}\right] \tag{3.22}$$

Figure 3.13 illustrates Equation 3.22 such that lateral flexural stiffness is normalized with $\frac{3EI}{L^3}$ and rotational spring constant (β_s) is normalized with $\frac{L}{EI}$. It is clear in Figure 3.13 that when spring constant is taken as zero meaning no rotational restrain at tip, lateral flexural stiffness approaches to $\frac{3EI}{L^3}$. On the other hand when spring constant is taken as infinity meaning full rotational restrain at tip, lateral flexural stiffness approaches to $\frac{12EI}{L^3}$.
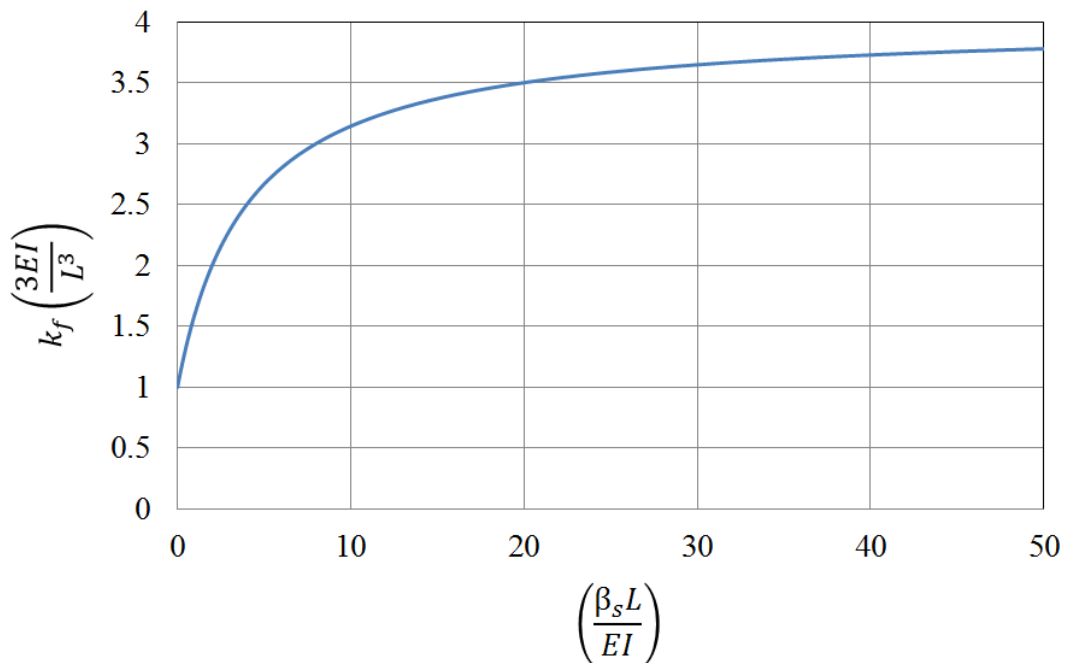
Figure 3.13 Normalized Lateral Flexural Stiffness versus Normalized Rotational Spring Constant of Rotationally Restrained Cantilever Wall

Although lateral flexural stiffness of rotationally restrained cantilever wall might be expressed in terms of normalized rotational spring constant, estimation of spring constant is uneasy. Instead, normalized rotational spring constant might be calculated from relative stiffnesses of piers and spandrels connecting to the pier in consideration. For that reason Equation 3.22 is manipulated as below.

$$k_f = \frac{3EI}{L^3} \left[\frac{\left(1 + 4 \frac{\beta_S}{\left(\frac{4EI}{L} \right)} \right)}{\left(1 + \frac{\beta_S}{\left(\frac{4EI}{L} \right)} \right)} \right] \tag{3.23}$$

In this equation, spring constant (β_s) is equal to sum of rotational stiffness's of piers and spandrels connecting to cantilever wall. If masonry piers are assumed to be axially rigid, rotational stiffness of connecting piers and spandrels might be approximated to be in between far end fixed wall rotational stiffness and far end pinned wall rotational stiffness (see Figure 3.14). These stiffness values are directly taken from element stiffness matrices of unmodified and modified shear deformations included beam element which is supplied in Appendix A.

$$\frac{EI(4 + \Psi)}{L(1 + \Psi)}$$

a)

$$\frac{12EI}{L(4 + \Psi)}$$

b)
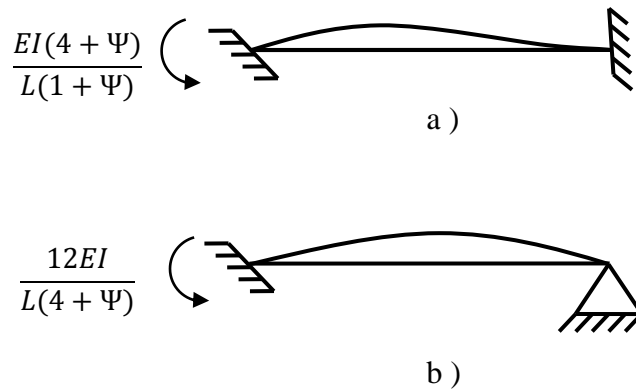
Figure 3.14 Rotational Stiffness of Shear Deformations Considered Beams: a) Far End Fixed Beam, b) Far End Pinned Beam

Although rotational stiffness depends on restrain on far end rotation of the beams, in order to further simplify Equation 3.23, a simple equation which is independent of far end support conditions is proposed below:

$$\beta_s = 1.75\sqrt{\lambda}\frac{EI}{L} \leq \frac{4EI}{L} \tag{3.24}$$

Comparison of proposed equation with its lower and upper limits, namely far end fixed and far end pinned beams is illustrated in Figure 3.15. It could be identified from figure that in addition to its being simple, proposed equation complies well with its upper and lower limits. Since upper boundary converges to $\frac{4EI}{L}$ when aspect ratio goes to infinity, contribution of each connecting pier or spandrel to spring constant is not allowed to go beyond that limit.
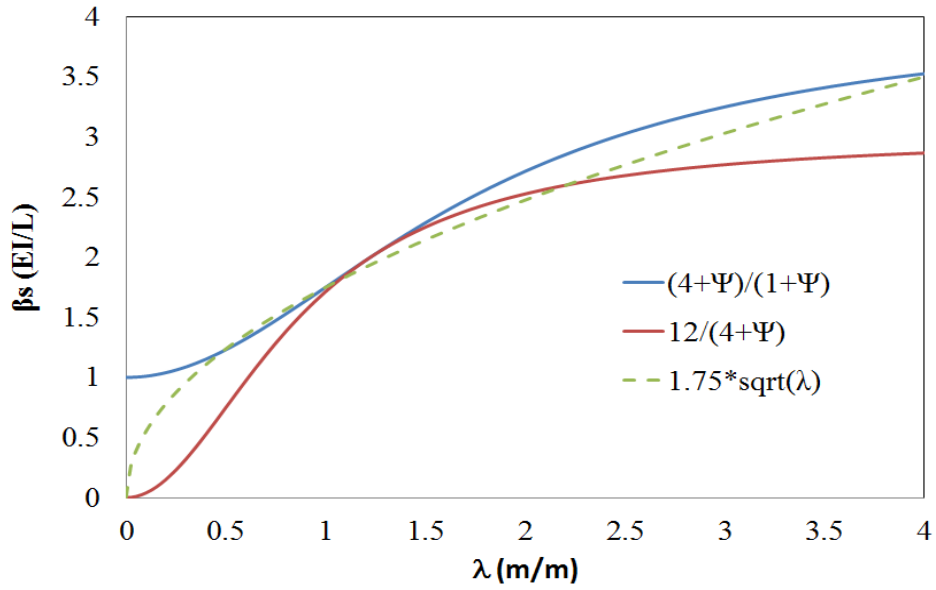
Figure 3.15 Comparison of Proposed Equation for Rotational Spring Constant with Upper and Lower Limits

When Equation 3.23 is combined with Equation 3.24, elastic lateral flexural stiffness of rotationally restrained cantilever pier with rectangular cross section and homogenous and isotropic material properties simplified to;

$$k_f = \frac{EI}{L^3}\left[\frac{\left(12+21\frac{\sum\sqrt{\lambda_i}I_i/L_i}{I/L}\right)}{\left(4+1.75\frac{\sum\sqrt{\lambda_i}I_i/L_i}{I/L}\right)}\right] \tag{3.25}$$

Where,

E is modulus of elasticity

I is moment of inertia of the pier

L is length of the pier

λ_i aspect ratio of spandrels and piers connecting to the wall.

I_i moment of inertia of spandrels and piers connecting to the wall.

L_i length of spandrels and piers connecting to the wall.

The term inside the parenthesis in Equation 3.25 is the boundary condition parameter utilized in Equation 3.1. When the ratio of total rotational stiffness of coupling spandrels and piers to the rotational stiffness of the wall approaches to zero (i.e. weak coupling), it converges to 3 which represent cantilever boundary conditions. Whereas if the spandrel coupling is infinite (i.e. strong coupling), it converges to 12 which represents both ends fixed boundary conditions.

3.2 Lateral Stiffness of Perforated URM Walls

3.2.1 Equivalent Frame Modeling of Perforated URM Walls

Masonry buildings are composed of internal and external walls. Internal walls are usually solid but in most cases peripheral walls are perforated as a result of both door and window openings. Structural components on perforated masonry walls are named as piers or spandrels due to their orientation (see Figure 3.16).
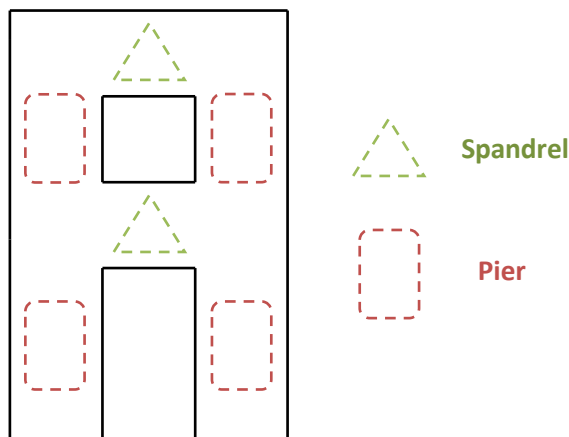
Figure 3.16 Spandrels and Piers on a Perforated Wall

Among the different modeling approaches to model perforated walls, equivalent frame modeling will be investigated in detail. In equivalent frame modeling method,

each pier and spandrel is modeled with frame elements passing through their centerline (see Figure 3.18a). Since cross sectional and mechanical properties of each member is squeezed to a line element, we expect each equivalent frame element to reflect similar structural behavior with their counterpart at perforated wall.

As it enables to implement displacement based concepts, equivalent frame method is frequently used for the modeling of masonry buildings in the literature. Compared to more sophisticated finite element models, equivalent frame models are simple and easy to apply. Besides, according to Magenes and Fontana (1998), "equivalent frame idealization of masonry structures are effective for; good prediction of strength of a building subjected to a pattern of increasing horizontal forces, good prediction of the failure mechanism in the single sub elements and good prediction of the overall deformation of the building particularly at the ultimate state."

3.2.2 Determination of Effective Height for Masonry Piers and Spandrels

Although it is easy to idealize each pier and spandrel as equivalent frames with their cross section dimensions, height and mechanical properties, defining connection between them is challenging. In order to take coupling effect between piers and spandrels into account rigid end offsets are assigned at the ends of frame elements.

Assigning full RO for spandrels is a widely used assumption. However, being the most important element of in plane load carrying mechanism, RO length of piers should be carefully assigned. Different methods for assigning rigidity at pier-spandrel interaction are found in the literature. One method proposed by Dolce (1989) is to take a portion of pier-spandrel interaction as rigid (see Figure 3.17) whereas another approach is to take pier-spandrel interaction as fully rigid (see Figure 3.18).

In order to decide which approach to use, a comparative study will be performed. The aim is to determine the closest approximation to finite element results of a perforated frame by equivalent frame models whose rigid end offset patterns are

variable. For this purpose, 3 different perforated frames are modeled with different modeling approaches and results are compared. Three criteria will be checked for comparison. Namely, story displacements, axial force on base piers and shear force on base piers.

ANSYS (2007) is utilized for finite element modeling and SAP2000 (2009) is utilized for equivalent frame modeling. ANSYS results are assumed to be exact and the method which approximates ANSYS results best will be selected to be used in following chapters.
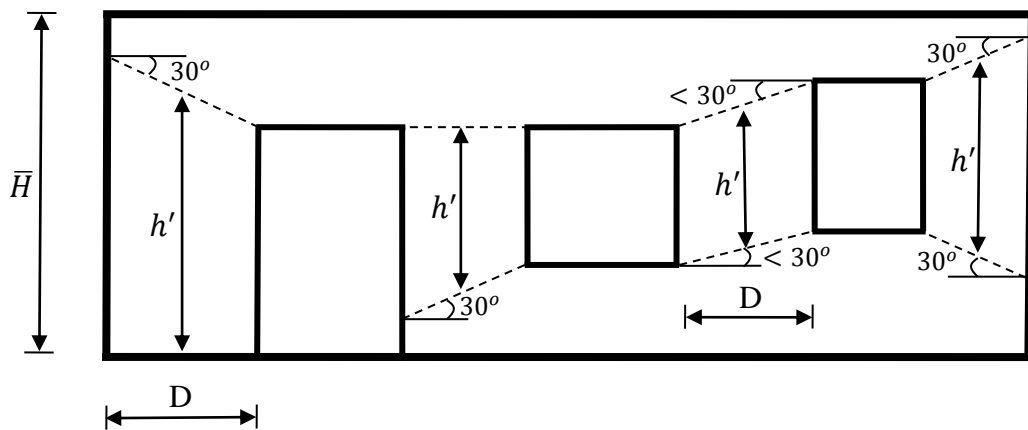
Figure 3.17 Effective Height Determination Offered by Dolce
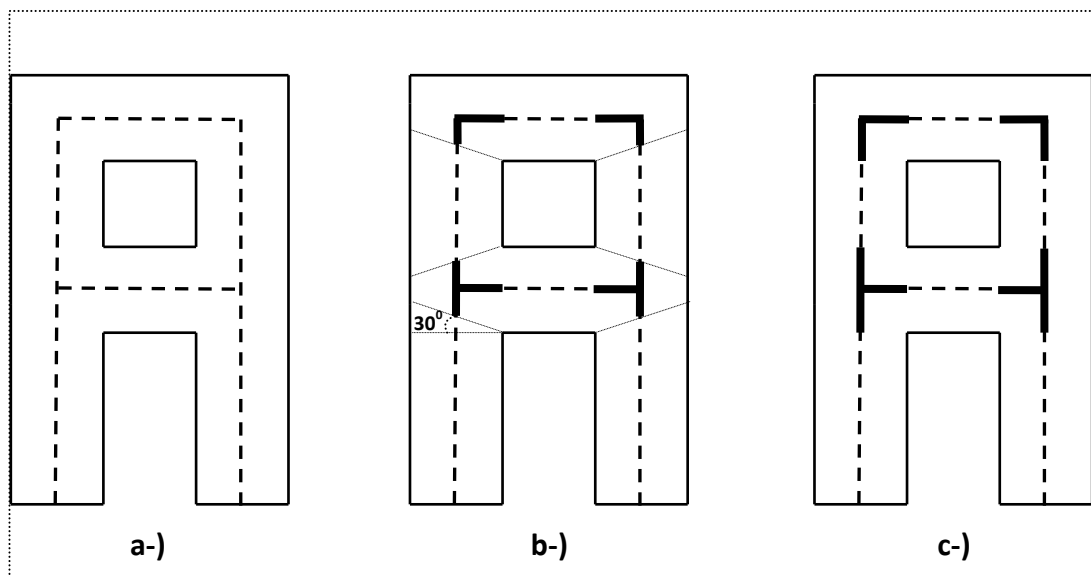
Figure 3.18 a-) Equivalent Frame Model, b-) EFM with Dolce RO, c-) EFM with Full RO

3.2.2.1 Comparative Elastic Analysis of 1 Bay 2 Story (1B2S) Perforated Masonry Frame

1 bay 2 story masonry frame whose nonlinear behavior is investigated by Salonikios et al. (2003) is chosen for linear comparative analysise(see Figure 3.19).
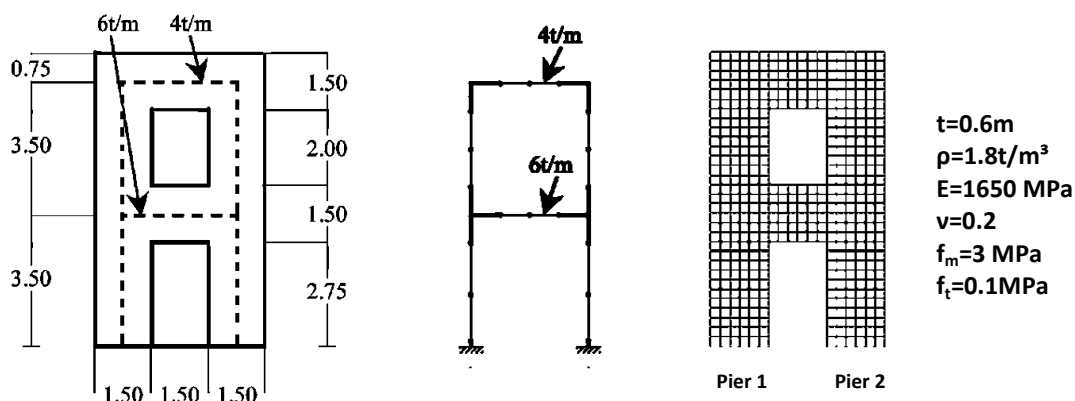
Figure 3.19 1B2S Masonry Frame Investigated by Salonikios et al., (2003)

Plane stress assumption is made for finite element modeling in ANSYS. Two dimensional, 8 node, rectangular, linear, isotropic shell281 element with constant thickness is selected. Mapped mesh with 444 elements is applied (see Figure 3.20d). In order to ensure that mesh size is sufficient a finer mesh with 1776 elements (see Figure 3.20e) is applied and results are compared in Table 3.1. According to the analysis results there is no need for a finer mesh size.

Table 3.1 Analysis Results of Coarse and Fine Meshed Models of 1B2S Masonry Frame

		ANSYS (Coarse)	**ANSYS (Fine)**	**% difference**
Axial Force (kN)	Pier1	229.4	229.6	-0.11
	Pier2	505.8	505.6	0.05
Base Shear (kN)	Pier1	44.4	44.3	0.21
	Pier2	66.6	66.7	-0.14
Lateral Roof Displacement (mm)	1st Floor	1.45	1.46	-0.55
	2nd Floor	3.07	3.09	-0.59

Linear beam element is used for equivalent frame modeling (EFM) in SAP2000. Analyses are conducted on three different rigid end offset (RO) alternatives (see

Figure 3.20a, 3.20b and 3.20c). Loading on each model is imposed in a two-step sequence. First, dead load plus distributed slab loading on spandrels are imposed. Second, lateral loads at story levels which sum up to 15% of total weight is applied in proportion to first mode story displacements calculated using EFM with Dolce offset. Floors are assumed to be rigid so diaphragm constraints are assigned at floor levels.

Pier 1   Pier 2
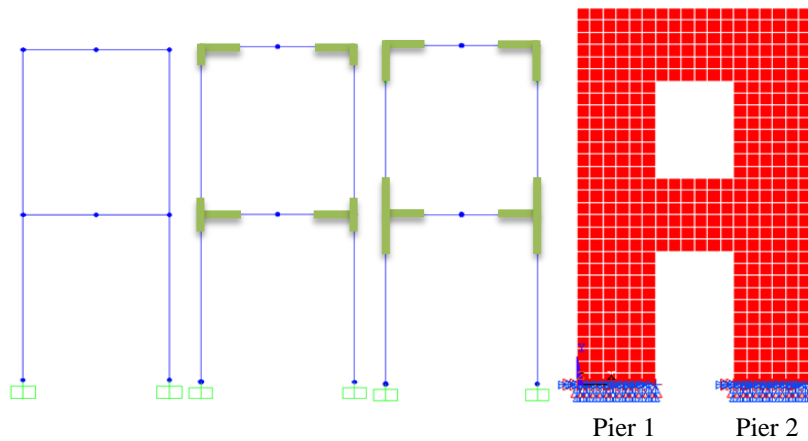
Figure 3.20 2B3S Frame Models a-) EFM without RO, b-) EFM with Dolce RO, c-) EFM with full RO, d-) FEM Coarse Mesh, e-) FEM Fine Mesh

Results of the analyses are summarized in Table 3.2. As it is clearly seen, RO proposed by Dolce (1989) gives the best approximation to finite element analyses considering deflected shape, axial force and shear force on base piers.

Not assigning any rigid end zone results in a more flexible behavior compared to finite element analysis. On the contrary assigning full rigid end offset results in a stiffer behavior.

For a better comparison between FEM and its best estimator EFM with Dolce offset, lateral story displacements are plotted below (see Figure 3.21).

Table 3.2 Analysis Results of FEM and EFM for 1B2S Masonry Frame

		ANSYS (FEM)	SAP (EFM)			% Differance		
			No RO	Dolce RO	Full RO	No RO	Dolce RO	Full RO
Axial Force (kN)	**Pier1**	229.4	245.3	230.4	226.3	6.9	0.5	-1.3
	Pier2	505.8	489.9	504.8	508.9	-3.2	-0.2	0.6
Base Shear (kN)	**Pier1**	44.4	46.1	44.2	43.4	3.9	-0.4	-2.2
	Pier2	66.6	64.9	66.8	67.6	-2.6	0.2	1.4
Lateral Roof Displacement (mm)	**1st Floor**	1.45	2.04	1.52	1.39	40.9	5.3	-4.3
	2nd Floor	3.07	4.56	3.18	2.84	48.5	3.6	-7.5
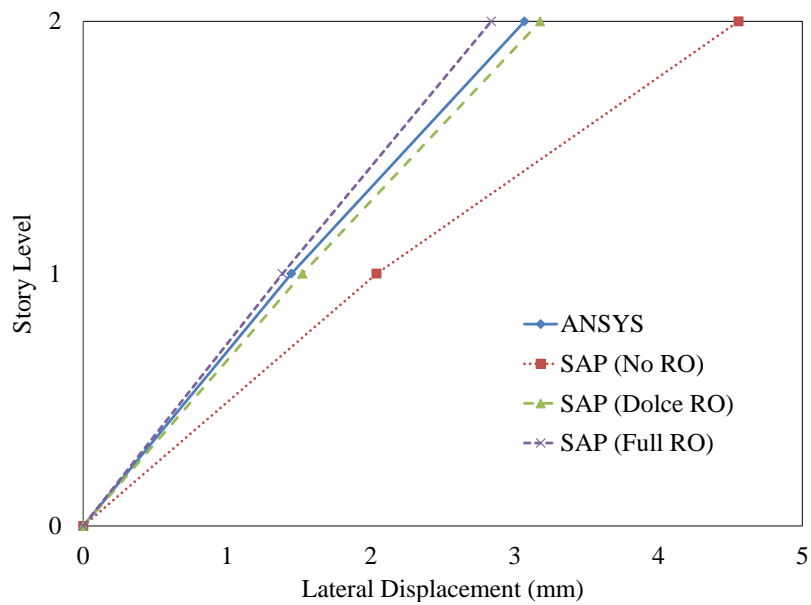
Figure 3.21 Lateral Story Displacements of FEM and EFM on 1B2S Masonry Frame

3.2.2.2 Comparative Elastic Analyses of 2 Bay 2 Story (2B2S) Perforated Masonry Frame with Strong Spandrels

Same analyses that were conducted on 1B2S masonry frame are also conducted for 2B2S masonry frame (see Figure 3.22). Meshing of the finite element model and rigid end offsets of equivalent frame models are drawn in Figure 3.23.
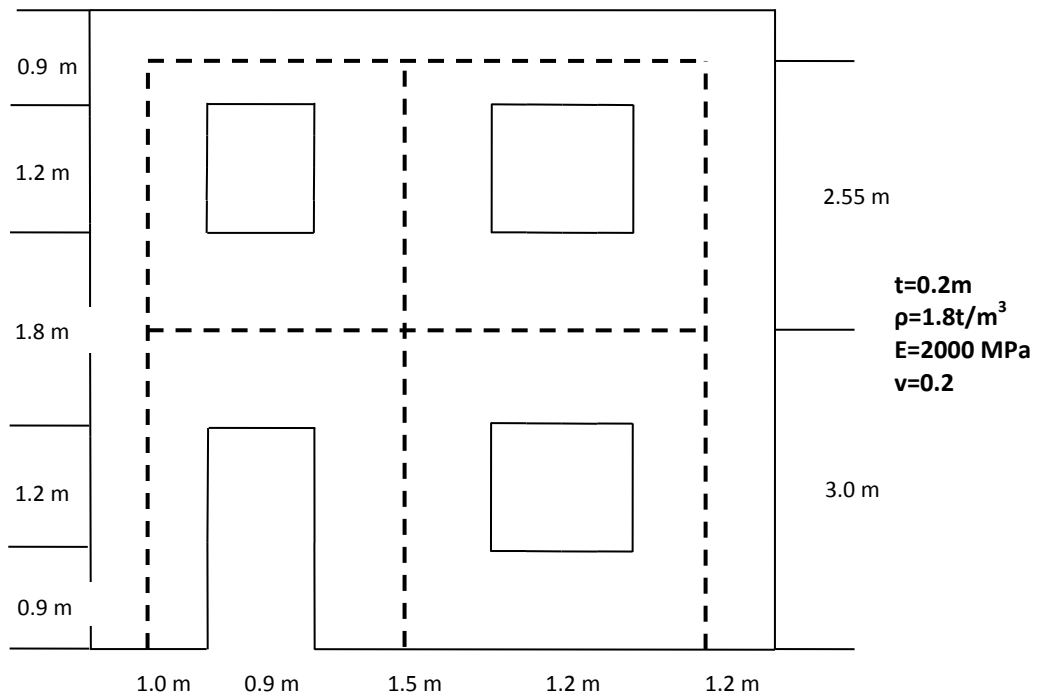
Figure 3.22 2B2S Masonry Frame with Strong Spandrels
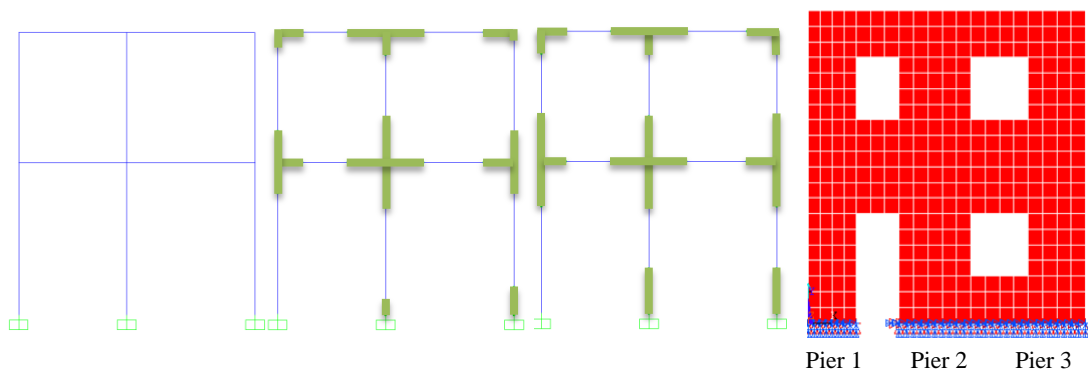
Figure 3.23 Models 2B2S Masonry Frame a-) EFM without RO, b-) EFM with Dolce RO, c-) EFM with full RO, d-) FEM

Results of the analyses are summarized in Table 3.3. Considering the shear and axial force on base piers, both Dolce and Full rigid end offsets give satisfactory results. Lateral displacement of first story which is most critical story under lateral loads is best approximated by Dolce offset. Again FEM results are in between full RO and Dolce RO.

For a visual comparison between FEM and its best estimator EFM with Dolce RO, lateral displacement at the base is drawn below (see Figure 3.24).

Table 3.3 Analyses Results of FEM and EFM for 2B2S Masonry Frame

		ANSYS (FEM)	**SAP (EFM)**			**% Differance**		
			No RO	**Dolce RO**	**Full RO**	**No RO**	**Dolce RO**	**Full RO**
Axial Force (kN)	Pier1	27.3	27.9	28.8	30.6	2.3	5.4	12.2
	Pier2	66.0	75.6	74.3	71.3	14.5	12.5	8.0
	Pier3	77.1	66.9	67.4	68.6	-13.2	-12.6	-11.1
Base Shear (kN)	Pier1	2.7	4.5	2.9	1.2	66.1	7.9	-53.7
	Pier2	12.9	12.7	11.9	13.6	-1.6	-7.3	5.4
	Pier3	10.2	8.6	10.9	10.9	-15.5	7.0	7.0
Lateral Roof Displacement (mm)	1st Floor	0.30	0.62	0.39	0.19	105.1	28.2	-35.8
	2nd Floor	0.57	1.18	0.80	0.42	106.5	40.3	-26.4
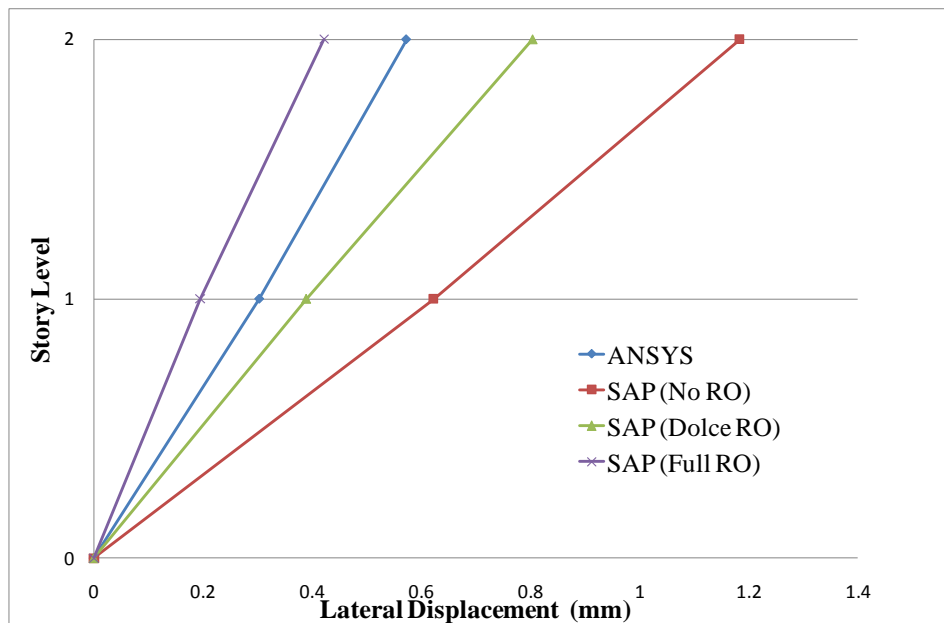
Figure 3.24 Lateral Story Displacements of FEM and EFM on 2B2S Frame

3.2.2.3 Comparative Elastic Analyses of 2 Bay 3 Story (2B3S) Perforated Masonry Frame with Weak Spandrels

2 bay 3 story masonry frame whose nonlinear behavior is investigated by Roca et al., (2005) is chosen for comparative linear analyses (see Figure 3.25). Same analyses

that were conducted on 1B1S and 1B2S frames are conducted again. Meshing of the finite element model and RO patterns of equivalent frame model are drawn below (see Figure 3.26).
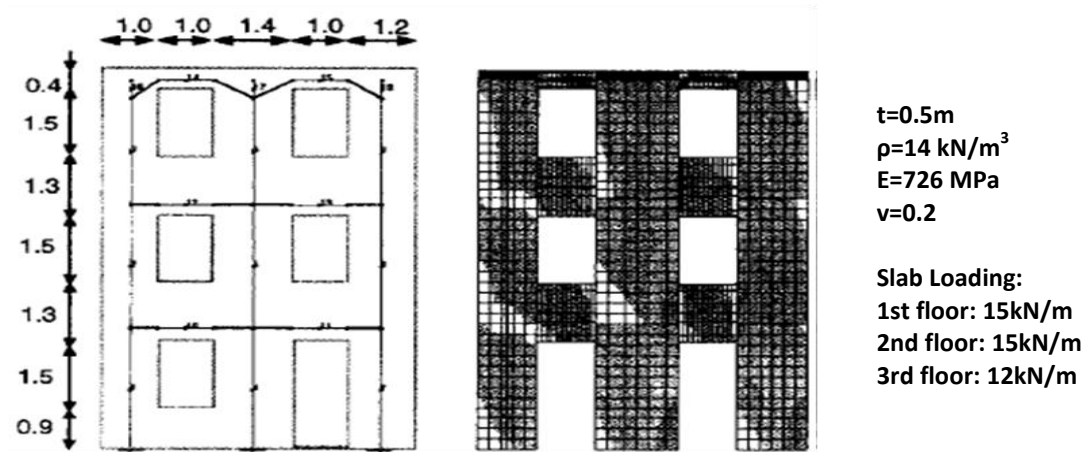
Figure 3.25 2B3S Masonry Frame Investigated by Roca et al., (2005)
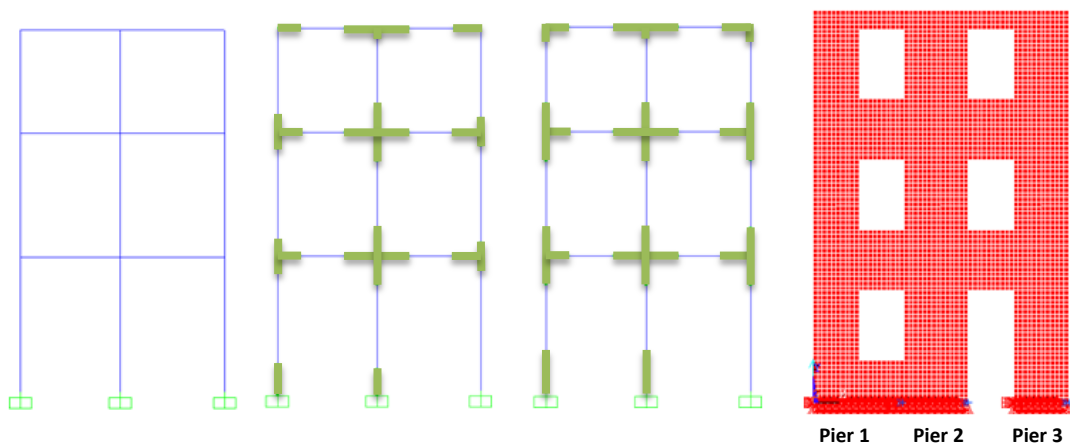
Figure 3.26 2B3S Frame Models a-) EFM without RO, b-) EFM with Dolce RO, c-) EFM with Full RO, d-) FEM

Results are summarized in Table 3.4. Similar to previous analyses considering the finite element model, SAP2000 model without RO results in larger story displacements indicating that equivalent frame without RO is flexible. Full RO model result in smaller displacements indicating that model is stiffer. Dolce RO is the best approximation to story displacements. It also approximates base shear and axial force in base piers satisfactorily.

Table 3.4 Analyses Results of FEM and EFM for 2B3S Masonry Frame

		ANSYS (FEM)	SAP (EFM)			% Difference		
			No RO	Dolce RO	Full RO	No RO	Dolce RO	Full RO
Axial Force (kN)	**Pier1**	52.9	70.3	70.8	74.6	33.0	34.0	41.0
	Pier2	211.3	206.7	200.2	198.4	-2.2	-5.2	-6.1
	Pier3	231.0	218.2	224.1	222.2	-5.5	-3.0	-3.8
Base Shear (kN)	**Pier1**	18.9	14.2	16.9	18.4	-24.9	-10.7	-2.9
	Pier2	32.6	35.2	40.2	43.5	8.0	23.4	33.5
	Pier3	22.7	24.9	17.2	12.4	9.7	-24.2	-45.3
Lateral Roof Displacement (mm)	**1st Floor**	1.51	2.57	1.28	0.96	70.13	-15.12	-36.5
	2nd Floor	3.08	5.41	2.71	2.22	75.34	-12.26	-27.9
	3rd Floor	4.34	7.60	3.83	3.27	74.95	-11.82	-24.6

For a visual comparison between FEM and its best estimator EFM with Dolce offset, lateral displacement profile at the base is plotted below (see Figure 3.27).
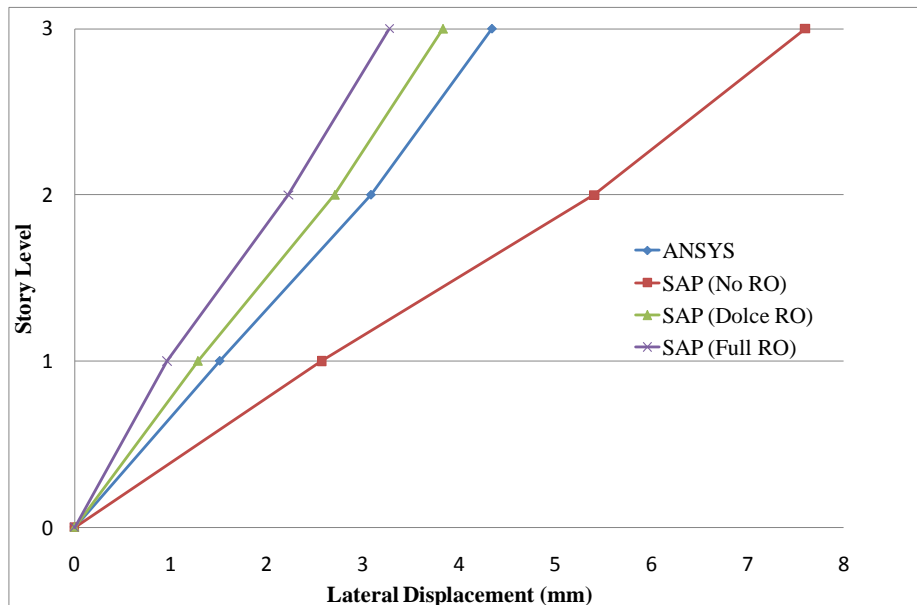
Figure 3.27 Lateral Story Displacements for FEM and EFM Analyses on 2B3S Masonry Frame

As a result of elastic linear analyses on perforated frames with different RO patterns, it might be concluded that considering story displacements, axial load on base piers and shear force on base piers, best approximation to finite element model is SAP2000 model with Dolce RO. Comparison of shear force (see Figure 3.28) and axial load at base piers (see Figure 3.29) between finite element method and its best approximation; EFM with Dolce RO are plotted below.
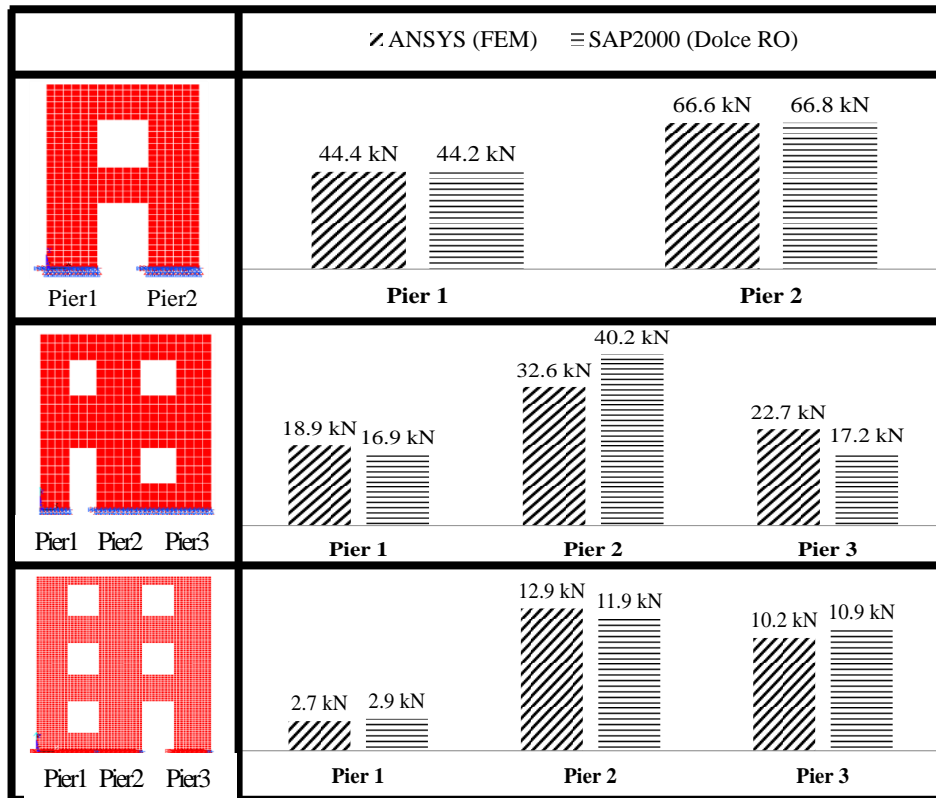
Figure 3.28 Comparison of Shear Forces on Base Piers of Masonry Frames
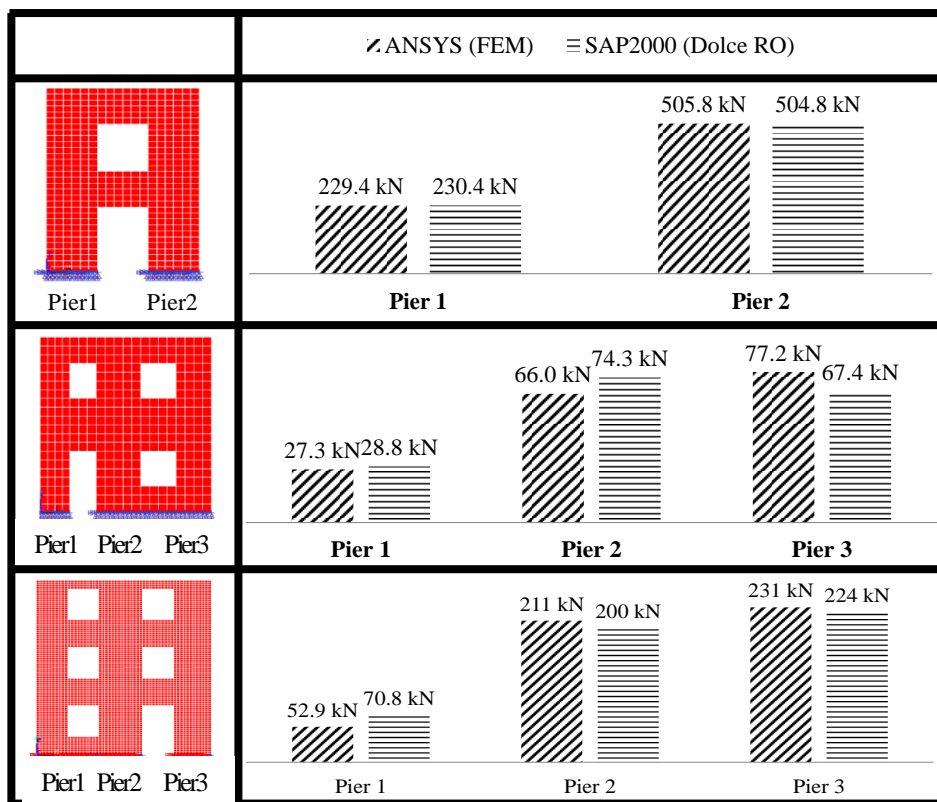
Figure 3.29 Comparison of Axial Load on Base Piers of Masonry Frames

CHAPTER 4

NONLINEAR FINITE ELEMENT MODEL FOR IN-PLANE ANALYSIS OF URM WALLS

Due to its complex nature, simulation of the in-plane lateral force-displacement relationship of masonry walls under varying material properties, axial loads and boundary conditions is a challenging job. Although simple strength equations, empirical formulas for softening behavior and ultimate drift values for URM walls are found in the literature, in order to obtain a reliable lateral force-displacement relationship, finite element modeling should be employed. Only finite element models give the opportunity to simulate crack pattern, distribution of damage and failure mechanism of masonry walls which are essential in simulation of nonlinear response of URM walls.

A finite element macro model which is capable of reflecting effects of cracking, estimating damage propagation and ultimate failure mechanism of masonry walls is built by Alper Aldemir (2010) utilizing ANSYS Software (2007). In forthcoming sections, modeling properties and assumptions made by Alper Aldemir are illustrated and then the reliability of the proposed model is tested. Results of the model proposed by Aldemir will form the basis for the nonlinear modeling of URM buildings in the following chapters.

4.1 Model Properties and Assumptions

Among various element types in ANSYS, Solid 65 which is built for the purpose of 3-D modeling of solids is selected for the modeling of URM masonry. Although it is usually utilized for reinforced concrete, as it is capable of implementing reinforcing bars in the element, masonry might also be modeled without defining reinforcement, selecting proper plasticity models and modifying material constants. It is stated in element reference for ANSYS that Solid 65 is also applicable to geological materials

such as rocks and probably masonry since it is capable of cracking in tension and crushing in compression.

The element is defined by eight nodes having three degrees of freedom at each node: translations in the nodal x, y, and z directions (see Figure 4.1).
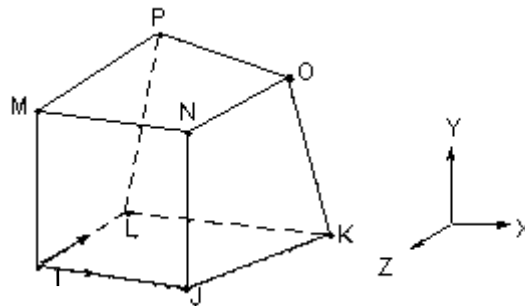
Figure 4.1 3-D Solid 65 Element Used to Model Masonry in ANSYS

Element assumptions which are either defined in Theory Reference or made by Aldemir (2010) are given below:

1. Cracking is permitted in three orthogonal directions
2. If cracking occurs, the cracking is modeled through an adjustment of material properties so as to insert a plane of weakness in the normal direction to the crack face.
3. The concrete material is assumed to be initially isotropic
4. If the material at an integration point fails in uni-axial, bi-axial or tri-axial compression, material is assumed to be crushed. Crushing is defined as the complete deterioration of the structural integrity of the material e.g. material spalling. The stiffness contribution of a crushed element is ignored by taking its value as 1×10^{-6}.
5. In addition to cracking and crushing, the concrete may also undergo plasticity, with the Drucker-Prager failure surface being most commonly used.
6. Shear transfer across an open crack is zero, whereas there is full shear transfer across a closed crack. (assumption made by Aldemir)
7. The stress relaxation after cracking is cancelled as it is only needed to accelerate the convergence. (assumption made by Aldemir)

8. The plasticity is defined as multilinear isotropic hardening (See Figure 4.2). (assumption made by Aldemir)
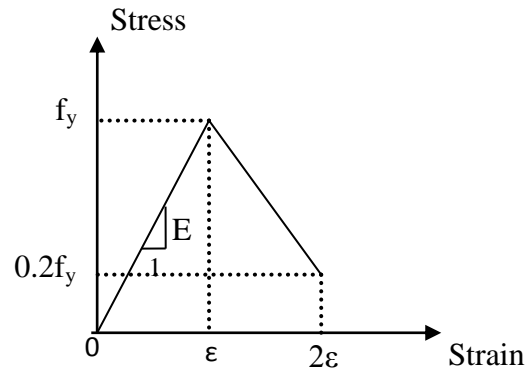
Figure 4.2 Multilinear Isotropic Plasticity Model used in Analytical Model (Aldemir, 2010)

Aldemir adopted Willam–Warnke's five parameter failure theory developed for modeling the tri-axial behavior of concrete in order to model the failure of masonry materials. Vyas and Reddy (2009) who modeled masonry wallets under compression with similar approach defines application of Willam–Warnke's failure theory for masonry as: When the state of stress reaches a certain critical value, the material fails by fracturing which means either cracking (tension-tension, compression-tension) or by crushing (compression–compression). For compressive type of stress, crushing is assumed to occur when the state of stress reaches the critical shear stress value. For a tensile type of stress, cracking is assumed to occur when the state of stress reaches the critical tensile stress value.

After derivation of finite element model, Aldemir conducted a parametric study on masonry walls taking thickness, length, aspect ratio, compressive strength of the wall and overburden pressure on the wall as variables. Investigating more than 300 imaginary walls, he derived capacity curves and bilinearized them using equal energy principle. Finally using bilinearized capacity curves he derived equations from regression analysis for the yield force, ultimate force (Equation 4.1), and ultimate displacement (Equation 4.2) capacities utilizing SPSS. Coefficients related to proposed equations are given in Table 4.1.

$$F_y, F_u = C_1 * p^{C_2} * f_m{}^{C_3} * e^{C_4 \lambda} * h * t \qquad (4.1)$$

$$\delta_u = C_1 * p^{C_2} * e^{C_3 f_m} * \lambda^{C_4} * h * t \qquad (4.2)$$

Where,

p = Overburden pressure on the wall

f_m = Compressive strength of masonry wall

λ = Aspect ratio of the wall

h = Height of cross section

t = Thickness of the wall

Table 4.1 Coefficients Utilized in Equation 4.1and Equation 4.2

Coefficients	Yield Lateral Load	Ultimate Lateral Load Capacity	Ultimate Lateral Displacement Capacity
C1	353.2	352.2	2.385
C2	0.604	0.498	-0.540
C3	0.414	0.501	0.319
C4	-0.931	-0.856	1.414

4.2 Verification of the Nonlinear Pier Model

In order to ensure reliability of the proposed equations; shear strength and displacement capacity of a total of 152 piers which belong to 3 case study buildings investigated in Chapter 6 is calculated according to proposed equations and compared with shear strength and ultimate drift values specified in FEMA 356. Then, analysis results of the proposed model is compared with the results of selected experimental studies. Two experimental studies are selected for this purpose such that shear dominated response and flexure dominated response is observed respectively. Detailed investigation of the model is made in terms of unique characteristics of shear and flexure dominated failures such as cracking patterns, stress distributions and strain distributions at various drift levels.

4.2.1 Comparison with FEMA 356

Definition of force displacement relation of masonry piers according to FEMA 356 is illustrated below:
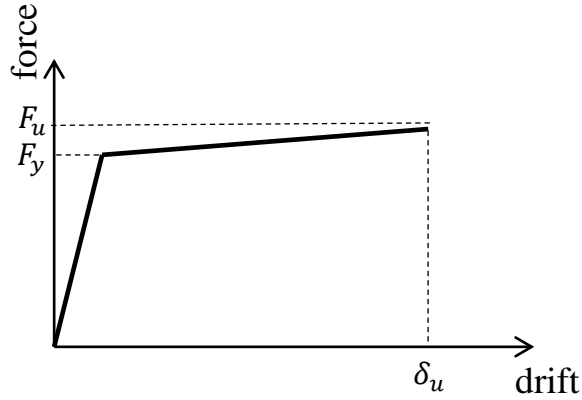
Figure 4.3 Force Displacement Relationship of Masonry Piers Defined in FEMA 356

Four primary failure modes are defined for URM piers in FEMA 356 (see Table 4.2). Rocking and sliding are described as displacement based failure modes. In addition to shear strengths, ultimate drifts associated to these failure modes are provided in FEMA 356. Diagonal tension and toe crushing are described as force based failure modes and only shear strengths associated to these modes are provided. It is believed that piers failing under these modes do not possess any plastic rotation capacity.

Table 4.2 Shear Strength Equations of URM Walls Defined in FEMA 356

Failure Mode	Equation
ROCKING	$V_r = 0.9\alpha P \dfrac{L}{h_{eff}}$
SLIDING	$V_{bjs} = 0.5(0.75v_{te} + p)Lt$
DIAGONAL TENSION	$V_{dt} = f'_{dt} A \dfrac{L}{h_{eff}} \sqrt{1 + \dfrac{p}{f'_{dt}}}$
TOE CRUSHING	$V_{tc} = \alpha P \dfrac{L}{h_{eff}} \left(1 - \dfrac{p}{0.7f'_m}\right)$

For the piers belonging to case study buildings investigated in Chapter 6, shear strengths and ultimate drifts are calculated according to proposed equations (Equation 4.1 and Equation 4.2) and equations proposed in FEMA 356. Results are tabulated in Appendix C.

Minimum shear strength calculated according to rocking, diagonal tension, sliding and toe crushing equations in FEMA 356 is identified as the shear strength of the wall and corresponding failure mode is identified as governing failure mode of the wall. Then ultimate drift values are determined corresponding to each displacement based failure mode (see Table 4.3).

Table 4.3 Ultimate Drift Limits of Masonry Walls Defined in FEMA 356

Failure Mode	δ_{max}	δ_u
ROCKING	0.4*λ	0.8*λ
SLIDING	0.4	0.8

After shear strength and displacement capacity of each pier is calculated according to proposed equations, comparison is made in terms of shear strength ratios and ultimate drift ratios.

Equation proposed by Aldemir (Equation 4.1) and the equation in FEMA 356 for rocking strength (Equation 2.1) is in a good agreement in terms of shear strength values with a mean value of 1.01. Proposed equation results in conservative shear strength values due to sliding and unconservative values due to toe crushing (see Figure 4.4). Unconservative values for toe crushing are expected since crushing is disabled in ANSYS model due to convergence problems. Diagonal tension failure has not been observed in any pier probably due to low level of axial load over compressive strength ratio.
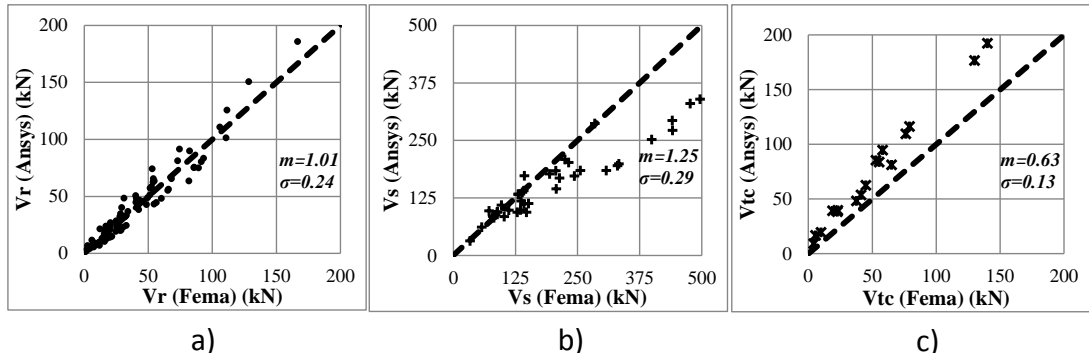
Figure 4.4 Comparison of Shear Strengths Due to Various Failure Modes a) Rocking b) Sliding c) Toe Crushing

Although there is some scatter, mean value of ultimate drift ratios for rocking (see Figure 4.5) and sliding (see Figure 4.6) is 1.05 and 1.13 respectively. Despite ultimate drift ratio for sliding failure is constant (i.e. 0.8%) in FEMA 356, depending on the aspect ratio and axial load level, ultimate drift changes in the proposed equations. So the scatter is expected.
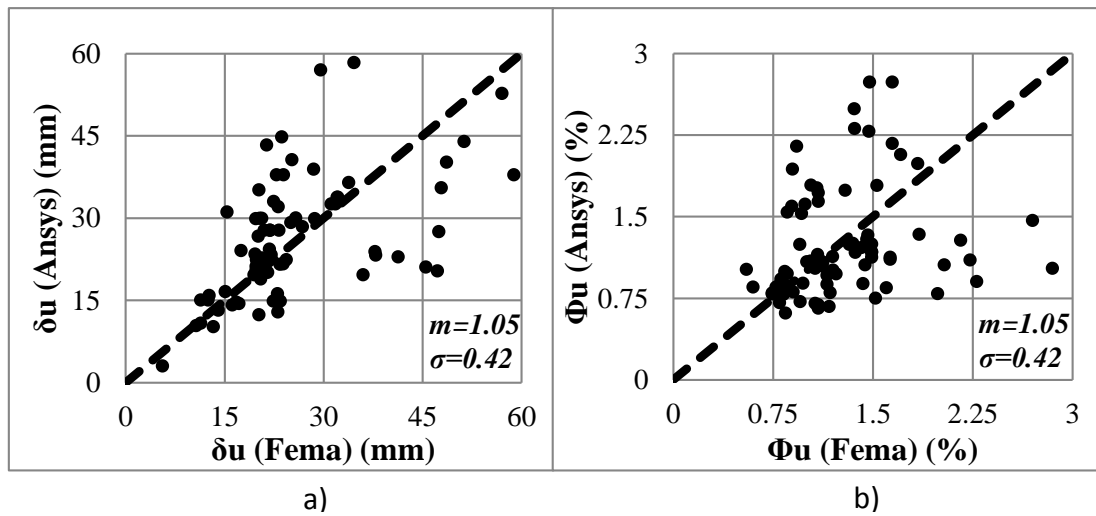
Figure 4.5 Comparison of Rocking Failure in terms of a) Ultimate Displacement b) Ultimate Drift
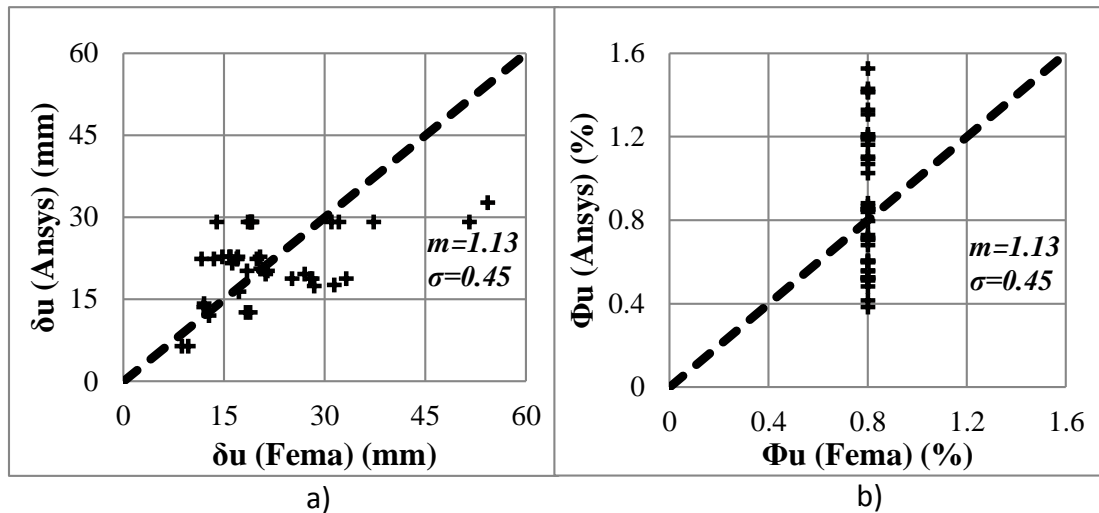
Figure 4.6 Comparison of Sliding Failure in terms of a) Ultimate Displacement, b) Ultimate Drift

4.2.2 Comparison with Experimental Results

In addition to shear strength and ultimate drift comparisons with literature, verification of the nonlinear pier model is further accomplished by a detailed investigation on crack patterns, stress variation and strain distributions of experimentally tested masonry walls.

Among many experimental studies available in literature, test conducted by Franklin et al. (2001) and Ganz and Thurlimann (1982) is chosen for verification. Franklin et al. (2001) worked on slender walls exhibiting flexure dominated behavior whereas Ganz and Thurlimann (1982) worked on squat walls exhibiting shear dominated behavior. 3-D models generated for nonlinear analysis of piers are presented below (see Figure 4.7).

<center>a)</center> <center>b)</center>
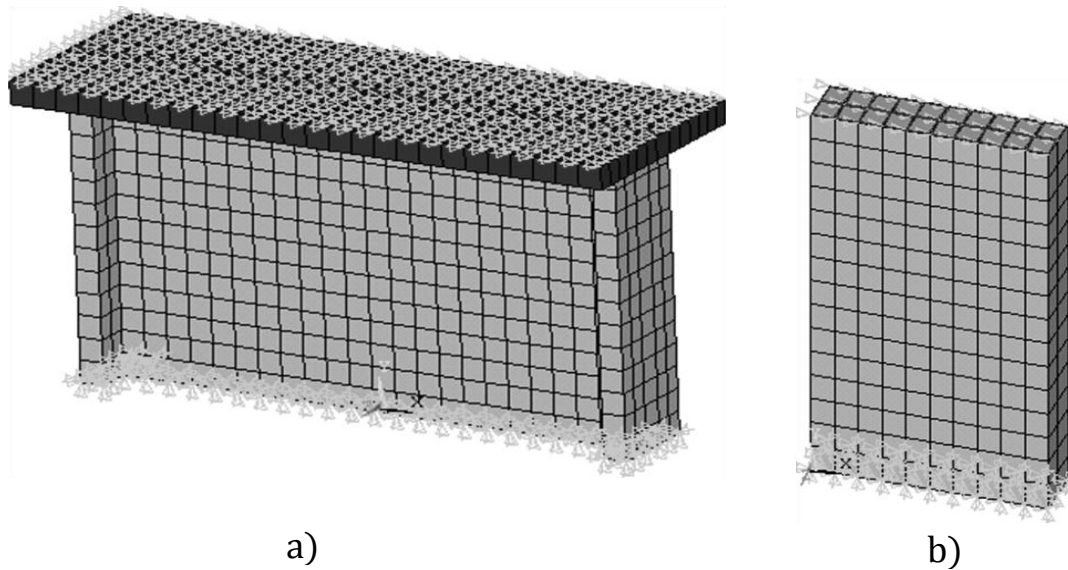
Figure 4.7 a) 3-D Model of Wall (1GT) Tested by Ganz and Thurlimann, (1982), b) 3-D Model of Wall (1F) Tested by Franklin et al., (2001)

4.2.2.1 URM Wall Tested by Franklin (1F)

Wall 1F investigated by Franklin has 840 mm length, 1500 mm height and 200 mm thickness. Compressive and tensile strength of the wall is determined as 7.86 MPa and 0.28 MPa respectively. Modulus of elasticity is measured as 4275 MPa. Overburden pressure on the wall is 0.29 MPa. Cantilever type boundary conditions are maintained through the test. Having a high aspect ratio (h/L=1.79) and low overburden pressure (σ/f_m=0.037), wall 1F exhibited a "ductile" response with ultimate drift of 1.3%.

Model properties of 1F are input into ANSYS as explained in section 4.5.1. $10 * 15 = 150$ mapped meshed elements are used for the model generation. Nonlinear solution properties of ANSYS such as line search, DOF predictor, convergence limit and maximum number of iterations are utilized whenever convergence is disturbed. Final force-displacement curve of the wall is displayed together with experimental data in Figure 4.8.

<center>72</center>
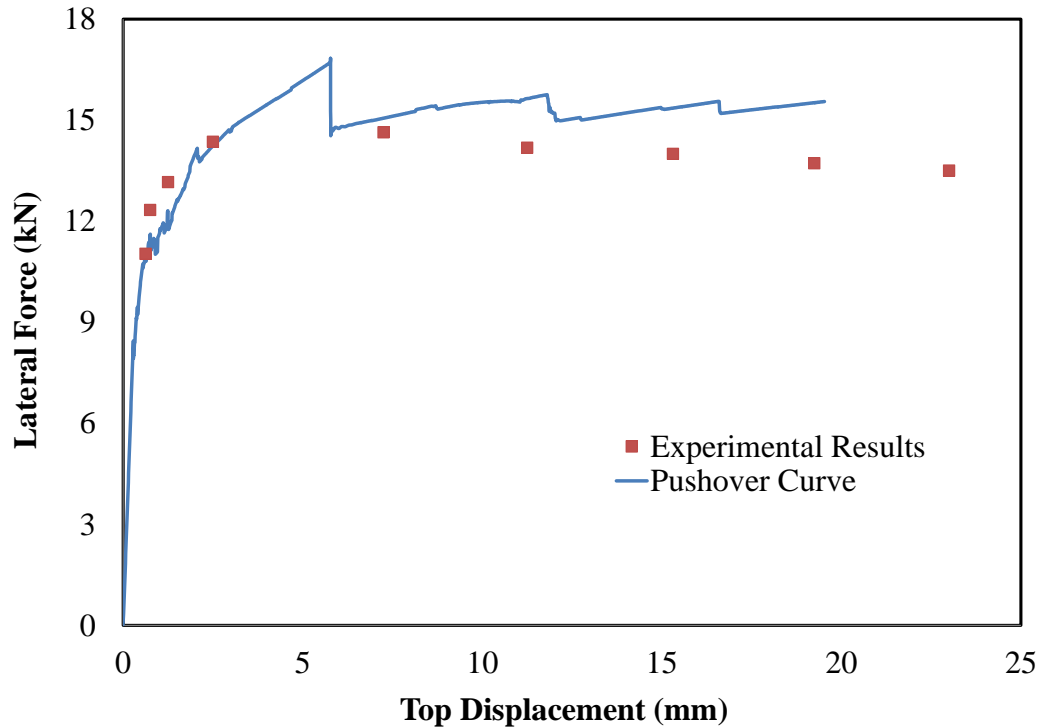
Figure 4.8 Comparison of PO Analysis Conducted on Finite Element Macro Model and Experimental Data for the Wall Tested by Franklin et al., (2001)

Pushover curve obtained by nonlinear pier model approximates experimental data well. Error in maximum strength is 13% and error in ultimate drift is 15%. Degradation of strength after maximum strength is observed in experiment. However nonlinear pier model could not catch degradation since Newton-Rapson iteration is used by ANSYS (Aldemir, 2010).

Minimum principal stress distribution, maximum principal strain distribution and crack pattern in which out of plane cracks and small cracks discarded are given for 0.1%, 0.5% and ultimate (1.3%) drift levels (See Figure 4.9).
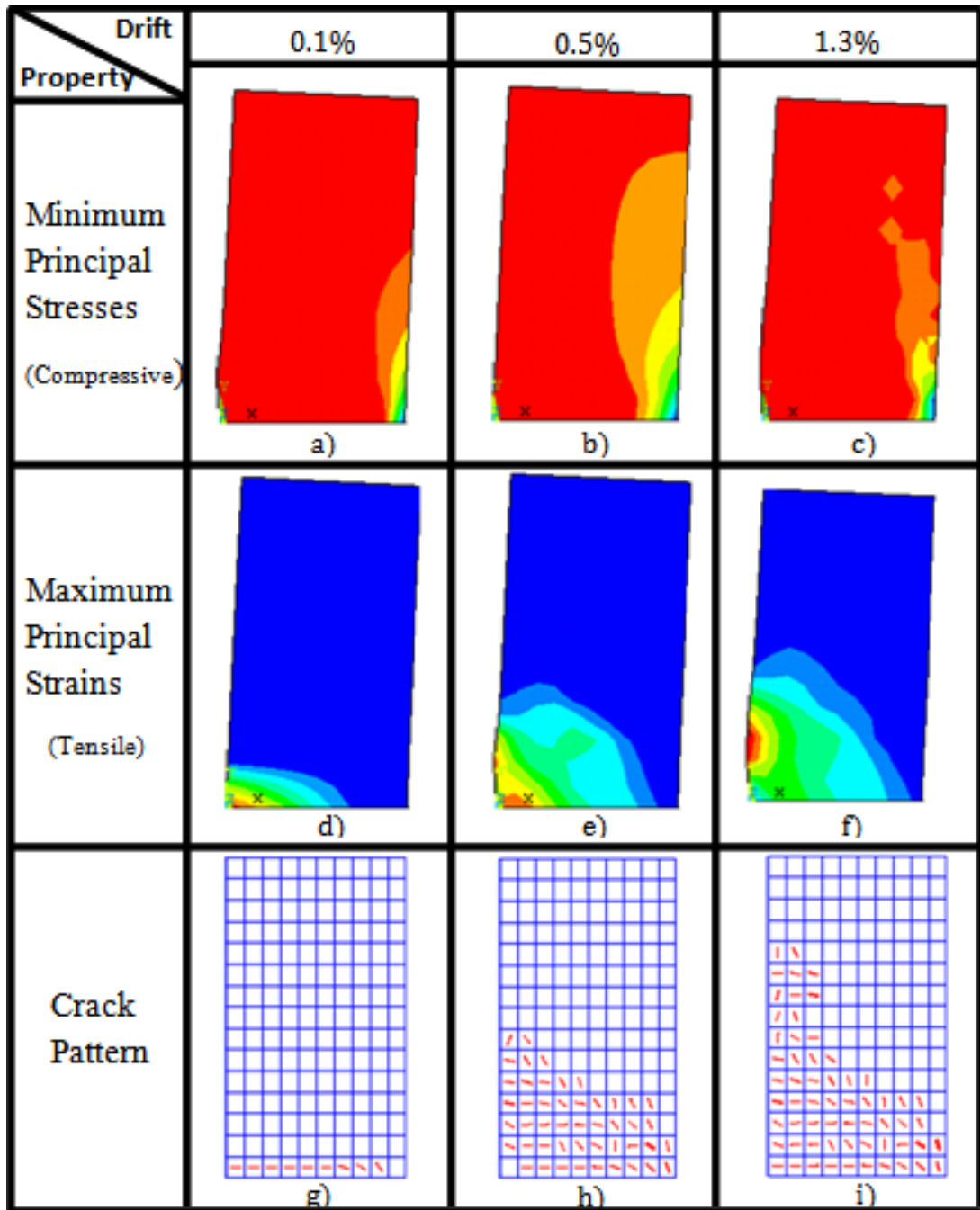
Figure 4.9 Minimum Principal Stress Distribution, Maximum Principal Strain Distribution and Crack Pattern Corresponding to 0.1%, 0.5% and 1.3% (ultimate) Drift of Wall 1F

Overturning effect produced by lateral force at top is clearly seen on Figure 4.9a, 4.9b and 4.9c. As drift increases, compressive stresses are concentrated at the toe located at lower right of the wall. However maximum compressive stress could not

reach to compressive strength of masonry. So rocking without toe crushing is observed as experienced in experiment.

Maximum principal strains illustrated in Figure 4.9d, 4.9e and 4.9f also points out typical rocking failure. As lateral displacements increase to the right, overturning moment creates tension at the lower left corner. Elongation of members at lower left corner forces the wall to make a turn over the toe.

Cracking pattern (see Figure 4.9g, 4.9h and 4.9i) also demonstrates flexure dominant behavior. Horizontal cracks which are formed at the early stages and propagate with increasing drift are indicators of tension in a direction perpendicular to crack surface. When tension produced by overturning moment is larger than compression supplied from overburden pressure plus tension strength of masonry, horizontal cracks takes place.

4.2.2.2 URM Wall Tested by Ganz and Thurlimann (1GT)

Wall investigated by Ganz and Thurlimann (1982) has 3600 mm length, 2000 mm height and 150 mm thickness. Compressive and tensile strength of the wall is 7.61 MPa and 0.28 MPa respectively. Modulus of elasticity is measured as 2460 MPa. Initial vertical stress of 0.61MPa is applied before implementing lateral displacement. Boundary conditions are fixed at bottom, concrete slab of 160 mm placed at top. Also additional brick units are placed at two ends in order to reflect flange effect of supporting walls (See Figure 4.7a). Wall aspect ratio is low (h/L=0.56) and low level of vertical pressure (σ/f_m=0.08) is applied on the wall. Diagonal tension failure might be expected due to low aspect ratio.

According to test results, despite diagonal tension failure is believed to be a brittle failure mode, an ultimate drift of 0.73 is observed. Lourencho (1996) explained this fact by confinement effect of flanges and concrete slab. Another explanation might be effect of sliding between masonry units because stair stepped failure going through mortar joints is observed.

Model properties of the wall are defined as explained in section 4.1. $24 * 13 = 312$ mapped meshed elements are used for the model generation. Again, nonlinear solution properties of ANSYS such as line search, DOF predictor, convergence limit and maximum number of iterations are utilized whenever convergence is disturbed. Final force-displacement curve of the wall is given in Figure 4.10.
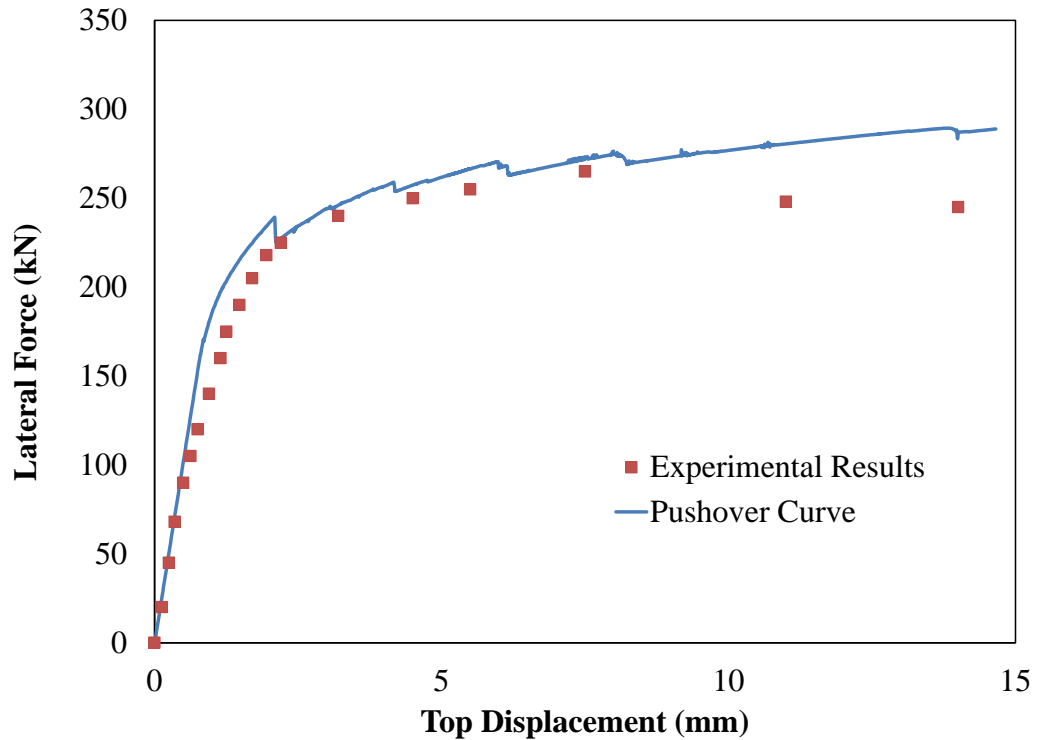
Figure 4.10 Comparison of PO Analysis Conducted on Finite Element Macro Model and Experimental Data for the Wall Tested by Ganz and Thürlimann (1982)

It can easily be realized that the nonlinear pier model approximates the response of the test wall well. Error in maximum lateral strength and top displacement is 8.3% and 4.5% respectively. Once again degradation of strength after maximum strength level could not be captured.

In order to make a detailed investigation, minimum principal stress distribution, maximum principal strain distribution and crack pattern in which out of plane cracks and small cracks discarded are drawn for 0.1%, 0.4% and ultimate (0.73%) drift levels (See Figure 4.12).

At the early levels of lateral displacement, failure mechanism could not be identified. Minimum principal stress is distributed such that compressive stress increases going from left to right which is an indication of effect of overturning moment (see Figure 4.12a). At this level, maximum tensile strains are cumulated at lower left (see Figure 4.12d) and cracks originated consistent to maximum tensile strains (see Figure 4.12g).

Further increasing lateral displacement, unique characteristics of diagonal tension failure arises such as formation of diagonal compression and tension struts (see Figure 4.11). Compression strut might be identified looking at Figure 4.12b. Two yellow bands of compression region are visible. Tension strut might be identified by looking at Figure 4.8e and 4.8h. Both maximum tensile strain and resulting cracks which are oriented perpendicular to tension strut is visible.

$$L_{DB'} < L_{DB}$$
$$L_{DB'} = compression\ strut$$
$$L_{AC'} > L_{AC}$$
$$L_{AC'} = tension\ strut$$
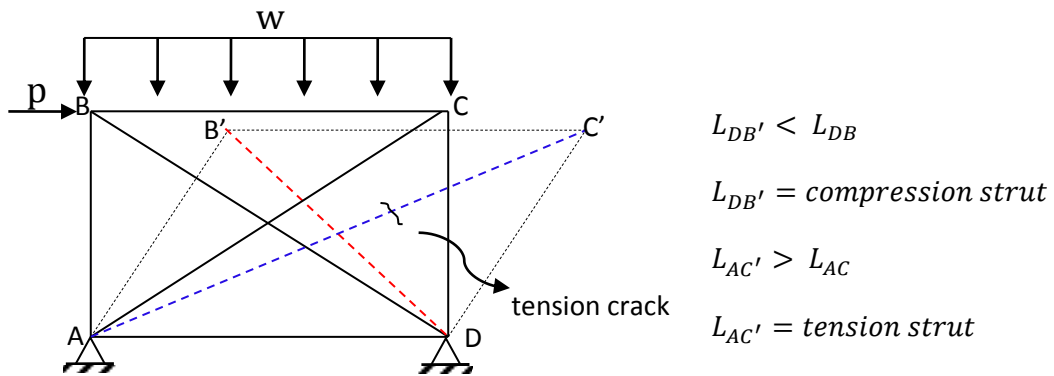
Figure 4.11 Compression and Tension Strut Formation in Diagonal Tension Failure

At the final stage two compression bands combined developing a final clear compression strut (see Figure 4.12c). Final principal strain distribution (see Figure 4.12f) is consistent with tension strut and final crack pattern (see Figure 4.12i) is compatible with experimental results.
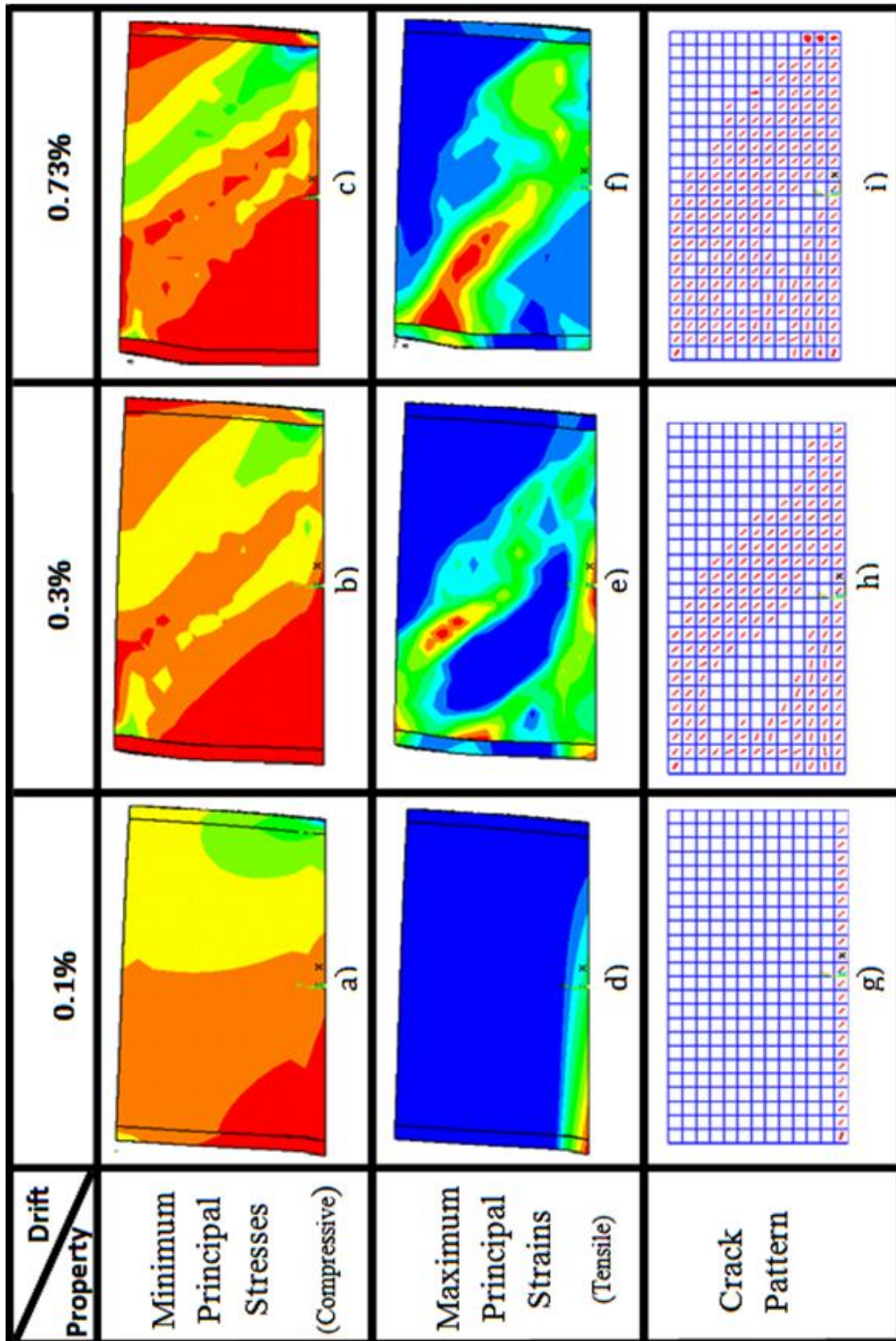
Figure 4.12 Minimum Principal Stress Distribution, Maximum Principal Strain Distribution and Crack Pattern Corresponding to 0.1%, 0.4% and 0.73% (ultimate) Drift of the Wall 1GT.

CHAPTER 5

COMPUTER MODEL FOR NONLINEAR ANALYSIS OF URM BUILDINGS

It has been revealed in Chapter 3 that when applied on perforated masonry frames, equivalent frame modeling technique yields acceptable results considering lateral displacement profile, base shear and axial load level on base story piers in the elastic range. In this chapter, the ability of this technique in modeling elastic behavior of masonry frames will be advanced by defining nonlinear force-deformation characteristics of masonry piers existing in equivalent frames utilizing so called shear hinges. Thus, nonlinear model of URM frames and buildings are developed for static pushover analysis which is essential for displacement based assessment of buildings.

Chapter 5 starts with definition of plastic hinges to be employed for the idealization of masonry piers passing into nonlinear range. Concepts which are discussed and accepted for the inelastic behavior of masonry walls in Chapter 4 will be briefly refreshed for this purpose. After definition of nonlinear behavior of each pier through shear hinges, equivalent frame model will be made capable of nonlinear response. Finally proposed nonlinear model for URM is verified by comparing the model with experimental results of one cyclic and one shake table tests conducted at University of Pavia and Ismes Laboratory at Bergamo respectively.

5.1 Plastic Hinge Definition to be used for Nonlinear Pushover Analysis

In the elastic range, lateral force is related to lateral displacement solely by lateral elastic stiffness (K_e) which is a function of aspect ratio, boundary conditions, modulus of elasticity and thickness of the wall (Equation 3.2). Whereas in the post elastic range, non-linear properties such as lateral strength (V_u), ultimate drift (δ_u) and post elastic stiffness (K_i) are needed to be determined for full identification of the bilinear idealization of force deformation relationship (see Figure 5.1).
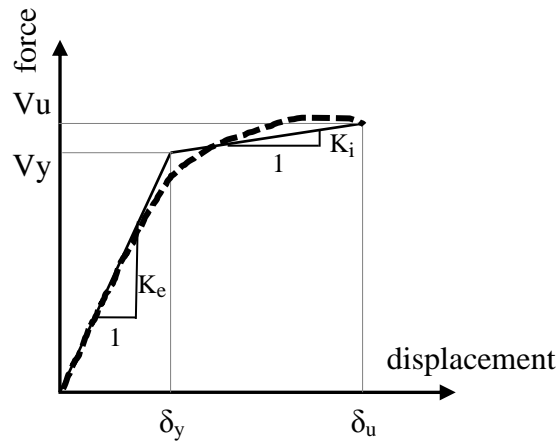
Figure 5.1 Bilinear Idealization of Force-Deformation Relationship for Masonry Walls

As it is discussed in Chapter 4, nonlinear response of masonry walls is very complex and there exists no properly determined simple method illustrating the nonlinear force-deformation characteristics of masonry walls on which failure mode is strongly dependent. As a result, nonlinear finite element modeling of masonry is probably the most sophisticated and convenient way of distinguishing between different failure modes and simulating nonlinear response of masonry walls.

A finite element model proposed by Aldemir (2010) to model masonry walls is investigated in the previous chapter and it performed well in terms of simulating flexure and shear dominated responses, damage propagation through cracking, base shear capacity and ultimate drift ratios. Since nonlinearity in URM walls is mainly due to shear, shear hinges whose constitutive relationship is determined according to Equations 4.1 and 4.2 are assigned at the base of each pier.

Proposed equations account for axial load level, aspect ratio and compressive strength of the wall on the force deformation relationship. In order to illustrate the influence of these variables on the response, force displacement curves of 4 cantilever walls each having a length of 1 meter and thickness of 0.25 meter and other properties given in Table 5.1 are determined according to proposed equations (see Figure 5.2).

Table 5.1 Compressive Strength, Overburden Pressure and Aspect Ratio of Piers Whose Force-Deformation Curves are drawn in Figure 5.2

	f_m (Mpa)	p (Mpa)	λ
P1	2	0.2	1.5
P2	6	0.2	1.5
P3	6	0.4	1.5
P4	6	0.4	1

Walls in Table 5.1 are selected such that going from P1 to P4, compressive strength and overburden pressure is increased and aspect ratio is decreased keeping all other variables constant in each step. Difference between; P1 and P2 is due only to increase in compressive strength, P2 and P3 is due only to increase in overburden pressure, P3 and P4 is due only to decrease in aspect ratio.
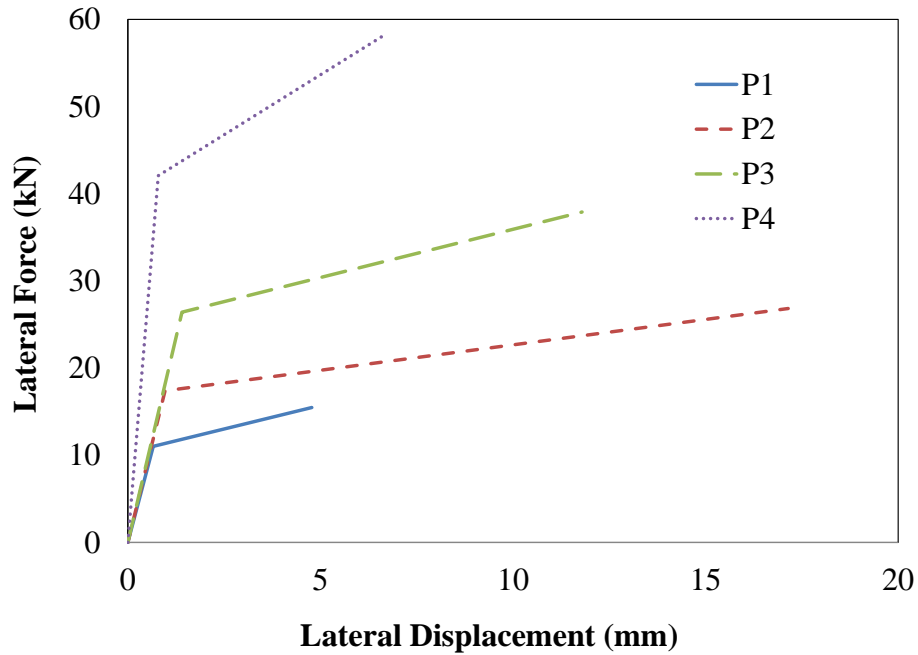
Figure 5.2 Shear Force versus Lateral Displacement Curves of Cantilever Walls Specified in Table 5.2.

As it is clearly seen from the figure, yield force and ultimate force capacity increases as aspect ratio decreases and axial load, compressive strength increases. At the same time, deformation capacity increases with the increase in aspect ratio, compressive strength and decrease in axial load on the wall.

Although aspect ratio, compressive strength and overburden pressure is reflected on derivation of these curves, effect of modulus of elasticity and boundary conditions are not taken into account due to assumptions made in their derivation (i.e. modulus of elasticity is taken as 2000MPa and cantilever boundary conditions are assumed for all walls). Since boundary conditions directly affect elastic lateral stiffness of walls, these curves could not be directly imposed on piers existed in a masonry building. Fortunately, as it is illustrated in Chapter 3, elastic lateral stiffness of masonry piers is successfully captured when equivalent frame method is applied. Since nonlinear hinges are activated after "yielding" take place, major drawback of the hinges is compensated.

5.2 Nonlinear Equivalent Frame Modeling Approach for Masonry Buildings

For reinforced concrete or steel structures, typical structural elements are the columns and the beams whose cross sectional dimensions are much smaller than their length. As a result, shear deformations of these members might be neglected and they might be idealized as flexural members. Under earthquake induced lateral loading, maximum moments are experienced at the ends of these flexural members. Consequently, curvature is accumulated at the end spans.

When a RC or steel structure is modeled with one dimensional frame elements, accumulation of plastic curvature might be idealized with plastic hinges. Moment curvature or moment rotation relation of these hinges might be defined from cross sectional properties of members taking axial load moment interaction into account.

In case of laterally loaded cantilever columns, lateral force versus tip deflection relationship might be derived analytically for RC and steel members. After determining yield moment from cross sectional properties, lateral tip deflection at yield might be calculated without significant error by neglecting shear deformations (see Figure 5.3.a).
Yielding due to moment takes place wherever curvature demand on the column is greater than yield curvature. As explained in the preceding paragraph, this

phenomenon usually takes places at the bottom or top of the columns. For a laterally loaded cantilever column, moment reaches its maximum value at the bottom (see Figure 5.3.a).

It might be assumed that sections which are forced to pass into nonlinear range fall inside plastic length of the column which might be approximated to be equal to the half of the height of the cross section (see Figure 5.3.b).

Upon determining distribution of curvature along the columns length, lateral deflection is calculated by summing lateral elastic and lateral plastic deflections. In order to calculate lateral plastic deflection, plastic rotation which is equal to integration of plastic curvature along plastic length is assumed to be lumped at the middle of the plastic length of the column (see Figure 5.3.c).

Multiplication of plastic rotation with the length of column above plastic hinge gives the plastic component lateral displacement.

a)

$$u_y = \frac{F_y h^3}{3EI}$$

M_y

Φ_y

b)

$$u_m = u_y + u_p$$

$$= \frac{F_y h^3}{3EI} + \theta_p \left(h - \frac{h_p}{2}\right)$$

M_y

M_p

Φ_y

Φ_p

c)

F_u

F_y

δ_u

$$\int_0^L \emptyset dx \approx \theta_y + (\emptyset_p - \emptyset_y)h_p \approx \theta_y + \theta_p \approx \theta_u$$
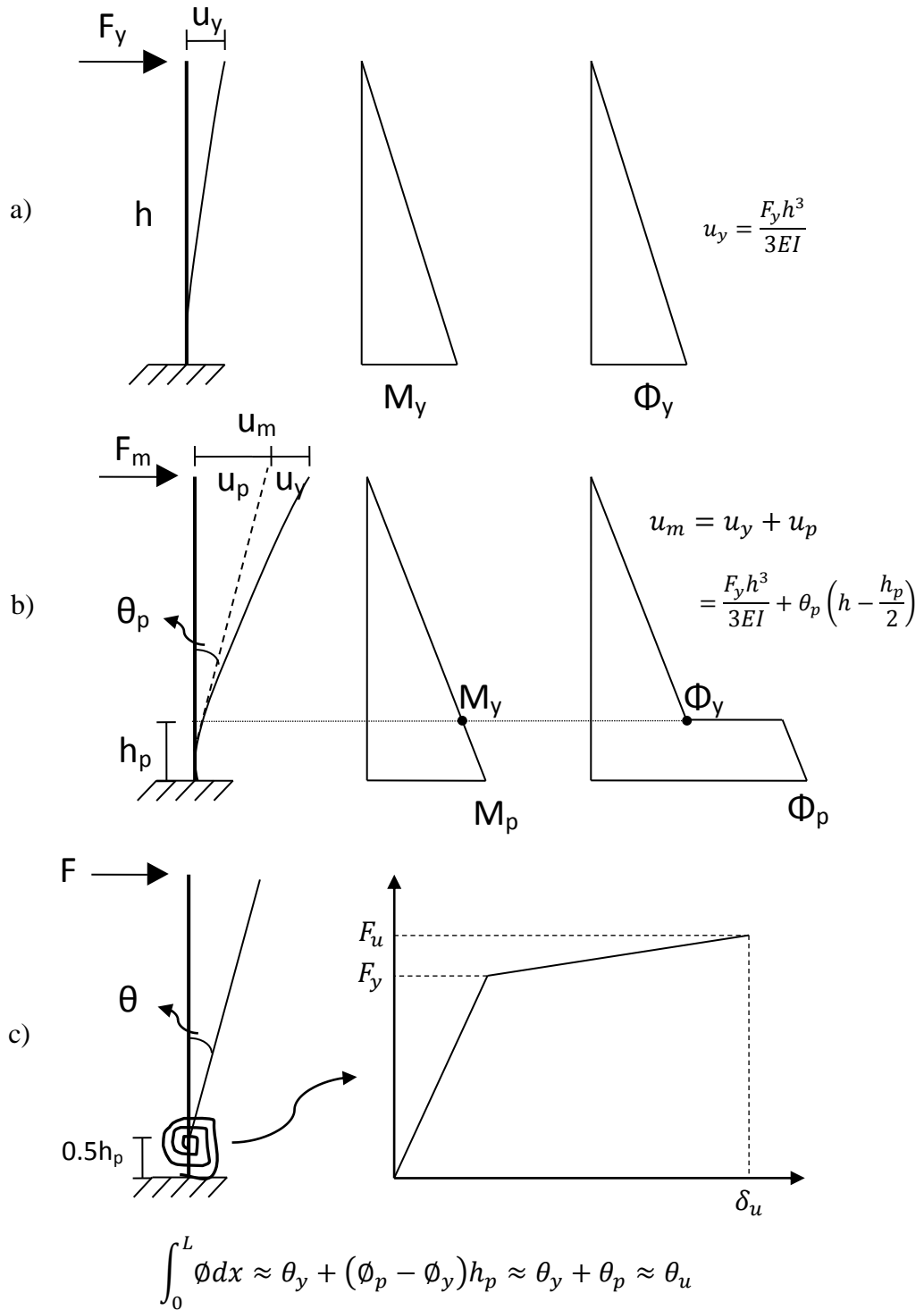
Figure 5.3 Derivation of Force Displacement Relationship for Flexural Members with Cantilever Boundary Conditions a) Distribution of Moment and Curvature at Yield, b) Distribution of Moment and Curvature at Plastic Range, c) Plastic Hinge Idealization

Contrary to typical RC or steel frame elements whose nonlinear behavior is governed by flexure, masonry piers and spandrels are squat members on which shear deformations are effective in the elastic range. Sinha et al. (1971) demonstrated experimentally that, after cracking, deformations due to shear become highly nonlinear in URM walls. Also, Gilmore et al. (2009) state that shear deformations dominate flexural deformations as level of damage increases and unlike the elastic response, shear domination in inelastic range is independent from aspect ratio of walls.

Moreover, unlike RC or steel frame elements, masonry piers and spandrels do not actually 'yield'. In the absence of reinforcement, masonry is not capable of resisting tension induced by moment action. Instead plastic response is achieved by cracking and crushing of masonry which results in various mechanisms namely; sliding, rocking, diagonal tension and toe crushing.

Plastic response of masonry elements could only be identified by sophisticated finite element analyses. However, the ability of equivalent frame modeling technique in computational easiness and the ability of computationally costly FEM in simulating the nonlinear behavior of masonry walls might be combined.

As it is illustrated in Chapter 3, when masonry frames are modeled with equivalent frames, satisfactory results are taken in the elastic range. In order to provide inelastic behavior to frame elements, plastic hinges might be assigned. Since hinge properties for masonry members could not be determined from cross section properties as in the case of reinforced concrete or steel members, force deformation relationship is taken directly from finite element analysis results. That is, although plastic hinge formation is not observed in reality; plastic hinges are assigned in order to reflect plastic response of masonry walls which are derived from sophisticated finite element analyses.

Since inelastic behavior in masonry walls is governed by shear, instead of moment hinge, shear hinge is assigned at the bottom of equivalent frames (see Figure 5.4).
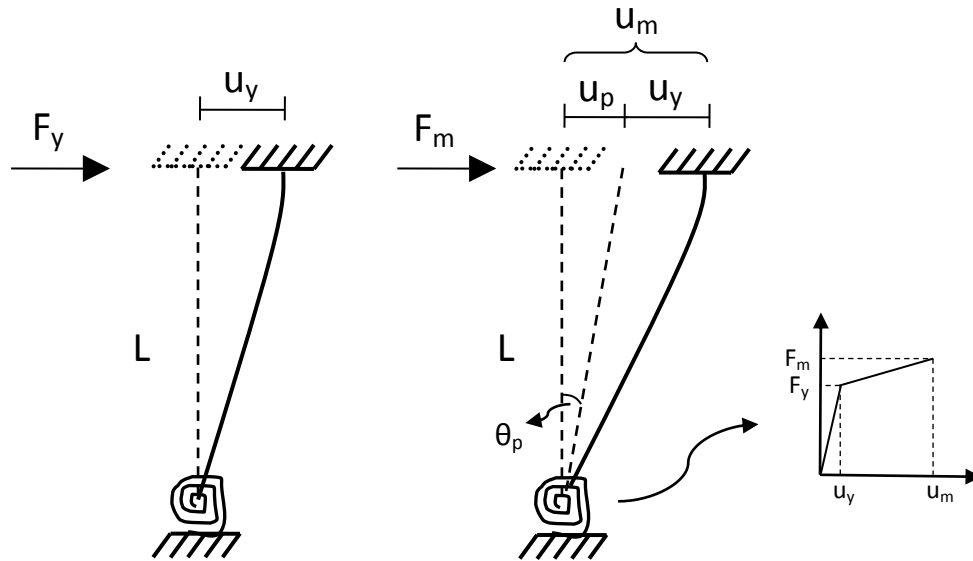
Figure 5.4 Equivalent Frame Idealization of URM Piers with Shear Hinge for Nonlinear Static Analysis

To sum up, after masonry walls are modeled with equivalent frame method which easily captures elastic behavior, a shear hinge is assigned for the idealization of nonlinear response. Properties of the shear hinge are determined from Equations 4.1, 4.2. Since these equations are derived from bilinearization of finite element analysis of the wall, they are assumed to simulate nonlinear behavior.

5.3 Application of Nonlinear Equivalent Frame Model on Computer Software

For the equivalent frame modeling of masonry buildings, well known computer software SAP2000 (2009) will be utilized. Nonlinear material behavior is available through the use of frame hinges which might be defined manually. Software is capable of conducting nonlinear static analyses through these hinges where all plastic deformation occurs within the point hinge (i.e. lumped plasticity).

User defined hinges that can be assigned to any degree of freedom according to SAP Reference Manual (2009) is defined by five points, A-B-C-D-E, as shown in Figure 5.5. For moment hinges horizontal and vertical axes represent moment and rotation whereas for a shear hinge they represent force and lateral translation respectively.
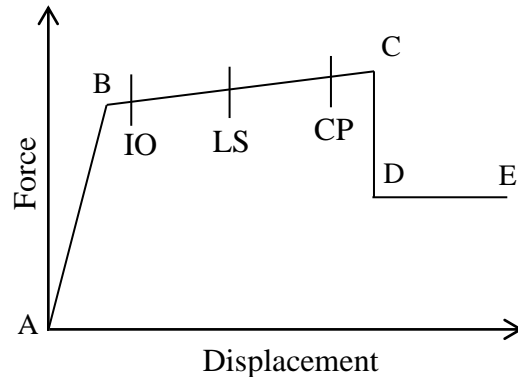
Figure 5.5 User Defined Plastic Hinge Definition in SAP2000

The shape of the curve in Figure 5.5 is inspired from hinge recommended by FEMA 356 for pushover analyses. Although 5 points (i.e. A, B, C, D, E) are available for definition of the curve, 3 points are enough for a bilinear curve. Thus, same values will be assigned for point C, D and E.

Definition of each point on the curve is explained below:

• Point A is the origin.
• Point B represents yielding. Deformation up to this point is elastic and linear relation between force and displacement is automatically determined from material, geometrical properties and boundary conditions. So, no deformation occurs in the hinge up to point B. When the force or moment associated with this point is reached force - displacement curve of the member starts to follow the hinge.
• Point C represents the ultimate capacity for pushover analysis.
• Point D represents a residual strength for pushover analysis.
• Point E represents total failure. Beyond point E the hinge might drop to zero or might be interpolated according to selection.

Although strength loss or negative slopes are permitted in the hinge definition, use of these features is not advised in the SAP2000 Reference Manual (2009). It is stated that sudden strength loss is often unrealistic and can be very difficult to analyze,

especially when elastic snap-back occurs. It is also stated that anytime negative stiffness's are present in the model, the solution may not be mathematically unique.

Hopefully, bilinear idealization of force deformation relationship which is used for shear hinge definition of masonry does not result in aforementioned discrepancies.

Hinges might also be defined such that axial force and two bending moments may be coupled through an interaction surface. Thus, yielding of the hinge takes place depending on the axial force and bi-axial bending moment levels at the hinge location. Unfortunately software does not allow definition of a hinge that accounts for coupling of axial load with shear. Since axial load on a masonry wall is an important parameter influencing plastic behavior, neglecting effect of change in axial load level on individual piers to the structural response will be investigated in section 5.4.1.3.

Another assumption made for the modeling is; nonlinearity is restricted to masonry piers only. Spandrels remain elastic through analysis but piers pass into nonlinear range when they are pushed above the elastic limit. This is because very little experimental information is available on cyclic behavior of unreinforced masonry beams, especially regarding the deformational behavior (Magenes and Fontana, 1998) and ultimate failure of the masonry buildings is controlled by piers.

5.4 Verification of Proposed Computer Model

Tests conducted on masonry specimens at the University of Pavia and Ismes Laboratory at Bergamo are the most preferred reference for the verification of different URM modeling techniques in the literature. After definition of experimental work, results of proposed nonlinear equivalent frame model will be compared with the results of these experiments for the purpose of verification.

5.4.1 Seismic testing of a Full-Scale, Two-Story Masonry Building at the University of Pavia

Seismic testing of a full-scale, two story URM building conducted at the University of Pavia and seismic dynamic testing of the 3/8 scaled prototype of the same buildings at the University of Illinois (Magenes et al, 1995) gives an opportunity to verify proposed computer model.

The geometry and the loading direction of the tested building are given in Figure 5.6. Displacements are applied in the longitudinal direction at the story levels. Transverse walls are solid whereas longitudinal walls are perforated such that the wall with door openings is named as door wall and the wall with window openings is named as window wall. Despite window wall is connected to transverse walls with an interlocking brick pattern around the corner, there exists no connection between door wall and the adjacent walls. As a result 2-D modeling of the door wall is implementable.
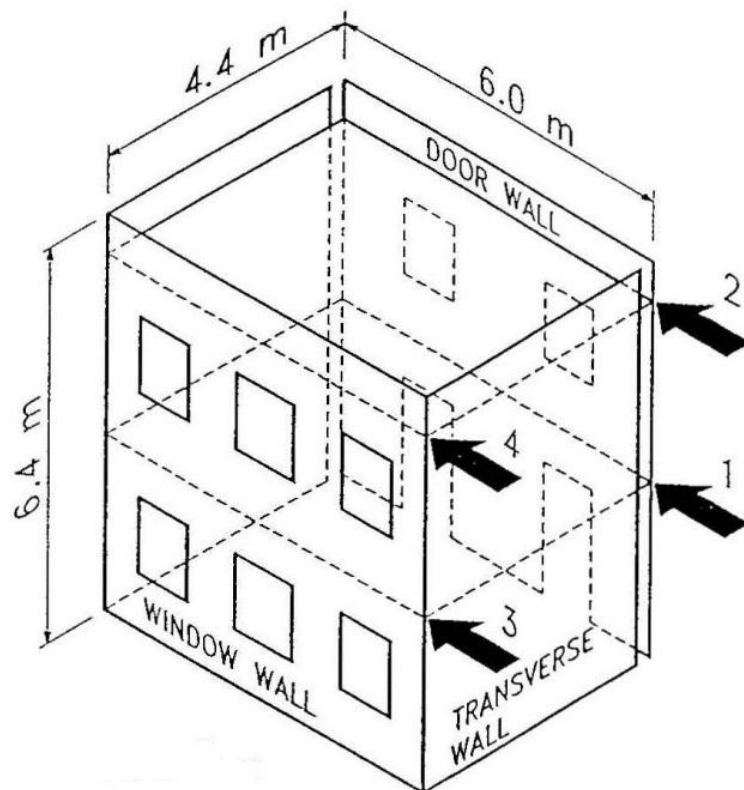
Figure 5.6 Two-Story Masonry Building Tested at the University of Pavia, (Magenes et al., 1995)

According to Magenes and Calvi, in determination of testing procedure for the masonry buildings two difficulties arise:

- Lumped mass approximation is not applicable in case of masonry buildings. Due to heavy weight of walls which is distributed over the buildings height, determination of mass matrix is challenging. As a result, pseudo dynamic testing methods are not considered applicable for these structures (Calvi et al., 1995).

- Since cracking is highly dependent on loading rate, monotonic testing methods are not considered to be realistic for URM systems (Paulson et al., 1990).

As a result, quasistatic application of standard pattern of displacement cycles (see Figure 5.7) is selected to be the most appropriate testing method for URM specimen tested at University of Pavia.

In order to determine the loading pattern of the full scale building tested at University of Pavia, 3/8 scaled prototype of the test building is tested dynamically on a shaking table at the University of Illinois. According to variation in effective height of restoring forces, general trend in effective height is observed towards 0.75 which indicates uniform distribution. (Magenes et al., 1995)

As a result, uniform loading pattern is applied at each floor level in the quasistatic tests. Roof displacement is selected as the main controlling parameter. First floor displacement is controlled such that the applied force at first floor is equated to applied force at the second floor.
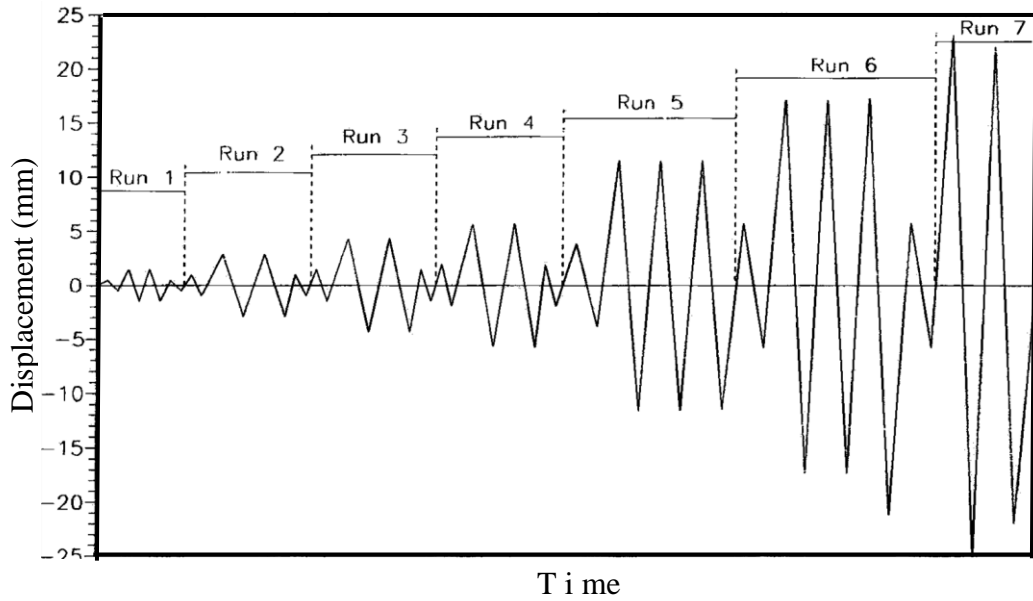
Figure 5.7 Sequence of Displacements Applied to the Second Floor of Tested Building in University of Pavia (Magenes et al., 1995)

The response of the tested frame to applied displacements is illustrated in Figure 5.8. It is reported that cracking started at a roof drift of 0.1% and maximum drift is measured as 0.3% at the end of run 6. Tested frame resisted approximately 150kN of base shear which corresponds to 40% of its total weight. Inter-story drift in the first floor at failure is measured as 0.37%.
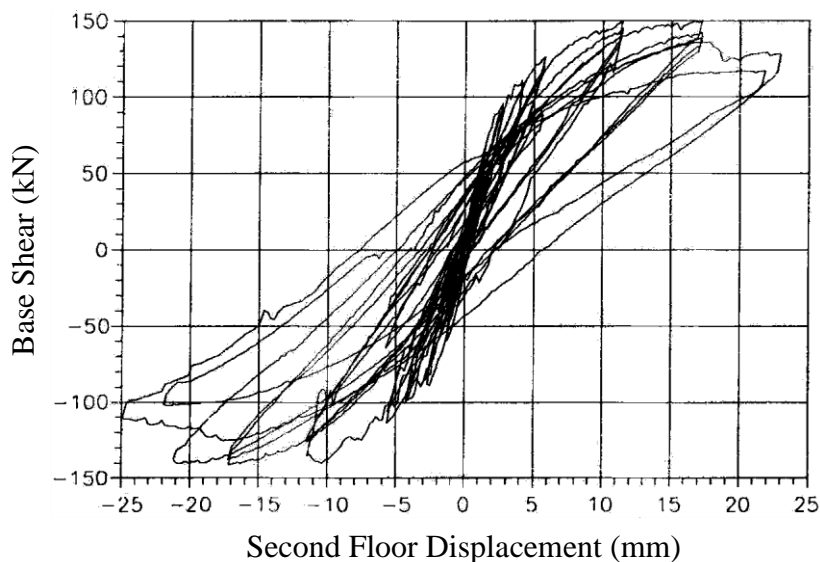
Figure 5.8 Total Base Shear vs. Top Displacement of Pavia Door Wall (Magenes et al., 1995)

91

Although cracking took place in the spandrels first, ultimate resistance is determined by pier failure. According to final crack pattern of the tested frame (see Figure 5.9), interior pier at the base experienced a clear diagonal shear failure. Whereas exterior piers at the base experienced a mixed failure mechanism where flexural dominated bed joint sliding and shear dominated diagonal shear modes are both observed.
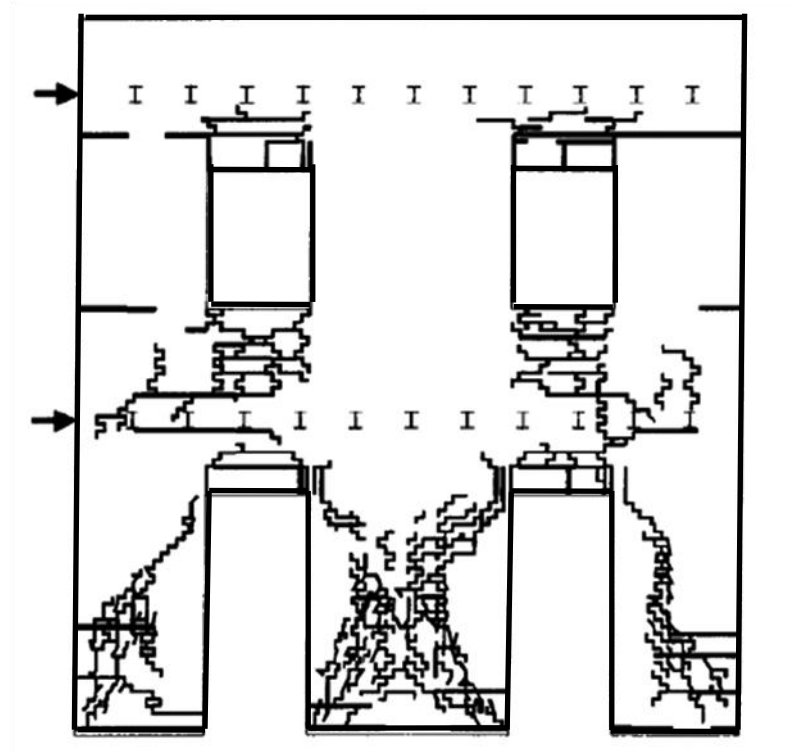
Figure 5.9 Final Crack Pattern of Pavia Door Wall (Magenes et al., 1995)

In order to conduct pushover analyses, computer model of the tested frame is built using SAP2000 software. Poisson's ratio and modulus of elasticity are the material constants to be defined since masonry is idealized as a homogenous and isotropic material. Poisson's ratio for masonry is taken as 0.2 and modulus elasticity is calculated as 1700 MPa from elastic stiffness of experimental data. RO lengths of piers are determined according to empirical approach proposed by Dolce (1989) as explained in Chapter 3, whereas full rigid offset is used for spandrels (Belmouden et al. 2007). Geometry of the model, rigid offsets and labels of the spandrels and piers are illustrated in the figure below.
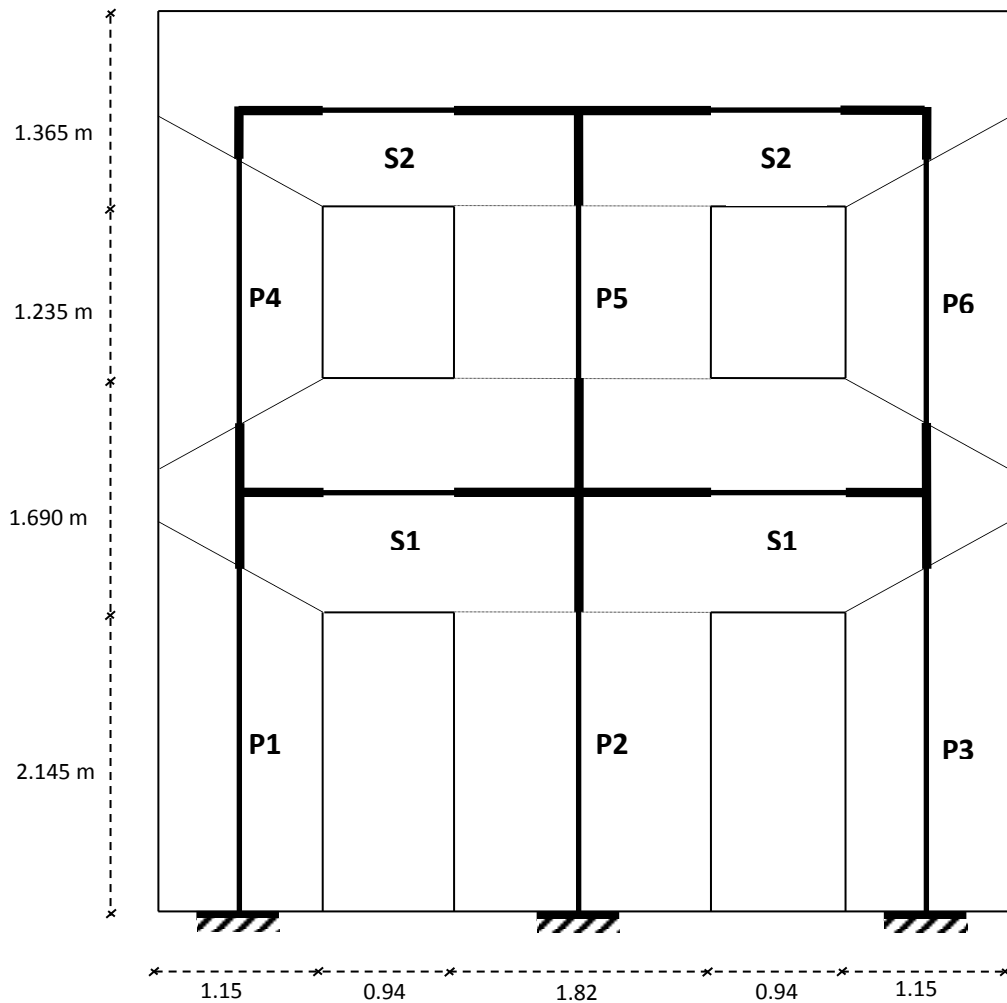
Figure 5.10 Equivalent Frame Model of Pavia Door Wall

Sectional properties of each pier are calculated from dimensions of the cross sections (see Table 5.2). Aspect ratio is calculated taking effective height of the member into account.

Table 5.2 Cross Sectional Properties of Pavia Door Wall Piers

Pier Label	L (m)	t (m)	h_{eff} (m)	λ	Area (m²)	Shear Area (m²)	I (m⁴)
P1	1.15	0.25	2.477	2.15	0.288	0.240	0.0317
P2	1.82	0.25	2.145	1.18	0.455	0.379	0.1256
P3	1.15	0.25	2.477	2.15	0.288	0.240	0.0317
P4	1.15	0.25	1.899	1.65	0.288	0.240	0.0317
P5	1.82	0.25	1.235	0.68	0.455	0.379	0.1256
P6	1.15	0.25	1.899	1.65	0.288	0.240	0.0317

In order to determine inelastic response of piers according to Equations 4.1 and 4.2; compressive strength, aspect ratio, axial load level, length and thickness of each individual pier is needed to be known.

Before testing Pavia Door Wall, tests were conducted on masonry wallets for the determination of material properties. According to test results, mean compressive strength of the masonry walls is calculated as 6.2MPa (Magenes et al., 1995). Thickness, length and aspect ratio of each wall might be determined from geometry of the test specimen (see Table 5.2). However determination of axial load level on each pier is required.

Due to overturning effect of earthquake induced lateral forces, axial load level on masonry piers are altered throughout the PO analysis of URM buildings. Unfortunately like many other structural analysis software, SAP2000 is incapable of taking coupling effect of axial load with shear force in the definition of shear hinges.

Since axial force is an important parameter affecting nonlinear response of masonry piers, 3 different approaches are employed and results are compared to determine the importance of overturning effect on the structural response.

First approach does not account for changes in the axial load level of piers on global response. Although second approach takes influence of axial load change on piers due to overturning effect of earthquake induced lateral loads, axial load level on piers are still assumed to be kept constant throughout the analysis. The third and the most sophisticated approach "step by step hand calculation" is capable of updating hinge properties in each step due to change in axial force as a result of overturning effect.

In PO analyses conducted on forthcoming sections (5.4.1.2 and 5.4.1.3), controlling parameter is selected as roof displacement. After force controlled nonlinear static analysis is conducted under dead load, displacement controlled nonlinear static analysis under uniform distribution of lateral forces are conducted from end state of the dead load analysis. Nonlinear parameters of the software, in which solution

control option and hinge unloading methods are determined, is taken as default values of the software.

PO analysis of section 5.4.1.4 is more sophisticated and it will be illustrated later on.

5.4.1.1 Hinge Properties Defined Under Dead Load

In order to calculate axial load level on each pier of the tested frame, linear analysis is conducted on computer model of the frame under the dead loads. Dead load of the test specimen has two sources: weight of the masonry walls calculated taking density of the masonry as 1.7 ton/m^3 and additional weights added to first and second floor levels idealizing slab load. As a result of dead load analysis, axial loads on each pier is determined as below.

Table 5.3 Vertical Load, Pressure and Stress over Strength Ratio of Pavia Door Wall Piers under Dead Load

	N (kN)	p (MPa)	p/fm (%)
P1	99.23	0.345	5.6
P2	178.6	0.393	6.3
P3	99.23	0.345	5.6
P4	44.62	0.155	2.5
P5	82.23	0.181	2.9
P6	44.62	0.155	2.5

After axial load on each pier is calculated, shear hinge properties are determined using equations 4.1 and 4.2 (see Figure 5.11).

Upon derivation of force displacement relationship of each pier, compatible shear hinges are assigned to each pier and PO analysis is conducted (see Figure 5.12). Base shear capacity is found to be 133kN which approximates experimental result with 12.8% error and ultimate drift is approximated less than 3% error.
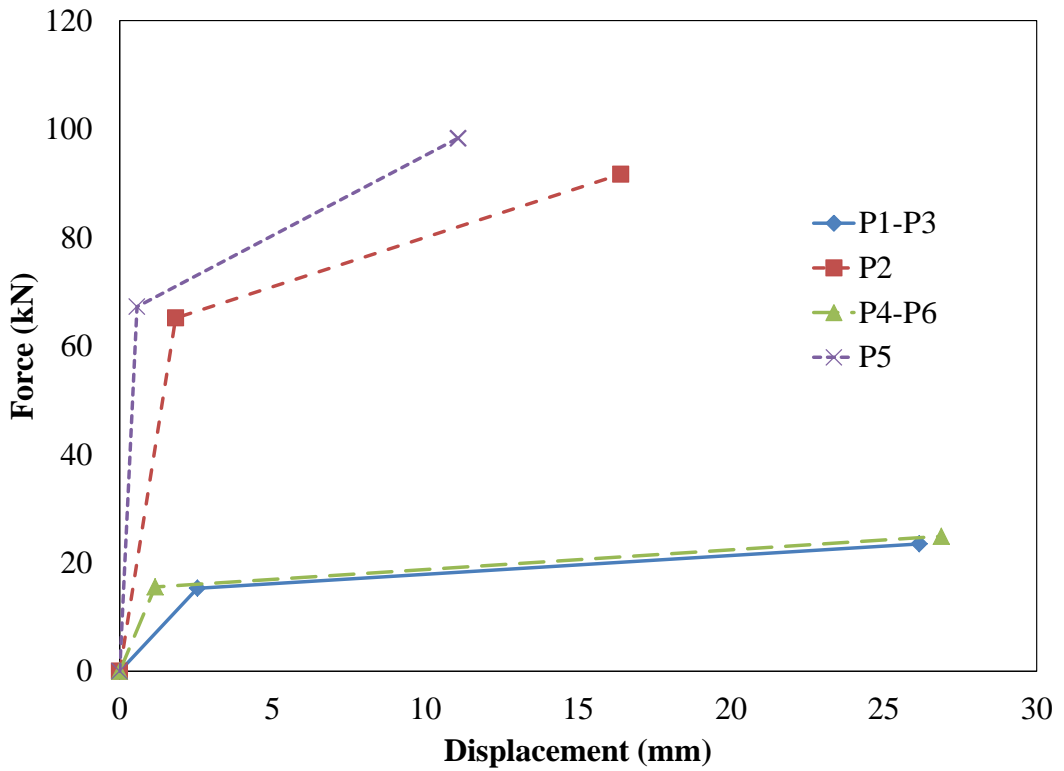
Figure 5.11 Idealized Nonlinear Pier Responses of Pavia Door Wall under Dead Load
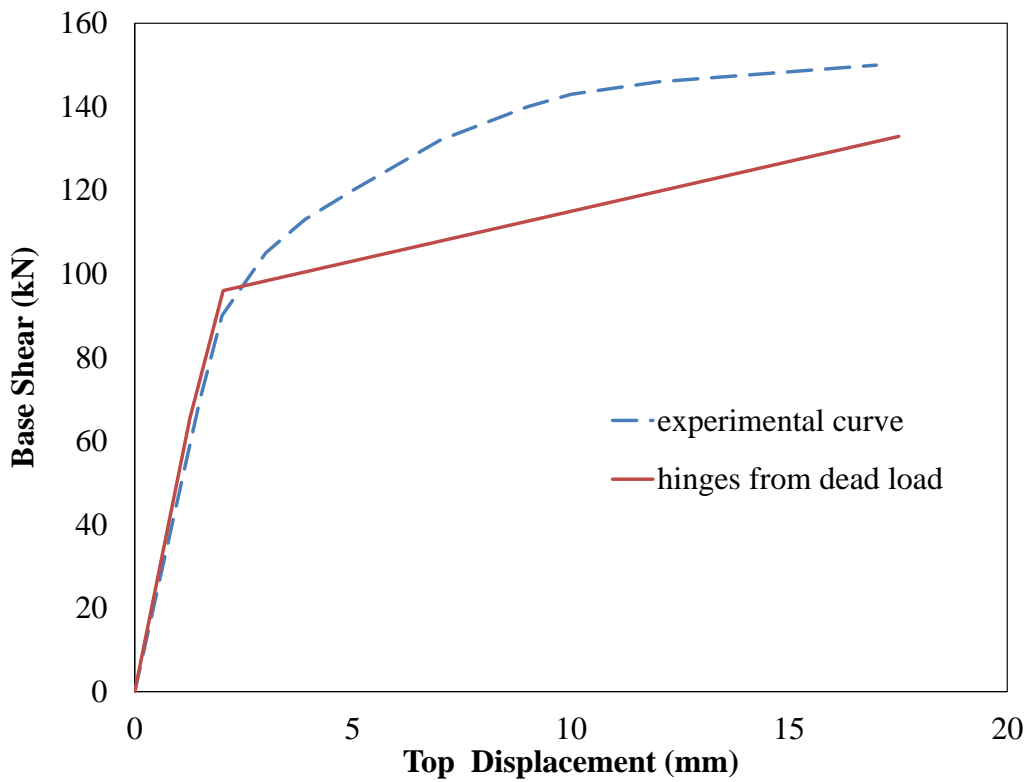
Figure 5.12 Comparison of Experimental Backbone Curve with Computer Model whose Hinges are Determined under Dead Load

Distribution of shear hinges at the final stage of the PO analysis is provided in Figure 5.13. Light grey hinges represent yielding of the hinge whereas dark grey hinge represents failure of the hinge. As it is understood from the figure, ultimate condition is reached when interior pier at the base reaches its ultimate capacity. Comparing final hinging pattern derived from computer model with experimental results (see Figure 5.9), it might be concluded that distribution of damage is well approximated by the computer model.
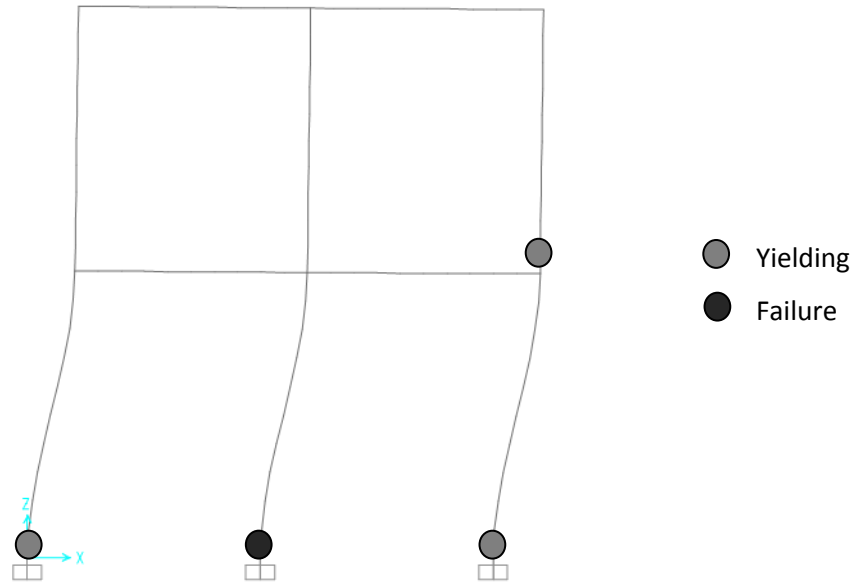
Figure 5.13 Final Hinging Pattern of Computer Model whose Hinges are Determined under Dead Load

5.4.1.2 Hinge Properties Defined Under Dead + EQ Load

In the second modeling approach, axial load level on each pier of the tested frame is determined from linear analysis of computer model under dead load plus lateral loads at floor levels idealizing earthquake induced lateral forces. 20% of the total weight (75kN) which approximately corresponds to the initiation of plastic region of structural response (see Figure 5.8) is applied laterally to computer model of the tested frame in a reverse triangular fashion.

It is assumed that axial load level on piers just before starting of plastification is a better approximation to exact behavior. As a result of dead plus earthquake load analysis, axial loads on each pier are determined as below (see table 5.4).

Table 5.4 Vertical Load, Pressure and Stress over Strength Ratio of Pavia Door Wall Piers under Dead plus Earthquake Load

	N (kN)	p (MPa)	p/fm (%)
P1	47.25	0.164	2.7
P2	179.98	0.396	6.4
P3	149.85	0.521	8.4
P4	30.93	0.108	1.7
P5	82.61	0.182	2.9
P6	57.92	0.201	3.2

After axial load on each pier is calculated, shear hinge properties are determined from Equations 4.1 and 4.2 (see Figure 5.14).
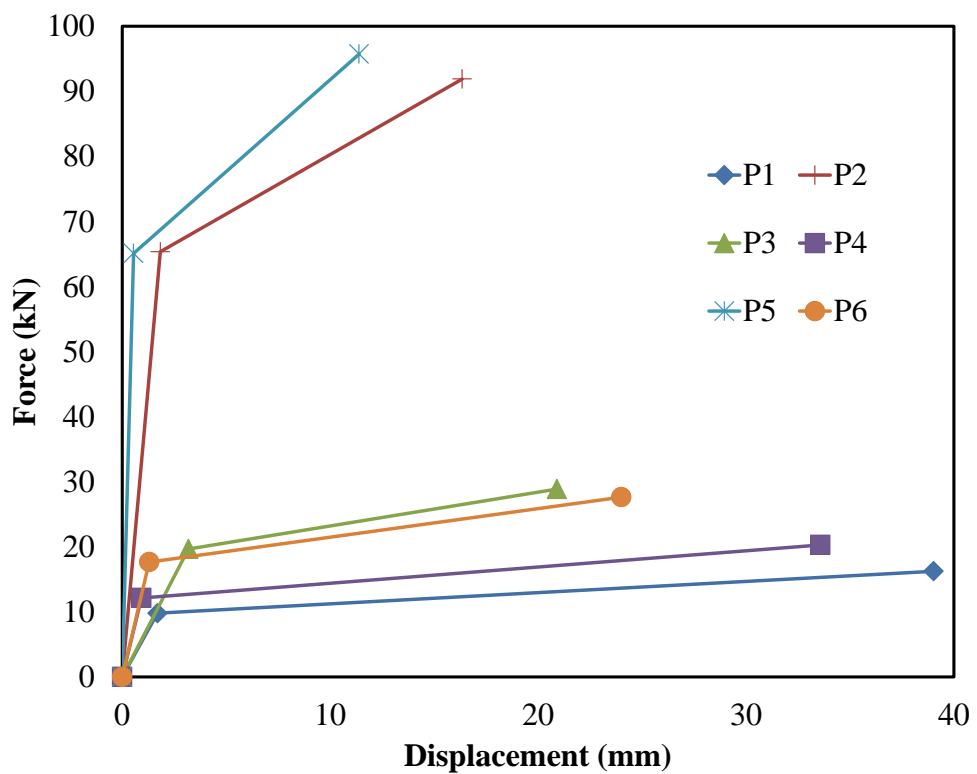
Figure 5.14 Idealized Nonlinear Pier Responses of Pavia Door Wall under Dead plus Earthquake Load

After shear hinge properties under dead plus earthquake load is determined pushover analysis is conducted (see Figure 5.15). Base shear capacity is found to be 132kN which approximates experimental result with 13.6% error and ultimate drift is approximated with 3.24% error.
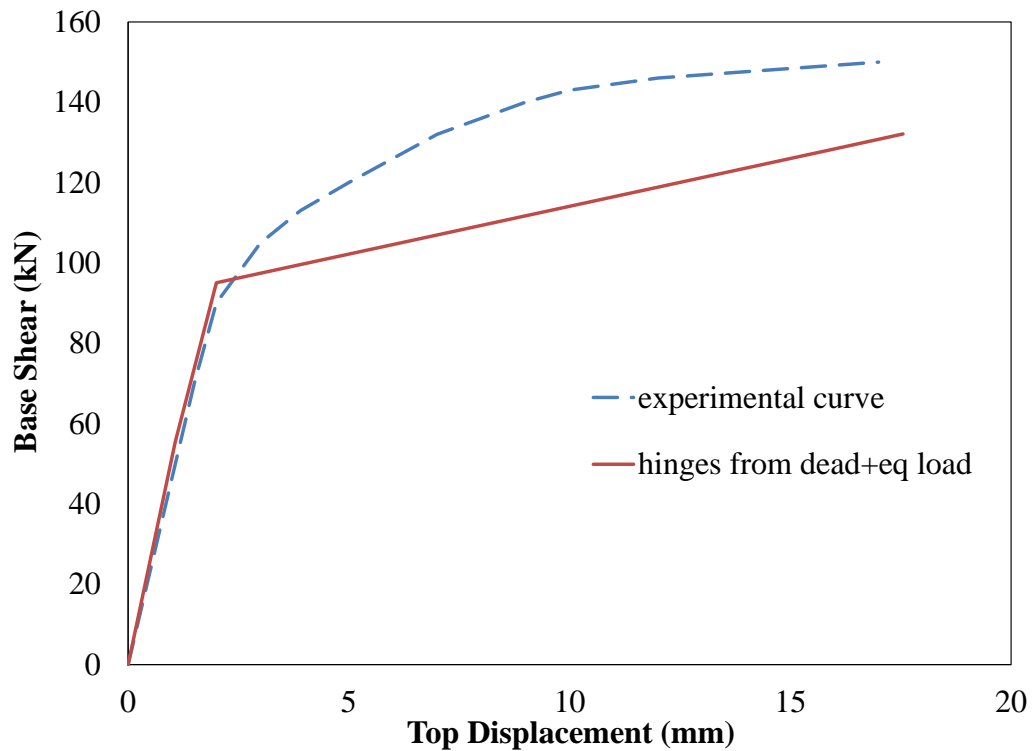
Figure 5.15 Comparison of Experimental Backbone Curve with Computer Model whose Hinges are Determined under Dead plus Earthquake Load

Distribution of shear hinges at the final stage of the pushover analysis is provided in Figure 5.16. Although force deformation relationship of individual piers altered due to change in axial load level final hinge pattern remained the same compared with previous analysis.
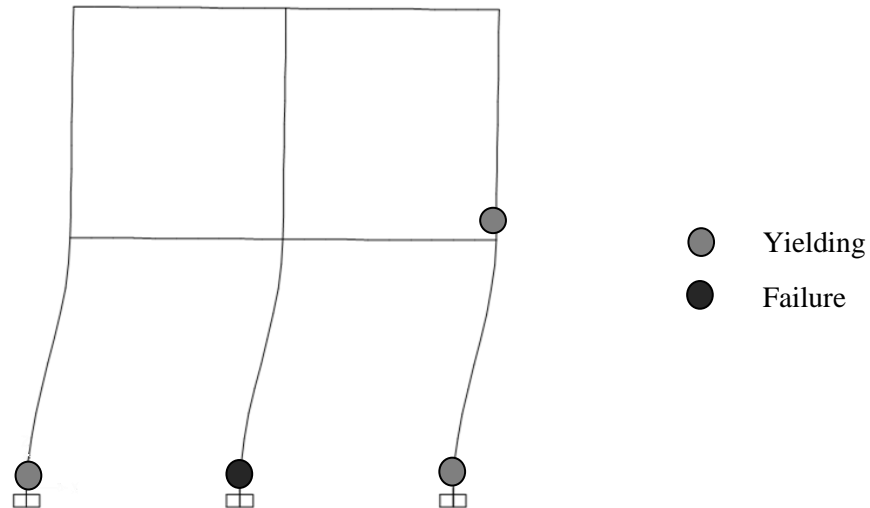
Figure 5.16 Final Hinging Pattern of Computer Model whose Hinges are Determined under Dead Load plus Earthquake Load

5.4.1.3 Step by Step Hand Calculation

In the third and the most sophisticated modeling approach, axial load level on the piers of the tested frame is updated in each step of the pushover analysis. This requires regeneration of shear hinge properties and imposes an iterative solution. Since utilized software is not capable of conducting such an analysis by default, PO analysis is conducted manually. Solution algorithm might be summarized in the flow chart below:

Table 5.5 Solution Algorithm for Incremental Nonlinear Static Analysis

Step 1	**1.** Model the masonry frame with equivalent frame method, **2.** Apply lateral load increment at story levels in an uniform pattern, **3.** Determine axial loads and shear forces on piers due to dead load plus applied lateral load, **4.** Determine yield capacity of each pier under calculated axial load, **5.** Compare shear force with yield capacity on each pier, **6.** If any pier reaches yield capacity stop and note axial force in each pier (N_{pier}), shear force in each pier (V_{pier}), base shear (V_{base}) and top displacement (u_{top}), **7.** Otherwise repeat steps from Step 1.2

Table 5.5 (Continued)

Step 2	**1.** Modify computer model to account for yielding, • Assign a shear hinge to yielded pier having zero yield force. In fact post elastic region of shear hinge defined under N_{pier} is assigned. **2.** Conduct PO analysis up to a top displacement increment, **3.** Determine incremental axial loads (N_{inc}), incremental shear forces (V_{inc}), incremenral base shear (V_{base_inc}) and incremental top displacement (u_{top_inc}) from pushover analysis, **4.** Determine final axial force and final shear force, • $N_{pier} = N_{pier} + N_{inc}$ • $V_{pier} = V_{pier} + V_{inc}$ **5.** Find yield (V_{yield}) and ultimate (V_{ult}) capacity of piers under N_{pier}, **6.** Compare V_{pier} with V_{yield} and V_{ult}, **7.** If any pier reaches yield or ultimate capacity stop and note: • Axial force in each pier (N_{pier}) • Shear force in each pier (V_{pier}) • $V_{base} = V_{base} + V_{base\_inc}$ • $u_{top} = u_{top} + u_{top\_inc}$ **8.** Otherwise repeat steps from Step2.2
Step 3	**1.** Modify computer model to account for yielding and failure, • This time in addition to just yielded or failed piers, previously yielded piers are also modified since N_{pier} is changing • Failed piers lose 80% of its load carrying capacity (FEMA 356) **2.** Follow Steps from Step 2.2
Step 4	**1.** Extract V_{base} and u_{top} from each step and plot the capacity curve for the entire structure

Because an incremental analysis is carried out after each successful step, computer model needs to be modified after any change in force displacement relationship of any pier. When yielding takes place in one of the piers, its stiffness should be

decreased for the modified computer model formation. Assigning a shear hinge with zero yield force satisfies this requirement since it yields at the very beginning of the analysis enforcing pier to follow post elastic region. However due to change in the axial load level, post elastic region of the pier also changes in the following steps. In order to reflect this change, force displacement relation of the assigned shear hinge is regenerated (see Figure 5.17). As a result together with recently yielded or failed piers, shear hinge properties of previously yielded piers are modified in each step.
\
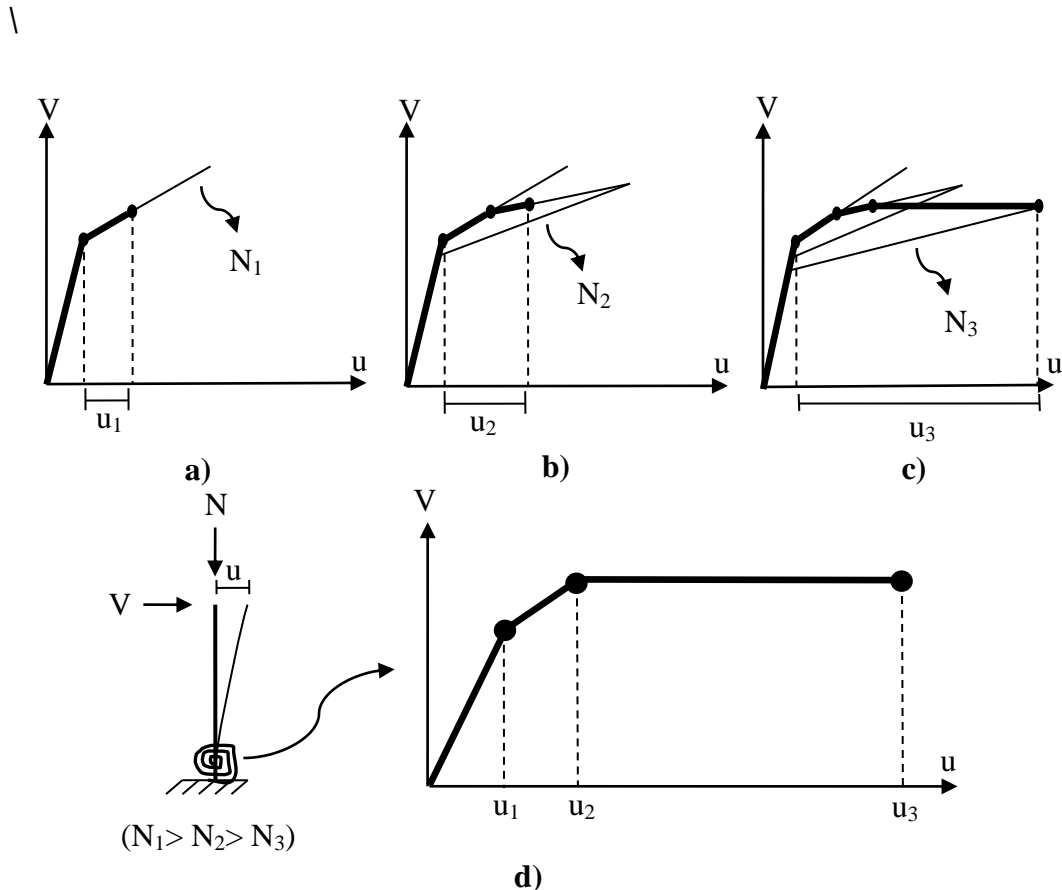
Figure 5.17 Definition and Regeneration of Shear Hinges Due to Change in Axial Load, a) V-u of Masonry Pier under N1, b) V-u of Masonry Pier under N2, c) V-u of Masonry Pier under N3, d) Definition and Regeneration of Shear Hinge under Decreasing Axial Load

Shear force on each pier changes through each step since base shear is increasing. Likewise shear capacity of the piers also change due to overturning effect of lateral forces through each step. Thus, comparison of capacity with demand requires an

iterative solution. Successful steps on which convergence is satisfied are given in Table 5.6.

Table 5.6 Successful Steps Involved in Iterative Nonlinear Static Analysis; grey = yielding of pier, dark grey = failure of pier

Step No	Pier Id	N (kN)	V (kN)	+N (kN)	+V (kN)	N_{final} (kN)	V_{final} (kN)	Vy (kN)	Vu (kN)
Step 1	P1	61.3	11.4	0.0	0.0	61.3	11.4	11.5	18.5
	P2	179.3	36.6	0.0	0.0	179.3	36.6	65.2	91.7
	P3	136.4	14.8	0.0	0.0	136.4	14.8	18.6	27.6
	P4	36.0	-0.9	0.0	0.0	36.0	0.9	13.3	21.8
	P5	82.1	19.0	0.0	0.0	82.1	19.0	64.8	95.3
	P6	53.6	13.3	0.0	0.0	53.6	13.3	16.9	26.6
Step 2	P1	61.3	11.4	-11.4	0.1	49.9	11.5	10.1	16.7
	P2	179.3	36.6	-1.1	15.1	178.2	51.7	64.9	91.4
	P3	136.4	14.8	12.6	4.8	149.0	19.6	19.6	28.8
	P4	36.0	-0.9	-3.3	2.7	32.7	1.8	12.5	20.8
	P5	82.1	19.0	0.7	5.5	82.9	24.5	65.1	95.8
	P6	53.6	13.3	2.5	1.8	56.2	15.1	17.4	27.2
Step 3	P1	49.9	11.5	-8.1	0.0	41.8	11.6	9.1	15.3
	P2	178.2	51.7	0.0	13.3	178.2	64.9	64.9	91.4
	P3	149.0	19.6	8.1	0.1	157.1	19.7	20.2	29.6
	P4	32.7	1.8	-2.0	1.8	30.7	3.6	12.1	20.2
	P5	82.9	24.5	0.0	3.2	82.9	27.7	65.1	95.8
	P6	56.2	15.1	2.0	1.7	58.2	16.8	17.7	27.7
Step 4	P1	41.8	11.6	-7.8	0.6	34.0	12.1	8.0	13.8
	P2	178.2	64.9	-0.6	9.9	177.7	74.8	64.8	91.2
	P3	157.1	19.7	8.4	3.0	165.4	22.7	20.9	30.3
	P4	30.7	3.6	-2.1	1.7	28.5	5.3	11.5	19.4
	P5	82.9	27.7	0.4	3.7	83.3	31.4	65.3	96.0
	P6	58.2	16.8	1.8	1.3	59.9	18.0	18.1	28.1
Step 5	P1	34.0	12.1	-7.0	0.2	26.9	12.3	7.0	12.3
	P2	177.7	74.8	-0.2	8.7	177.5	83.5	64.8	91.2
	P3	165.4	22.7	7.2	3.0	172.6	25.6	21.4	31.0
	P4	28.5	5.3	-2.1	1.7	26.5	7.0	11.0	18.7
	P5	83.3	31.4	0.7	4.2	84.0	35.6	65.6	96.4
	P6	59.9	18.0	1.4	0.0	61.3	18.1	18.3	28.5
Step 6	P1	26.9	12.3	-6.4	0.0	20.6	12.3	5.9	10.7
	P2	177.5	83.5	-0.3	7.7	177.2	91.2	64.7	91.1
	P3	172.6	25.6	6.7	3.2	179.3	28.8	21.9	31.6
	P4	26.5	7.0	-1.9	1.6	24.6	8.6	10.5	18.1
	P5	84.0	35.6	0.7	3.8	84.7	39.4	66.0	96.8
	P6	61.3	18.1	1.2	0.0	62.5	18.1	18.5	28.7

Since an incremental solution is carried out, force and displacement values at the end of step "i" become initial force and displacement values of step i+1. Each successful step provides information (i.e. incremental force and displacement values) needed to pass to the further step (see Table 5.6).

In order to draw pushover curve of the frame base shear and top displacement values associated to each successful step should be extracted. This information is provided in Table 5.7 and plotted in Figure 5.18.

Table 5.7 Base Shear and Top Displacement Values Associated with Successful Steps in Iterative Nonlinear Static Analysis

	Step1	Step2	Step3	Step4	Step5	Step6
Incremental Base Shear (kN)	0.00	19.96	13.39	13.45	11.86	10.88
Total Base Shear (kN)	62.80	82.76	96.15	109.60	121.46	132.34
Incremental Roof Displacement (mm)	0.00	0.44	0.35	6.00	5.20	4.51
Total Roof Displacement (mm)	1.21	1.66	2.00	8.00	13.20	17.72
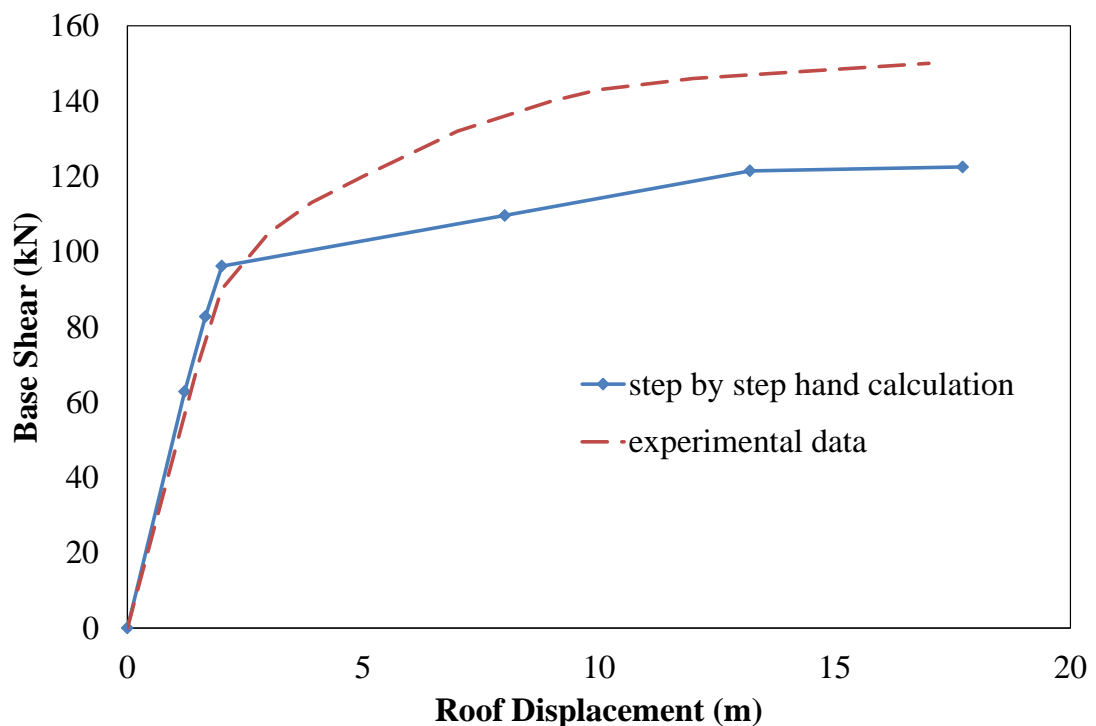
Figure 5.18 Comparison of Experimental Backbone Curve with Step by Step Hand Calculation

Distribution of shear hinges at the final stage of the step by step hand solution is provided in Figure 5.20. Unlike other two analyses P1 failed due to decrease in axial load. As axial load decreases on P1 during the analysis, shear capacity of the pier decreases and it reaches to ultimate capacity before P2. Compared to experimental final crack pattern (see Figure 5.19) hand solution gives satisfactory results.
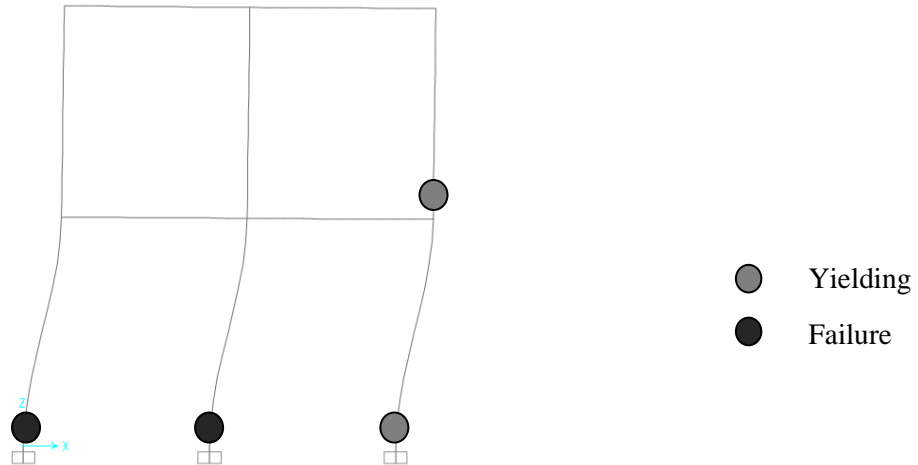
Figure 5.19 Final Hinging Pattern of Step by Step Hand Solution

5.4.2 Seismic testing of a Half-Scale, Two-Story URM Building at the ISMES Laboratory at Bergamo

2 story brick URM building (see Figure 5.20) tested on a shake table located at Ismes Laboratory at Bergamo is selected for verification of the proposed nonlinear equivalent frame model. Due to capability of the shake table, a length scale of ½ is used in the experiments. Thus, in order to achieve similitude between model and the real behavior, time scale is taken as $1/\sqrt{2}$ and density scale is taken as 2. However since same material is used for the scaled model, additional masses of the same order of the total mass is applied at the slabs.
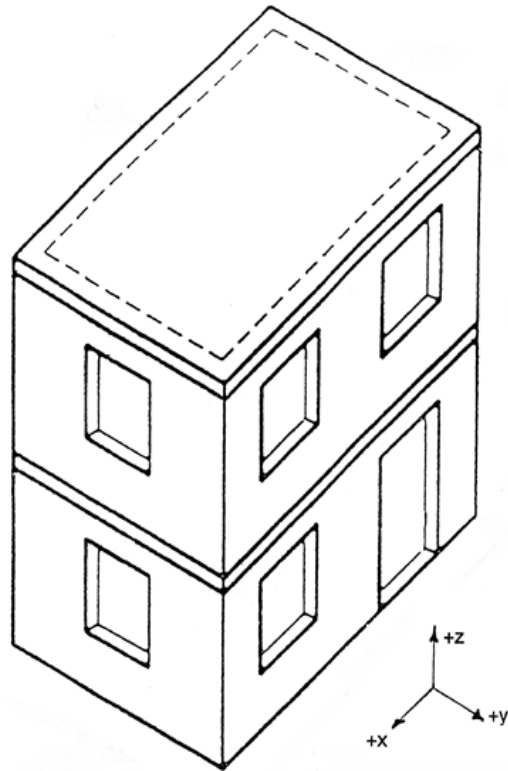
Figure 5.20 Geometry of the Building Tested at ISMES Laboratory

Base excitations derived from the signal recorded at Calitri during Irpinia earthquake is simultaneously applied at two orthogonal directions and the vertical direction (see Figure 5.21). Increasing order of 5 sets of base inputs obtained by scaling accelerations of mentioned earthquake is applied to the specimen. Peak values of the accelerations in x and y directions are shown in the Table 5.8.

a)   b)
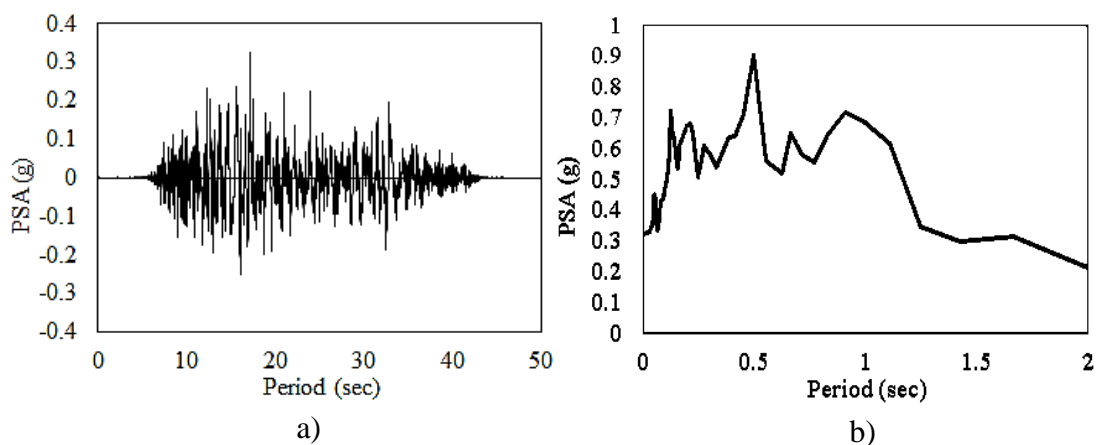
Figure 5.21 a) Ground Acceleration and b) Corresponding Response Spectrum (ζ = 5%) of Irpinia Earthquake

It is stated in the test report (Benedetti et al., 1996) that for the first excitation set P7, a fairly linear response is observed. However for the ultimate shock P11 strong non-linearity is observed. Comparing first and ultimate shocks, two dominant periods in x and y directions increase 240 % and 253 % respectively.

Third shock P9 is stated to be the event marking the yield point of the building with a base shear coefficient of 19 % in x direction. Ultimate lateral resistance and ultimate roof drift is identified as 22 % of the total weight and 0.33 % in the x direction respectively.

Table 5.8 Peak Ground Accelerations Applied to Specimen at Ismes Laboratory

TEST	$a_{x,max}$ (g)	$a_{y,max}$ (g)
P7	0.055	0.064
P8	0.098	0.098
P9	0.179	0.155
P10	0.250	0.217
P11	0.326	0.275

In order to conduct nonlinear THA, computer model of the tested building is built using SAP2000 software. Poisson's ratio for masonry is taken as 0.2 and modulus of elasticity is calculated as 920 MPa from elastic stiffness of experimental data. Mean compressive strength of the walls is given as 2.2MPa (Benedetti et al, 1996).

RO proposed by Dolce (1979) is utilized for the perforated walls of the tested building. Spandrel and pier labels of equivalent frame model of the tested building is illustrated in the figure below.
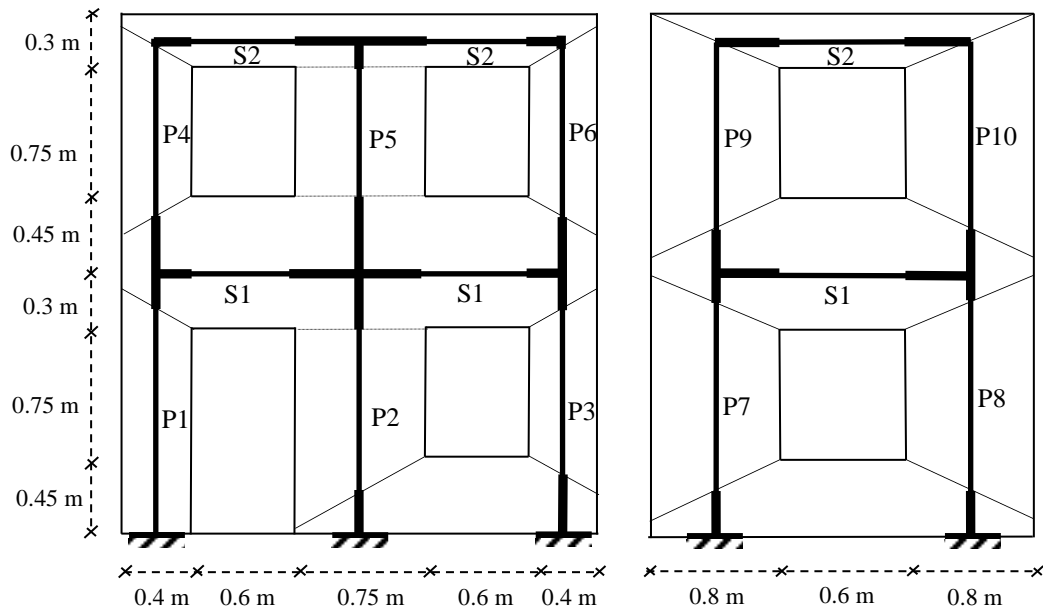
Figure 5.22 Equivalent Frame Model of URM Building Tested at ISMES Laboratory, (dimensions refer to the half-scale model)

After sectional properties of each pier are calculated from dimensions of the cross sections, linear dead load analysis is conducted and compressive stress on each pier is determined (see Table 5.9). Aspect ratio is calculated taking effective height of the walls into account. Out of plane stiffness of the equivalent frames are neglected as recommended by FEMA 356.

Table 5.9 Cross Sectional Properties and Axial Load Levels of Piers of ½ Scaled ISMES Test Specimen

Pier Label	L (m)	t (m)	h_{eff} (m)	λ	Area (m²)	Shear Area (m²)	I (m⁴)	p (MPa)
P1	0.40	0.225	1.316	3.29	0.090	0.075	0.0012	0.137
P2	0.75	0.225	0.975	1.30	0.169	0.141	0.0079	0.138
P3	0.40	0.225	0.981	2.45	0.090	0.075	0.0012	0.131
P4-P6	0.40	0.225	0.981	2.45	0.090	0.075	0.0012	0.058
P5	0.75	0.225	0.750	1.00	0.169	0.141	0.0079	0.057
P7-P8	0.80	0.225	1.125	1.41	0.180	0.150	0.0096	0.125
P9-P10	0.80	0.225	1.125	1.41	0.180	0.150	0.0096	0.057

After axial load level and effective height of piers are calculated, shear hinges corresponding to each pier is determined (see Figure 5.23) according to finite element macro model illustrated in Chapter 4.
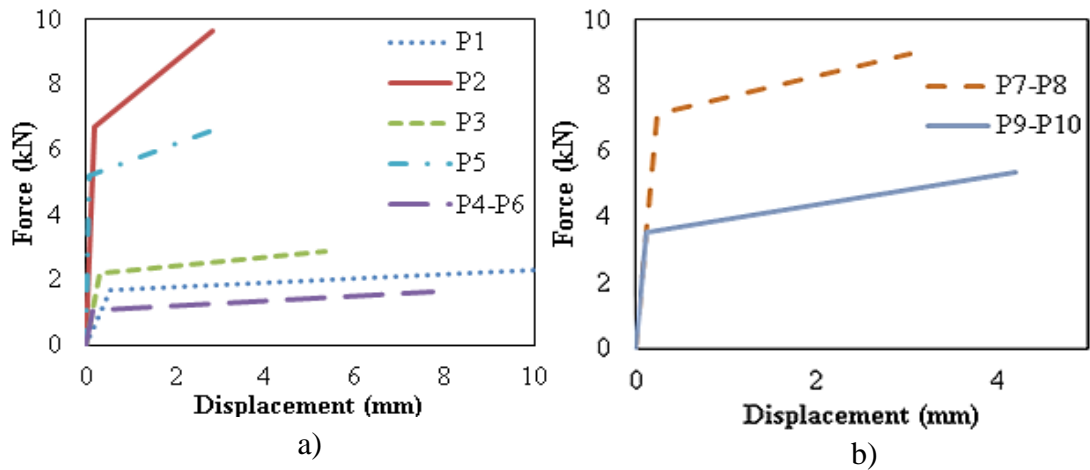
Figure 5.23 Idealized Nonlinear Pier Responses of the Building Tested at Ismes a) X-direction b) Y-direction

In order to simulate the cyclic behavior of masonry walls, degrading hysteresis model developed by Takeda et al. (1970) is employed. It is stated in Analysis Reference Manual of SAP2000 (2009) that this model is suitable for concrete and other brittle materials. It is also the default hysteresis model for concrete materials in the program.

In Takeda model, hinges follow backbone curve defined according to Equations 4.1 and 4.2 until unloading. Up to horizontal axis, hinge unloads parallel to initial stiffness. After crossing the horizontal axis, curve follows a secant path to the backbone force deformation relationship for the opposite loading direction (SAP2000 Analysis Reference Manual, 2009).

For visual illustration of the hysteresis model, response of pier 2 of the test specimen to excitation P9 is drawn (see Figure 5.24).
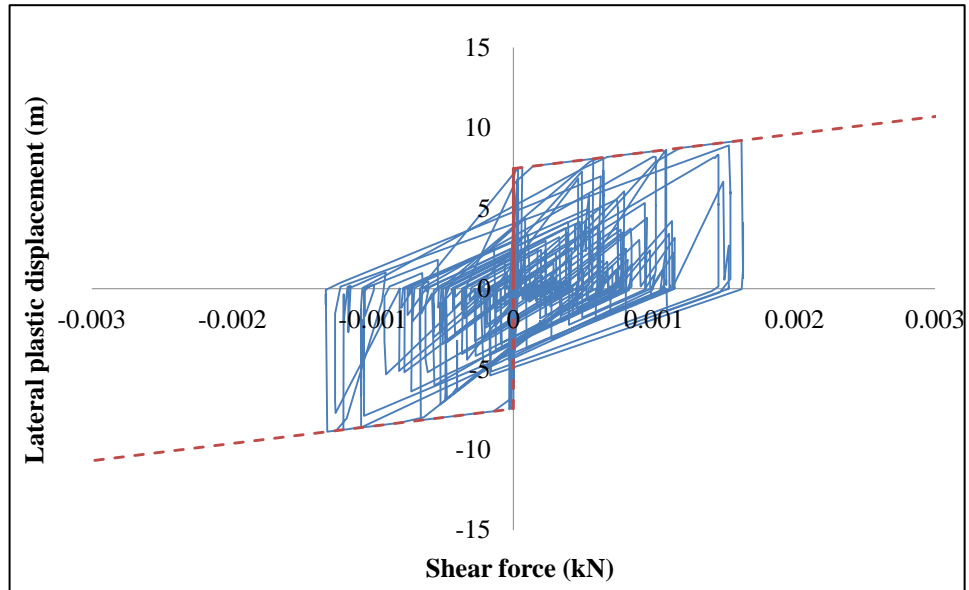
Figure 5.24 Cyclic Response of P2 to Excitation P9 according to Takeda Hysteresis Model

After test specimen is modeled with proposed nonlinear EFM and Takeda hysteresis model is assigned to shear hinges, nonlinear direct integration time history analysis is conducted.

Since Rayleigh damping is utilized in time history analyses, 2 damping values associated to fundamental modes in x and y directions are needed. Luckily these values are provided in the test report (Benedetti et al, 1996). 6 % and 5.8 % damping ratios are assigned to fundamental mode in x direction (i.e. 0.154 sec) and fundamental mode in y direction (i.e. 0.132 sec) respectively.

Number of output time step is taken as 4420 and output step size is taken as 0.011314 seconds which corresponds to experimental measurements (i.e. 4420*0.011314=50 seconds).

Comparison of Nonlinear THA results with experimental records are illustrated in Appendix B. During shake table tests absolute acceleration records are taken in X and Y directions and at first and second stories. Since 5 sets of base excitations with increasing order of peak ground accelerations (see Table 5.9) are applied in both

directions; totally 2 directions * 2 stories * 5 excitations = 20 absolute acceleration records are compared (see Appendix B).

Since frequency of acceleration data is high, for a better visualization, comparison is made only between 10th and 20th seconds where the peak responses are observed.

Table 5.10 shows the ratios of peak response accelerations to the peak ground displacements at the two storey levels in both x and y directions. Both experimental and analytical results are illustrated.

Table 5.10 Analytical and Experimental Results of Peak Response Accelerations over Peak Ground Accelerations for Ismes Test Specimen

| | | PGA (g) | Peak Response Acceleration / Peak Ground Acceleration | | | | | |
| | | | Experiment | | Computer Model | | % error | |
	TEST		1st storey	2nd storey	1st storey	2nd storey	1st storey	2nd storey
X-direction	P7	0.055	1.770	2.756	1.417	2.012	20.0 %	27.0 %
	P8	0.098	1.496	2.246	0.949	1.651	36.3 %	26.5 %
	P9	0.179	1.342	1.867	1.159	1.216	13.6 %	34.9 %
	P10	0.250	1.102	1.728	0.797	0.938	27.6 %	45.7 %
	P11	0.326	1.008	1.458	0.741	0.827	26.6 %	43.3 %
Y-direction	TEST		1st storey	2nd storey	1st storey	2nd storey	1st storey	2nd storey
	P7	0.065	1.097	1.305	0.950	1.414	13.4 %	-8.4 %
	P8	0.098	1.135	1.392	1.043	1.556	8.1 %	-11.8 %
	P9	0.155	1.276	1.598	1.380	1.460	-8.2 %	8.6 %
	P10	0.217	1.341	1.650	1.071	1.308	20.1 %	20.8 %
	P11	0.275	1.050	1.467	0.933	1.129	11.1 %	23.0 %

5.4.3 Discussion of Results

5.4.3.1. Pavia Tests

In order to predict envelope of cyclic response, three analysis methods are proposed. PO curves and final cracking patterns of methods have been provided. For comparison, capacity curve of the Pavia door wall achieved from experimental data and results of three methods are plotted together (see Figure 5.25).

Although capacity curves derived from three different methods are slightly different from each other, this is unique case for this specific structure only. As it is understood from experimental and analytical results, ultimate and yield resistance of the Pavia door wall is dictated by piers at the base. Especially being large in length and short in height, interior pier at the base (P2) is dominant on the response. Although three methods differ in dealing with influence of axial load level on individual piers, axial load on P2 is nearly the same and constant throughout the analyses in all methods due to symmetry of the structure. As lateral loads increase axial load on P1 decreases and axial load on P3 increases but axial load on P2 does not change. Because ultimate condition is reached by failure of P2 in all three methods, ultimate drift is nearly the same for all.

Furthermore due also to symmetry of the system, when lateral forces are applied, decrease in yield force of P1 is nearly equal to increase in yield force of P3 since decrease in axial load level of P1 is nearly equal to increase in axial load level of P3. As a result, sum of the yield forces of P1, P2 and P3 which identifies yielding of the frame is the same for three methods. To illustrate yield force of P1, P3 and P2 are equal to 15.3kN, 15.3kN and 65.14kN respectively for hinge properties defined under dead load case. On the other hand yield force of same piers are equal to 9.78kN, 19.66kN and 65.34kN due to overturning effect of lateral forces (i.e. hinge properties defined under dead plus earthquake load). Since sum of first set (15.3+15.3+65.14=95.74) is nearly equal to sum of second set (9.78+19.66+65.34=94.78), both systems yield at the same base shear.
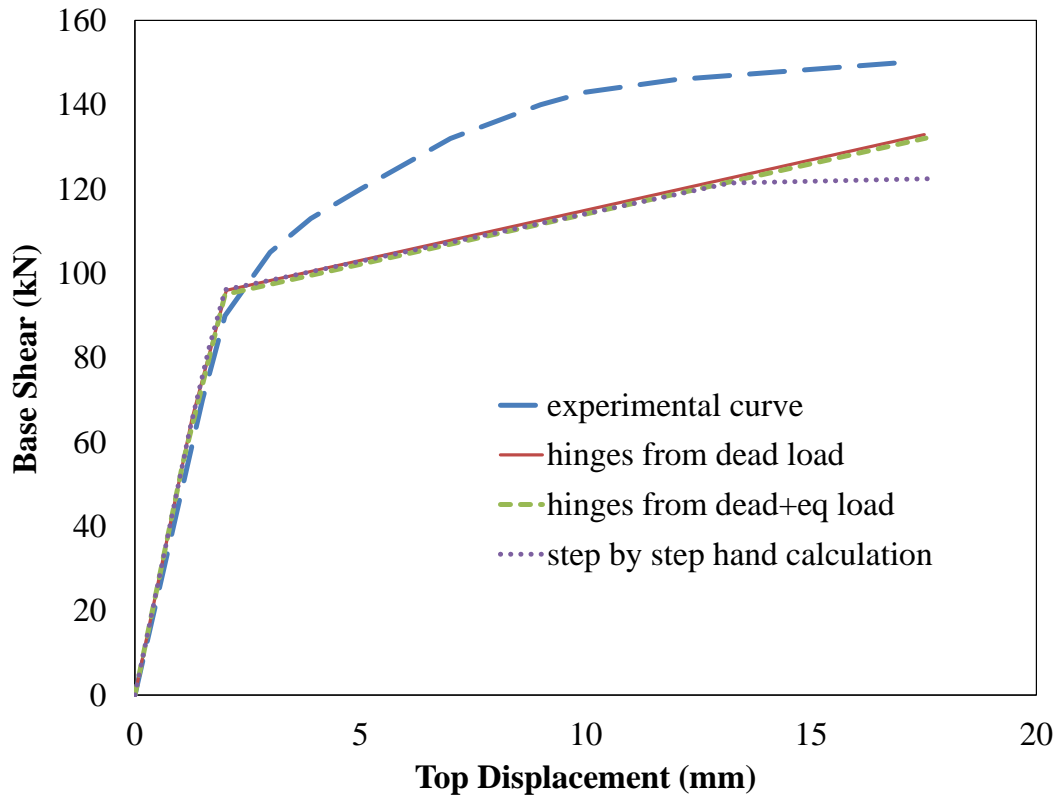
Figure 5.25 Comparison of Capacity Curves Derived from Different Methods

Difference between step by step hand calculation and others at the end of the analysis might be understood by comparing final hinge pattern of three analyses. Different from other two analyses base pier at left (P1) failed during step by step hand calculation due to decrease in axial load level. The reason for the difference is failure of P1 before P2.

According to Magenes and Fontana (1998), "Variation in the axial force of the piers may take place under the overturning effect of the horizontal loads, affecting the flexural and shear strength of the individual piers. This effect may not be of relevance in low-rise squat buildings but it can be in a more general context." In addition to their statement, it can be said that for symmetric frames effect of overturning minimizes as decrease in resistance of axial load decreasing piers are compensated by increase in resistance of axial load increasing piers.

To conclude, all methods describe general state of damage well and reflect structural degradation in the critical story of the tested frame satisfactorily. Hinge properties

determined under gravity load gives satisfactory results for modeling of low-height URM buildings.

5.4.3.2. Ismes Tests

According to figures listed in Appendix B, it might be stated that general trend in variation of recorded accelerations are successfully captured by the proposed model especially for the initial shocks. According to Table 5.11, recorded maximum accelerations and maximum accelerations calculated from the proposed model are in good correlation in Y direction with a maximum error of 23 %.

As it is stated in the experimental report (Benedetti et al., 1996), significant yielding point is identified as the end of shock P9 in the X direction. However nonlinearity started at the end of shock P8 in the model. During shock P9 high hysteresis dissipation is observed for the central pier at the base (see Figure 5.25). Also ultimate lateral resistance of the test specimen in X direction, which is calculated from multiplication of joint accelerations with corresponding mass, is stated as 22 % whereas it is calculated as 17.5% in the computer model.

The main reason for these shortcomings is that hinge capacities predicted by the Equation 4.1 is low for the building. Also assumptions made during the modeling and limitations of the model which are listed below might be the other reasons.

- Although the test specimen is modeled as 3-D, out of plane resistance of the walls are neglected. Thus, interaction of out-of-plane walls with resisting in-plane walls (i.e. flange effect) is not taken into account.

- Base accelerations in 3 orthogonal directions are applied simultaneously in the experiment. Whereas shocks in each direction is applied separately in the computer model.

- Although steel connector is utilized to achieve connection between the slab and the walls, 2cm thick wooden plate over wooden beams are employed to idealize flexible boundary conditions in the experiment. However rigid diagrahm is assigned to each floor in the computer model.

- Takeda model which is employed to idealize hysteresis behavior of URM is not the best model to represent exact masonry behavior which is strongly dependent on the failure mechanism of the pier (see Figure 2.1). It is clearly seen that energy dissipation capacity of this model (see Figure 5.24) is superior that the experimental recordings illustrated in Figure 2.1.

- It is assumed in the proposed approach that nonlinearity is restricted in piers only. Spandrels are modeled as elastic. However, although ultimate failure is due to piers, high spandrel damage is also observed in the experiment

- The reason for better correlation for the first, less better correlation for second story might be shortcoming of finite element macro model. Equations 4.1 and 4.2 which are utilized for the definition of nonlinear response are derived using walls with cantilever boundary conditions. Although first story walls are fixed at the base, base of second story walls are flexible. Also second story piers have less overburden pressure resulting in bad prediction of finite element results with Equations 4.1 and 4.2.

CHAPTER 6

PERFORMANCE ASSESSMENT OF EXISTING URM BUILDINGS USING PROPOSED NONLINEAR MODEL

Performance assessment of three brick URM buildings (see Figure 6.2, 6.17 and 6.27) which was exposed to Dinar earthquake of October 1995 (see Figure 6.1) and investigated after the earthquake (METU-EERC, 1996) will be carried out.

Capacity curves of the buildings are determined through pushover analyses on the proposed nonlinear equivalent frame models of the buildings. Member force-displacement relationships are determined both according to equations proposed by Aldemir (i.e. Equations 4.1 and 4.2) and equations recommended by FEMA 356 (see Tables 4.2 and 4.3) for comparison. After capacity curves are bilinearized using the method recommended by FEMA 356 (2000), earthquake demands of the buildings are calculated according to TEC2007.

In order to check reliability of the calculated demands, nonlinear time history analyses of the buildings are made under Dinar earthquake east-west ground motion component. Roof displacement demands calculated from nonlinear THA will be compared with demands calculated according to method proposed by TEC2007.

After plastic deformation demands of each pier belonging to performance point of the buildings are determined, they are compared with critical drifts identifying performance limit states to assess the expected performances of the buildings.

Finally, simple approach proposed by Tomazevic (2007) for the assessment of performance of a building using its capacity curve will be utilized for performance assessment and results will be discussed.
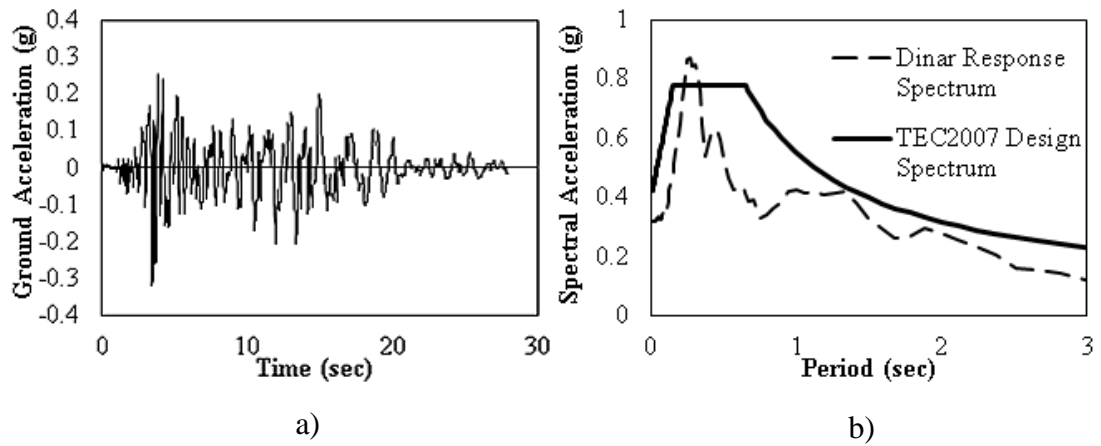
Figure 6.1 a) Ground Acceleration and b) Corresponding Response and Design Spectrums ($\zeta = 10\%$) of Dinar Earthquake East-West Component

6.1 Case Study Building No: 1

2 story brick URM building located at Konak District no: 39 which is investigated by METU-EERC research team after Dinar earthquake of 1995, is selected for performance assessment (see Figure 6.2). Damage score of the building after a preliminary assessment is reported as medium (Özcebe, 1996).

Figure 6.2 General View of the CSB No: 1

6.1.1. Generation of the Computer Model

In order to perform performance assessment, equivalent frame model of the URM building is generated using computer software (see Figure 6.3). Labels of the walls on the first and second story plans are provided in Figure D.1 and Figure D.2 respectively.
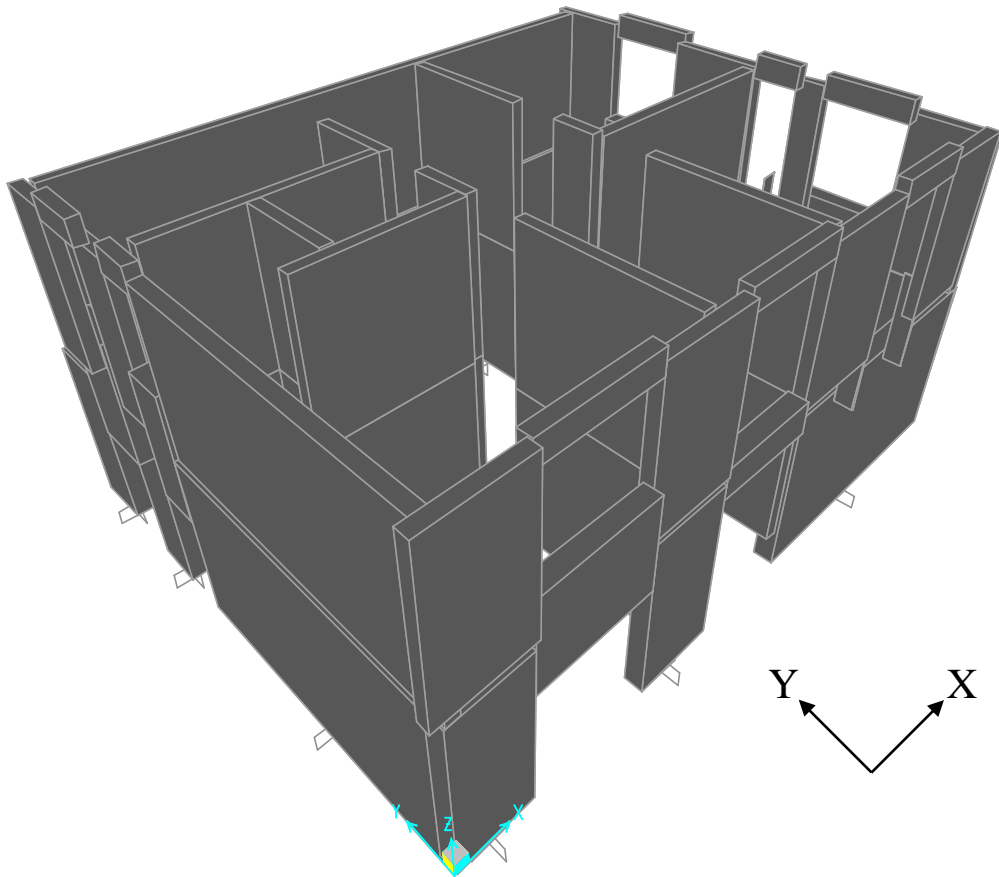
Figure 6.3 Computer Model of CSB No: 1

Since there is no laboratory data illustrating material properties of the building, average values representing Turkish construction practice is utilized (Aldemir, 2010). Compressive strength, modulus of elasticity and Poisson's ratio are taken as 5 MPa, 2000 MPa and 0.2 respectively. Unit weight of the concrete slab is taken as 2.5 ton/m³ and unit weight of the brick masonry walls is taken as 1.8 ton/m³ for the weight calculations.

Geometrical properties of the walls such as area, shear area in strong direction and moment of inertia in strong direction are calculated from dimensions of the walls and used as input data for the computer software. Walls are assumed to resist in-plane forces acting on their strong direction only.

Rigid end offsets of the perforated walls which are crucial in EFM are determined according to method proposed by Dolce (1989) (see Figure 6.4).

Story masses compatible with story weights are calculated taking both the weight of the slabs and the walls into account. Slab weight is calculated considering dead load of the slab and 30 % of the live load on the slab recommended by TS 498 (1997). At the roof level, additional dead load representing roof weight is applied on the slab according to TS ISO 9194 (1997). After center of mass of the stories are calculated at which story masses are lumped, rigid diaphragm is assigned at each story level.

Then, modal analysis is conducted and dynamic characteristics of the building are identified (see Table 6.1). Due to non-symmetric distribution of walls in the plan, although modal participating mass ratios in both directions are low, they are slightly higher than code allowed limits for PO analysis which is equal to 0.7 (TEC2007).

Table 6.1 Modal Properties of CSB No: 1

mode number	direction	period (sec)	modal participating mass ratio (α)	modal participation factor (PF)	PF*Φ_r
1	y-direction	0.118	0.715	11.46	1.104
2	x-direction	0.103	0.720	11.50	1.082
3	torsion	0.068			
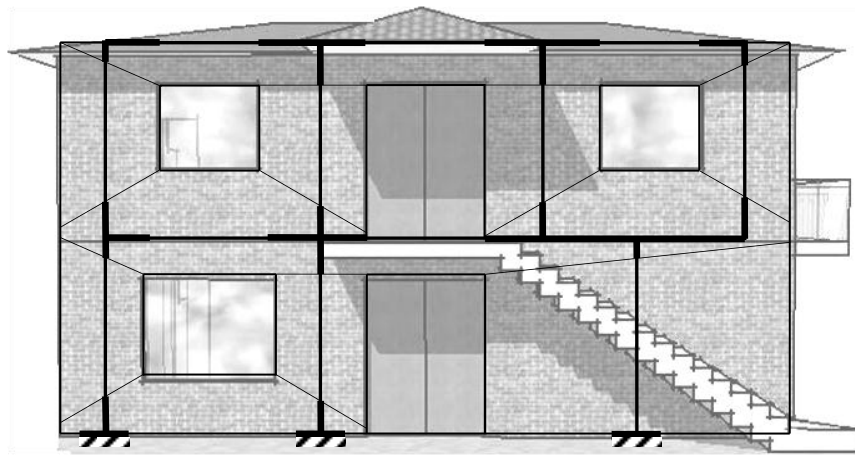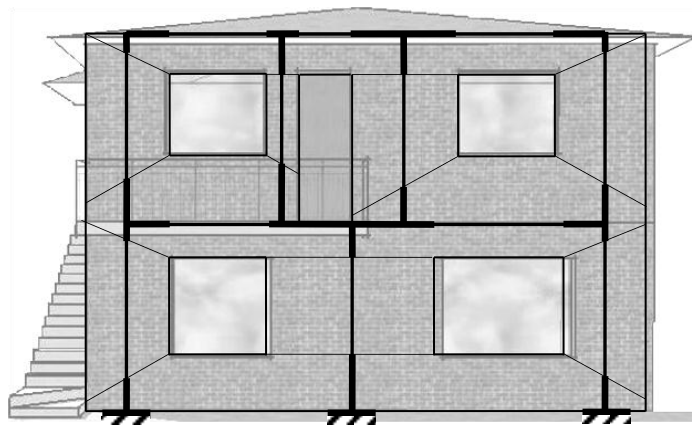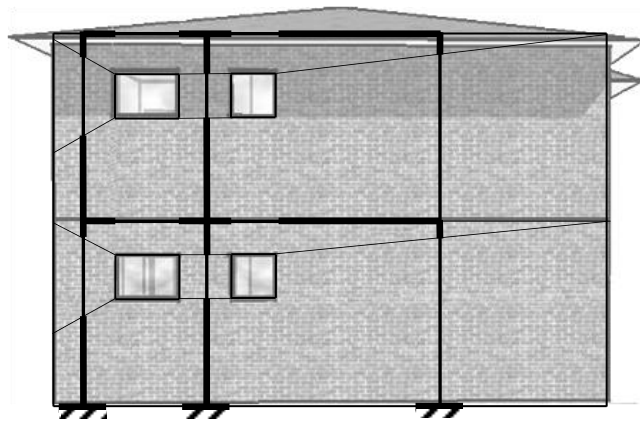
Figure 6.4 Equivalent Frame Modeling of Perforated Walls of CSB No: 1; a) Front View, b) Right View c) Left View

Before pushover analysis of the case study building is conducted, force-deformation relationship of its walls in the nonlinear range should be determined. Equations proposed by Aldemir (2010) are utilized for this purpose. However, since axial load is an important input to equations influencing nonlinear behavior of piers, an initial linear dead load analysis is conducted to determine axial load level of each wall.

In order to conduct linear analysis under dead load of the building, slab loads should be distributed to surrounding walls. For one way slabs, loads are distributed in short direction only whereas for two way slabs, loads are distributed in both directions according to corresponding trapezoidal or triangular areas.

After slab loads are distributed to walls, building is analyzed under gravity loads. Using compressive stress on each wall, nonlinear properties of each wall are determined utilizing Equations 4.1 and 4.2. Calculations are tabulated in Table C.1. Average ultimate drift of first story and second story walls are found to be 0.67% and 0.77% respectively.

6.1.2. Static Pushover Analysis

After nonlinear shear hinges compatible with calculated nonlinear properties of each wall is assigned, pushover analysis is conducted. Building is pushed in positive X direction, negative X direction, positive Y direction and negative Y direction separately. Because hinge properties are not dependent on the change in the axial load level of walls throughout the pushover analysis, there is no difference between capacity curves of positive and negative directions.

In order to check the reliability of the equations utilized for the determination of nonlinear response of URM walls, capacity curve of the building is also derived according to procedure recommended by FEMA 356.

However, force-deformation relationship defined for URM walls in FEMA 356 is vulnerable to convergence problems due to perfectly plastic plateau between B – C

and sudden drop at point C (see Figure 6.5a). It is observed that when default hinges defined by FEMA 356 (HP1) is utilized, unreliable results are encountered upon "yielding" of every member at one of the stories. In order to satisfy equilibrium upon increasing roof displacement to pass to the next step, hinges violate their predefined force-displacement path. Since "yielding" takes place at the very early stages of displacement increment due to the high initial stiffness of wall elements, analysis results might be considered as unreliable.

To overcome this drawback of elastic-perfectly plastic hinges, a small post elastic stiffness is needed to be implemented. This is achieved by 10% increment of "yield" force at point C (HP2). This corresponds to a strain hardening ratio of 2.1% at maximum which does not alters hinge behavior noticeably.

Although hinges follow their predefined force-displacement curve after the modification, this time convergence problems arise when first hinge arises to point C due to sudden drop in force. Although base shear capacity of the building is not affected, low ultimate drift values are encountered in this case. To overcome this shortcoming of the modified HP2 hinges, second modification is made and sudden drop in force is removed (HP3). With this final modification, no convergence problems or unreliable solutions arise throughout the analysis and a sound solution is achieved.
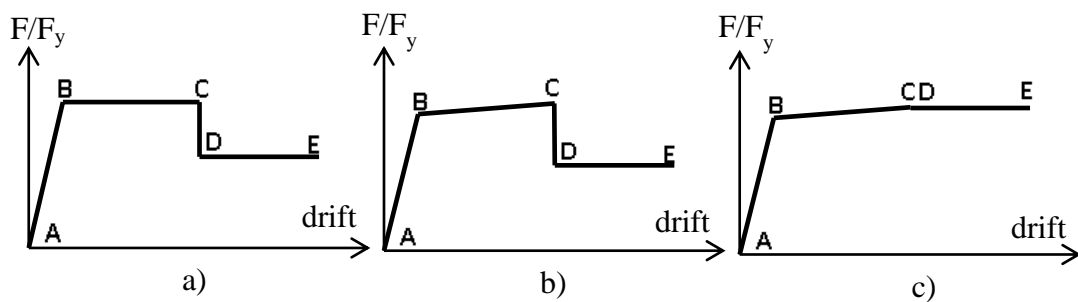
Figure 6.5 Modification of Hinges Defined in FEMA 356. a) Hinge Pattern 1 (HP1), b) Hinge Pattern 2 (HP2), c) Hinge Pattern 3 (HP3)

Final PO curves in X and Y directions are illustrated in Figure 6.6 and 6.7 respectively. Vertical axis of the capacity curve represents lateral resistance of the building which is normalized with weight of the building. Horizontal axis of the capacity curve represents lateral roof displacement which is expressed in terms of story rotations instead of story translations.
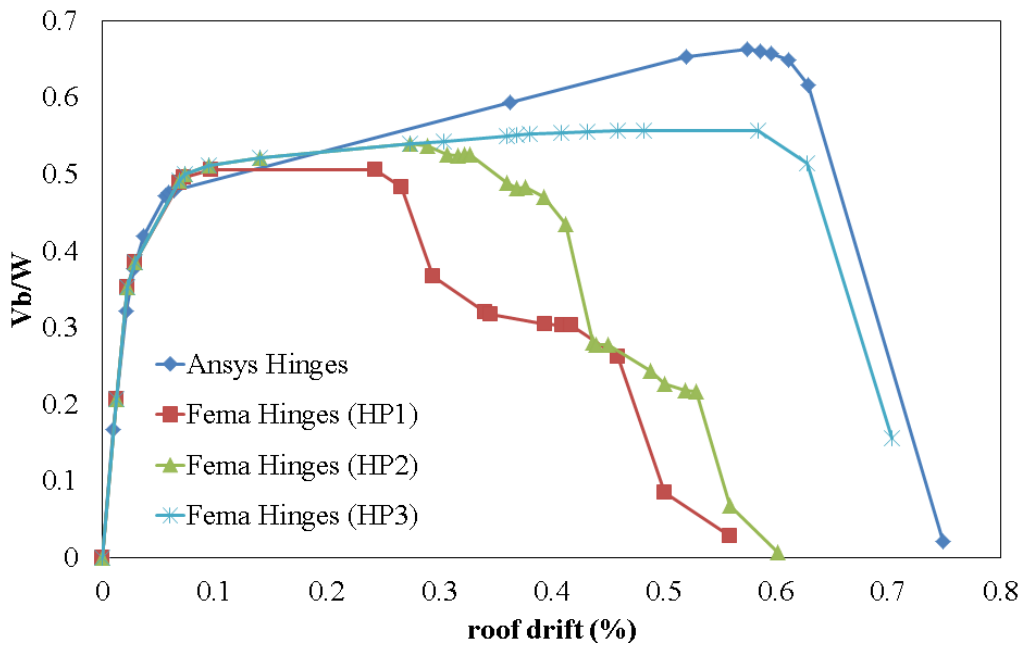
Figure 6.6 Normalized Capacity Curves of the CSB No: 1 in X-direction
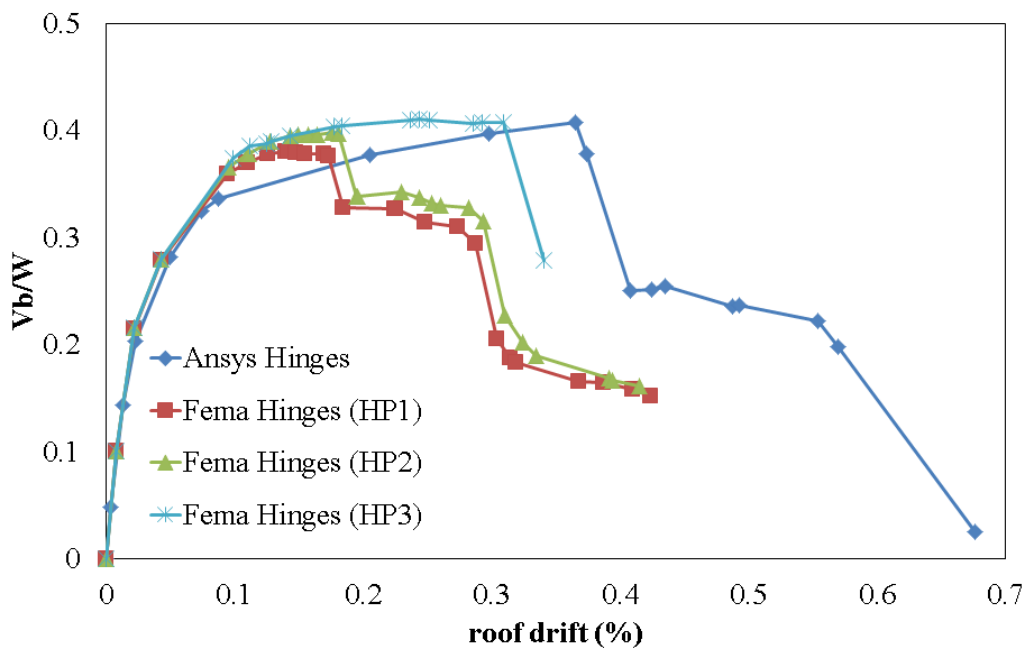
Figure 6.7 Normalized Capacity Curves of the CSB No: 1 in Y-direction

PO curve with hinges derived from equations 4.1 and 4.2 (i.e. Ansys Hinges) is similar to PO curve in which modified hinges proposed by FEMA 356 (i.e. HP3) is utilized in terms of "yield" force, base shear capacity and ultimate roof drift.

The building is capable of carrying 66 % of its total weight in strong direction and 41 % of its total weight in weak direction. Ultimate total drift of the building is 0.56 % and 0.36 % in strong and weak directions respectively. Also ultimate ISD of 1st story is 63% and 34 % in strong and weak directions respectively.

Ultimate failure is dictated by base story walls in X direction. Thinner interior walls (i.e. W1017, W1018 and W1019) failed and thicker outer walls cracked at the ultimate state. In Y direction, failure of predominantly first story and some second story walls (i.e. W201, W202, W203 and W2012a) in perforated frames dictated the ultimate condition.

6.1.3. Bilinearization of Capacity Curve

In order to calculate displacement demand of the buildings, PO curve derived from nonlinear static analysis with ansys hinges will be utilized. Method proposed by FEMA 356 (2000) will be employed for bilinearization process. Proposed method requires an iterative graphical procedure which equates the areas under capacity curve and bilinear idealization.

Elastic lateral stiffness should be taken as secant stiffness calculated at a base shear force equal to 60 % of the effective yield strength of the structure. Post-elastic range is determined by a line connecting effective yield point to final point on capacity curve (FEMA 356).

Bilinearized curves are illustrated below (see Figure 6.8).
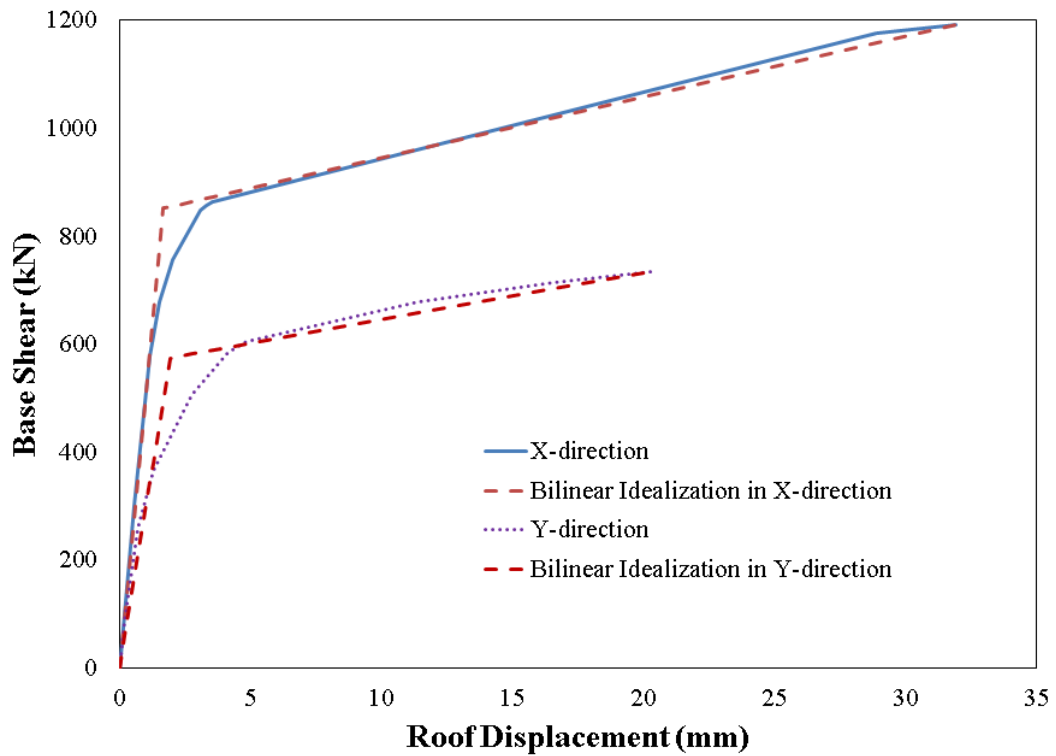
Figure 6.8 Bilinearized Capacity Curves of CSB No: 1 According to FEMA 356

6.1.4. Calculation of Demand According to TEC2007

For the roof displacement demand calculation of the building, design spectrum provided by TEC2007 will be utilized. Earthquake zone and soil type are selected as Zone 1 and Z3 respectively.

Unfortunately, design spectrum is specified for 5% damping ratio only. Yet, dissipation of energy in masonry buildings is usually idealized with higher equivalent damping ratios.

According to Magenes and Calvi (1997), depending on the domination of shear or flexure on behavior, equivalent damping increases with damage (see Figure 6.9). A total equivalent viscous damping (i.e. hysteretic + radiation + impact damping) of 15 per cent for rocking and 10 per cent for diagonal cracking is recommended.
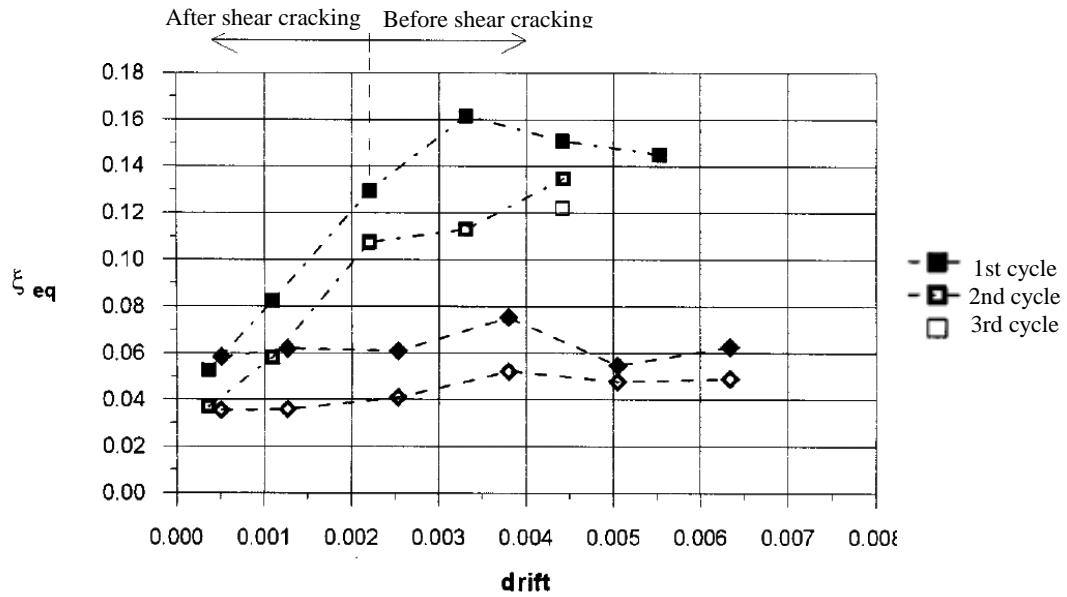
Figure 6.9 Equivalent Hysteretic Damping from the Cyclic Tests, (Magenes and Calvi, 1997)

According to shaking table tests on 24 sample masonry buildings Benedetti et al. (1998) also state that initial viscous damping is between 6% and 10% for undamaged brick masonry buildings.

As a result, design spectrum specified in TEC2007 for 5% damping ratio is only applicable to undamaged URM buildings, yet 10% equivalent damping is appropriate for damaged URM buildings.

Thus elastic design spectrum specified in TEC2007 for 5% damping should be converted to elastic design spectrum with 10% damping. For this purpose method illustrated by Chopra (2007) which utilizes amplification factors proposed by Newmark and Hall (1982) will be used (see Equations 6.1 and 6.2).

$$\alpha_A = 3.21 - 0.68 \ln \zeta \qquad (6.1)$$

$$\alpha_V = 2.31 - 0.41 \ln \zeta \qquad (6.2)$$

Where,

ζ = Damping ratio in per cent

In order to derive design spectrum with 10% damping, constant acceleration region of the spectrum is scaled with $\alpha'_A = \alpha_{A\ (\zeta=0.10)} / \alpha_{A\ (\zeta=0.05)}$ and constant velocity region of the spectrum is scaled with $\alpha'_V = \alpha_{V\ (\zeta=0.10)} / \alpha_{V\ (\zeta=0.05)}$. Since scale factors are different to the right and to the left of the corner period (i.e. T_B in TEC2007), corner period shifts to the right. New value of the corner period might be calculated with the Equation 6.3.

$$T'_B = T_B * \left(\frac{\alpha'_V}{\alpha'_A}\right)^{1.25} \tag{6.3}$$

Elastic design spectra to be used for the demand calculation of the case study building are plotted below (see Figure 6.10).
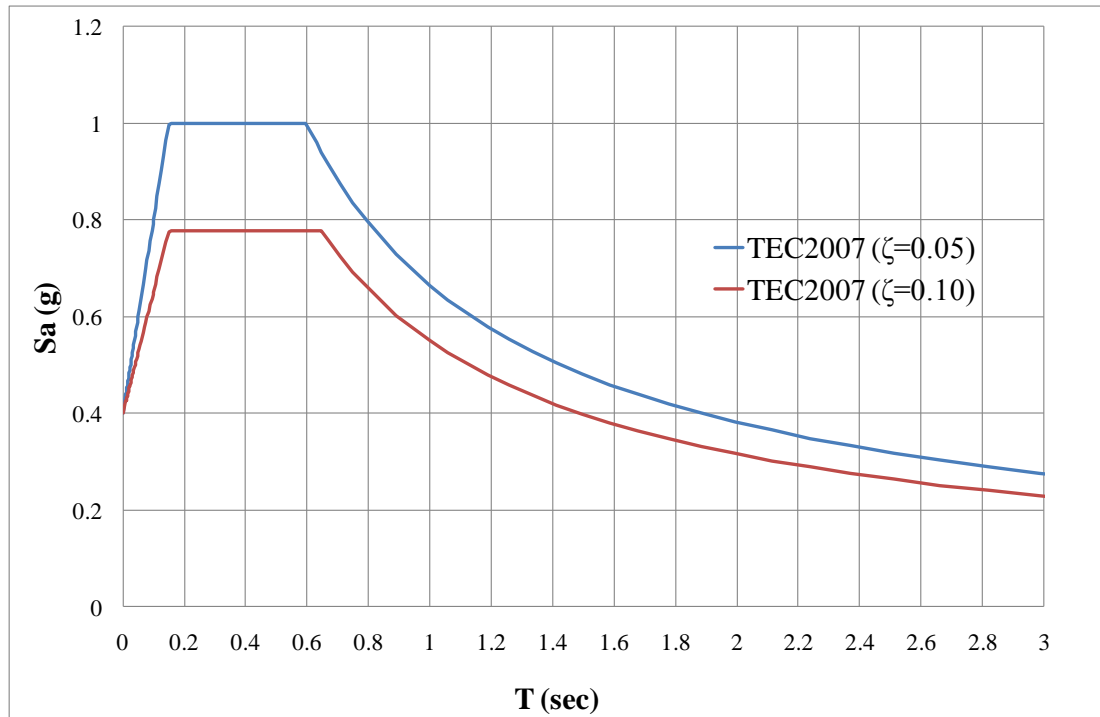
Figure 6.10 Elastic Design Spectrums for Earthquake Region 1 and Soil Type Z3

In order to calculate earthquake demand of the case study building, both bilinearized capacity curves of the building and the 10% design spectrum should be converted to ADRS format (see Figure 6.11). Conversion of design spectra is made according to simple relation between spectral displacements and spectral accelerations (see Equation 6.4). Since spectral accelerations corresponding to periods are presented in design spectrum, spectral displacements are easily calculated.

$$S_a = \left(\frac{2*\pi}{T}\right)^2 S_d \qquad (6.4)$$

Where,

S_a = Spectral Acceleration

S_d = Spectral Displacement

T = Period

Conversion of bilinearized capacity curves are made according to equations below (see Equation 6.5 and 6.6). Since modal mass participation, modal participation factor and amplitude of the mode at roof level are determined from modal analysis before (see table 6.1) spectral acceleration and spectral displacements are easily calculated.

$$S_{a,i} = \frac{V_i}{\eta W} \qquad (6.5)$$

Where,

V = Base shear

η = Mass participation factor

W = Weight of the building

$$S_{d,i} = \frac{u_i}{PF*\varphi_r} \qquad (6.6)$$

Where,

u = Roof displacement

PF = Modal participation factor

φ_r = Modal amplitude at roof
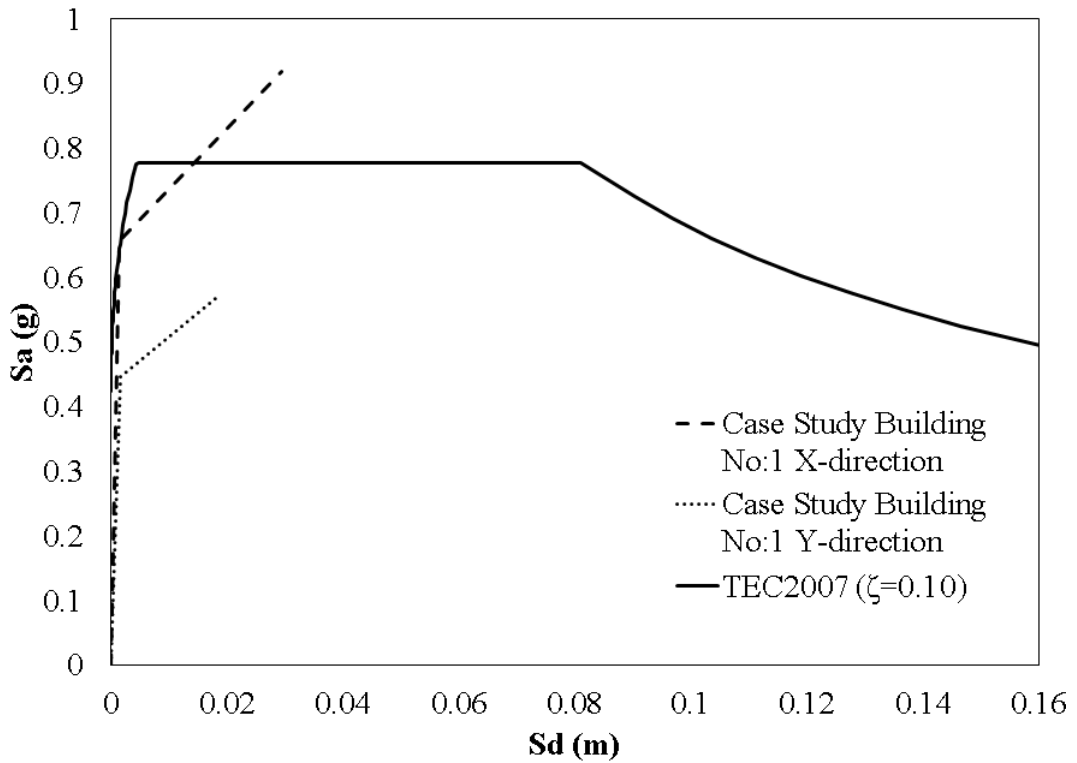
Figure 6.11 ADRS Representation of Capacity and Demand for CSB No: 1

Finally inelastic spectral displacement demand of the CSB no: 1 in X and Y directions are calculated according to 10% design spectrum using procedure proposed by TEC2007. Since effective periods of the building in both directions are smaller than the corner period T_B, instead of equal displacement rule, equal energy rule is implemented which requires an iterative solution.

Final roof displacement demands of the building is calculated as 8.8 mm (0.16 %) and 1.7 mm (0.03%) in x and y directions respectively. Calculated demands are pointed with a black dot on the capacity curves of the building in the following graphs.

Displacement demand calculated according to TEC2007 relies on design spectrum and results in larger values compared to nonlinear THA results which relies of response spectrum (see Figure 6.2b). This trend is observed in all case study buildings.

6.1.5. Nonlinear Time History Analysis

Nonlinear THA of the CSB no: 1 is made in both directions utilizing the proposed nonlinear EFM. East-West component of the Dinar ground motion is utilized in both directions. Cyclic behavior of equivalent frame members is defined according to hysteresis response proposed by Takeda et al. (1970).

In addition to energy dissipation due to hysteresis behavior, 5 % viscous damping is assigned to the building.

Analysis results are illustrated in Table 6.2. Maximum base shear demand of the CSB no: 1 is 34 % and 32% of its weight in X and Y directions respectively.

Table 6.2 Nonlinear Time History Analyses Results for CSB No: 1

	X-Direction	Y-Direction
$\emptyset_{1st\ story,max}$	0.019%	0.053%
$\emptyset_{roof,max}$	0.023%	0.074%
$V_{b,max}/W$	0.34	0.32

Figure 6.12 and Figure 6.13 illustrates normalized base shear - roof displacement relationship of the CSB no: 1 together with normalized PO curve drawn according to ansys hinges in x and y directions respectively. Roof demand calculated according to procedure recommended by TEC2007 in the previous section is identified with a black dot on the PO curves.

A significant increase of loop areas in Y-direction denotes increasing energy dissipation due to nonlinear response which is an identification of increase damage.
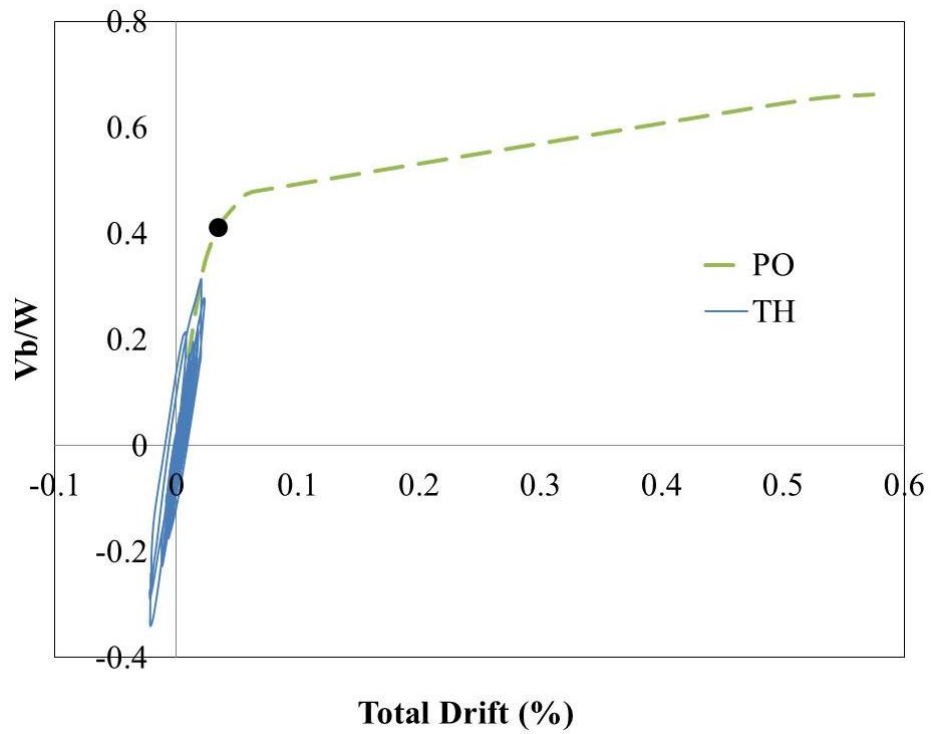
Figure 6.12 Nonlinear THA Results with Capacity Curve of CSB No: 1 in X-direction
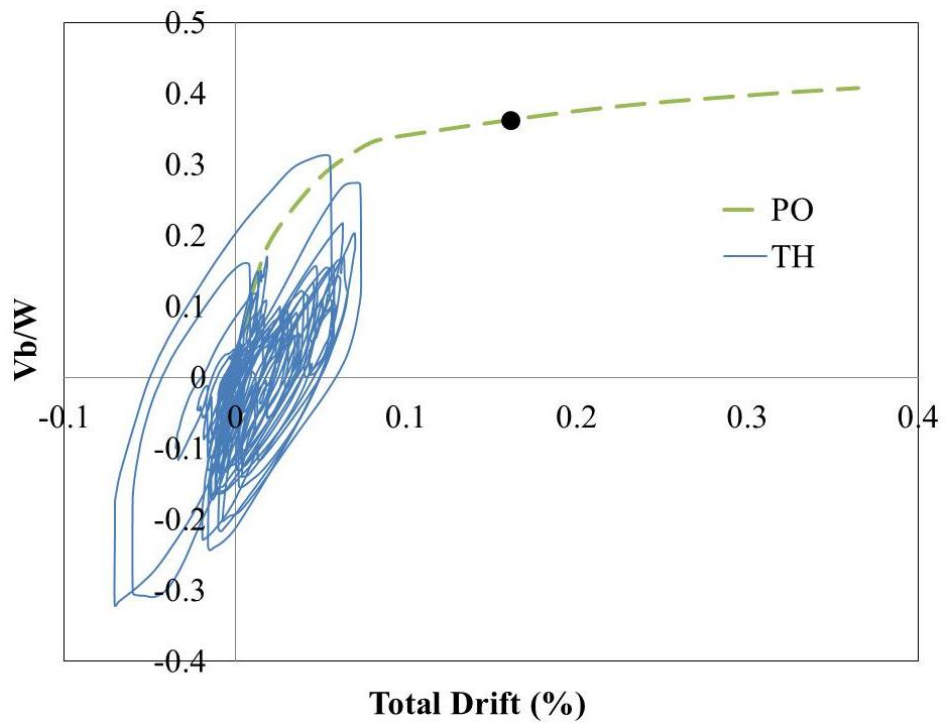
Figure 6.13 Nonlinear THA Results with Capacity Curve of CSB No: 1 in Y-direction

6.1.6. Determination of Performance Level

Performance level of the building in each direction will be determined according to 2 methods; from element plastic displacement demands and from simple approach proposed by Tomazevic (2007).

In the first method, performance of the building is determined by comparing element displacement demands with the capacity of the members. Performance states of each member are illustrated on the figure below (see Figure 6.14).
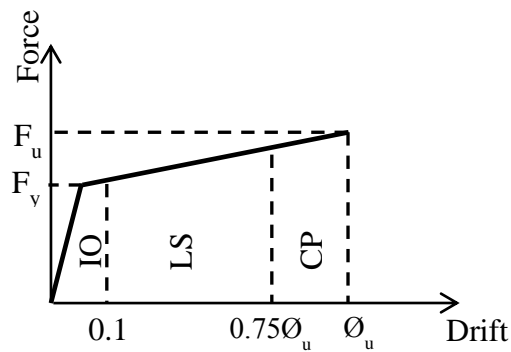
Figure 6.14 Performance Limit States of URM Walls

Immediate occupancy performance level is restricted below 0.1 % drift level. This limit is widely accepted as the initiation of the cracking by many authors (see Table 2.5). Upper limit of LS performance level is associated with 0.75 % of the ultimate drift limit calculated according to Equation 4.2. Remaining part of the curve marks the collapse prevention performance level.

After the building is pushed to the performance point calculated in section 6.1.4, deformation demand of each pier belonging to CSB no: 1 is determined and compared to capacities of piers which are tabulated in Table C.1. Results are given in the table below (see Table 6.3).

In addition to performance level of the piers, total curvature over ultimate curvature ratios are given to have a better understanding of what percent of total capacity is reached for each pier.

Table 6.3 Element Performance States of CSB No: 1

		Frame Id	Performance Limits			Performance Point		Performance	
			Φ_{IO} (%)	Φ_{LS} (%)	Φ_{CP} (%)	Φ_p (%)	Φ_t (%)	Status	Φ_t/Φ_u
Y-Direction	1st story	W101	0.10	0.51	0.68	0.16	0.21	LS	31%
		W102	0.10	0.73	0.97	0.50	0.53	LS	54%
		W103	0.10	0.86	1.15	0.28	0.30	LS	26%
		W104	0.10	0.66	0.89	0.07	0.13	LS	15%
		W105	0.10	0.42	0.56	0.08	0.14	LS	24%
		W106	0.10	0.68	0.90	0.07	0.14	LS	15%
		W107	0.10	0.56	0.75	0.06	0.14	LS	18%
		W108	0.10	0.42	0.55	0.08	0.14	LS	25%
		W109	0.10	0.77	1.02	0.09	0.14	LS	14%
		W110	0.10	0.43	0.57	0.07	0.14	LS	25%
		W111	0.10	0.93	1.25	0.17	0.19	LS	15%
		W112	0.10	0.64	0.85	0.25	0.28	LS	32%
		W113	0.10	0.91	1.22	0.17	0.20	LS	16%
	2nd story	W201	0.10	0.53	0.70	0.23	0.27	LS	38%
		W202	0.10	0.76	1.01	0.77	0.83	CP	82%
		W203	0.10	0.93	1.24	0.40	0.43	LS	34%
		W204	0.10	0.94	1.25	0.06	0.17	LS	14%
		W205	0.10	0.60	0.80	0.08	0.18	LS	22%
		W206	0.10	0.96	1.28	0.05	0.18	LS	14%
		W207	0.10	0.79	1.06	0.04	0.18	LS	17%
		W208	0.10	0.59	0.79	0.08	0.18	LS	23%
		W209	0.10	1.10	1.46	0.08	0.18	LS	13%
		W210	0.10	0.61	0.81	0.06	0.18	LS	23%
		W211	0.10	0.81	1.08	0.23	0.29	LS	26%
		W212a	0.10	0.83	1.10	0.37	0.37	LS	34%
		W212b	0.10	0.75	0.99	0.28	0.30	LS	30%
		W213	0.10	0.82	1.09	0.24	0.28	LS	26%
X-Direction	1st story	W114	0.10	0.88	1.17	0.09	0.11	LS	10%
		W115	0.10	0.79	1.05	0.10	0.13	LS	12%
		W116	0.10	0.60	0.80	0.07	0.09	IO	12%
		W117	0.10	0.46	0.61	0.03	0.08	IO	13%
		W118	0.10	0.39	0.52	0.03	0.08	IO	16%
		W119	0.10	0.45	0.60	0.04	0.08	IO	13%
		W120	0.10	0.54	0.71	0.05	0.08	IO	11%
	2nd story	W214	0.10	0.81	1.09	0.10	0.15	LS	14%
		W215	0.10	0.73	0.98	0.12	0.17	LS	17%
		W216a	0.10	0.69	0.92	0.14	0.17	LS	18%
		W216b	0.10	0.80	1.06	0.14	0.16	LS	15%
		W217	0.10	0.65	0.87	0.00	0.09	IO	11%
		W218	0.10	0.54	0.72	0.02	0.09	IO	13%
		W219	0.10	0.64	0.85	0.02	0.08	IO	10%
		W220	0.10	0.45	0.60	0.05	0.08	IO	12%

133

It might be concluded that CSB no: 1 satisfies life safety performance level in strong y-direction and immediate occupancy performance level in weak x-direction.

In the second method, as discussed in Chapter 2, limit states defined by Tomazevic on the PO curve of the URM buildings indicating different performance levels (see Figure 2.13) are utilized.

Cracking limit state is reached when first influencing cracks resulting in degradation of elastic stiffness takes place. Up to this level slight damage is observed. When story drifts reaches three times the story drifts attained at the first crack formation, acceptable damage limit state is reached. Although moderate level of damage is observed, building is still assumed to be safe and usable. Remaining region of the capacity curve is associated with heavy damage up to collapse of the building. Structural damages are beyond acceptable level for this region.

Displacement demands of the building in both directions are shown on the PO curves below (see Figure 6.15 and 6.16). CSB no: 1 is slightly below the cracking limit in strong direction satisfying immediate occupancy performance level. However, in weak direction it is between cracking and acceptable damage limits which corresponds to life safety performance level.

According to method proposed by Tomazevic, CSB no: 1 is expected to show slight damage in strong direction and moderate damage in weak direction under expected earthquake defined in TEC2007.
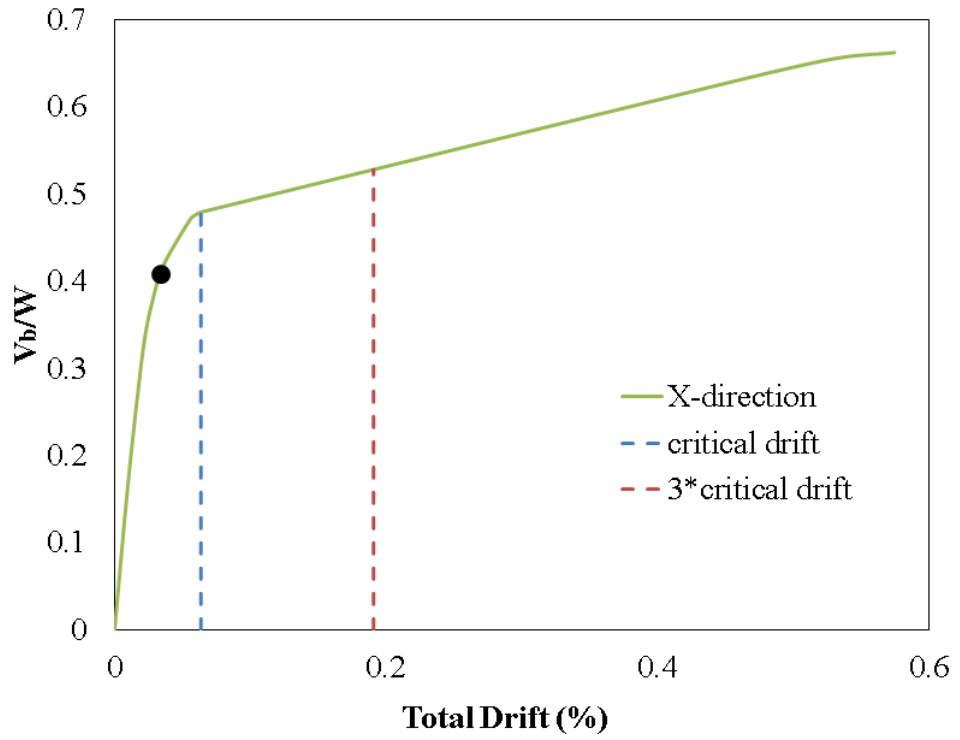
Figure 6.15 Performance Assessment of CSB No: 1 in x-direction
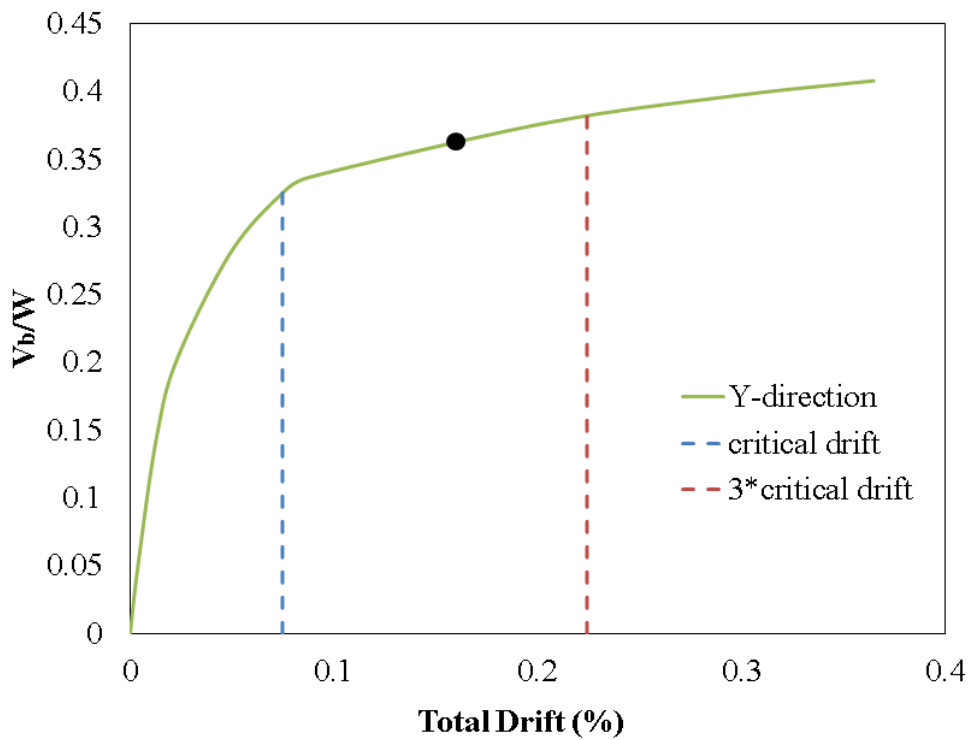
Figure 6.16 Performance Assessment of CSB No: 1 in y-direction

6.2 Case Study Building No: 2

2 story historical URM building which is built in 1934 is investigated by METU-EERC research team after Dinar earthquake of 1995 (see Figure 6.17). Building is located at Adliye District no: 7, Dinar. According to a preliminary assessment, building damage is reported as medium (Balkaya, 1996) and it is strengthened by wire mesh application with concrete shotcrete on outer walls. Solid brick and concrete is used as construction materials for walls and the slabs respectively.
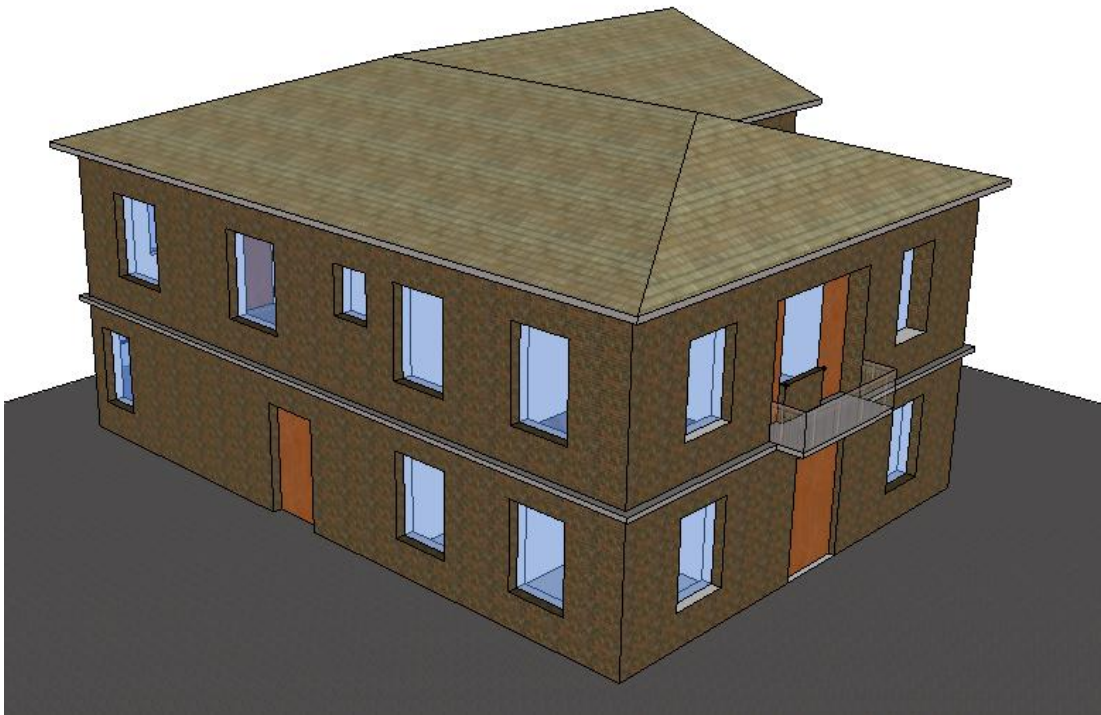
Figure 6.17 General View of the CSB No: 2

6.2.1. Generation of the Computer Model

In order to perform performance assessment, equivalent frame model of the CSB no: 2 is generated using computer software (see Figure 6.18). Labels of the walls on the first and second story plans are provided in Figure D.3 and Figure D.4 respectively.
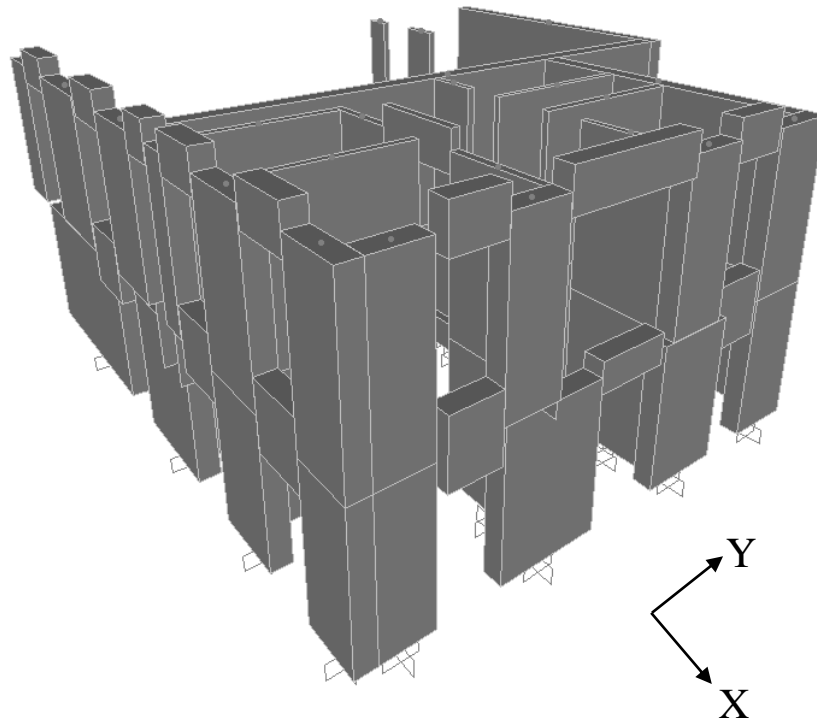
Figure 6.18 Computer Model of CSB No: 2

Since there are no laboratory tests illustrating material properties, same material properties which are assigned to CSB no: 1 is assumed for the CSB no: 2.

Rigid end offsets of the perforated walls are determined according to method proposed by Dolce (1989) (see Figure 6.19).

Story masses compatible with story weights are calculated taking both the weight of the slabs and the walls into account. Slab and roof weights are calculated according to TS 498 (1997) and TS ISO 9194 (1997) respectively. Since first story wall at the rear side of the building (See Figure D.3) is removed, second story walls above the removed wall are taken as additional weight on the slab.

After story masses are lumped to center of mass of each story, rigid diaphragm is assigned at each story level and modal analysis is conducted. Dynamic characteristics of the building are illustrated in Table 6.4. Due to L-shaped irregular

story plan and non-symmetric distribution of walls in the plan, modal participating mass ratios of the building in both directions are slightly lower than the minimum limit (i.e. 0.7) specified in TEC2007.

Table 6.4 Modal Properties of CSB No: 2

mode number	direction	period (sec)	modal participating mass ratio (α)	modal participation factor (PF)	PF*Φ_r
1	y-direction	0.155	0.694	22.73	0.998
2	x-direction	0.125	0.689	22.65	1.069
3	torsion	0.115			

a)

b)
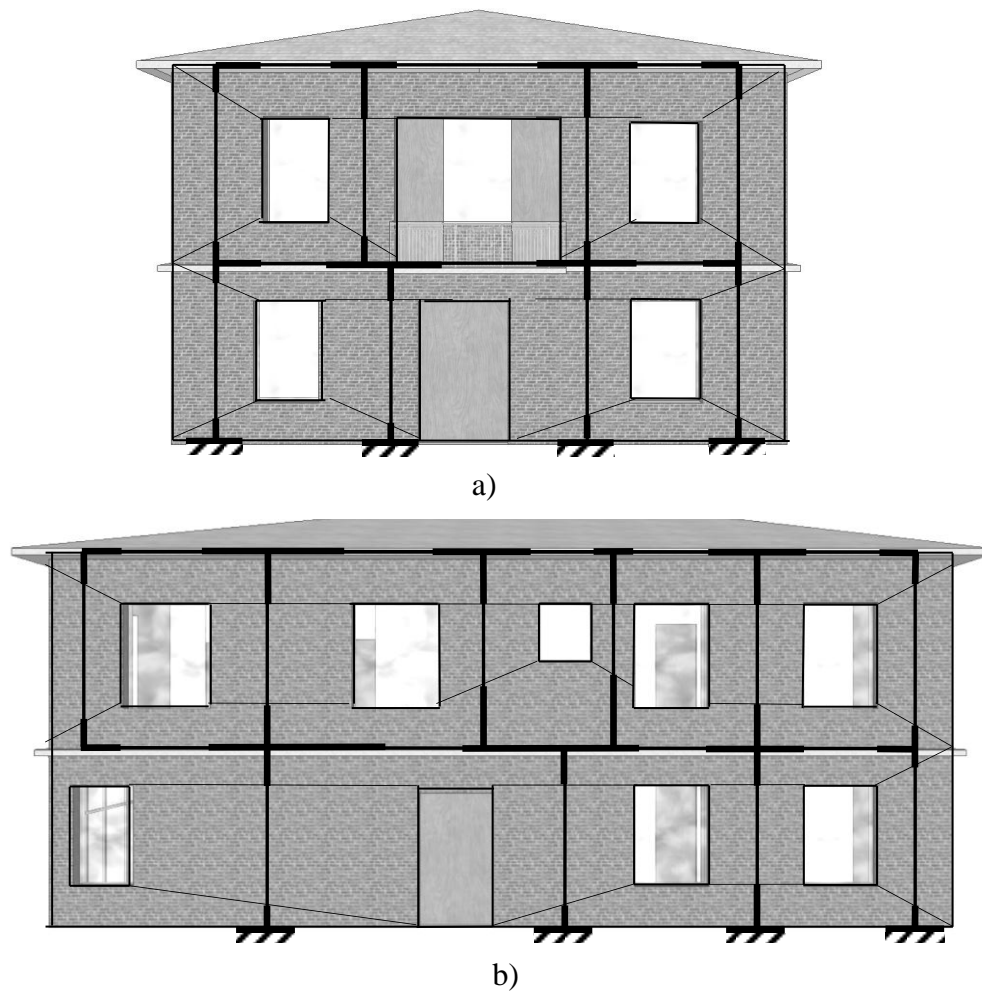
Figure 6.19 Equivalent Frame Modeling of Perforated Walls of CSB No: 2; a) Front View, b) Left View

6.2.2. Static Pushover Analysis

In order to conduct PO analyses, building is first analyzed under gravity loads to calculate compressive stresses on each pier. Nonlinear properties of each wall are determined utilizing Equations 4.1 and 4.2 (see Table C.2). Average ultimate drift of first story and second story walls are found to be 0.98% and 1.55% respectively. The reason why ultimate drift values are high is the story height of the case story building no: 2 which is equal to 3.65 m and 4.10 m for the first and second stories.

Normalized PO curves of the case story building no: 2 in x and y directions are drawn both according to hinges proposed by Aldemir (2010) and according to hinges proposed by FEMA 356 (2000). Default hinges proposed by FEMA 356 is modified as discussed in section 6.1.2 (see Figure 6.5).
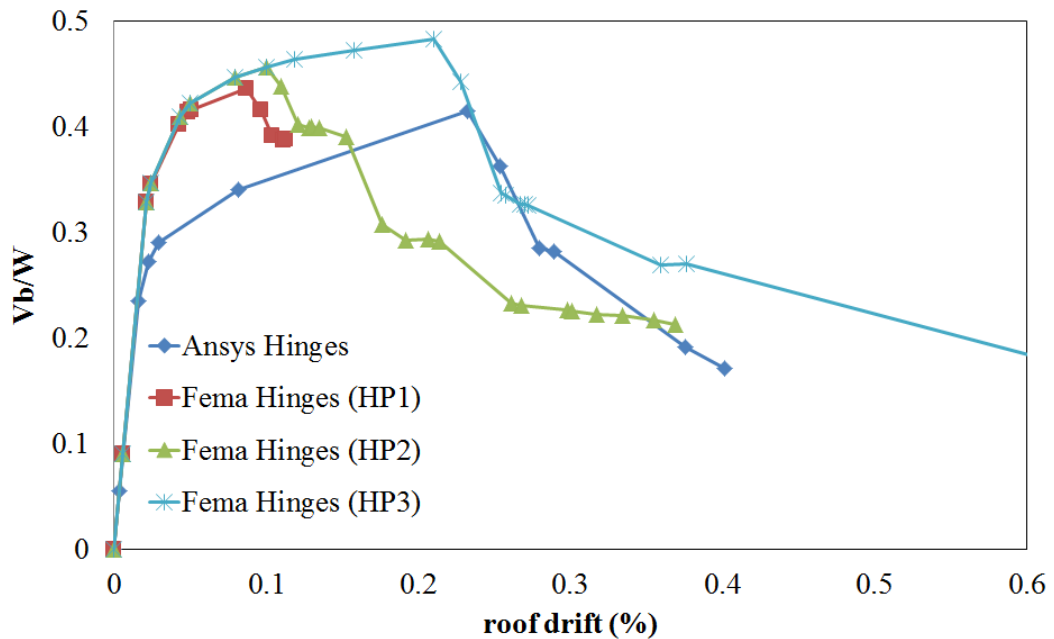
Figure 6.20 Normalized Capacity Curves of the CSB No: 2 in x-direction
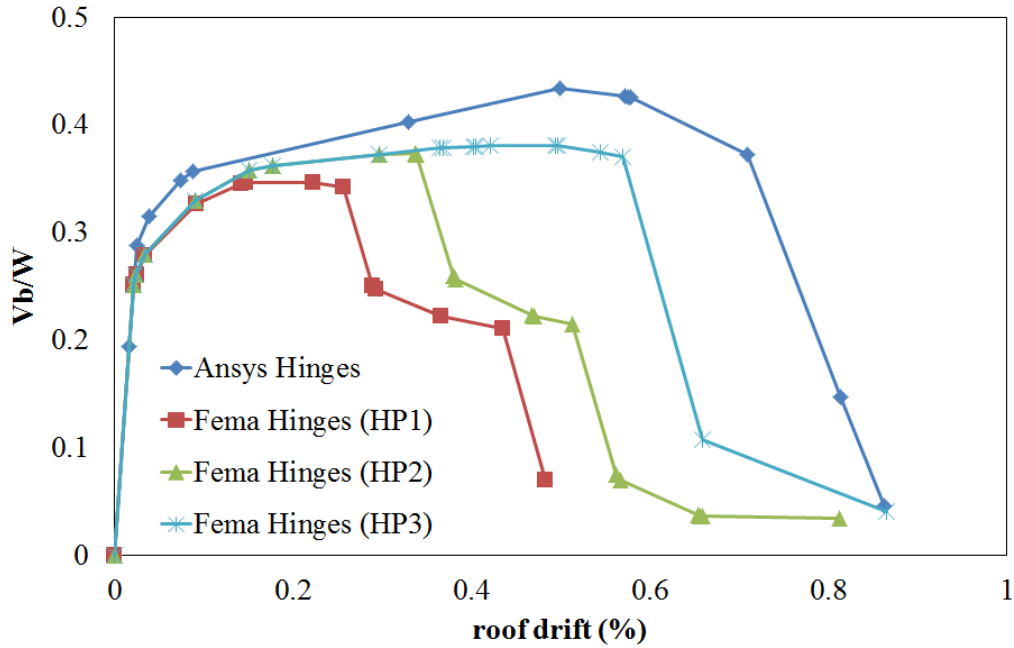
Figure 6.21 Normalized Capacity Curves of the CSB No: 2 in y-direction

PO curve with hinges derived from equations 4.1 and 4.2 (i.e. Ansys Hinges) is similar to PO curve in which modification of hinges proposed by FEMA 356 (i.e. HP3) is utilized in terms of "yield" force, base shear capacity and ultimate roof drift for y-direction. Although there is a disagreement in base shear capacity and "yield" force in x-direction, hinges derived from equations 4.1 and 4.2 results in conservative values.

The building is capable of carrying 43 % of its total weight in strong direction and 42 % of its total weight in weak direction. Ultimate total drift of the building is 0.23 % and 0.50 % in strong and weak directions respectively.

6.2.3. Bilinearization of Capacity Curve

After capacity curves of the CSB no: 2 is derived they are bilinearized according to procedure recommended by FEMA 356 (2000) to calculate the seismic demand of the building (see Figure 6.22).
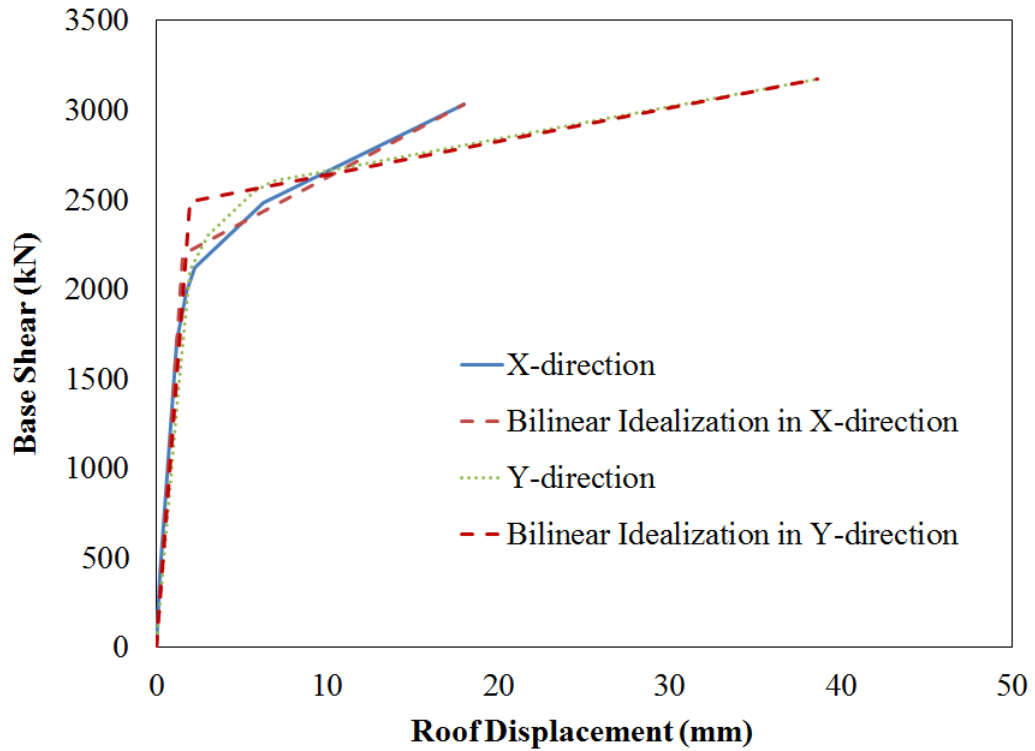
Figure 6.22 Bilinearized Capacity Curves of CSB No: 2 According to FEMA 356

6.2.4. Calculation of Demand According to TEC2007

For the roof displacement demand calculation of the building, design spectrum provided by TEC2007 for earthquake zone 1, soil type Z3 and 5% damping is converted to design spectrum for 10% damping as illustrated in section 6.1.4.

After capacity curve of the CSB no: 2 and the 10% design spectrum is converted to ADRS format, inelastic spectral displacement demand of the CSB no: 2 is determined for x and y directions according to iterative procedure recommended by TEC2007.

Final roof displacement demands of the building in both directions are calculated as 7.86 mm (0.10 %) and 12.39 mm (0.16%) in x and y directions respectively. Calculated demands are pointed with a black dot on the capacity curves of the building in the following graphs.

6.2.5. Nonlinear Time History Analysis

After hysteresis response proposed by Takeda et al. (1970) is assigned to the predefined shear hinges, nonlinear THA of the CSB no: 2 is made in x and y directions.

In addition to energy dissipation due to hysteresis behavior, 5 % viscous damping is assigned to the building similar to CSB no: 1.

As it is illustrated in Table 6.5, maximum base shear demand of the CSB no: 2 is 33 % and 34 % of its weight in X and Y directions respectively.

Table 6.5 Nonlinear Time History Analyses Results for CSB No: 2

	X-Direction	Y-Direction
$\emptyset_{1st\,story,max}$	0.016%	0.020%
$\emptyset_{roof,max}$	0.032%	0.036%
$V_{b,max}/W$	0.33	0.34

Base shear coefficient versus roof drift of the CSB no: 2 is drawn together with normalized PO curves in Figure 6.23 and Figure 6.24 for x and y directions respectively. Roof demand calculated according to procedure recommended by TEC2007 is identified with a black dot on the PO curves.

It is inferred from increase of loop areas that nonlinear response is observed both in x and y directions.
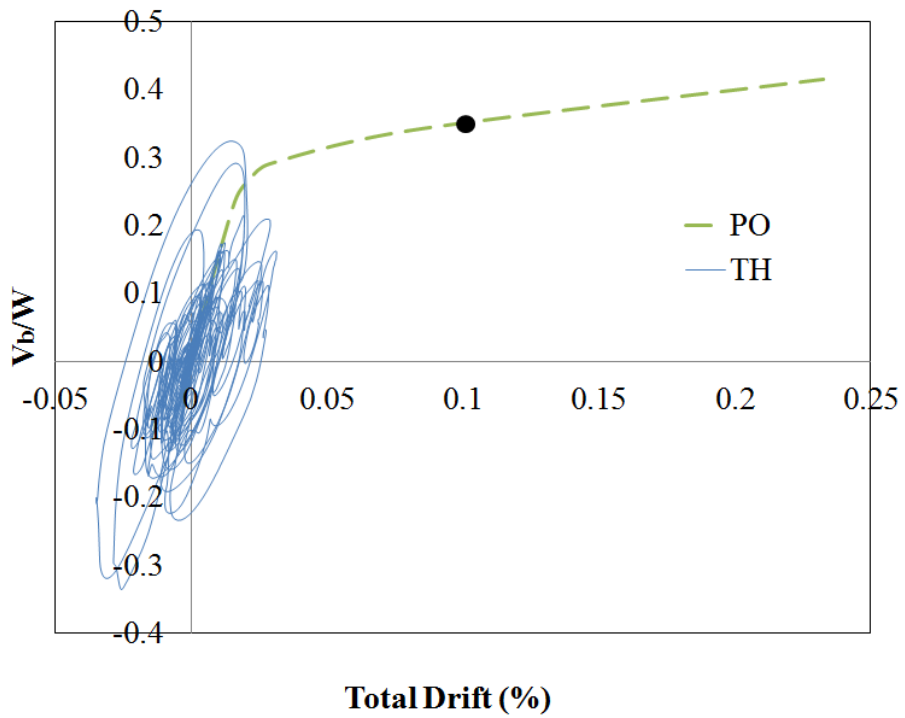
Figure 6.23 Nonlinear THA Results with Capacity Curve of CSB No: 2 in x-direction
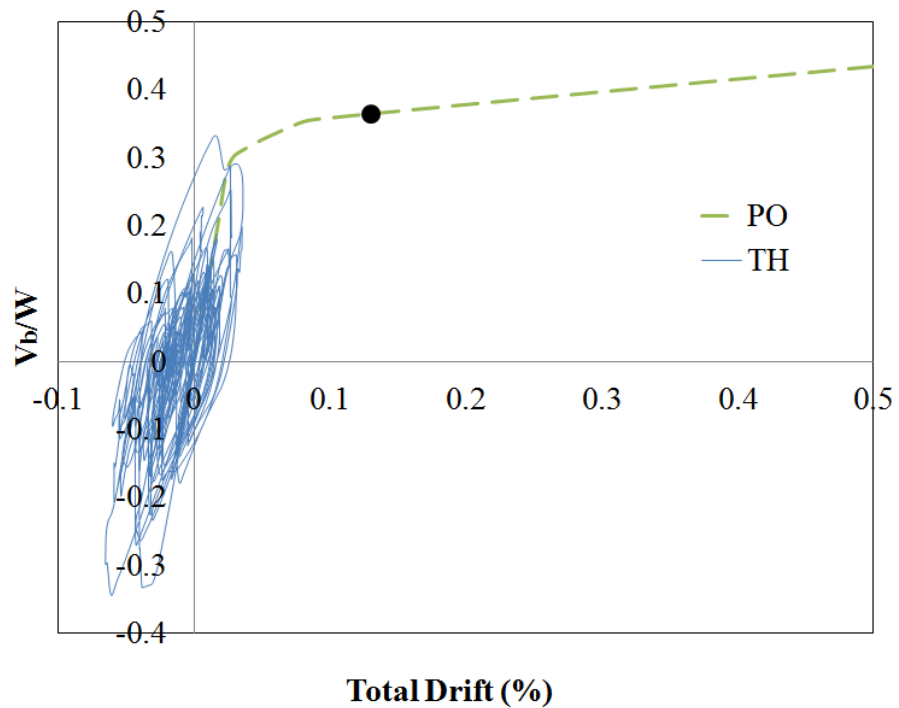
Figure 6.24 Nonlinear THA Results with Capacity Curve of CSB No: 2 in y-direction

6.2.6. Determination of Performance Level

After inelastic roof displacement demand of the building is calculated according to TEC2007 (2007), CSB no: 2 is pushed to the performance point. Pier displacement demands calculated at the performance point is then compared with the displacement capacity of the piers which are tabulated in Table C.2.

Performance state of each pier belonging to CSB no: 2 which are illustrated in Figure D.3 and Figure D.4 is tabulated below (see Table 6.6).

It might be inferred from table 6.6 that CSB no: 2 satisfies life safety performance level in both directions with a better performance in x-direction.

Table 6.6 Element Performance States of CSB No: 2

		Frame Id	\multicolumn{3}{c}{Performance Limits}			\multicolumn{2}{c}{Performance Point}		\multicolumn{2}{c}{Performance}
			Φ_{IO} (%)	Φ_{LS} (%)	Φ_{CP} (%)	Φ_p (%)	Φ_t (%)	Status	Φ_t/Φ_u
Y-Direction	1st Story	W101	0.10	0.29	0.38	0.09	0.12	LS	33%
		W102	0.10	0.64	0.85	0.09	0.12	LS	14%
		W103	0.10	0.39	0.53	0.06	0.12	LS	23%
		W104	0.10	0.39	0.52	0.06	0.12	LS	23%
		W105	0.10	0.39	0.53	0.06	0.12	LS	23%
		W106	0.10	0.38	0.51	0.06	0.12	LS	23%
		W107	0.10	1.49	1.99	0.13	0.15	LS	7%
		W108	0.10	1.16	1.54	0.14	0.16	LS	10%
		W109	0.10	1.15	1.53	0.03	0.17	LS	11%
		W110	0.10	1.31	1.74	0.05	0.15	LS	9%
	2nd Story	W202	0.10	1.00	1.33	0.17	0.19	LS	27%
		W203	0.10	0.59	0.79	0.09	0.19	LS	14%
		W204	0.10	0.58	0.78	0.09	0.19	LS	24%
		W205	0.10	0.59	0.79	0.09	0.19	LS	24%
		W206	0.10	0.57	0.76	0.09	0.19	LS	25%
		W207	0.10	2.26	3.01	0.22	0.24	LS	8%
		W208	0.10	1.71	2.29	0.27	0.29	LS	13%
		W209	0.10	1.73	2.31	0.24	0.28	LS	12%
		W210	0.10	2.05	2.74	0.21	0.24	LS	9%

Table 6.6 (Continued)

		Frame Id	Φ_{IO} (%)	Φ_{LS} (%)	Φ_{CP} (%)	Φ_p (%)	Φ_t (%)	Status	Φ_t/Φ_u
			Performance Limits			**Performance Point**		**Performance**	
X-Direction	1st Story	W111	0.10	0.65	0.87	0.00	0.03	IO	4%
		W112	0.10	0.83	1.10	0.01	0.03	IO	3%
		W113	0.10	1.00	1.33	0.01	0.04	IO	3%
		W114	0.10	1.34	1.79	0.01	0.03	IO	2%
		W115	0.10	1.06	1.42	0.00	0.02	IO	1%
		W116	0.10	0.36	0.48	0.00	0.03	IO	5%
		W117	0.10	0.35	0.46	0.00	0.02	IO	5%
		W118	0.10	0.41	0.55	0.00	0.02	IO	4%
		W119	0.10	0.36	0.48	0.00	0.02	IO	5%
		W120	0.10	0.66	0.88	0.00	0.02	IO	2%
		W121	0.10	0.77	1.03	0.00	0.02	IO	2%
	2nd Story	W211a	0.10	1.63	2.17	0.40	0.41	LS	19%
		W211b	0.10	1.07	1.43	0.52	0.58	LS	41%
		W212a	0.10	1.34	1.79	0.46	0.48	LS	27%
		W212b	0.10	1.87	2.49	0.88	0.88	LS	15%
		W213	0.10	1.61	2.15	0.54	0.58	LS	48%
		W214	0.10	2.05	2.74	0.39	0.41	LS	43%
		W216	0.10	0.50	0.67	0.23	0.33	LS	26%
		W217	0.10	0.49	0.66	0.21	0.28	LS	30%
		W218	0.10	0.59	0.79	0.08	0.21	LS	10%
		W219	0.10	0.52	0.69	0.09	0.21	LS	30%
		W220a	0.10	1.31	1.74	0.08	0.18	LS	10%
		W220b	0.10	0.41	0.55	0.10	0.16	LS	30%
		W220c	0.10	0.50	0.67	0.03	0.15	LS	23%
		W221	0.10	1.14	1.53	0.10	0.24	LS	16%

Performance assessment of the CSB no: 2 is further made by the simple method proposed by Tomazevic (2007). For this purpose performance levels proposed by Tomazevic is drawn together with the normalized PO curves of the building in both directions (see Figures 6.25 and 6.26).

CSB no: 2 is slightly above the acceptable limit in weak direction satisfying collapse prevention performance level and between acceptable and cracking performance limits in strong direction satisfying life safety performance level under expected earthquake defined in TEC2007.
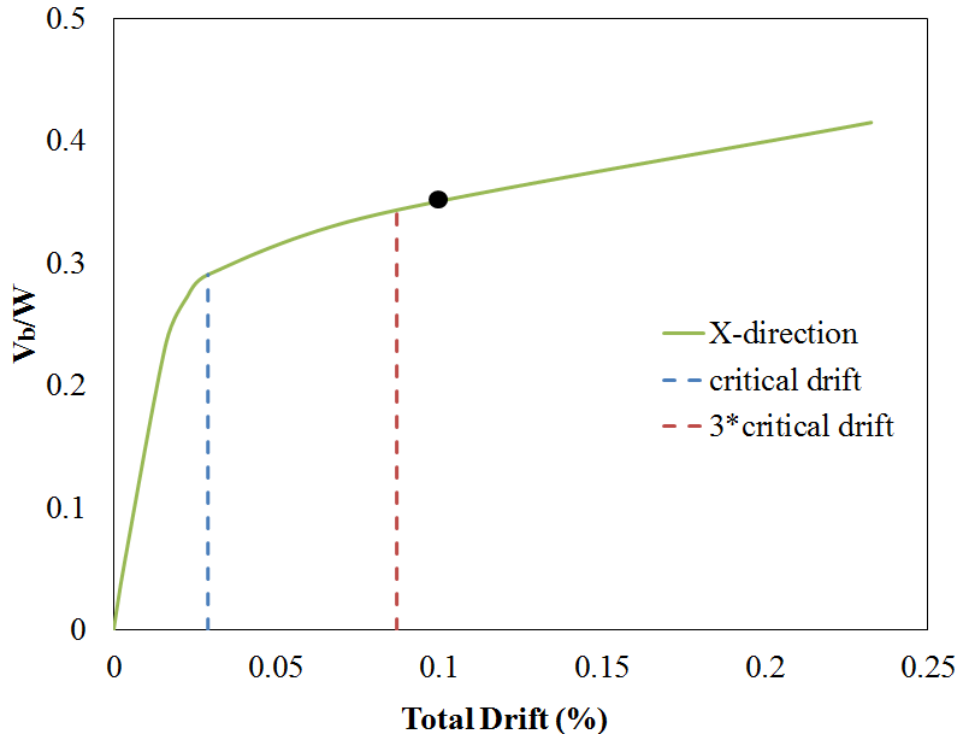
Figure 6.25 Performance Assessment of CSB No: 2 in X-direction
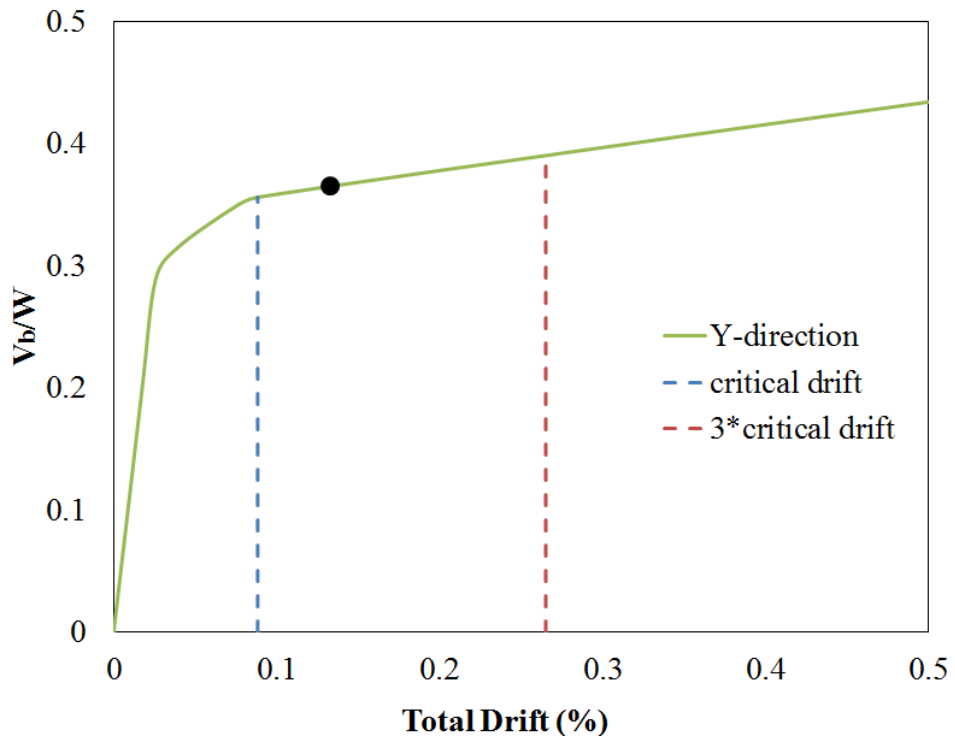
Figure 6.26 Performance Assessment of CSB No: 2 in Y-direction

6.3 Case Study Building No: 3

3 storey URM building located at Konak District no: 5 which is investigated by METU-EERC research team after Dinar earthquake of 1995 (see Figure 6.27) is selected for performance assessment using proposed nonlinear equivalent frame model. According to a preliminary assessment, building damage is reported as low (Özcebe, 1996) and in addition to reducing window openings it is strengthened by wire mesh application with concrete shotcrete on outer walls. Solid factory brick and concrete is used as construction materials for walls and the slabs respectively.

Height of the base, first and second stories are 2.4m, 2.75m and 2.75m respectively. Also thickness of the perforated walls in the base, first and second stories are 40cm, 30cm and 20cm respectively.
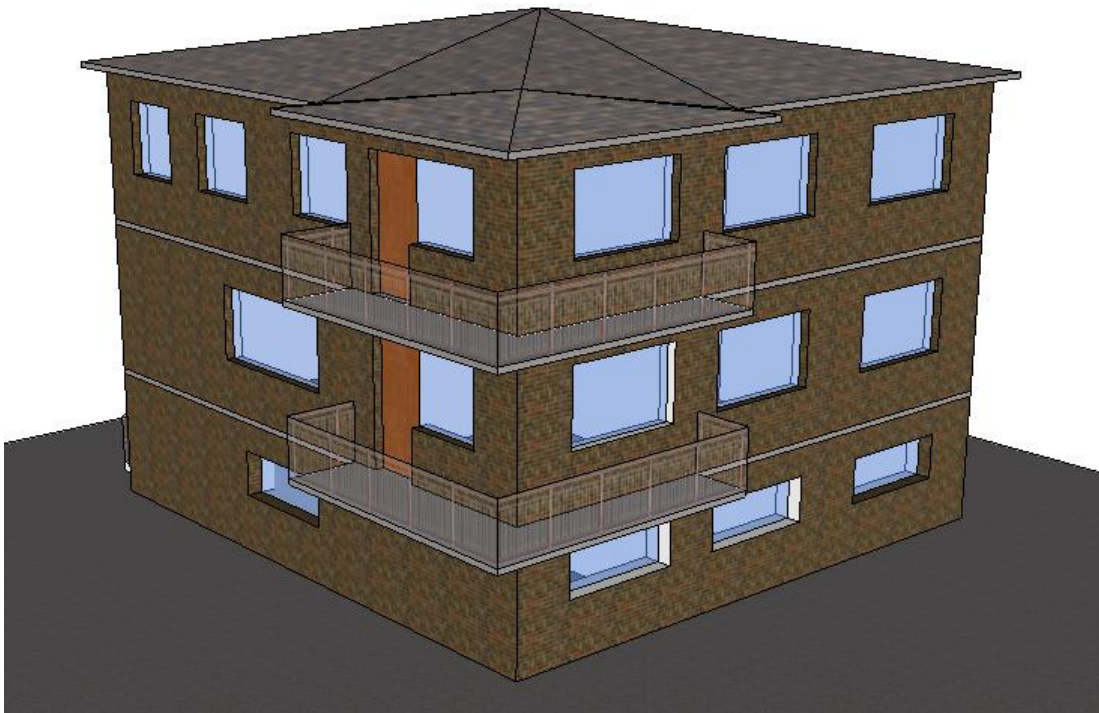
Figure 6.27 General View of the CSB No: 3

6.3.1. Generation of the Computer Model

Equivalent frame model of the CSB no: 2 is generated using computer software (see Figure 6.18) to conduct performance assessment of the building. Labels of the walls on the first, second and third story plans are provided in Figure D.5, Figure D.6 and Figure D.7 respectively.
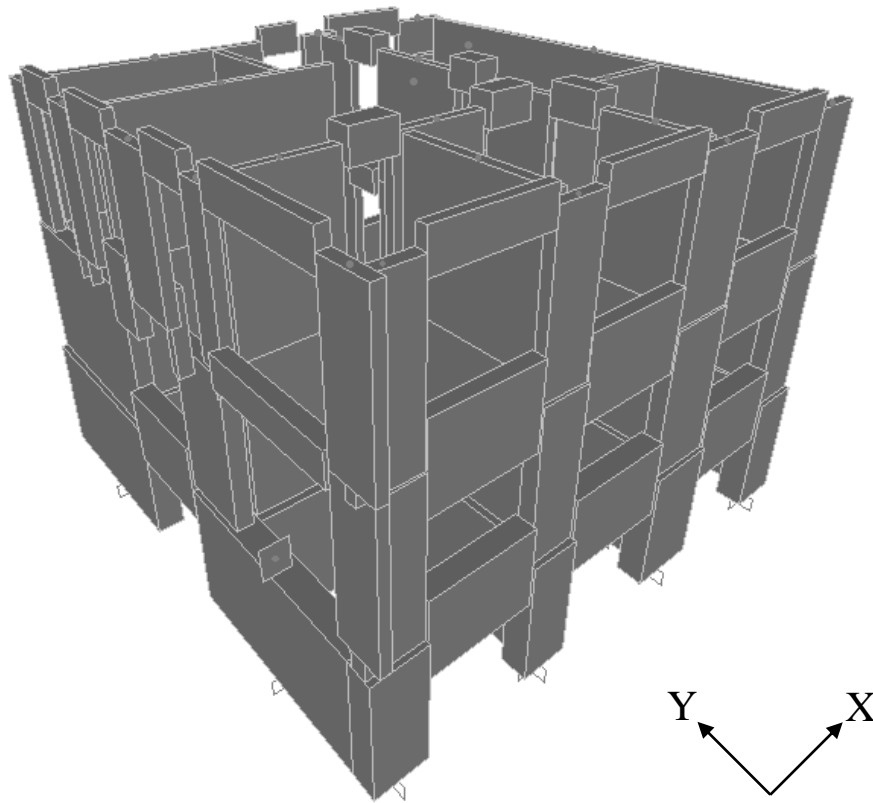
Figure 6.28 Computer Model of CSB No: 3

Since there are no laboratory tests illustrating material properties, same material properties which are assigned to CSB no: 1 and CSB no: 2 is also assumed for the CSB no: 3.

Rigid end offsets of the perforated walls determined according to method proposed by Dolce (1989) is illustrated in Figure 6.29.

Story masses compatible with story weights are calculated taking both the weight of the slabs and the walls into account. Slab and roof weights are calculated according to TS 498 (1997) and TS ISO 9194 (1997) respectively.

Then, modal analysis is conducted and dynamic characteristics of the building are identified. Initially due to thick and low walls at the base, distribution of stiffness along the height of the CSB no: 3 was irregular and modal participating mass ratios were calculated well below the code allowed limits. Conducting PO analyses on the building illustrated that due to high stiffness and strength, base story walls actually stands still as second and third storey walls pass into plastic range.

As a result, assuming base story walls satisfies immediate occupancy performance level, they are removed from the building and the calculations are made for the remaining two storeys.

Modal properties of modified 2 story CSB no: 3 is recalculated and it is realized that modal mass participation factors are now sufficiently large to conduct PO analyses (see Table 6.7).

Table 6.7 Modal Properties of CSB No: 3

mode number	direction	period (sec)	modal participating mass ratio (α)	modal participation factor (PF)	PF*Φ_r
1	y-direction	0.122	0.776	12.08	1.144
2	x-direction	0.114	0.647	11.03	0.985
3	torsion	0.078			
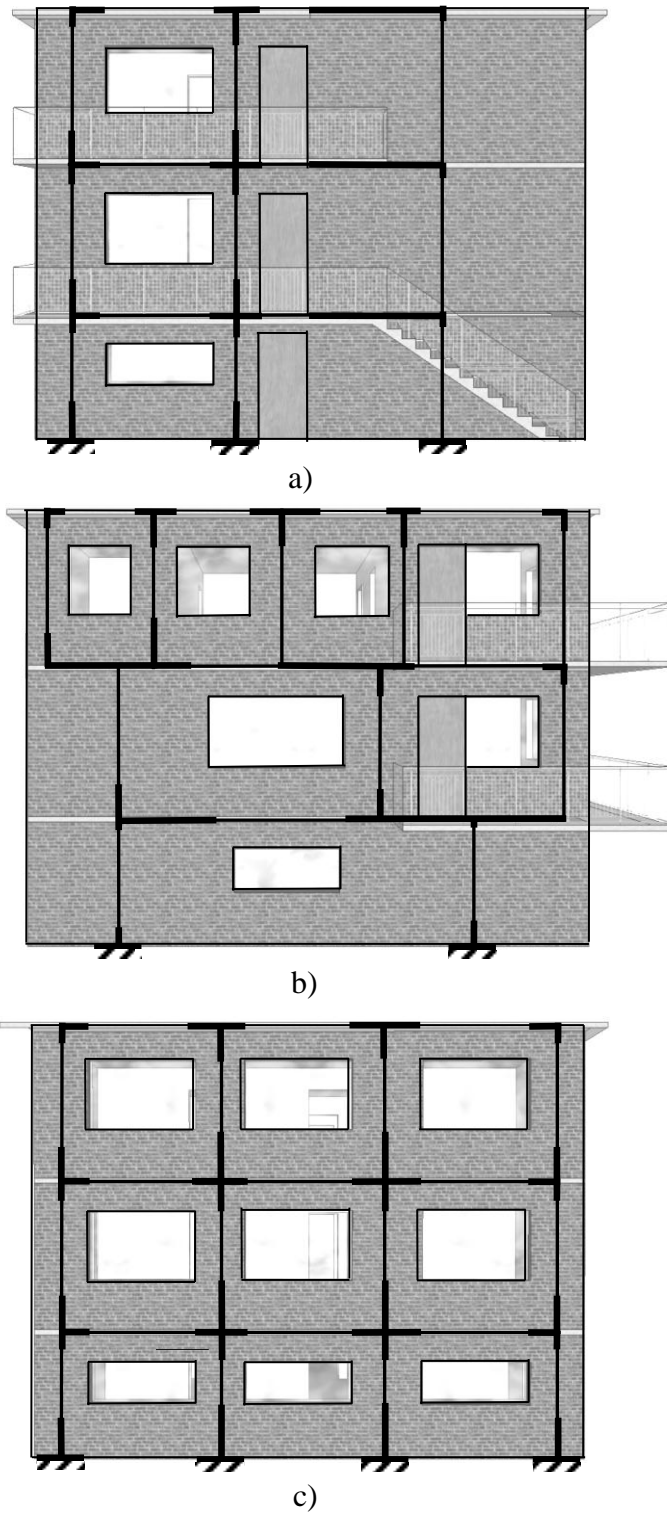
Figure 6.29 Equivalent Frame Modeling of Perforated Walls of CSB No: 3; a) Front View, b) Right View, c) Rear View

6.3.2. Static Pushover Analysis

In order to conduct PO analyses, an initial dead load analysis of the CSB no: 3 is made to calculate compressive stresses on each pier. Nonlinear force-displacement relationship of each wall is determined utilizing Equations 4.1 and 4.2 (see Table C.3). Average ultimate drift of second and third storey walls are calculated as 0.78% and 0.89% respectively. The reason why ultimate drift values are high for the upper story is low level of compressive stresses.

Normalized PO curves of the case story building no: 3 in x and y directions are drawn according to hinges proposed by Aldemir (2010) and according to hinges proposed by FEMA 356 (2000). Default hinges proposed by FEMA 356 is modified as discussed in section 6.1.2 (see Figure 6.5).
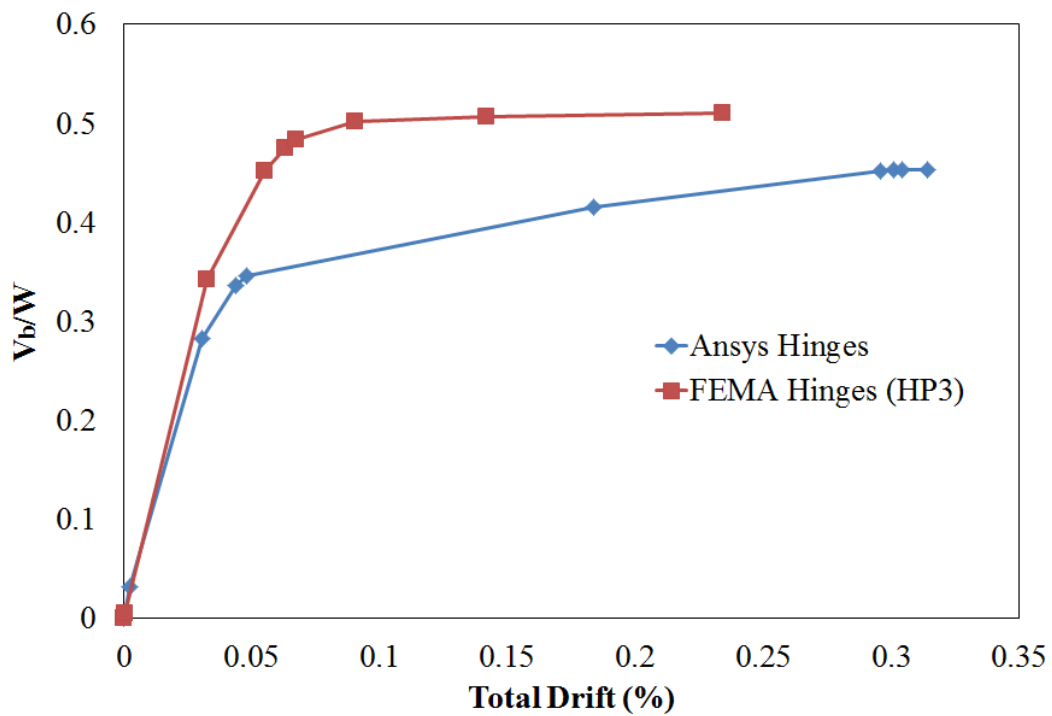
Figure 6.30 Normalized Capacity Curves of the CSB No: 3 in x-direction
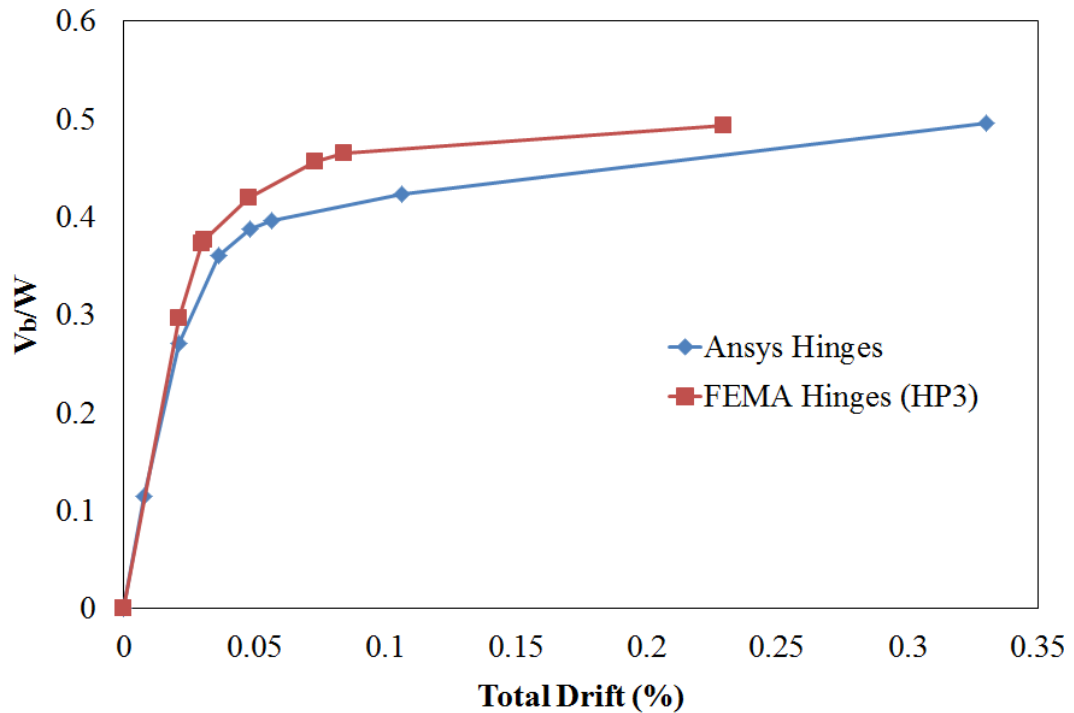
Figure 6.31 Normalized Capacity Curves of the CSB No: 3 in y-direction

It might be inferred from Figure 6.30 and Figure 6.31 that PO curves derived using ansys hinges yields higher ultimate drift values compared with PO curves derived using modified FEMA 356 hinges. There is a good match between base shear capacities in y-direction. Ansys hinges give conservative base shear capacity in x-direction.

The building is capable to carry 45 % of its total weight in weak (X) direction and 50 % of its total weight in strong (y) direction. Ultimate roof drift of the building is 0.30 % and 0.33 % in weak and strong directions respectively.

6.3.3. Bilinearization of Capacity Curve

After capacity curves of the CSB no: 3 is derived they are bilinearized according to FEMA 356 (2000) to calculate the seismic demand of the building (see Figure 6.32).
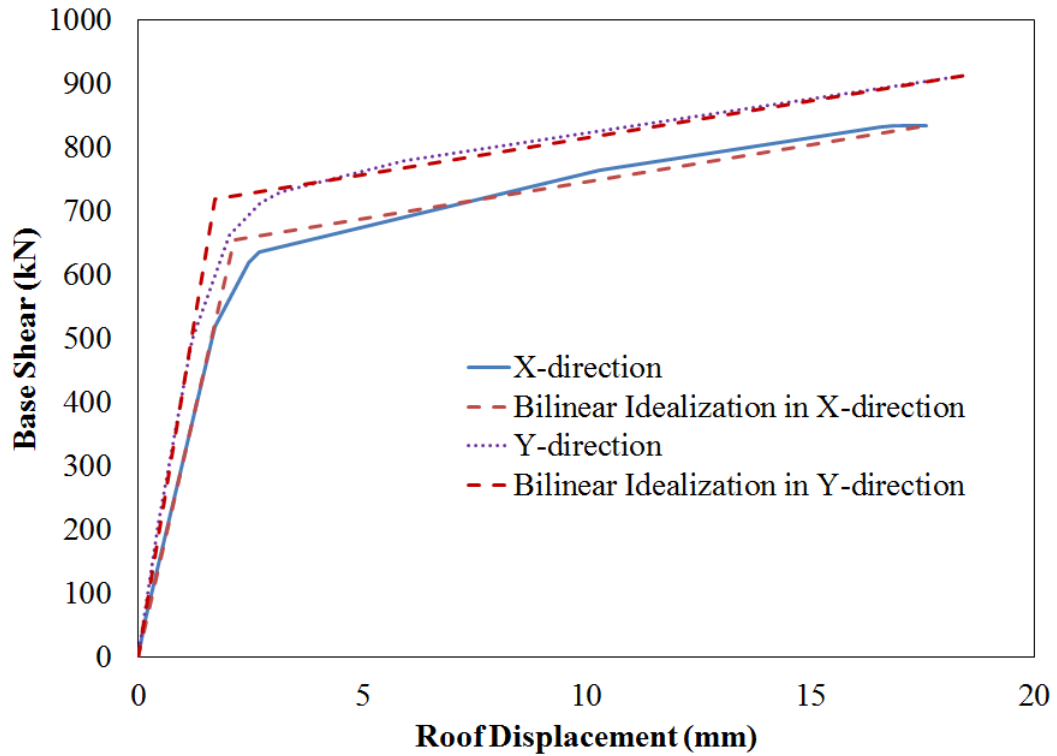
Figure 6.32 Bilinearized Capacity Curves of CSB No: 3 According to FEMA 356

6.3.4. Calculation of Demand According to TEC2007

10 % design spectrum for earthquake zone 1 and soil type Z3 is utilized for roof displacement demand calculation of the CSB no: 3 (see Figure 6.10).

After capacity and 10% design spectrum is converted to ADRS format, inelastic spectral displacement demand of the CSB no: 3 is determined according to TEC2007.

Final roof displacement demands of the building in both directions are calculated as 8.50 mm (0.15 %) and 3.26 mm (0.06%) in x and y directions respectively.

Calculated demands are pointed with a black dot on the capacity curves of the building in the following graphs.

6.3.5. Nonlinear Time History Analysis

Nonlinear THA of the CSB no: 3 is made in x and y directions after hysteresis response proposed by Takeda et al. (1970) is assigned to the predefined shear hinges. 5 % viscous damping is assigned to the building similar to CSB no: 1and CSB no: 2.

As it is illustrated in Table 6.8, maximum base shear demand of the CSB no: 3 is 34 % and 33 % of its total weight in x and y directions respectively.

Table 6.8 Nonlinear Time History Analyses Results for CSB No: 3

	X-Direction	Y-Direction
$\emptyset_{1st\ story,max}$	0.051%	0.019%
$\emptyset_{roof,max}$	0.048%	0.034%
$V_{b,max}$/ W	0.34	0.33

Base shear coefficient versus roof drift of the CSB no: 3 is drawn together with normalized PO curves in Figure 6.33 and Figure 6.34 for x and y directions respectively. Roof demand calculated according to procedure recommended by TEC2007 is identified with a black dot on the PO curves.

It is inferred from increase of loop areas in x-direction that nonlinearity and the damage in x direction is more than y direction.
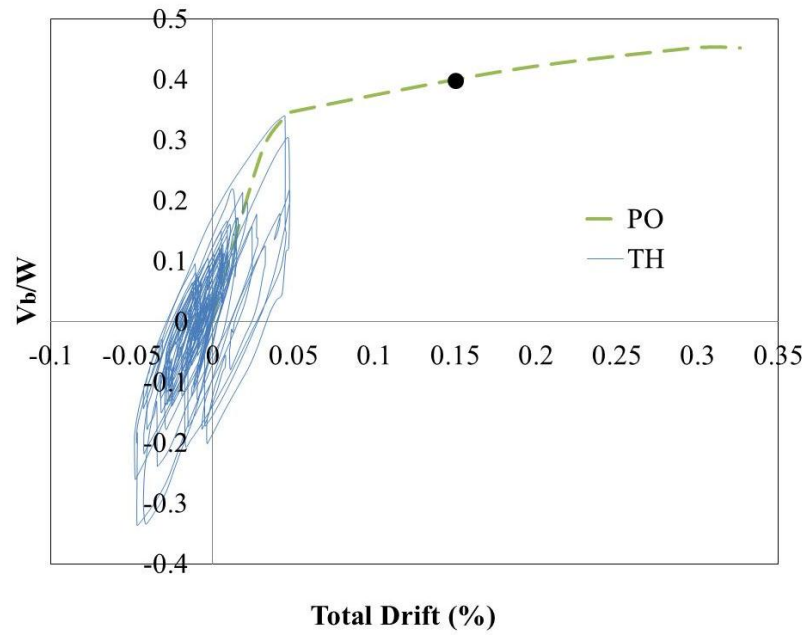
Figure 6.33 Nonlinear THA Results with Capacity Curve of CSB No: 3 in X-direction
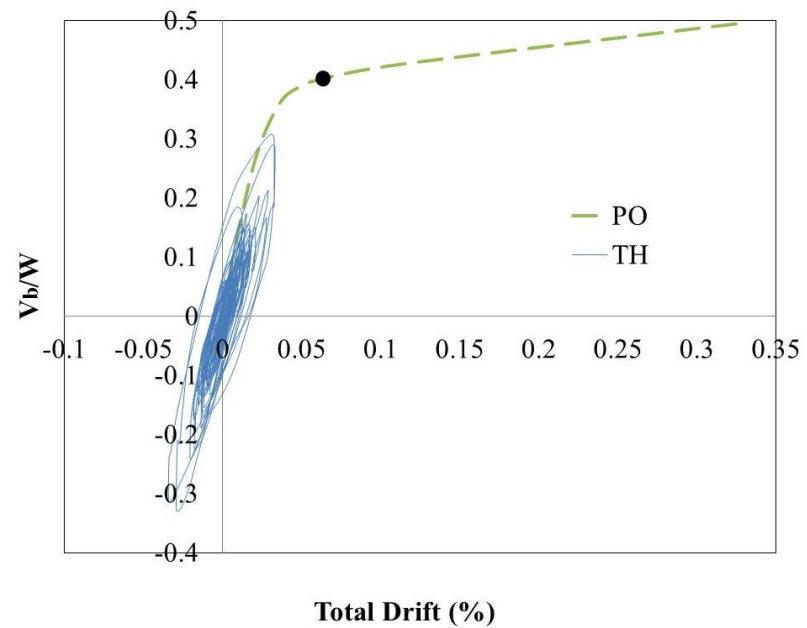
Figure 6.34 Nonlinear THA Results with Capacity Curve of CSB No: 3 in y-direction

6.3.6. Determination of Performance Level

After inelastic roof displacement demand of the CSB no: 3 is calculated according to TEC2007, it is pushed to the performance point. Pier displacement demands

155

calculated at the performance point is then compared with the displacement capacity of the piers which are tabulated in Table C.3.

Since base story of the building is removed, performance state of each piers belonging to second and third storeys of CSB no: 3 (see Figure D.6 and D.7) is tabulated below (see Table 6.9). Note that Φ_t/Φ_u ratio at the last column of the table indicates percent of total capacity reached by the corresponding pier.

It might be inferred from table 6.9 that CSB no: 3 satisfies life safety performance level in both directions with a better performance in y-direction.

Table 6.9 Element Performance Level of CSB No: 3

		Frame Id	Performance Limits			Performance Point		Performance	
			Φ_{IO} (%)	Φ_{LS} (%)	Φ_{CP} (%)	Φ_p (%)	Φ_t (%)	Status	Φ_t/Φ_u
Y-Direction	2nd Story	W201	0.10	0.53	0.71	0.04	0.06	IO	8%
		W202	0.10	0.54	0.72	0.05	0.07	IO	9%
		W203a	0.10	0.37	0.50	0.03	0.07	IO	13%
		W203b	0.10	0.43	0.58	0.05	0.07	IO	12%
		W204	0.10	0.41	0.55	0.03	0.07	IO	12%
		W205	0.10	0.53	0.70	0.01	0.07	IO	10%
		W206	0.10	0.44	0.59	0.02	0.07	IO	13%
		W207	0.10	0.63	0.84	0.08	0.11	LS	13%
		W208a	0.10	0.67	0.89	0.10	0.13	LS	15%
		W208b	0.10	0.84	1.13	0.09	0.12	LS	11%
	3rd Story	W301	0.10	0.45	0.61	0.12	0.15	LS	24%
		W302	0.10	0.79	1.06	0.15	0.17	LS	16%
		W303a	0.10	0.54	0.72	0.12	0.17	LS	23%
		W303b	0.10	0.63	0.85	0.17	0.17	LS	20%
		W304	0.10	0.60	0.80	0.12	0.17	LS	21%
		W305	0.10	0.77	1.02	0.07	0.18	LS	18%
		W306	0.10	0.64	0.85	0.09	0.18	LS	21%
		W307a	0.10	1.00	1.34	0.29	0.32	LS	24%
		W307b	0.10	0.73	0.97	0.39	0.43	LS	44%
		W308a	0.10	0.66	0.88	0.38	0.43	LS	49%
		W308b	0.10	0.56	0.74	0.33	0.37	LS	50%
		W308c	0.10	0.83	1.11	0.26	0.30	LS	28%

Table 6.9 (Continued)

		Frame Id	**Performance Limits**			**Performance Point**		**Performance**	
			Φ_{IO} (%)	Φ_{LS} (%)	Φ_{CP} (%)	Φ_p (%)	Φ_t (%)	Status	Φ_t/Φ_u
X-Direction	2nd Story	W209	0.10	0.85	1.13	0.29	0.32	LS	28%
		W210	0.10	1.00	1.33	0.39	0.39	LS	30%
		W211	0.10	0.64	0.85	0.21	0.24	LS	29%
		W212	0.10	0.45	0.60	0.17	0.22	LS	37%
		W213	0.10	0.31	0.42	0.17	0.22	LS	53%
		W214	0.10	0.36	0.48	0.18	0.23	LS	47%
		W215	0.10	0.33	0.44	0.20	0.23	LS	52%
		W216	0.10	0.31	0.42	0.17	0.23	LS	54%
		W217	0.10	0.93	1.25	0.32	0.34	LS	28%
		W218	0.10	0.65	0.86	0.45	0.49	LS	57%
		W219	0.10	0.72	0.96	0.47	0.49	LS	51%
		W220	0.10	0.88	1.17	0.33	0.34	LS	29%
	3rd Story	W309	0.10	0.76	1.01	0.05	0.10	LS	10%
		W310	0.10	0.97	1.29	0.17	0.17	LS	13%
		W311	0.10	0.55	0.73	0.04	0.08	IO	11%
		W312	0.10	0.65	0.87	0.00	0.08	IO	9%
		W313	0.10	0.45	0.60	0.01	0.08	IO	13%
		W314	0.10	0.53	0.71	0.03	0.09	IO	12%
		W315	0.10	0.48	0.63	0.07	0.09	IO	14%
		W316	0.10	0.45	0.61	0.03	0.09	IO	14%
		W317	0.10	0.88	1.18	0.10	0.14	LS	12%
		W318	0.10	0.62	0.82	0.14	0.20	LS	24%
		W319	0.10	0.66	0.88	0.17	0.20	LS	23%
		W320	0.10	0.85	1.13	0.12	0.14	LS	12%

Performance assessment of the CSB no: 3 is also made by the simple method proposed by Tomazevic (2007). For this purpose performance levels proposed by Tomazevic is drawn together with the normalized PO curves of the building in both directions (see Figures 6.35 and 6.36).

CSB no: 2 is just on the acceptable limit in weak direction satisfying life safety performance level and between acceptable and cracking performance limits in strong direction satisfying life safety performance level under expected earthquake defined in TEC2007.
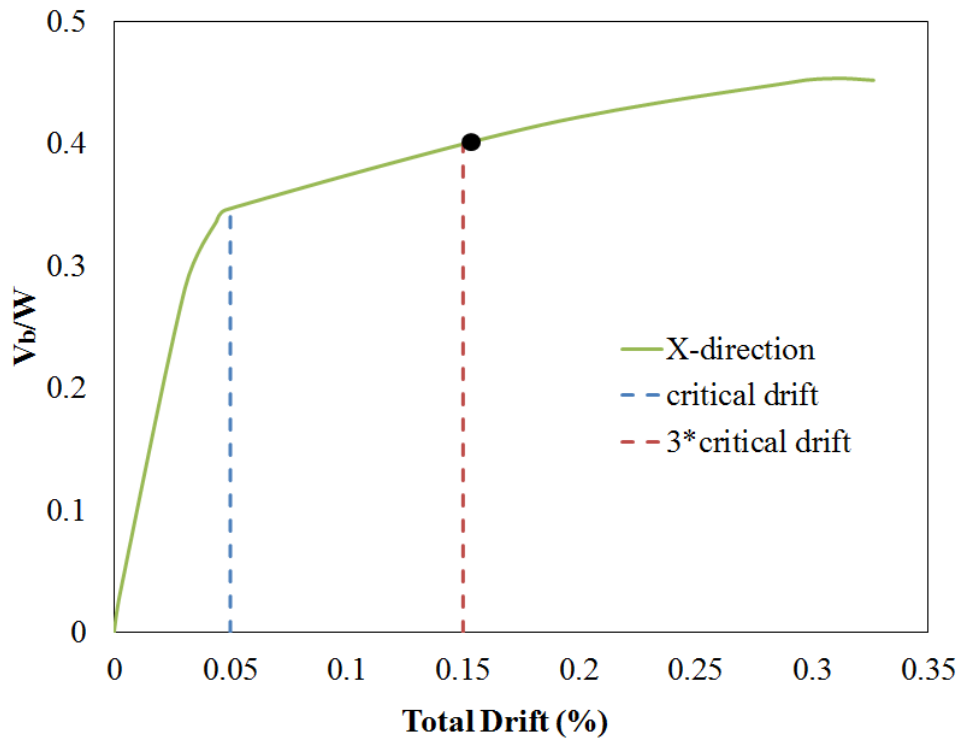
Figure 6.35 Performance Assessment of CSB No: 3 in x-direction
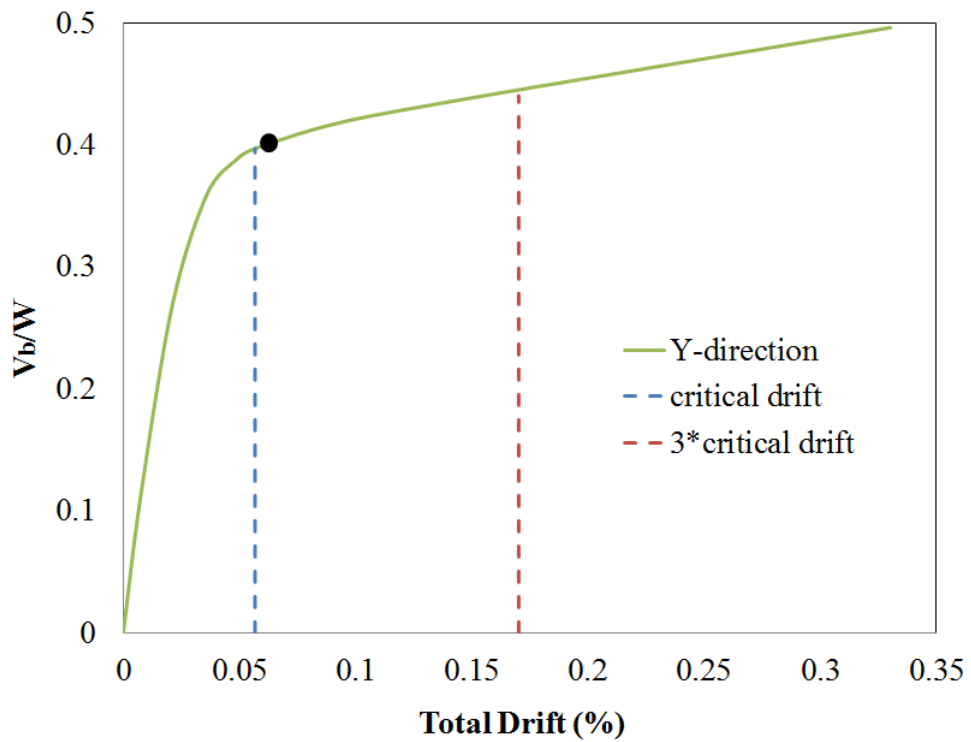
Figure 6.36 Performance Assessment of CSB No: 3 in y-direction

CHAPTER 7

CONCLUSIONS AND RECOMMENDATIONS

The work presented in this thesis is mainly concentrated on the nonlinear modeling and structural assessment of URM buildings through equivalent frame method.

Proposed method encloses an integrated technique in which component response is determined from simple equations which are results of reliable monotonic finite element analyses on a macro model proposed by Aldemir (2010), whereas structural response is determined through nonlinear static or nonlinear dynamic analysis of equivalent frame model of the URM building.

Nonlinearity is adopted into equivalent frames through lumped shear hinges. Input parameters to simulate shear hinge response are geometrical properties, aspect ratio, axial load level and compressive strength of the wall. Effective height of the frames are identified through rigid end offsets whose length is determined according to approach proposed by Dolce (1989).

In the component level, reliability is checked against shear strength equations and ultimate drift limits proposed by FEMA 356. In the structural level verification of the proposed model is made through:

- Nonlinear static analysis of a full scale, two-story URM building tested with a reversed cyclic experiment conducted at the University of Pavia
- Nonlinear dynamic analysis of a ½ scale URM building tested on a shake table at the ISMES Laboratory at Bergamo.
- Nonlinear static and nonlinear dynamic analyses of three existing case study buildings damaged after Dinar earthquake of 1995.

Performance assessment of three existing case study buildings are made and compared with their damages after Dinar earthquake of 1995. Capacities of the case study buildings are established by proposed nonlinear equivalent frame method. Earthquake demand is calculated according to iterative procedure suggested by TEC2007. Performance of the buildings is determined through two different methods. In the first method, hinge performance levels are compared with hinge displacement demands for each wall and building performance is identified through performance of hinges. In the second simple method, which is proposed by Tomazevic (2007), after performance point on the capacity curve is calculated, performance limits associated to a specific level of displacements on the capacity curve is utilized in order to assess performance of the structure for the expected seismic action.

Chapter 3 illustrates elastic response of solid and perforated URM walls to lateral forces. Effect of aspect ratio and boundary conditions on the response of solid walls is investigated in detail. Equations which take shear deformations into account are derived for extreme boundary conditions (i.e. both ends fixed, cantilever) and intermediate cases where coupling of spandrels are idealized with rotational hinges. An equation (Equation 3.25) is proposed for elastic lateral stiffness calculation of coupled walls. Equation requires cross-section properties of connecting members and complies well with upper and lower limits.

In order to simulate elastic lateral response of perforated walls equivalent frame method is employed. Rigid offset lengths of piers and spandrels are calibrated by comparing equivalent frame model results with finite element model results. According to analyses results conducted on various perforated walls, equivalent frame method with Dolce offset approximates finite element solution satisfactory in terms of lateral stiffness, shear force on base piers and axial force on base piers (see Table 7.1).

Table 7.1 Percent Error Between FEM and EFM with Dolce RO

	Story Drift	Axial Force at Base Piers			Shear Force at Base Piers		
1B2S Frame	4.8	0.5		0.2	0.4		0.2
	3.5						
2B2S Frame	30.0	5.4	12.5	12.6	7.9	7.3	7.0
	40.4						
2B3S frame	15.1	34.0	5.2	3.0	10.7	23.4	24.2
	12.3						
	11.8						

Chapter 4 is about presentation and verification of finite element macro model, strength equation (Equation 4.1) and ultimate drift equation (equation 4.2) proposed by Aldemir (2010). Reliability of the proposed equations is tested against simple strength formulas and ultimate drift values specified in FEMA 356. 152 URM walls which belong to three case study buildings are utilized for comparison. There is a good agreement between rocking strength and sliding strength with mean values of 1.01 and 1.25 respectively. Mean value of ultimate drift ratios for rocking and sliding modes is 1.05 and 1.13 respectively.

Reliability of proposed macro model is tested by comparison of two experimental results with model results. Experiments are selected such that shear dominated diagonal tension failure and flexure dominated rocking failure are both observed. Proposed model succeeds in prediction of final crack pattern, distribution of damage, ultimate strength and ultimate drift. Error in prediction of ultimate strength and ultimate drift is 8.3% and 4.5% for shear dominated response and 13% and 15% in flexure dominated response respectively.

Chapter 5 presents application of nonlinearity to equivalent frame method. Validation of the nonlinear equivalent frame model is first performed with a comparison between the calculated analytical results and test results of full scale, two-story URM building tested in University of Pavia. Good prediction of base shear

capacity, failure mechanism and overall deformation of the building is achieved. Base shear capacity and ultimate drift are approximated with errors 13.6% and 3.24% respectively.

Additionally three different distributions of axial loads on piers resulting in different nonlinear properties are assumed and results are compared. It is concluded that in case of low-rise structures with symmetric distribution of piers, determination of nonlinear force-displacement relation of piers under dead load is sufficient. Regeneration of axial load level at each step of the pushover analysis or determination of axial load on piers under dead plus earthquake load does not alter structural response noticeably for low-rise buildings.

Validation of the nonlinear equivalent frame model is further performed with a comparison between the nonlinear time history analyses results and test results of half scale, two-story URM building tested in ISMES Laboratory at Bergamo through shake table. Base shear capacity in x direction is predicted with 20.5% error. Maximum accelerations on first and second story of the test specimen are approximated with a maximum error of 23% for 5 incremental shocks in Y direction. Possible reasons of insufficient performance in X direction with a maximum error of 45.7% are explained in section 5.4.3.2.

Chapter 6 illustrates performance assessment of three existing case study URM buildings exposed to Dinar earthquake of 1995. Calculated performance of the buildings is in good agreement with observed performances (see Table 7.2).

Table 7.2 Observed Damages and Calculated Damages in Weak Direction

	Observed Damage	**Element Displacement Demands**	**Tomazevic (2007)**	**Nonlinear THA**
Case Study Building No: 1	Medium	Medium	Medium	Low to Medium
Case Study Building No: 2	Medium to Heavy	Medium	Medium to Heavy	Medium
Case Study Building No: 3	Medium	Medium	Medium	Medium

The reason why second story performs worse performance than first stoy in CSB2 and CSB3 is increase of openings and decrease of wall thicknesses for the second story.

Limitations of the proposed model are illustrated below:

At material level, simple assumptions are made for brick masonry walls constructed in Turkey. Compressive strength is assumed to be 5 MPa and modulus of elasticity is assumed to be 2000 MPa. Thus, main limitation of the proposed model is assumptions made in material level. On one hand, utilized material properties represent overall characteristics of masonry employed in Turkey. So they can be used for analysis of a couple of buildings in Turkey. On the other hand, analysis of a specific building requires determination of unique material properties such as modulus of elasticity of the analyzed building at which proposed model is incapable.

At component level, plasticity is adopted for piers only. Spandrels remain elastic throughout the analysis. Although depending on the low level of axial loading spandrels are prone to early cracking, it is assumed that ultimate response of the structure is characterized by pier failure. Also, Takeda hysteresis model employed in nonlinear THA is not a good representative of cyclic behavior of masonry which is strongly dependent on the failure mechanism.

At structural level, coupling between shear strength and compressive force on the pier is not taken into account. Although proposed step by step hand calculation compensates this limitation, application is time consuming unless it is imposed into computer software. Moreover rigid diaphragm is required to be assigned at floor levels. URM buildings without concrete slabs could not be analyzed.

For future research, displacement controlled experimental analyses on URM walls and frames representing Turkish construction practice might be conducted in order to calibrate nonlinear force-displacement parameters of utilized shear hinges and support reliability of the model with experiments.

REFERENCES

Abrams, D.P., (2001), "Performance-Based Engineering Concepts for Unreinforced Masonry Building Structures," Progress in Structural Engineering and Materials, vol.3, pp.48-56.

Akan, A.E., (2008), "A Comparative Study on Earthquake Resistance of Reinforced Concrete and Masonry Residential Buildings in Small-Scale Cities of Turkey," PhD Dissertation, Department of Architecture, Middle East Technical University, Turkey.

Akkar, S., Aldemir, A., Askan, A., Bakır, S., Canbay, E., Demirel, İ.O., Erberik, M.A., Gülerce, Z., Gülkan, P., Kalkan, E., Prakash, S., Sandıkkaya, M.A., Sevilgen, V., Ugurhan, B., Yenier, E., (2010), "8 March 2010 Elazıg-Kovancılar (Turkey) Earthquake: Observations on Ground Motions and Building Damage," Seismological Research Letters (accepted, in publication).

Alcocer, S.M., Arias, J.G., Flores, L.E., (2004), "Some Developments on Performance-Based Seismic Design of Masonry Structures, Performance-Based Seismic Design Concepts and Implementation," Proceeding of an International Workshop, 233-244.

Aldemir, A., (2010), "A Simple Seismic Performance Assessment Technique for Unreinforced Masonry Structures," MS Dissertation, Middle East Technical University, Turkey.

Anderson, D., Brzev, S., (2009), "Seismic Design Guide for Masonry Buildings," Canadian Concrete Masonry Producers Association.

ANSYS Inc. (2007), "Element Reference for ANSYS 11", SAS IP Inc.

ANSYS Inc. (2007), "Structural Analysis Guide for ANSYS 11", SAS IP Inc.

ANSYS Inc. (2007), "Theory Reference for ANSYS 11", SAS IP Inc.

Balkaya, C., (1996), "Repair and Strengthening Project of Non-Engineered Buildings After 1 October 1995 Earthquake of Dinar," Adliye District, no.7, Earthquake Engineering Research Center, METU. (in Turkish)

Belmouden, Y., Lestuzzi, P., (2007), "An Equivalent Frame Model for Seismic Analysis of Masonry and Reinforced Concrete Buildings," Construction and Building Materials, vol.23, No.1, pp. 40-53.

Benedetti D. and Pezzoli P., (1996), "Shaking table tests on masonry buildings. Results and comments, ISMES" Politecnico di Milano, Report.

Binici B., Ozcebe, G. and Ozcelik R., (2007), "Analysis and Design of FRP Composites for Seismic Retrofit of Infill Walls in Reinforced Concrete Frames Composites" Part B: Engineering, vol.38, pp. 575-583.

Bosiljkov, V., Page, A.W., Bokan-Bosiljkov, V., Zarnic,R., (2008), "Evaluation of the Seismic Performance of Brick Masonry Walls",Structural Control and Health Monitoring, vol. 17, no.1, 100-118.

Bosiljkov, Vlatko Z., Totoev, Yuri Z., Nichols, John M., (2005), "Shear modulus and stiffness of brickwork masonry: an experimental perspective." Structural Engineering and Mechanics Vol. 20, Issue 1, pp. 21-43.

Calvi, G.M., Kingsley, G.R., (1995), "Problems and certainties in the experimental simulation of the seismic response of MDOF structures," Engineering Structures, vol.18,No.5,pp. 213-220.

Calvi, G. M., Kingsley, G. R., and Magenes, G., (1996) "Testing of Masonry Structures for Seismic Assessment", Earthquake Spectra, Vol. 12, No. 1.

Calvi, G.M., (1999), "A Displacement-Based Approach for Vulnerability Evaluation of Classes of Buildings," Journal of Earthquake Engineering, vol. 3, 411-438.

Chopra, A.K., (2007), "Dynamics of Structures-Theory and Applications to Earthquake Engineering: Third Edition," Pearson Prentice Hall Press, pp.203-239.
Costa, A., (2007), "A Experimental Testing of Lateral Capacity of Masonry Piers. An Application to Seismic Assessment of AAC Masonry Buildings", Ms Dissertation, Rose School, Italy.

Dolce M., (1989), "Models for in-plane loading of masonry walls," Corso sul consolidamento degli edifici in muratura in zona sismica, Ordine degli Ingegneri, Potenza. (in Italian).

Elgawady, M.A., Lestuzzi, P., Badoux, M., (2006), "Analytical Model for In-plane Shear Behaviour of URM Walls Retrofitted with FRP," Composites Science and Technology, vol.66, pp. 459-474.

Erbay, O.O., (2007), "A Methodology to Assess Seismic Risk for Populations of Unreinforced Masonry Buildings," Mid-America Earthquake Center Report 07-10.

Erdik, M. and Aydinoglu N., (2002), "Earthquake Performance and Vulnerability of Buildings in Turkey, Report prepared for World Bank Disaster Management Faculty," Washington DC.

FEMA 306, (1999), "Evaluation of Earthquake Damaged Concrete and Masonry Wall Buildings-Basic Procedures Manual," Federal Emergency Management Agency, Washington, D.C..

FEMA 307, (1999), "Evaluation of Earthquake Damaged Concrete and Masonry Wall Buildings-Technical Resources," Federal Emergency Management Agency, Washington, D.C..

FEMA-356, (2000), "Prestandard and Commentary for the Seismic Rehabilitation of Buildings," Federal Emergency Management Agency, Washington, D.C.

Franklin, S., J. Lynch, and D. P. Abrams, (2001), "Performance of Rehabilitated URM Shear Walls: Flexural Behavior of Piers," ST-6 Project Final Report, Mid-America Earthquake Center Publications, University of Illinois at Urbana-Champaign, Urbana, IL.

Ganz, H. R. and Thurlimann, B. (1982). Versuche Uber Die Festigkeit Von Zweiachsig Beanspruchtem Mauerwerk. Bericht Nr. 7502-3, Institut Fur Baustatik Und Konstruktion Eth, Zurich, Switzerland (In German).

Garcia, R.J. and Alcocer, S.M., (1998), "Experimental performance of confined masonry structures retrofitted with welded wire mesh, Revista de Ingenieria Sismica, nmo. 59, pp.59-79.

Gilmore., A.T., Cuevas, O.Z., Garcia, J.R., (2009), "Displacement-Based Seismic Assessment of Low-Height Confined Masonry Buildings," Earthquake Spectra, vol.25, no.2, pp.439-464.

Gürel, M.A., Kısa, M., Çılı, F., (2005), "Lateral Stiffness of Unreinforced Masonry Circular Columns under Cracked Conditions."

Javed, M., (2009), "Seismic Risk Assessment of Unreinforced Brick Masonry Buildings System of Northern Pakistan," PhD Dissertation, N.W.F.P. University of Engineering and Technology, Pakistan.

Kappos, A.J., Penelis, G.G., Drakopoulos, C.G., (2002), "Evaluation of Simplified Models for Lateral Load Analysis of Unreinforced Masonry Buildings," Journal of Structural Engineering, vol.128, pp.890-897.

Lourenco P.J.B.B., (1996), "Computational Strategies for Masonry Structures", PhD Dissertation, Delft University of Technology, Holland.

Magenes, G., Calvi, G.M., (1997), "In-plane seismic response of brick masonry walls," Earthquake Engineering & Structural Dynamics, vol. 26, 1091-1112.

Magenes, G., Calvi, G.M., Kingsley, G.R., (1995), "Seismic Testing of a Full-Scale, Two-Story Masonry Building: Test Procedure and Measured Experimental Response," Experimental and Numerical Investigation on a Brick Masonry Building Prototype, Report 3.0, University of Pavia

Magenes, G., Fontana, A.D., (1998), "Simplified Non-linear Seismic Analysis of Masonry Buildings," Proceeding of British Masonry Society, No.8, pp. 190-195.

Magenes, G., Kingsley, G. R., and Calvi, G. M. (1995). "Seismic testing of a full-scale, two-story masonry building: Test procedure and measured experimental response." Experimental and Numerical Investigation on a Brick Masonry Building Prototype Rep. No. 3.0, Gruppo Nazionale La Difesa Dai Terremoti, Univ. of Pavia, Pavia, Italy.

Moon, F.L., (2004), "Seismic Strengthening of Low-Rise Unreinforced Masonry Structures with Flexible Diaphragms," PhD Dissertation, Georgia Institute of Technology, USA.

Newmark, N.M., Hall, W.J., (1982), "Earthquake Spectra and Design," Earthquake Engineering Research Institute, Berkeley, California.

Oliveira, Daniel Vitorino de Castro, (2003), "Experimental and Numerical Analysis of Blocky Masonry Structures under Cyclic Loading," PhD Dissertation, University of Minho, Portugal.

Orduna, A., (2003), "Seismic Assessment of Ancient Masonry Structures by Rigid Blocks Limit Analysis," PhD Dissertation, University of Minho, Portugal.

Özcebe, G., (1996), "Repair and Strengthening Project of Non-Engineered Buildings After 1 October 1995 Earthquake of Dinar," Konak District, no.5, Earthquake Engineering Research Center, METU. (in Turkish)

Özcebe, G., (1996), "Repair and Strengthening Project of Non-Engineered Buildings After 1 October 1995 Earthquake of Dinar," Konak District, no.39, Earthquake Engineering Research Center, METU. (in Turkish)

Pasticier, L., Amadio, C., Fragiacomo, M., (2007), "Non-linear Seismic Analysis and Vulnerability Evaluation of a Masonry Building by Means of the SAP2000 V.10 Code," Earthquake Engineering and Structural Dynamics, no.37, pp. 467-485.

Paulson, T.J., Abrams, D.P., (1990), "Correlation Between Static and Dynamic Response of Model Masonry Structures," Earthquake Spectra, vol. 6, No. 3.

Penelis, G.G., (2006), "An Efficient Approach for Pushover Analysis of URM Structures," Journal of Earthquake Engineering. Vol.10, no.3, pp. 359-379.

Ruiz-García, J., and Alcocer, S. M., (1998). Experimental performance of confined masonry structures retrofitted with welded wire mesh (in Spanish), Revista de Ingeniería Sísmica 59, 59–79

Roca, P., Molins, C., Mari, A.R., (2005), "Strength Capacity of Masonry Wall Structures by the Equivalent Frame Method," Journal of Structural Engineering, vol.131, pp. 1601-1610

Salonikios, T., Karakostas, C., Lekidis, V., Anthoine, A., (2003), "Comparative Inelastic Pushover Analysis of Masonry Frames," Engineering Structures, no.25, pp.1515-1523.

SAP Reference Manual, (2009), Computers and Structures, University of Ave. Berkeley

Sap2000 v14.1.0, (2009), Structural Analysis Program, Computers and Structures, University of Ave. Berkeley

Sinha, B.P., Maurenbrecher H.P., Hendry, A.W., (1971), "Model and Full-scale Tests on a Five-story Cross-wall Structure under Lateral Loading," Proceedings of 2nd International Brick Masonry Conference, Stoke-on-Trent, U.K.

Takeda, T., Sozen, M.A., Nielsen, N.N., (1970), "Reinforced Concrete Response to Simulated Earthquakes, " Journal of the Structural Engineering Division, Asce, Vol 96, No. 12, pp.2257-2573.

Tomazevic, M., Lutman, M., Petkovic, L., (1996), "Seismic Behavior of Masonry Walls: Experimental Simulation," Journal of Structural Engineering, no.122, pp.1040-1047.

Tomazevic, M., (2007), "Damage as a Measure for Earthquake Resistant Design of Masonry Structures: Slovenian Experience," Canadian Journal of Civil Engineering, vol.34, pp. 1403-1412.

Tomazevic, M., Bosiljkov, V., Weiss, P., (2004), "Structural Behavior Factor for Masonry Structures," 13th World Conference on Earthquake Engineering, Vancouver, B.C., Canada.

TS 498, (1997), "Design Loads for Buildings", Turkish Standards Institute.

TS ISO 9194, (1997), "Bases for Design of Structures; Actions due to Self-Weight of Structures, Non-structural Elements and Stored Materials; Density", Turkish Standards Institute.

Turkish Earthquake Code, (2007), "Specifications for Design of Buildings in Seismic Regions", Ministry of Public Works, Ankara.

Turkish Earthquake Code, (1997), "Specifications for Design of Buildings in Seismic Regions," Ministry of Public Works, Ankara.

Turnsek, V. and Cacovic, F., (1971). "Some experimental results on the strength of brick masonry walls", Proceedings, 2nd International Brick Masonry Conference, Stoke-on-Trent, 149-156

Vasconcelos, G.F.M., (2005), "Experimental Investigations on the Mechanics of Stone Masonry," PhD Dissertation, University of Minho, Portugal.

Vyas, C.V.U., Reddy, B.V.V., (2009), "Prediction of Solid Block Masonry Prism Compressive Strength using Finite Element Model," Materials and Structures, vol.43, no.5, pp.719-735.

Yi, T., Moon, F.L., Leon, R.T., Kahn, L.F., (2006), "Lateral Load Testing on a Two-Story Unreinforced Masonry Building, Journal of Structural Engineering, ASCE, vol. 132, no.5, 643-652.

Yi, T., Moon, F., Leon, R., Kahn, L., (2003), "Structural Analysis of a Prototype Unreinforced Masonry Low-rise Building," Proceedings of the 9th North American Masonry Conference, Clemson, SC.

Yi, T., (2004), Experimental investigation and numerical simulation of an unreinforced masonry structure with flexible diaphragms. PhD dissertation, Georgia Institute of Technology, USA

ELEMENT STIFFNESS MATRICES WITH SHEARING DEFORMATIONS

Frame Element Stiffness Matrix with Shearing Deformations Considered

$$
\begin{bmatrix}
\dfrac{AE}{h} & 0 & 0 & -\dfrac{AE}{h} & 0 & 0 \\[2mm]
0 & \dfrac{12EI}{h^3(1+\varPsi)} & \dfrac{6EI}{h^2(1+\varPsi)} & 0 & -\dfrac{12EI}{h^3(1+\varPsi)} & \dfrac{6EI}{h^2(1+\varPsi)} \\[2mm]
0 & \dfrac{6EI}{h^2(1+\varPsi)} & \dfrac{EI(4+\varPsi)}{h(1+\varPsi)} & 0 & -\dfrac{6EI}{h^2(1+\varPsi)} & \dfrac{EI(2-\varPsi)}{h(1+\varPsi)} \\[2mm]
-\dfrac{AE}{h} & 0 & 0 & \dfrac{AE}{h} & 0 & 0 \\[2mm]
0 & -\dfrac{12EI}{h^3(1+\varPsi)} & -\dfrac{6EI}{h^2(1+\varPsi)} & 0 & \dfrac{12EI}{h^3(1+\varPsi)} & -\dfrac{6EI}{h^2(1+\varPsi)} \\[2mm]
0 & \dfrac{6EI}{h^2(1+\varPsi)} & \dfrac{EI(2-\varPsi)}{h(1+\varPsi)} & 0 & -\dfrac{6EI}{h^2(1+\varPsi)} & \dfrac{EI(4+\varPsi)}{h(1+\varPsi)}
\end{bmatrix}
$$
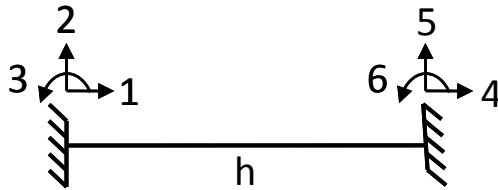
$$\varPsi = \dfrac{12EI}{A_s G h^2}$$

Condensed Frame Element Stiffness Matrix with Shearing Deformations Considered

$$
\begin{bmatrix}
\dfrac{AE}{h} & 0 & 0 & -\dfrac{AE}{h} & 0 \\[2mm]
0 & \dfrac{12EI}{h^3(4+\varPsi)} & \dfrac{12EI}{h^2(4+\varPsi)} & 0 & -\dfrac{12EI}{h^3(4+\varPsi)} \\[2mm]
0 & \dfrac{12EI}{h^2(4+\varPsi)} & \dfrac{12EI}{h(4+\varPsi)} & 0 & -\dfrac{12EI}{h^2(4+\varPsi)} \\[2mm]
-\dfrac{AE}{h} & 0 & 0 & \dfrac{AE}{h} & 0 \\[2mm]
0 & -\dfrac{12EI}{h^3(4+\varPsi)} & -\dfrac{12EI}{h^2(4+\varPsi)} & 0 & \dfrac{12EI}{h^3(4+\varPsi)}
\end{bmatrix}
$$
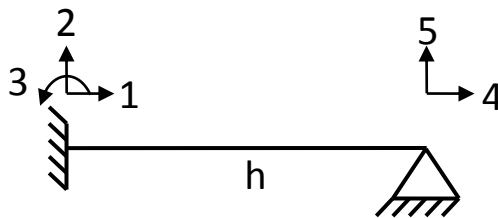
$$\varPsi = \dfrac{12EI}{A_s G h^2}$$

**COMPARISON OF ISMES SHAKE TABLE TEST RESULTS with
NONLINEAR THA ANALYSES**

Figure B.1 Y-direction 1st Story Accelerations of ISMES Specimen under Shock P7 (PGA=0.064g)
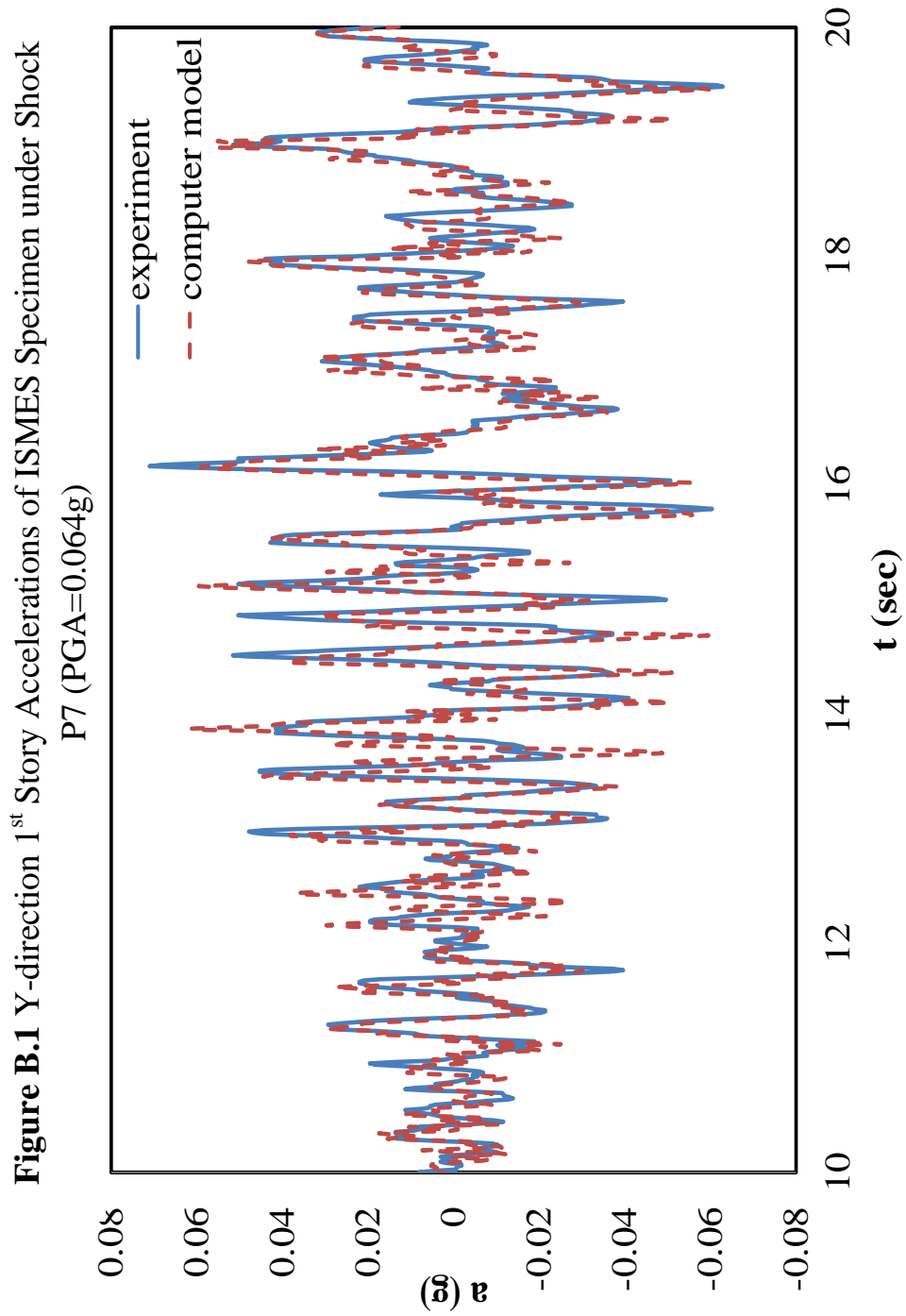
Figure B.2 Y-direction 1st Story Accelerations of ISMES Specimen under Shock P8 (PGA=0.098g)
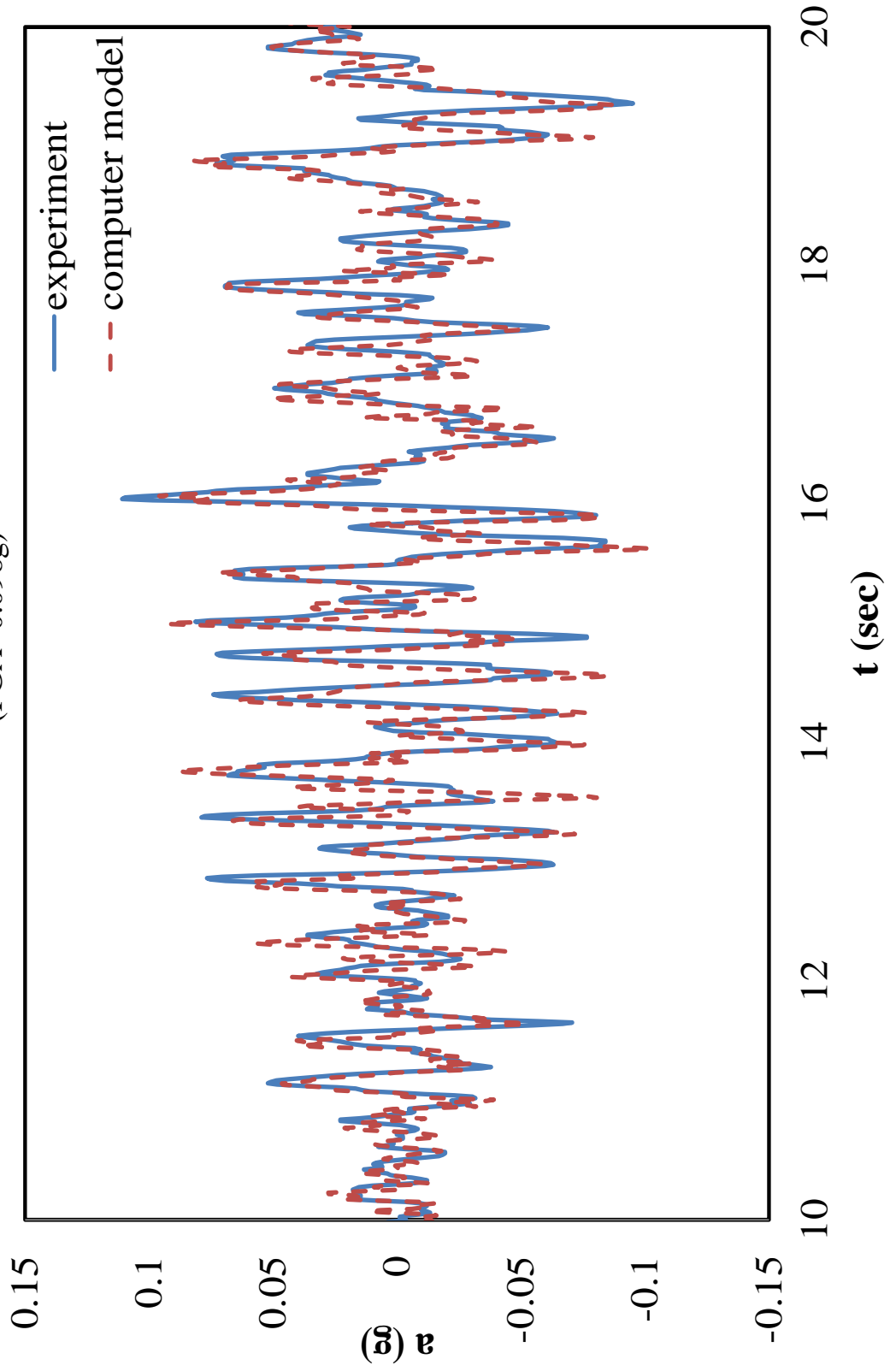
Figure B.3 Y-direction 1st Story Accelerations of ISMES Specimen under Shock P9 (PGA=0.155g)
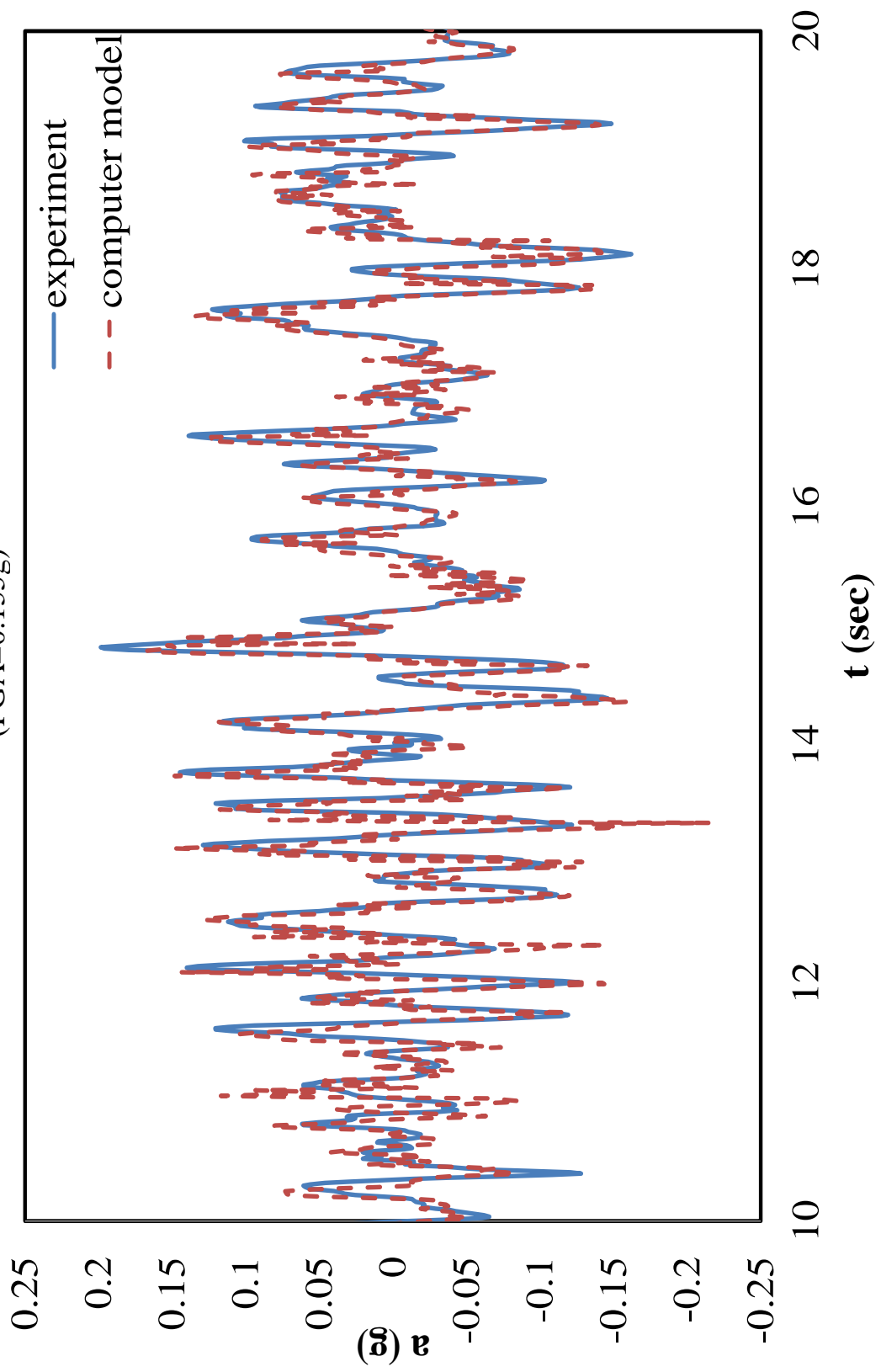
Figure B.4 Y-direction 1st Story Accelerations of ISMES Specimen under Shock P10 (PGA=0.217g)
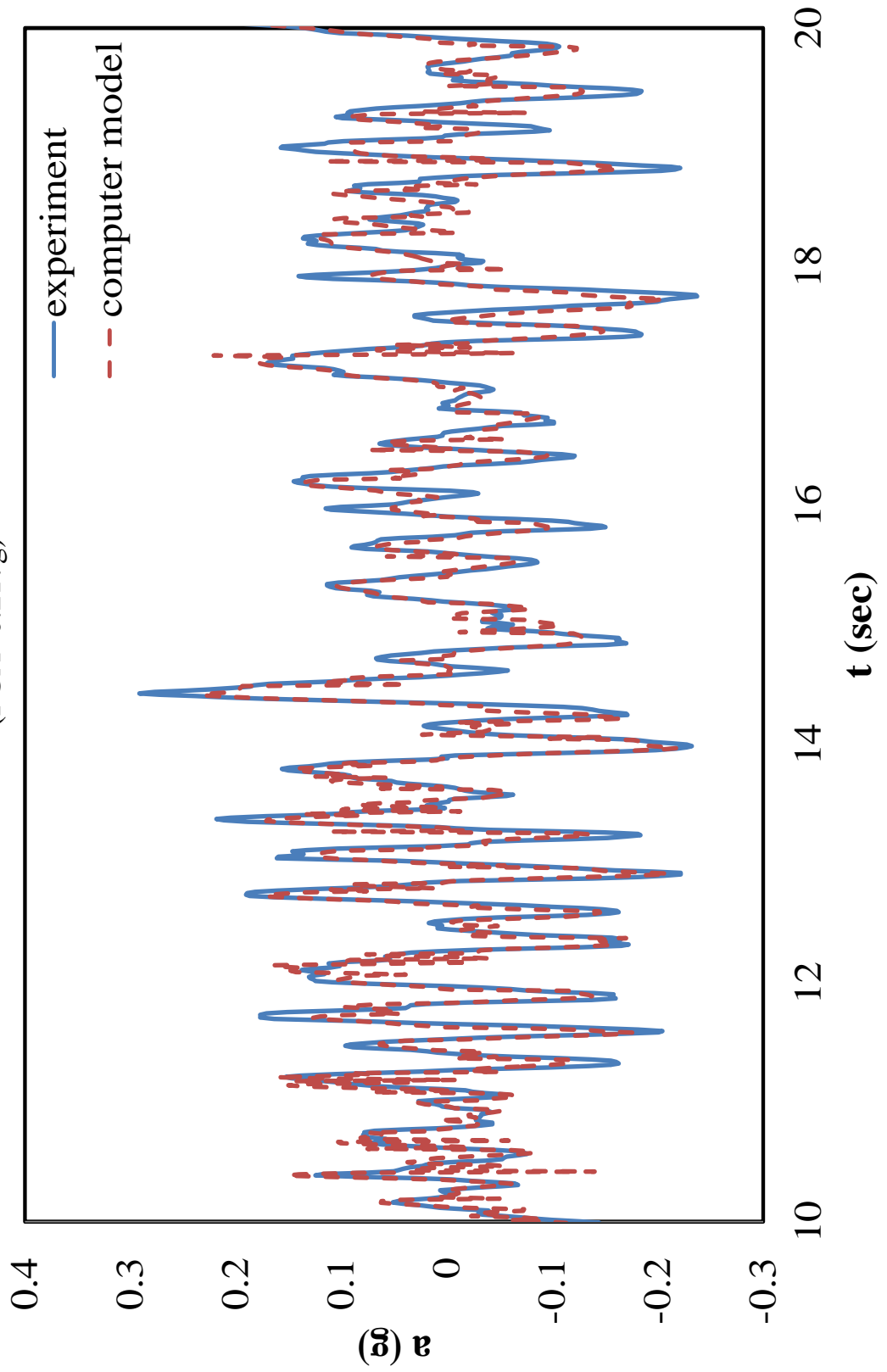
Figure B.5 Y-direction 1ˢᵗ Story Accelerations of ISMES Specimen under Shock P11 (PGA=0.275g)

177
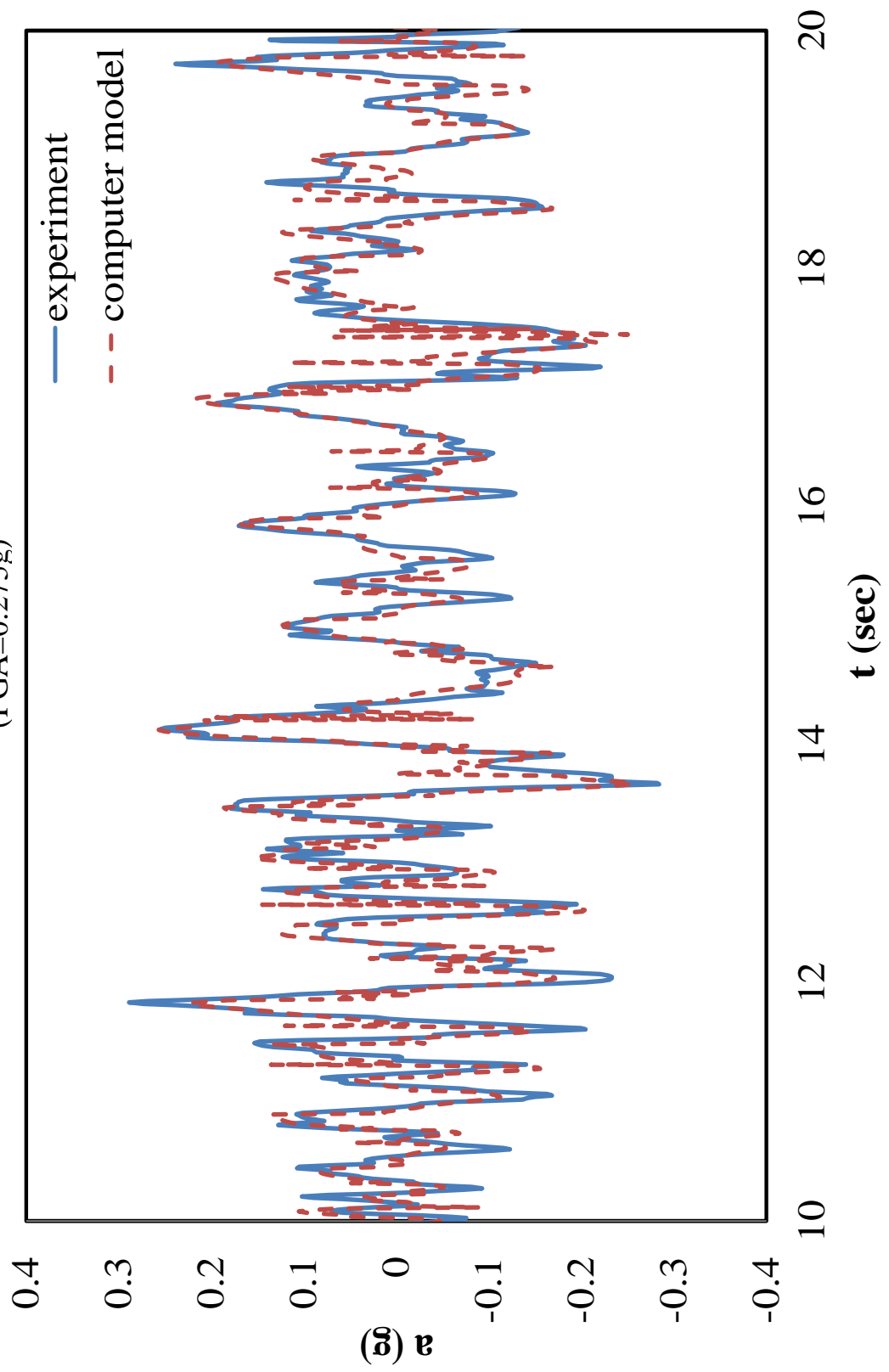
Figure B.6 Y-direction 2nd Story Accelerations of ISMES Specimen under Shock P7 (PGA=0.064g)
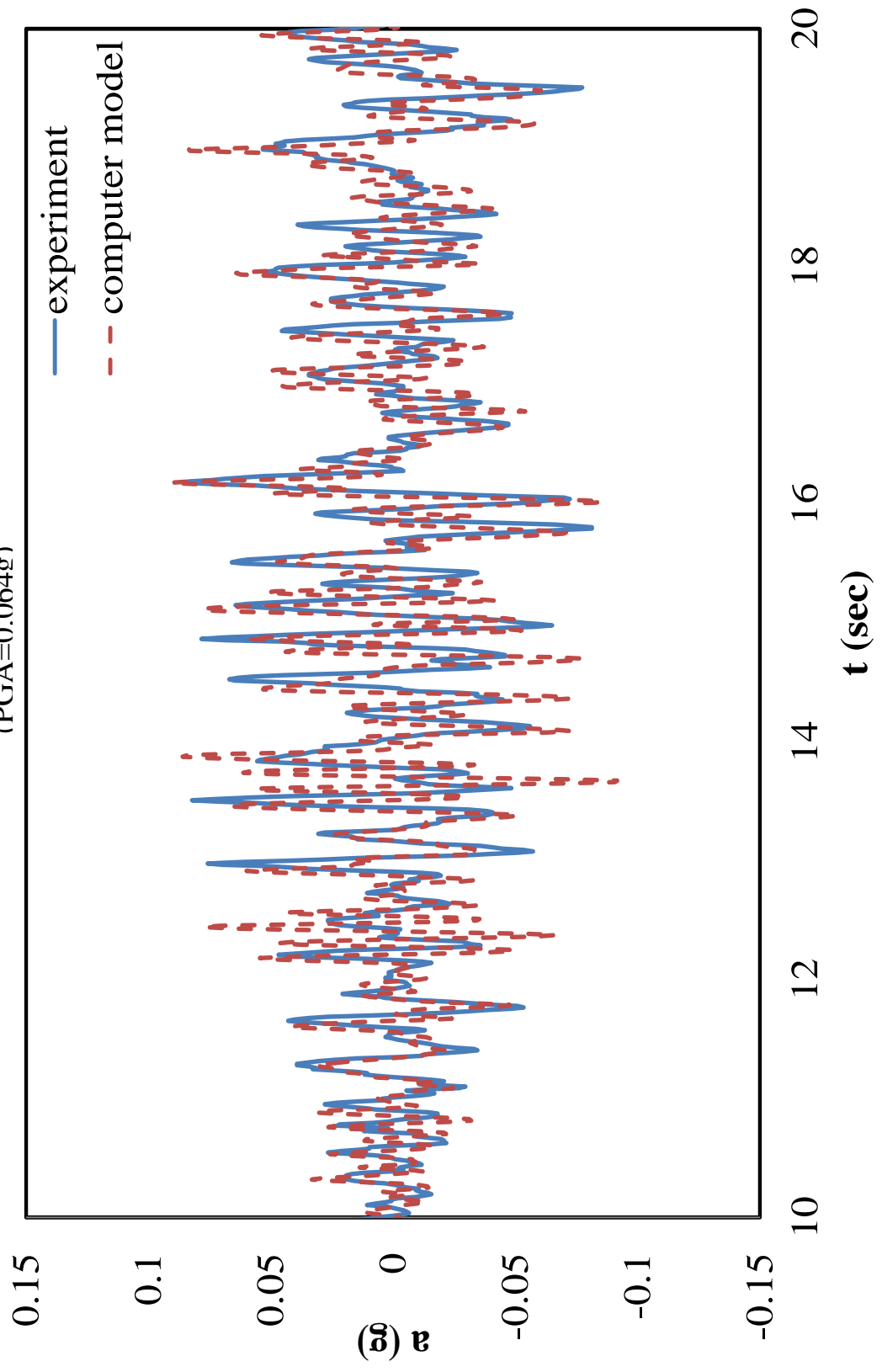
Figure B.7 Y-direction 2nd Story Accelerations of ISMES Specimen under Shock P8 (PGA=0.098g)
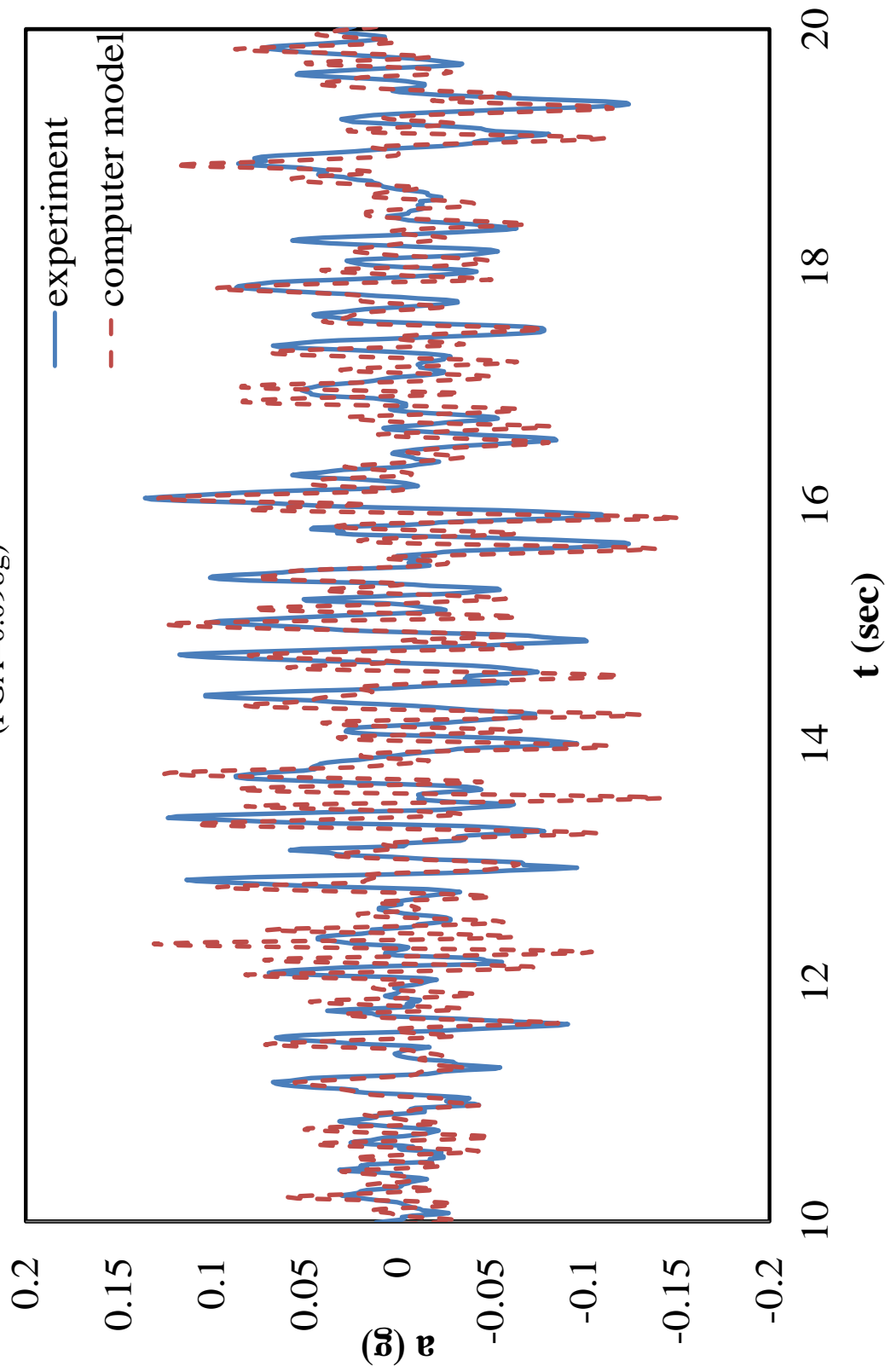
Figure B.8 Y-direction 2nd Story Accelerations of ISMES Specimen under Shock P9 (PGA=0.155g)
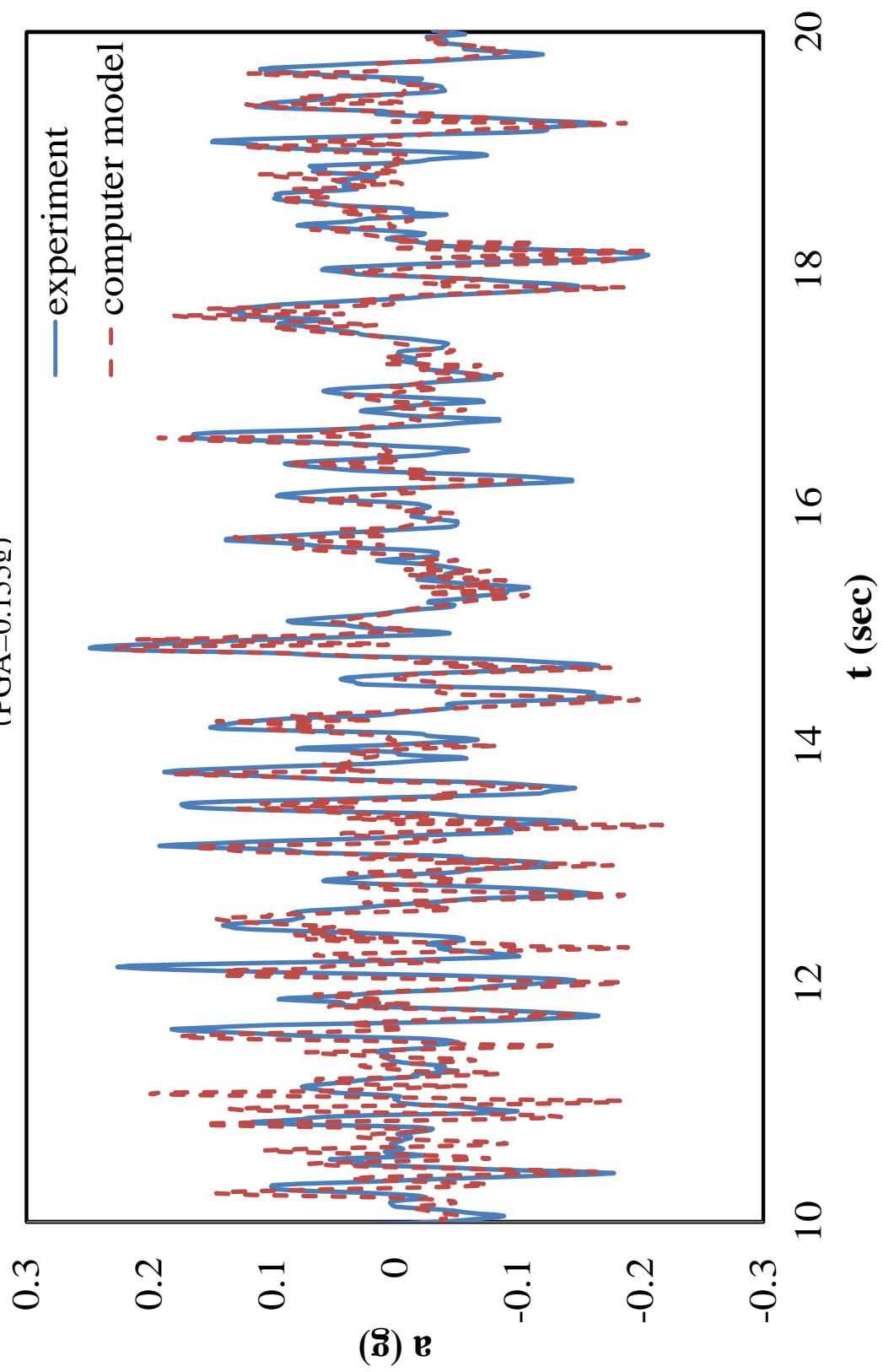
Figure B.9 Y-direction 2nd Story Accelerations of ISMES Specimen under Shock P10 (PGA=0.217g)
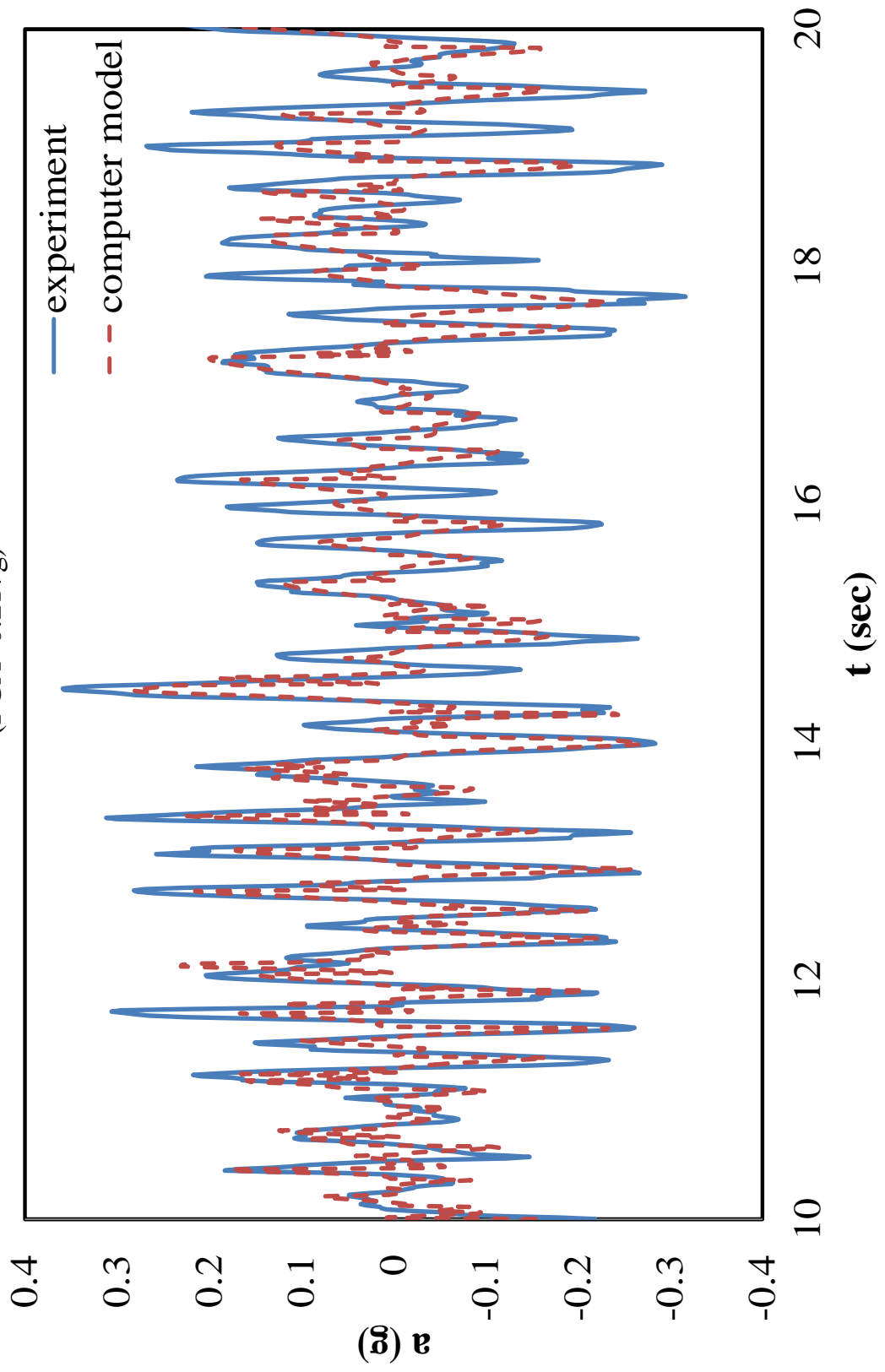
Figure B.10 Y-direction 2nd Story Accelerations of ISMES Specimen under Shock P11 (PGA=0.275g)
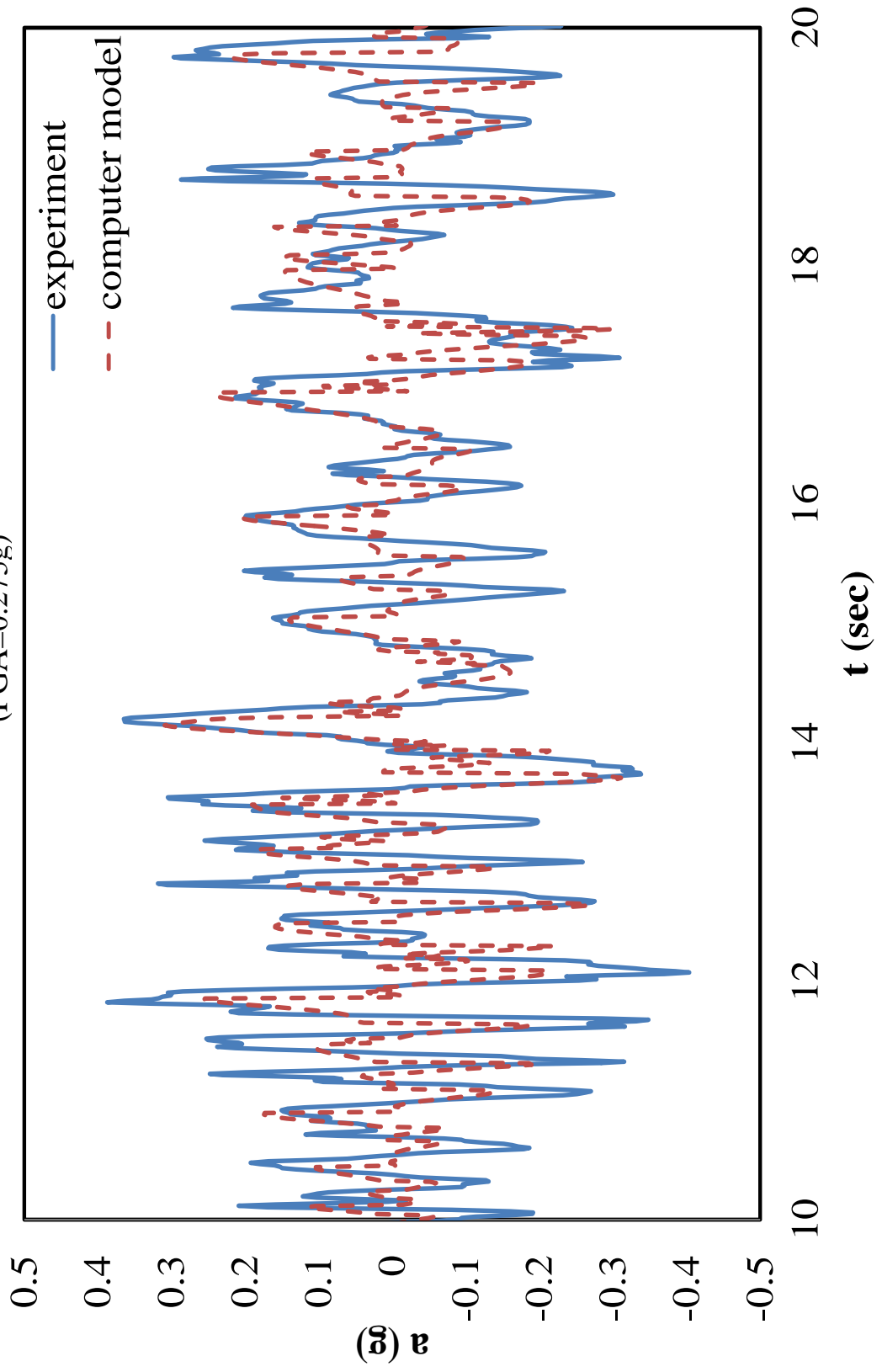
Figure B.11 X-direction 1st Story Accelerations of ISMES Specimen under Shock P7 (PGA=0.055g)
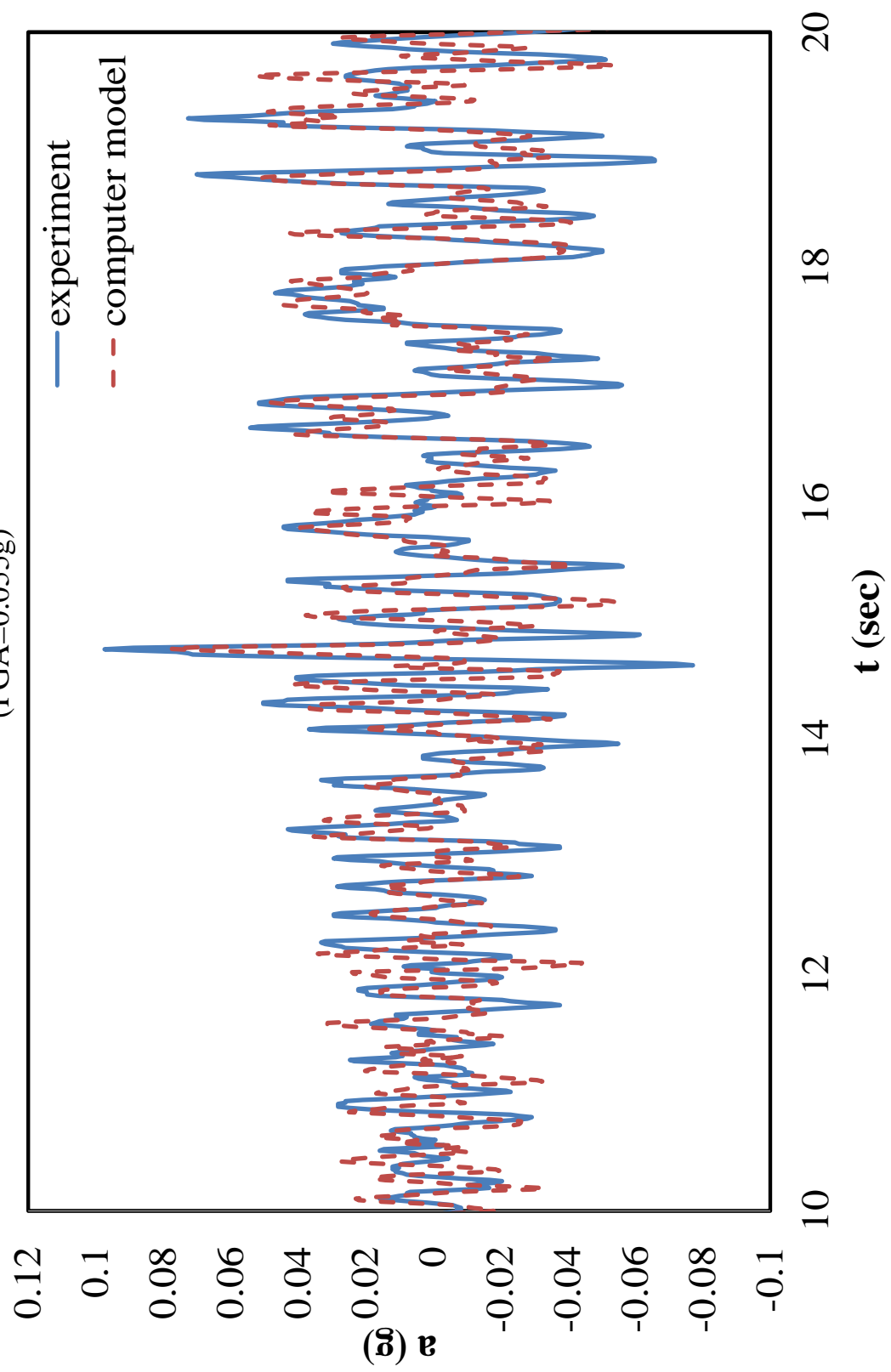
Figure B.12 X-direction 1st Story Accelerations of ISMES Specimen under Shock P8
(PGA=0.098g)
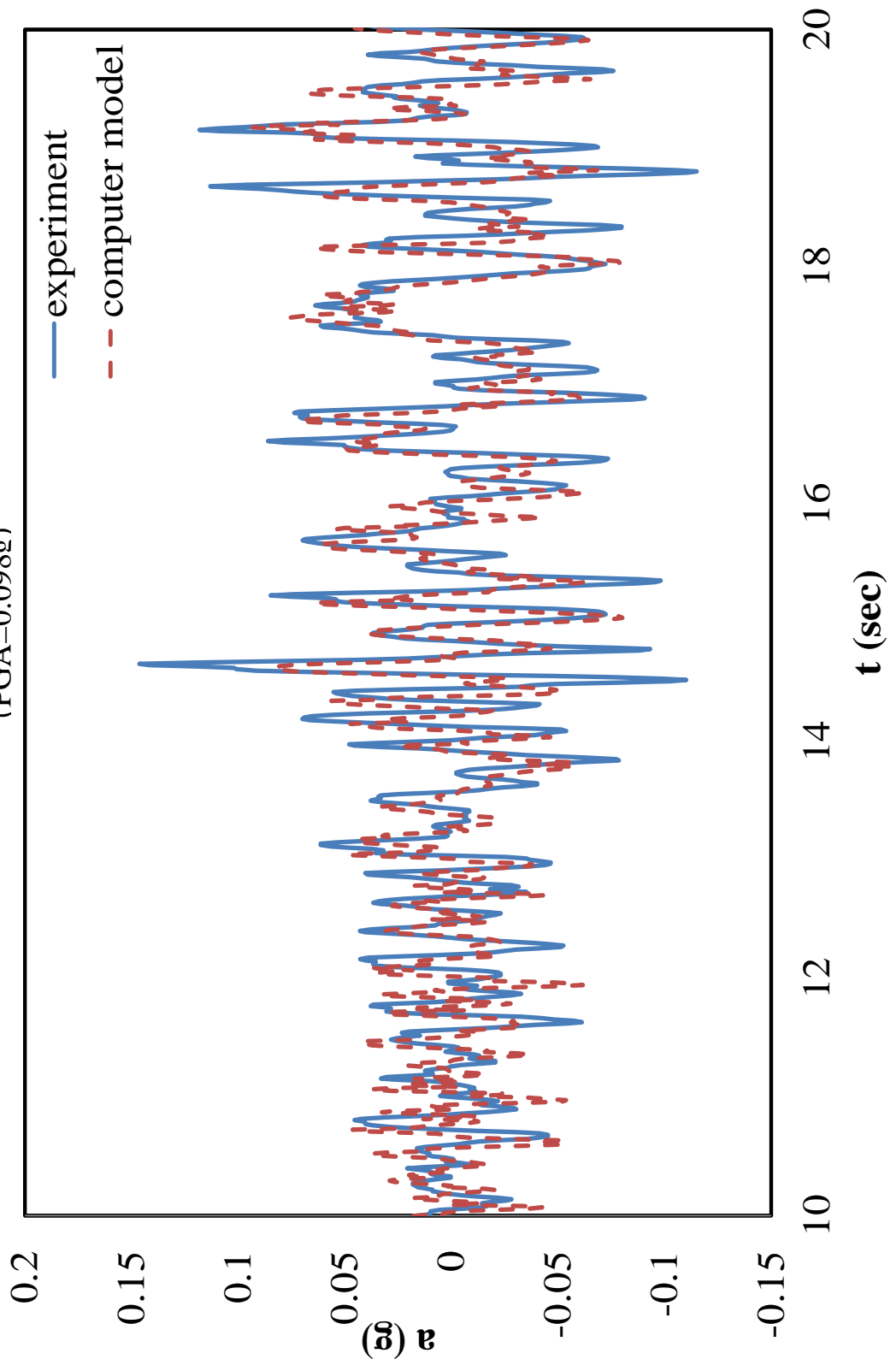
Figure B.13 X-direction 1st Story Accelerations of ISMES Specimen under Shock P9 (PGA=0.179g)
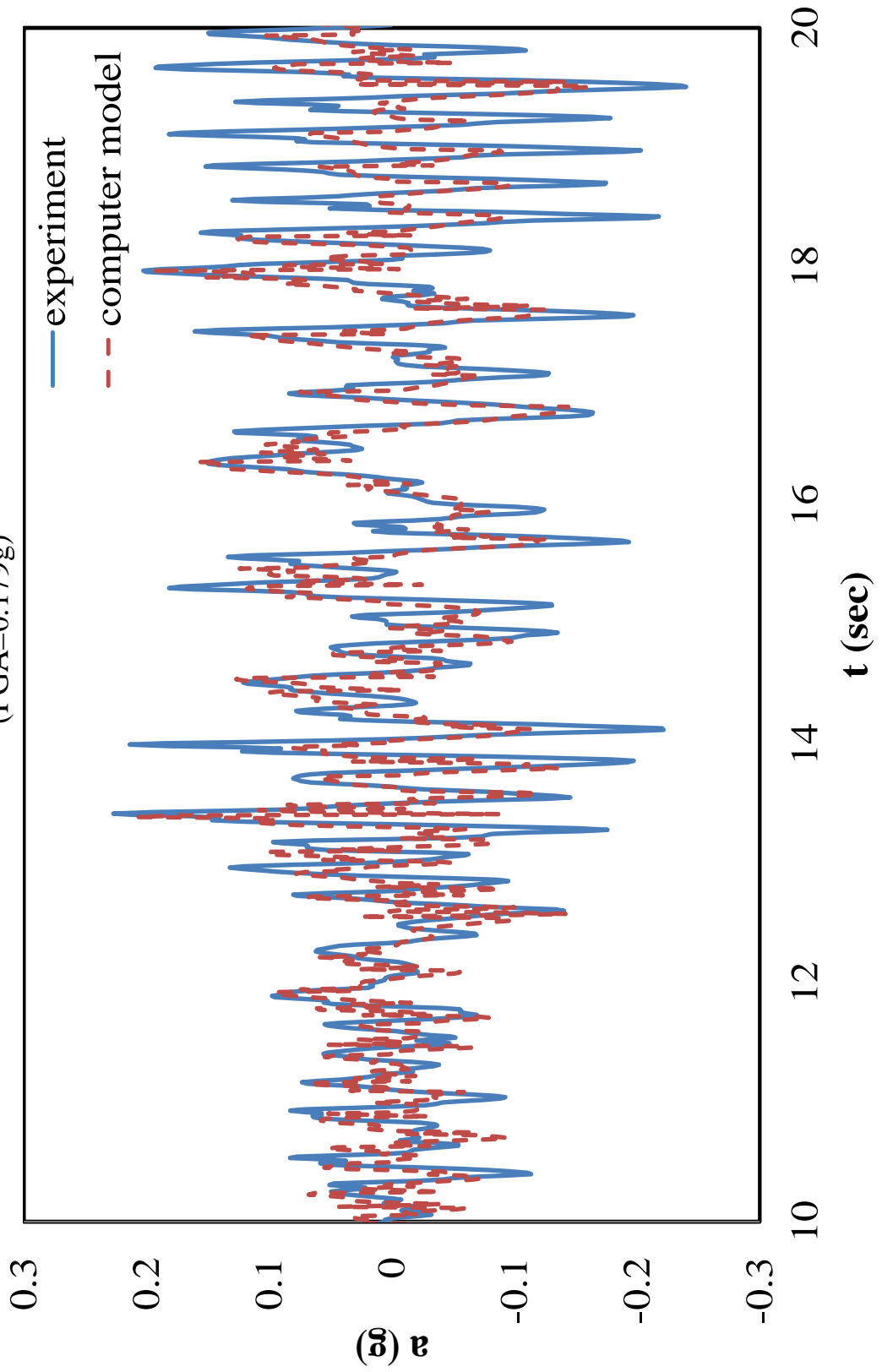
Figure B.14 X-direction 1st Story Accelerations of ISMES Specimen under Shock P10 (PGA=0.250g)
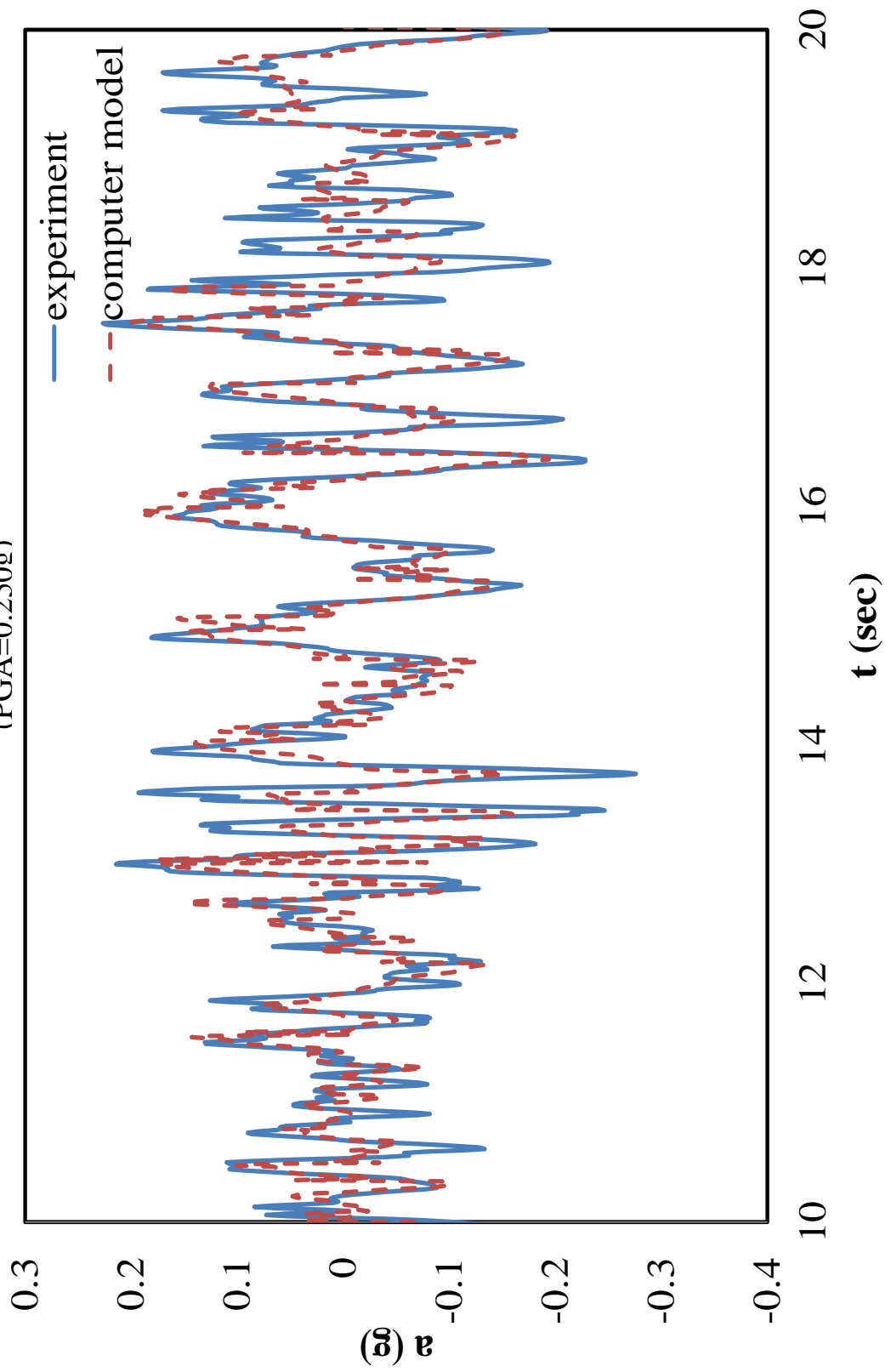
Figure B.15 X-direction 1st Story Accelerations of ISMES Specimen under Shock P11 (PGA=0.326g)
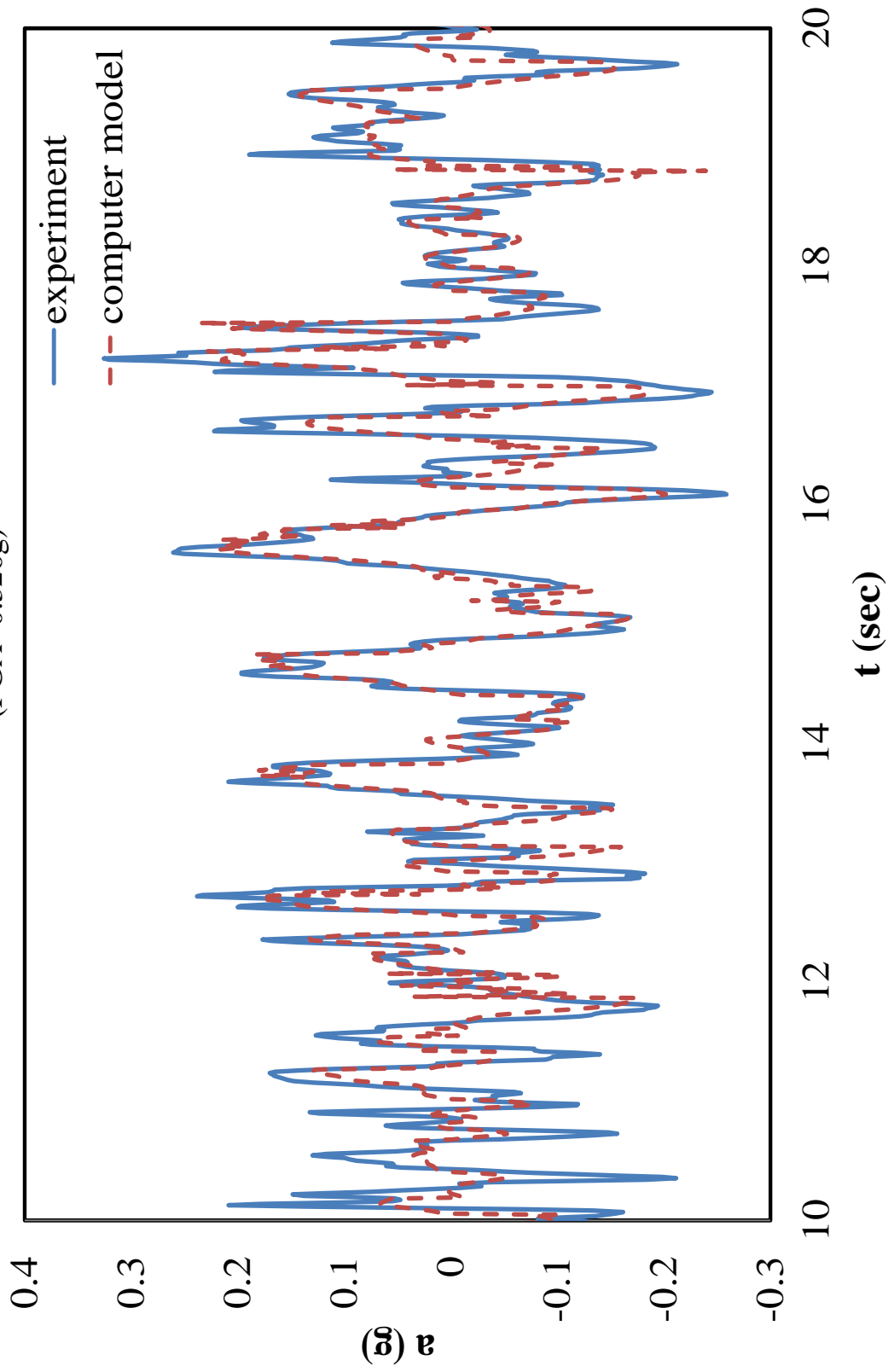
Figure B.16 X-direction 2nd Story Accelerations of ISMES Specimen under Shock P8 (PGA=0.055g)
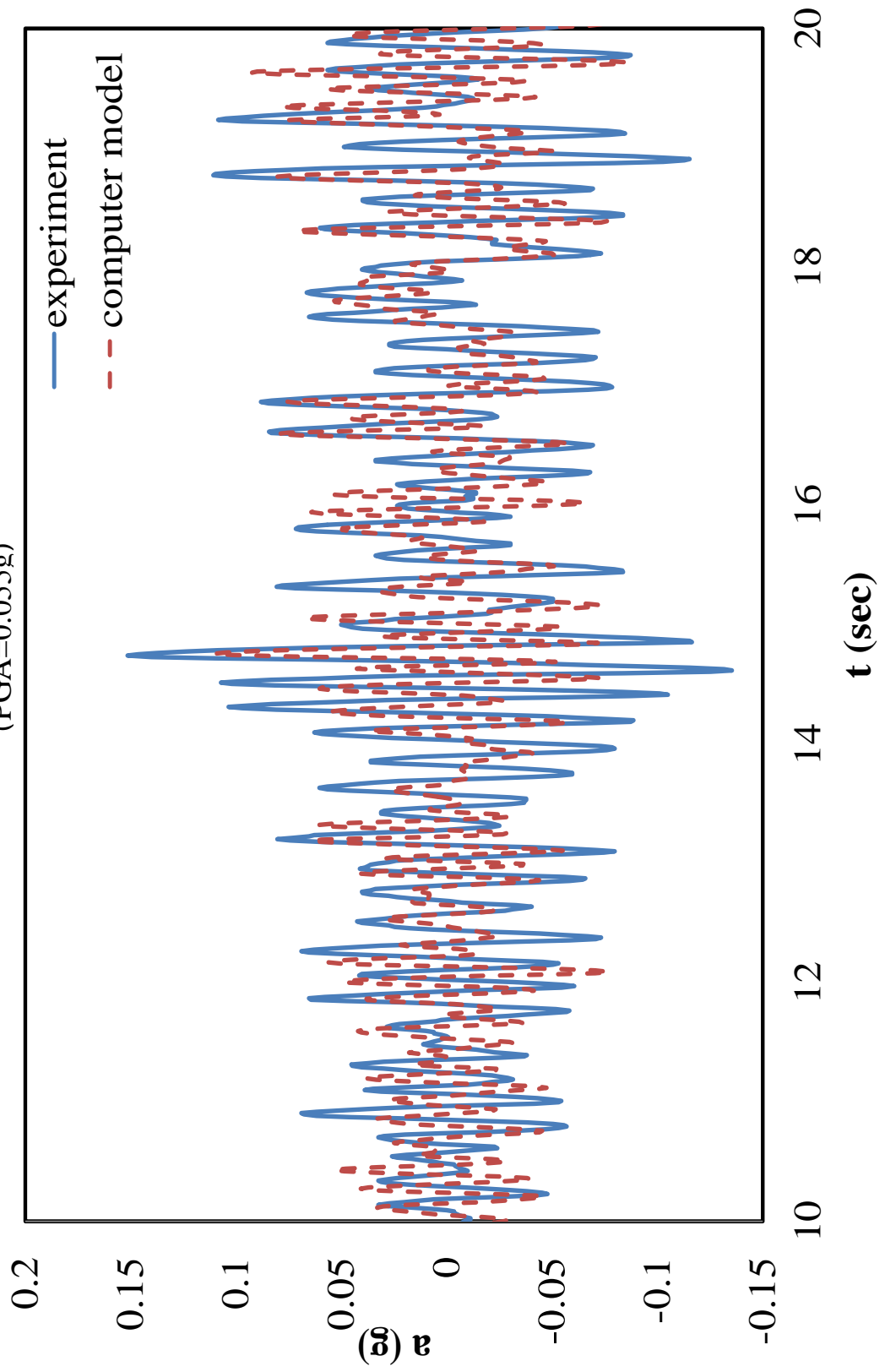
Figure B.17 X-direction 2nd Story Accelerations of ISMES Specimen under Shock P8 (PGA=0.098g)
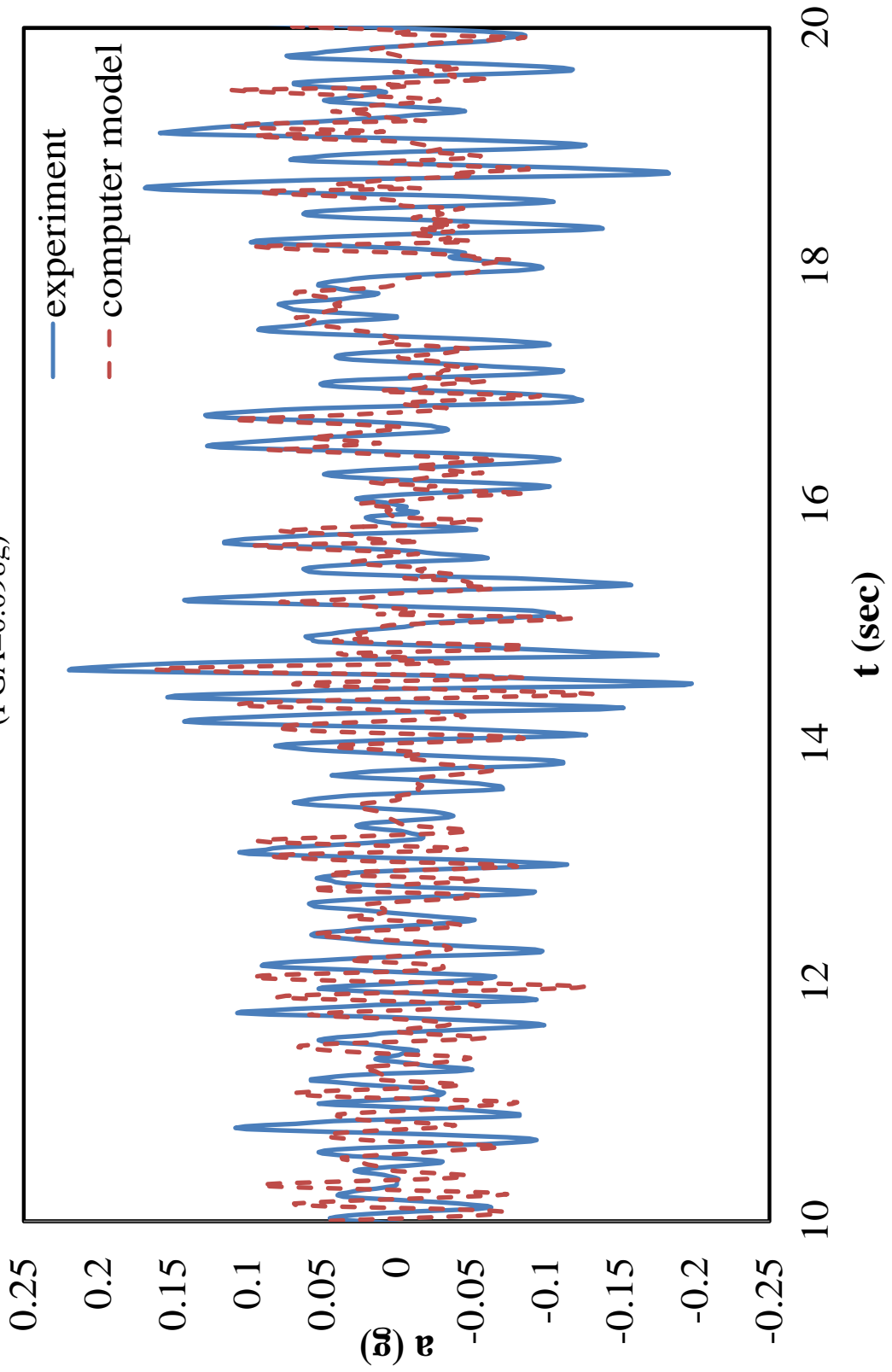
Figure B.18 X-direction 2nd Story Accelerations of ISMES Specimen under Shock P9 (PGA=0.179g)
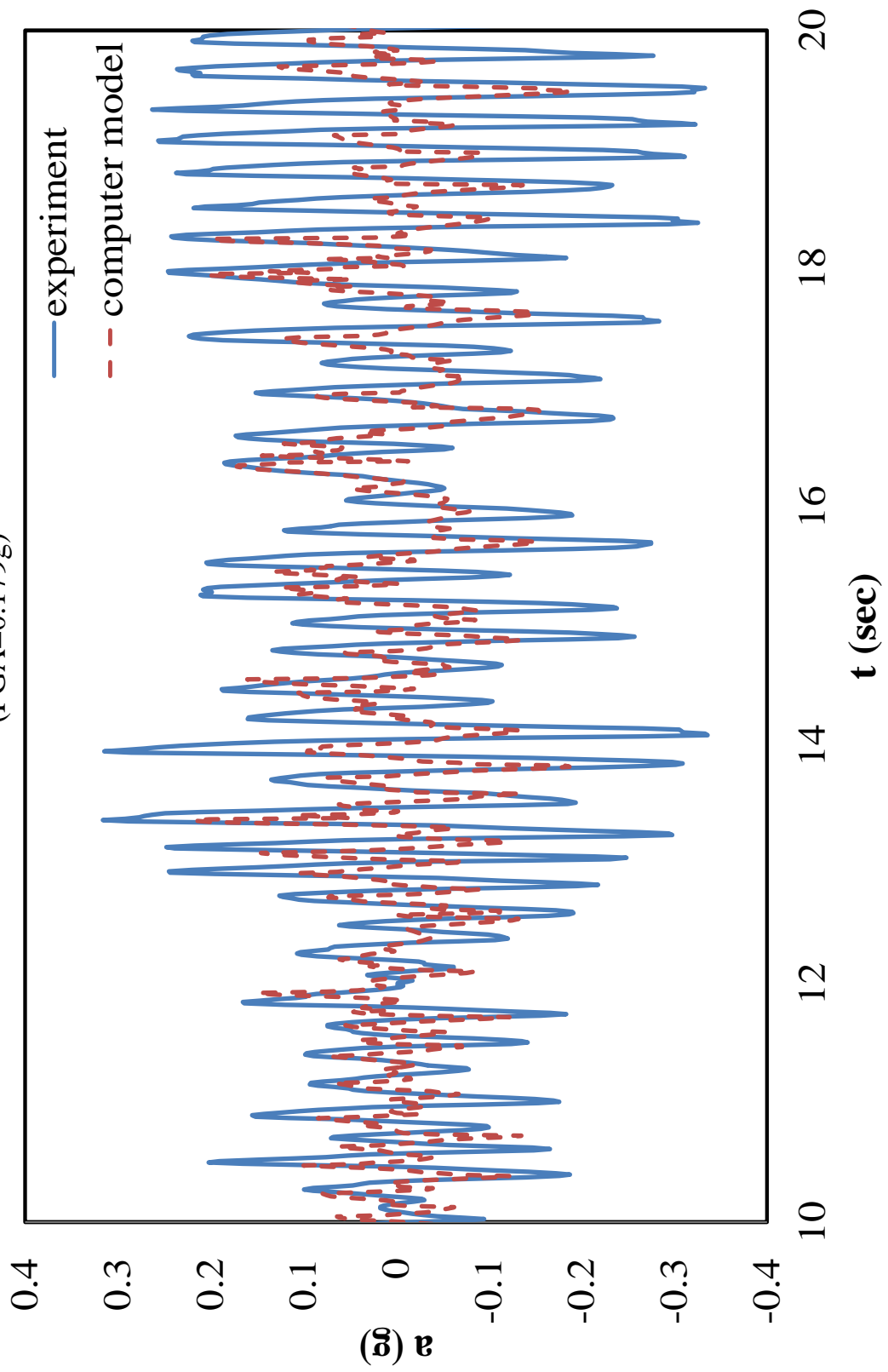
Figure B.19 X-direction 2nd Story Accelerations of ISMES Specimen under Shock P10 (PGA=0.250g)
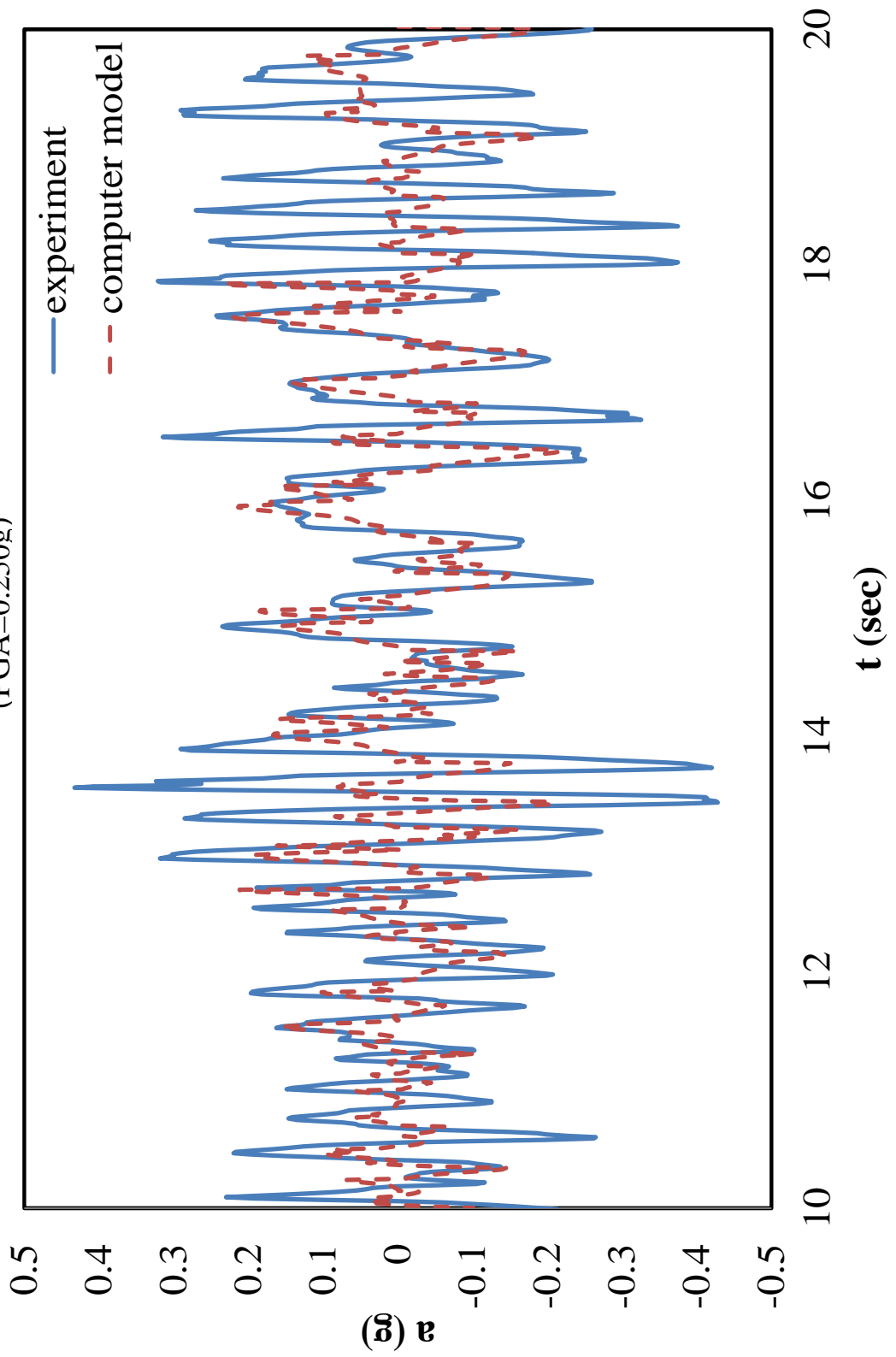
Figure B.20 X-direction 2nd Story Accelerations of ISMES Specimen under Shock P11 (PGA=0.326g)
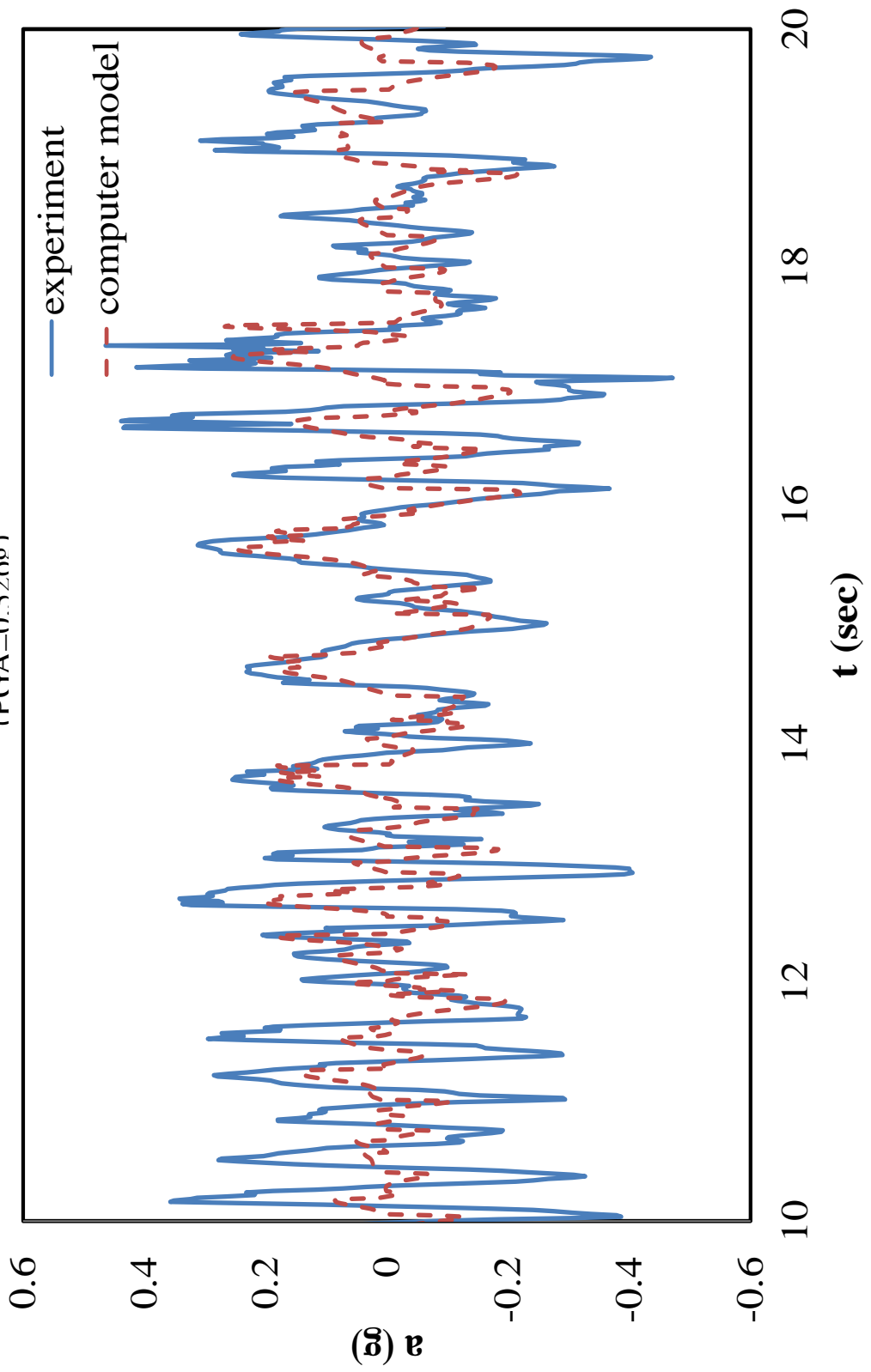
HINGE PROPERTIES of PIERS BELONGING TO CASE STUDY BUILDINGS

Table C.1 Hinge Properties of CSB No:1 Piers According to Equations 4.1 and Equation 4.2

Pier Id	L (m)	t (m)	h$_{eff}$ (m)	p (Mpa)	λ	p/fm (%)	Fy (kN)	Fu (kN)	δu (mm)
W101	5.20	0.3	1.78	0.13	0.34	2.6	228.5	333.2	12.06
W102	0.80	0.3	0.70	0.14	0.88	2.8	22.2	33.5	6.80
W103	0.90	0.3	1.22	0.14	1.36	2.8	16.2	25.2	14.04
W104	1.60	0.2	2.85	0.13	1.78	2.7	12.5	20.2	25.22
W105	2.90	0.2	2.85	0.20	0.98	4.0	60.2	88.1	15.97
W106	1.00	0.2	2.85	0.19	2.85	3.7	3.5	5.9	25.75
W107	1.50	0.2	2.85	0.19	1.90	3.8	13.0	20.4	21.41
W108	2.90	0.2	2.85	0.20	0.98	4.0	60.9	89.0	15.80
W109	0.80	0.2	2.85	0.17	3.56	3.5	1.4	2.5	29.17
W110	2.40	0.2	2.85	0.22	1.19	4.5	44.3	65.0	16.17
W111	1.30	0.3	2.15	0.14	1.65	2.9	17.8	28.3	26.79
W112	2.60	0.3	1.50	0.13	0.58	2.6	90.8	135.0	12.78
W113	1.20	0.3	2.12	0.16	1.77	3.1	15.6	24.9	25.78
W114	1.25	0.3	2.14	0.16	1.71	3.3	17.6	27.8	25.03
W115	1.35	0.3	1.89	0.17	1.40	3.5	26.2	40.2	19.80
W116	4.60	0.3	2.58	0.14	0.56	2.8	173.9	255.4	20.48
W117	2.70	0.2	2.85	0.18	1.06	3.5	48.9	72.8	17.49
W118	3.80	0.2	2.85	0.19	0.75	3.7	94.4	136.7	14.76
W119	3.60	0.2	2.85	0.15	0.79	3.0	75.1	111.6	17.05
W120	10.40	0.3	2.85	0.10	0.27	2.0	415.3	619.4	20.37
W201	5.20	0.2	1.70	0.06	0.33	1.1	92.4	147.2	11.98
W202	0.80	0.2	0.55	0.05	0.69	1.0	9.5	15.8	5.58
W203	0.90	0.2	1.07	0.05	1.19	1.0	6.9	11.8	13.31
W204	1.60	0.2	2.70	0.07	1.69	1.4	9.0	15.6	33.83
W205	2.90	0.2	2.70	0.10	0.93	2.0	41.5	65.1	21.54
W206	1.00	0.2	2.70	0.09	2.70	1.9	2.7	4.8	34.64
W207	1.50	0.2	2.70	0.10	1.80	2.0	9.5	15.9	28.49
W208	2.90	0.2	2.70	0.10	0.93	2.0	42.0	65.7	21.31
W209	0.80	0.2	2.70	0.09	3.38	1.7	1.1	2.1	39.54
W210	2.40	0.2	2.70	0.11	1.13	2.2	30.9	48.5	21.79
W211	1.30	0.2	1.83	0.08	1.40	1.5	10.3	17.2	19.77
W212a	0.50	0.2	1.39	0.13	2.79	2.5	1.5	2.6	15.35
W212b	1.65	0.2	1.73	0.07	1.05	1.4	17.5	28.6	17.16
W213	1.45	0.2	1.87	0.07	1.29	1.4	12.2	20.3	20.42

Table C.1 (Continued)

Pier Id	L (m)	t (m)	h_eff (m)	p (Mpa)	λ	p/fm (%)	Fy (kN)	Fu (kN)	δu (mm)
W214	1.50	0.2	1.88	0.07	1.26	1.4	12.9	21.5	20.45
W215	1.60	0.2	1.71	0.08	1.07	1.5	17.1	27.9	16.75
W216a	1.73	0.2	1.75	0.08	1.01	1.6	20.2	32.7	16.18
W216b	1.37	0.2	1.84	0.08	1.34	1.5	11.5	19.2	19.46
W217	2.70	0.2	2.70	0.09	1.00	1.8	34.1	54.3	23.43
W218	3.80	0.2	2.70	0.10	0.71	2.0	66.3	102.4	19.39
W219	3.60	0.2	2.70	0.07	0.75	1.5	51.1	81.6	23.05
W220	10.40	0.2	2.70	0.06	0.26	1.3	211.0	330.5	16.23

Table C.2 Hinge Properties of CSB No:2 Piers According to Equations 4.1 and Equation 4.2

Pier Id	L (m)	t (m)	h_eff (m)	p (Mpa)	λ	p/fm (%)	Fy (kN)	Fu (kN)	δu (mm)
W101	11.70	0.2	3.64	0.17	0.31	3.3	407.3	577.75	13.95
W102	16.50	0.5	3.64	0.16	0.22	3.2	1518	2150.3	31.01
W103	3.95	0.2	3.64	0.21	0.92	4.2	90.30	130.64	19.17
W104	4.10	0.2	3.64	0.21	0.89	4.2	96.25	139.01	18.96
W105	3.95	0.2	3.64	0.21	0.92	4.3	90.58	130.97	19.11
W106	4.10	0.2	3.64	0.22	0.89	4.4	98.46	141.64	18.58
W107	1.25	0.5	2.87	0.20	2.30	4.0	19.14	30.88	57.07
W108	2.50	0.5	2.68	0.18	1.07	3.5	111.7	166.43	41.30
W109	2.05	0.5	2.47	0.20	1.21	3.9	86.16	128.26	37.81
W110	1.70	0.5	2.75	0.19	1.62	3.9	48.26	74.22	47.88
W111	5.75	0.5	2.45	0.25	0.43	5.1	581.6	795.46	21.24
W112	2.85	0.5	2.45	0.28	0.86	5.6	203.3	284.51	27.06
W113	1.90	0.5	2.10	0.24	1.11	4.8	98.63	142.77	27.88
W114	1.50	0.5	2.87	0.21	1.91	4.2	33.96	52.92	51.29
W115	6.80	0.5	3.64	0.12	0.54	2.4	398.8	594.27	51.56
W116	2.05	0.2	3.00	0.36	1.46	7.2	38.87	55.39	14.41
W117	2.55	0.2	3.29	0.35	1.29	7.0	56.12	79.12	15.16
W118	1.40	0.2	3.29	0.40	2.35	8.1	12.51	18.81	18.01
W119	2.55	0.2	3.29	0.33	1.29	6.5	53.67	76.25	15.78
W120	17.70	0.5	3.64	0.14	0.21	2.8	1537.8	2202	32.11
W121	9.90	0.5	3.64	0.17	0.37	3.3	818.4	1165.	37.32
W202	16.50	0.5	4.09	0.08	0.25	1.5	949.6	1456.1	54.32
W203	3.95	0.2	4.09	0.11	1.03	2.2	54.71	85.54	32.16
W204	4.10	0.2	4.09	0.11	1.00	2.2	58.54	91.35	31.81
W205	3.95	0.2	4.09	0.11	1.03	2.2	54.87	85.75	32.08
W206	4.10	0.2	4.09	0.11	1.00	2.3	59.84	93.02	31.19
W207	1.25	0.5	3.09	0.10	2.47	2.0	10.57	18.62	93.00
W208	1.40	0.5	2.58	0.13	1.84	2.6	25.32	41.31	58.85
W209	1.55	0.5	2.64	0.12	1.70	2.4	30.31	49.36	61.04
W210	1.70	0.5	3.14	0.09	1.84	1.9	25.04	42.33	85.83

Table C.2 (Continued)

Pier Id	L (m)	t (m)	h_eff (m)	p (Mpa)	λ	p/fm (%)	Fy (kN)	Fu (kN)	δu (mm)
W211a	1.50	0.5	3.09	0.15	2.06	3.1	24.65	40.12	67.11
W211b	2.85	0.5	2.20	0.16	0.77	3.2	157.28	232.0	31.45
W212a	2.05	0.5	2.66	0.16	1.30	3.1	68.79	105.7	47.48
W212b	0.85	0.5	1.45	0.10	1.70	2.1	15.32	25.31	36.01
W213	1.90	0.5	2.20	0.10	1.16	2.0	56.03	89.12	47.26
W214	1.50	0.5	3.09	0.10	2.06	2.0	19.06	32.44	84.50
W216	2.05	0.2	3.00	0.19	1.46	3.8	26.66	40.57	20.19
W217	2.55	0.2	3.48	0.19	1.36	3.8	36.13	54.66	22.86
W218	1.40	0.2	3.48	0.21	2.48	4.2	7.51	12.19	27.54
W219	2.55	0.2	3.48	0.17	1.36	3.5	34.35	52.43	23.92
W220a	7.80	0.5	4.09	0.08	0.52	1.6	363.70	564.7	71.08
W220b	1.32	0.2	2.60	0.35	1.97	7.1	15.49	22.96	14.23
W220c	0.90	0.2	2.85	0.35	3.17	7.1	3.47	5.62	18.99
W221	9.90	0.5	4.09	0.09	0.41	1.7	530.68	812.0	62.35

Table C.3 Hinge Properties of CSB No:3 Piers According to Equations 4.1 and Equation 4.2

Pier Id	L (m)	t (m)	h_eff (m)	p (Mpa)	λ	p/fm (%)	Fy (kN)	Fu (kN)	δu (mm)
W101	9.60	0.5	2.35	0.11	0.24	2.2	703.3	1034.1	25.12
W102	1.10	0.5	2.35	0.17	2.14	3.5	18.1	29.2	48.66
W103	4.80	0.5	2.35	0.16	0.49	3.2	343.7	496.6	27.87
W104	1.90	0.5	2.35	0.18	1.24	3.6	73.9	111.2	37.92
W105	2.10	0.5	2.35	0.12	1.12	2.4	71.0	110.6	45.50
W106	2.90	0.5	2.35	0.13	0.81	2.6	136.5	206.3	38.27
W107	3.90	0.5	1.58	0.13	0.40	2.7	273.1	399.1	18.90
W108	4.20	0.5	1.58	0.13	0.38	2.7	302.6	441.2	18.30
W109	1.30	0.5	1.45	0.17	1.11	3.4	54.7	82.1	23.08
W110	0.85	0.5	1.15	0.16	1.35	3.3	28.1	43.1	20.22
W111	4.65	0.5	2.18	0.13	0.47	2.6	298.6	440.6	28.43
W112	2.80	0.5	2.35	0.13	0.84	2.6	127.8	193.6	38.98
W113	4.65	0.5	2.35	0.16	0.51	3.2	329.7	476.5	28.12
W114	2.80	0.5	2.35	0.17	0.84	3.5	152.8	224.5	33.21
W115	1.85	0.5	2.35	0.28	1.27	5.6	90.1	130.0	30.50
W116	1.90	0.5	2.35	0.29	1.24	5.8	97.7	140.0	29.56
W117	1.00	0.5	1.36	0.17	1.36	3.5	33.7	51.4	23.43
W118	1.30	0.5	0.80	0.22	0.62	4.4	100.8	142.0	8.75
W119	0.90	0.5	0.80	0.24	0.89	4.8	57.2	81.4	9.70
W120	1.00	0.5	1.36	0.19	1.36	3.8	35.5	53.7	22.38
W201	9.60	0.3	2.80	0.11	0.29	2.1	390.5	579.6	19.91
W202	1.10	0.2	2.80	0.26	2.55	5.1	6.2	10.0	20.27
W203a	2.35	0.2	2.80	0.29	1.19	5.8	50.3	71.9	13.90

Table C.3 (Continued)

Pier Id	L (m)	t (m)	h$_{eff}$ (m)	p (Mpa)	λ	p/fm (%)	Fy (kN)	Fu (kN)	δu (mm)
W203b	1.40	0.2	2.80	0.32	2.00	6.4	15.1	22.7	16.20
W204	1.90	0.2	2.80	0.28	1.47	5.6	30.6	44.9	15.45
W205	2.10	0.2	2.80	0.16	1.33	3.3	28.1	43.0	19.71
W206	2.90	0.2	2.80	0.18	0.97	3.6	57.6	85.0	16.44
W207	3.90	0.3	2.05	0.12	0.53	2.5	139.2	207.1	17.21
W208a	1.40	0.3	1.71	0.21	1.22	4.2	36.4	53.9	15.12
W208b	0.90	0.3	1.84	0.20	2.04	4.0	10.6	16.8	20.64
W209	1.30	0.3	1.95	0.16	1.50	3.1	21.8	34.0	22.06
W210	0.85	0.3	1.55	0.14	1.83	2.7	9.6	15.6	20.66
W211	4.65	0.3	2.53	0.12	0.54	2.5	163.4	243.4	21.47
W212	2.80	0.2	2.80	0.18	1.00	3.6	53.6	79.4	16.76
W213	4.65	0.2	2.80	0.24	0.60	4.7	152.9	213.6	11.65
W214	2.80	0.2	2.80	0.27	1.00	5.3	68.2	96.9	13.50
W215	1.85	0.2	2.80	0.44	1.51	8.7	37.8	52.9	12.24
W216	1.90	0.2	2.80	0.47	1.47	9.3	41.9	58.1	11.68
W217	1.00	0.3	1.86	0.16	1.86	3.1	11.9	19.0	23.22
W218	1.30	0.3	1.30	0.19	1.00	3.8	38.9	57.3	11.23
W219	0.90	0.3	1.30	0.21	1.44	4.2	18.8	28.3	12.50
W220	1.00	0.3	1.86	0.17	1.86	3.5	12.7	20.1	21.86
W301	9.60	0.2	2.80	0.07	0.29	1.3	197.7	307.9	16.98
W302	1.10	0.2	2.80	0.13	2.55	2.5	4.1	7.0	29.57
W303a	2.35	0.2	2.80	0.14	1.19	2.9	33.3	51.1	20.11
W303b	1.40	0.2	2.80	0.16	2.00	3.2	9.9	16.0	23.68
W304	1.90	0.2	2.80	0.14	1.47	2.8	20.2	31.8	22.44
W305	2.10	0.2	2.80	0.08	1.33	1.6	18.5	30.5	28.65
W306	2.90	0.2	2.80	0.09	0.97	1.8	37.9	60.2	23.90
W307a	0.75	0.2	1.73	0.08	2.31	1.5	2.5	4.5	23.15
W307b	0.85	0.2	1.30	0.10	1.53	2.0	7.0	11.5	12.64
W308a	1.25	0.2	1.30	0.09	1.04	1.8	15.3	24.4	11.41
W308b	0.55	0.2	1.52	0.26	2.76	5.2	2.6	4.2	11.25
W308c	0.90	0.2	1.84	0.10	2.04	2.0	4.6	7.8	20.31
W309	1.30	0.2	1.95	0.09	1.50	1.8	10.5	17.3	19.65
W310	0.85	0.2	1.55	0.07	1.82	1.4	4.2	7.4	19.94
W311	4.65	0.2	2.53	0.08	0.54	1.5	82.2	128.7	18.41
W312	2.80	0.2	2.80	0.09	1.00	1.8	35.2	56.2	24.36
W313	4.65	0.2	2.80	0.12	0.60	2.4	100.7	151.2	16.93
W314	2.80	0.2	2.80	0.13	1.00	2.6	44.4	68.0	19.82
W315	1.85	0.2	2.80	0.22	1.51	4.4	25.0	37.6	17.74
W316	1.90	0.2	2.80	0.23	1.47	4.7	27.6	41.1	16.98
W317	1.00	0.2	1.86	0.08	1.86	1.6	5.4	9.2	21.89
W318	1.30	0.2	1.30	0.10	1.00	2.0	17.4	27.5	10.69
W319	0.90	0.2	1.30	0.12	1.44	2.3	8.8	14.1	11.39
W320	1.00	0.2	1.86	0.09	1.86	1.8	5.6	9.6	21.01

Table C.4 Hinge Properties and Failure Modes of CSB No:1 Piers According to FEMA 356

Pier Id	Vr (kN)	Vbjs (kN)	Vdt (kN)	Vtc (kN)	Failure Mode	Fy (kN)	δu (mm)
W101	536.7	199.3	715.1	560.7	SLIDING	199.3	14.2
W102	34.3	31.7	44.9	35.6	SLIDING	31.7	5.60
W103	25.4	36.0	33.1	26.4	ROCKING	25.4	13.23
W104	21.7	41.5	28.7	22.6	ROCKING	21.7	40.61
W105	105.3	93.7	127.2	106.4	SLIDING	93.7	22.80
W106	11.7	31.0	14.3	11.9	ROCKING	11.7	64.98
W107	27.1	47.4	33.1	27.5	ROCKING	27.1	43.32
W108	107.4	94.9	129.3	108.3	SLIDING	94.9	22.80
W109	7.1	24.0	8.8	7.2	ROCKING	7.1	81.23
W110	81.4	83.7	96.2	81.2	TOE CRUSHING	81.2	NA
W111	30.2	52.2	39.4	31.4	ROCKING	30.2	28.45
W112	156.1	98.8	209.0	163.3	SLIDING	98.8	12.00
W113	28.8	50.8	36.6	29.7	ROCKING	28.8	29.99
W114	32.3	54.1	40.7	33.2	ROCKING	32.3	29.20
W115	45.0	60.3	56.0	46.0	ROCKING	45.0	21.17
W116	316.0	184.5	411.5	328.2	SLIDING	184.5	20.60
W117	81.5	81.5	100.8	83.2	ROCKING	81.5	24.07
W118	170.0	118.3	208.0	172.8	SLIDING	118.3	22.80
W119	121.7	98.5	156.8	126.1	SLIDING	98.5	22.80
W120	1028.1	351.5	1480.8	1090.0	SLIDING	351.5	22.80
W201	159.4	94.0	288.1	172.6	SLIDING	94.0	13.60
W202	10.5	14.0	19.9	11.4	ROCKING	10.5	3.03
W203	7.1	16.0	13.3	7.7	ROCKING	7.1	10.18
W204	11.5	30.8	19.2	12.4	ROCKING	11.5	36.45
W205	55.4	64.9	80.2	58.8	ROCKING	55.4	20.11
W206	6.2	21.8	9.1	6.6	ROCKING	6.2	58.32
W207	14.6	33.4	21.3	15.5	ROCKING	14.6	38.88
W208	56.5	65.5	81.3	59.9	ROCKING	56.5	20.11
W209	3.7	16.9	5.6	3.9	ROCKING	3.7	72.90
W210	42.9	56.8	59.8	45.3	ROCKING	42.9	24.30
W211	12.8	26.2	20.3	13.7	ROCKING	12.8	20.50
W212a	4.1	12.6	5.5	4.3	ROCKING	4.1	31.09
W212b	20.4	32.5	33.1	21.9	ROCKING	20.4	14.44
W213	14.3	28.4	23.4	15.4	ROCKING	14.3	19.27
W214	15.1	29.3	24.7	16.2	ROCKING	15.1	18.91
W215	20.3	32.1	32.3	21.8	ROCKING	20.3	14.65

Table C.4 (Continued)

Pier Id	Vr (kN)	Vbjs (kN)	Vdt (kN)	Vtc (kN)	Failure Mode	Fy (kN)	δu (mm)
W216a	24.7	35.5	38.4	26.4	ROCKING	24.7	14.15
W216b	14.2	27.7	22.4	15.2	ROCKING	14.2	19.66
W217	43.4	57.9	65.0	46.3	ROCKING	43.4	21.60
W218	93.9	84.6	136.5	99.7	SLIDING	84.6	21.60
W219	63.8	71.6	102.4	68.5	ROCKING	63.8	16.20
W220	451.2	195.1	774.8	487.0	SLIDING	195.1	21.60

Table C.5 Hinge Properties and Failure Modes of CSB No:2 Piers According to FEMA 356

Pier Id	Vr (kN)	Vbjs (kN)	Vdt (kN)	Vtc (kN)	Failure Mode	Fy (kN)	δu (mm)
W101	1121.6	340.1	1408.4	1151.8	SLIDING	340.1	29.12
W102	5321.7	1167.8	6755.2	5485.6	SLIDING	1167.8	29.12
W103	163.2	133.0	194.8	163.8	SLIDING	133.0	29.12
W104	174.5	137.3	208.5	175.3	SLIDING	137.3	29.12
W105	164.1	133.4	195.6	164.6	SLIDING	133.4	29.12
W106	181.2	140.6	215.0	181.2	SLIDING	140.6	29.12
W107	48.7	101.1	58.8	49.2	ROCKING	48.7	52.72
W108	186.0	188.7	230.1	189.9	ROCKING	186.0	22.93
W109	150.8	165.2	182.5	152.5	ROCKING	150.8	23.87
W110	91.7	135.4	111.3	92.8	ROCKING	91.7	35.51
W111	1541.1	544.5	1780.8	1513.7	SLIDING	544.5	19.60
W112	414.3	286.9	472.0	401.9	SLIDING	286.9	19.60
W113	185.3	173.1	216.2	183.3	SLIDING	173.1	16.80
W114	74.3	125.8	88.7	74.6	ROCKING	74.3	43.93
W115	695.9	419.5	945.4	730.2	SLIDING	419.5	29.12
W116	90.2	99.0	99.3	83.9	TOE CRUSHING	83.9	NA
W117	124.8	121.3	137.6	116.4	TOE CRUSHING	116.4	NA
W118	43.3	74.1	47.0	39.2	TOE CRUSHING	39.2	NA
W119	115.9	114.9	129.0	109.6	TOE CRUSHING	109.6	NA
W120	5438.6	1174.5	7108.4	5654.9	SLIDING	1174.5	29.12
W121	2011.8	720.3	2524.9	2065.6	SLIDING	720.3	29.12
W202	2270.6	827.9	3610.5	2435.5	SLIDING	827.9	32.68
W203	75.4	92.7	105.6	79.6	ROCKING	75.4	33.80
W204	80.6	95.9	113.2	85.1	ROCKING	80.6	32.56
W205	75.8	92.9	106.0	80.0	ROCKING	75.8	33.80
W206	83.6	97.5	116.1	88.1	ROCKING	83.6	32.56
W207	22.2	69.6	32.3	23.6	ROCKING	22.2	61.23

Table C.5 (Continued)

Pier Id	Vr (kN)	Vbjs (kN)	Vdt (kN)	Vtc (kN)	Failure Mode	Fy (kN)	δu (mm)
W208	44.3	89.1	59.2	46.4	ROCKING	44.3	37.89
W209	49.0	94.8	66.9	51.4	ROCKING	49.0	36.03
W210	38.5	92.6	56.9	41.0	ROCKING	38.5	46.25
W211a	50.8	105.0	64.8	52.5	ROCKING	50.8	50.86
W211b	263.4	202.0	334.1	271.4	SLIDING	202.0	17.60
W212a	111.0	143.9	141.3	114.5	ROCKING	111.0	27.51
W212b	23.4	48.7	33.3	24.8	ROCKING	23.4	19.68
W213	75.2	107.7	107.7	79.6	ROCKING	75.2	20.38
W214	33.2	84.8	47.6	35.1	ROCKING	33.2	50.86
W216	48.3	64.9	58.8	49.0	ROCKING	48.3	35.12
W217	63.7	80.1	77.7	64.7	ROCKING	63.7	37.88
W218	21.6	47.2	25.7	21.6	ROCKING	21.6	69.00
W219	58.6	76.2	72.8	59.9	ROCKING	58.6	37.88
W220a	548.1	403.2	846.8	586.2	SLIDING	403.2	32.68
W220b	42.6	63.1	46.9	39.7	TOE CRUSHING	39.7	NA
W220c	18.1	43.0	19.9	16.8	TOE CRUSHING	16.8	NA
W221	937.2	524.2	1417.3	1000.0	SLIDING	524.2	32.68

Table C.6 Hinge Properties and Failure Modes of CSB No:3 Piers According to FEMA 356

Pier Id	Vr (kN)	Vbjs (kN)	Vdt (kN)	Vtc (kN)	Failure Mode	Fy (kN)	δu (mm)
W101	1984.3	569.9	2758.6	2091.4	SLIDING	569.9	18.80
W102	40.4	82.3	50.2	41.3	ROCKING	40.4	40.16
W103	696.9	339.5	884.8	718.4	SLIDING	339.5	18.80
W104	125.7	145.8	154.7	128.1	ROCKING	125.7	23.25
W105	101.5	128.7	138.4	106.6	ROCKING	101.5	21.04
W106	208.1	184.3	278.1	217.6	SLIDING	184.3	18.80
W107	579.5	251.9	767.8	604.7	SLIDING	251.9	12.60
W108	674.0	271.7	892.2	703.1	SLIDING	271.7	12.60
W109	90.0	96.2	112.2	92.2	ROCKING	90.0	12.87
W110	46.8	61.6	58.8	48.0	ROCKING	46.8	12.36
W111	570.4	293.6	764.8	596.8	SLIDING	293.6	17.41
W112	192.7	177.3	257.9	201.5	SLIDING	177.3	18.80
W113	659.1	330.4	835.4	679.1	SLIDING	330.4	18.80
W114	259.2	208.4	322.5	265.3	SLIDING	208.4	18.80
W115	182.2	186.4	207.5	176.7	TOE CRUSHING	176.7	NA
W116	199.5	196.4	225.9	192.4	TOE CRUSHING	192.4	NA

Table C.6 (Continued)

Pier Id	Vr (kN)	Vbjs (kN)	Vdt (kN)	Vtc (kN)	Failure Mode	Fy (kN)	δu (mm)
W117	57.5	74.8	71.4	58.8	ROCKING	57.5	14.86
W118	207.9	111.7	246.6	207.9	SLIDING	111.7	6.40
W119	109.2	82.1	127.4	108.1	SLIDING	82.1	6.40
W120	62.7	78.7	76.4	63.6	ROCKING	62.7	14.86
W201	944.7	333.1	1336.0	998.6	SLIDING	333.1	22.40
W202	19.9	41.9	23.0	19.5	TOE CRUSHING	19.5	NA
W203a	102.1	97.0	115.7	98.5	SLIDING	97.0	22.40
W203b	40.6	62.6	45.3	38.5	TOE CRUSHING	38.5	NA
W204	64.6	76.6	73.5	62.6	TOE CRUSHING	62.6	NA
W205	46.5	60.7	58.6	47.8	ROCKING	46.5	29.87
W206	96.9	88.2	119.6	98.8	SLIDING	88.2	22.40
W207	246.1	145.0	333.5	258.1	SLIDING	145.0	16.40
W208a	65.6	70.7	78.3	65.9	ROCKING	65.6	16.61
W208b	24.1	44.2	29.0	24.3	ROCKING	24.1	29.93
W209	36.9	55.1	46.9	38.0	ROCKING	36.9	23.33
W210	17.1	33.3	22.6	17.9	ROCKING	17.1	22.73
W211	284.2	172.9	385.1	298.1	SLIDING	172.9	20.20
W212	89.6	84.8	110.7	91.4	SLIDING	84.8	22.40
W213	328.4	168.0	384.1	325.5	SLIDING	168.0	22.40
W214	133.7	109.3	153.4	130.6	SLIDING	109.3	22.40
W215	96.2	104.0	103.5	85.5	TOE CRUSHING	85.5	NA
W216	108.3	112.5	115.7	94.7	TOE CRUSHING	94.7	NA
W217	22.6	42.2	28.8	23.3	ROCKING	22.6	27.77
W218	67.0	61.6	81.6	67.9	SLIDING	61.6	10.40
W219	34.9	44.9	41.8	35.1	ROCKING	34.9	15.02
W220	25.3	44.9	31.4	25.9	ROCKING	25.3	27.77
W301	399.1	184.7	664.6	429.8	SLIDING	184.7	22.40
W302	9.9	27.7	13.3	10.4	ROCKING	9.9	57.02
W303a	51.5	63.4	66.7	53.4	ROCKING	51.5	26.69
W303b	20.1	39.8	25.5	20.7	ROCKING	20.1	44.80
W304	32.3	50.2	42.3	33.6	ROCKING	32.3	33.01
W305	23.3	43.5	35.9	24.9	ROCKING	23.3	29.87
W306	48.5	62.2	72.5	51.6	ROCKING	48.5	21.63
W307a	4.5	15.1	7.1	4.8	ROCKING	4.5	32.04
W307b	10.0	19.1	14.4	10.6	ROCKING	10.0	15.91
W308a	19.5	26.9	29.1	20.8	ROCKING	19.5	10.82
W308b	9.3	21.2	10.7	9.1	TOE CRUSHING	9.1	NA
W308c	7.8	20.1	11.3	8.3	ROCKING	7.8	29.93

Table C.6 (Continued)

Pier Id	Vr (kN)	Vbjs (kN)	Vdt (kN)	Vtc (kN)	Failure Mode	Fy (kN)	δu (mm)
W309	14.4	28.3	21.3	15.3	ROCKING	14.4	23.40
W310	5.7	16.4	9.5	6.1	ROCKING	5.7	22.47
W311	118.9	94.0	187.7	127.5	SLIDING	94.0	20.20
W312	44.8	59.9	67.2	47.7	ROCKING	44.8	22.40
W313	164.2	113.1	225.0	172.6	SLIDING	113.1	22.40
W314	65.6	71.5	87.5	68.6	ROCKING	65.6	22.40
W315	48.4	63.8	57.3	48.4	TOE CRUSHING	48.4	NA
W316	54.2	68.1	63.5	53.8	TOE CRUSHING	53.8	NA
W317	7.9	20.7	12.2	8.5	ROCKING	7.9	27.77
W318	23.1	29.1	33.4	24.5	ROCKING	23.1	10.40
W319	13.0	21.7	18.0	13.7	ROCKING	13.0	15.02
W320	8.6	21.4	12.9	9.1	ROCKING	8.6	27.77

PLAN VIEWS AND WALL LABELS OF CASE STUDY BUILDINGS
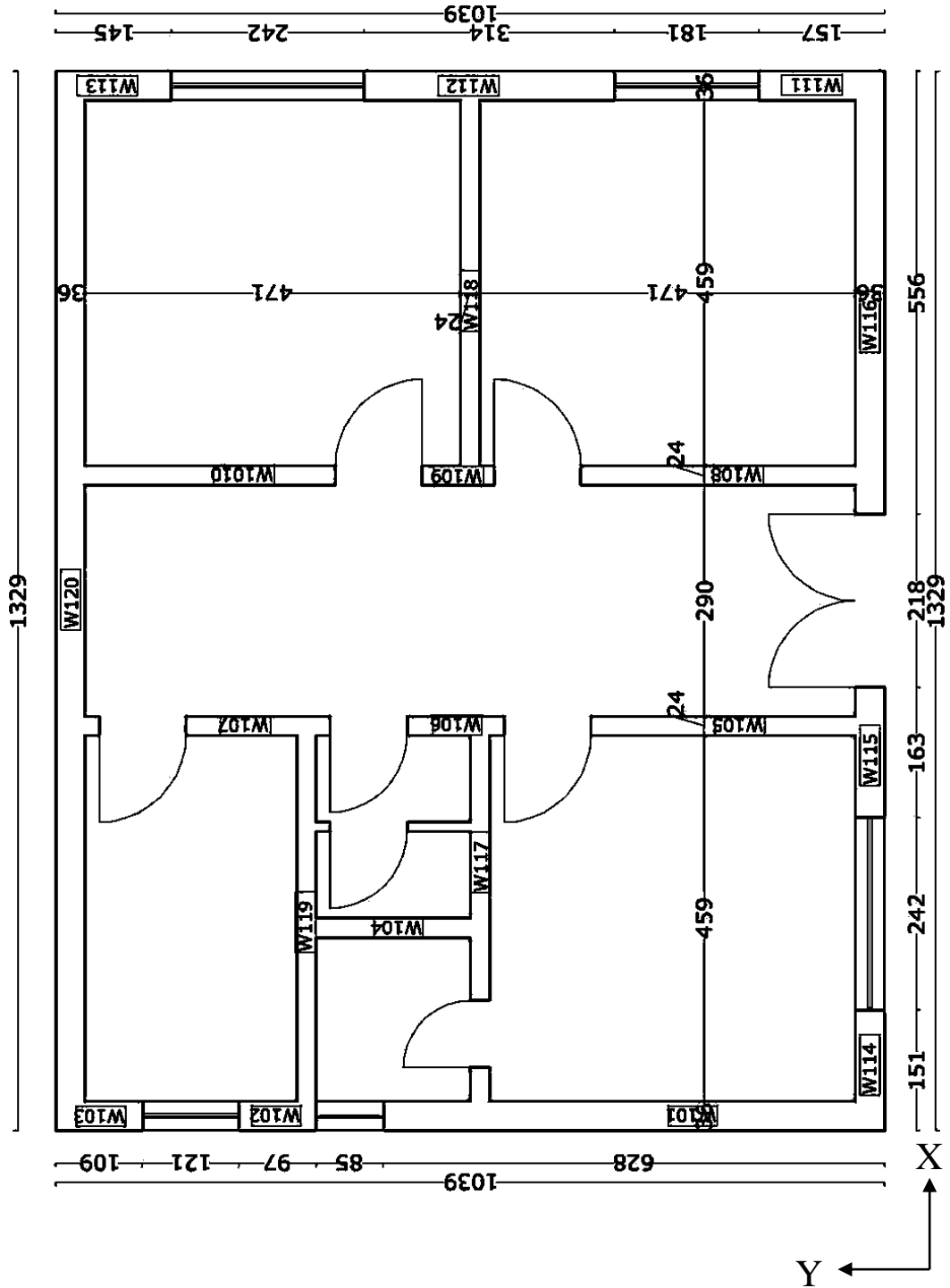
Figure D.1 Plan View of CSB No:1 – First Floor
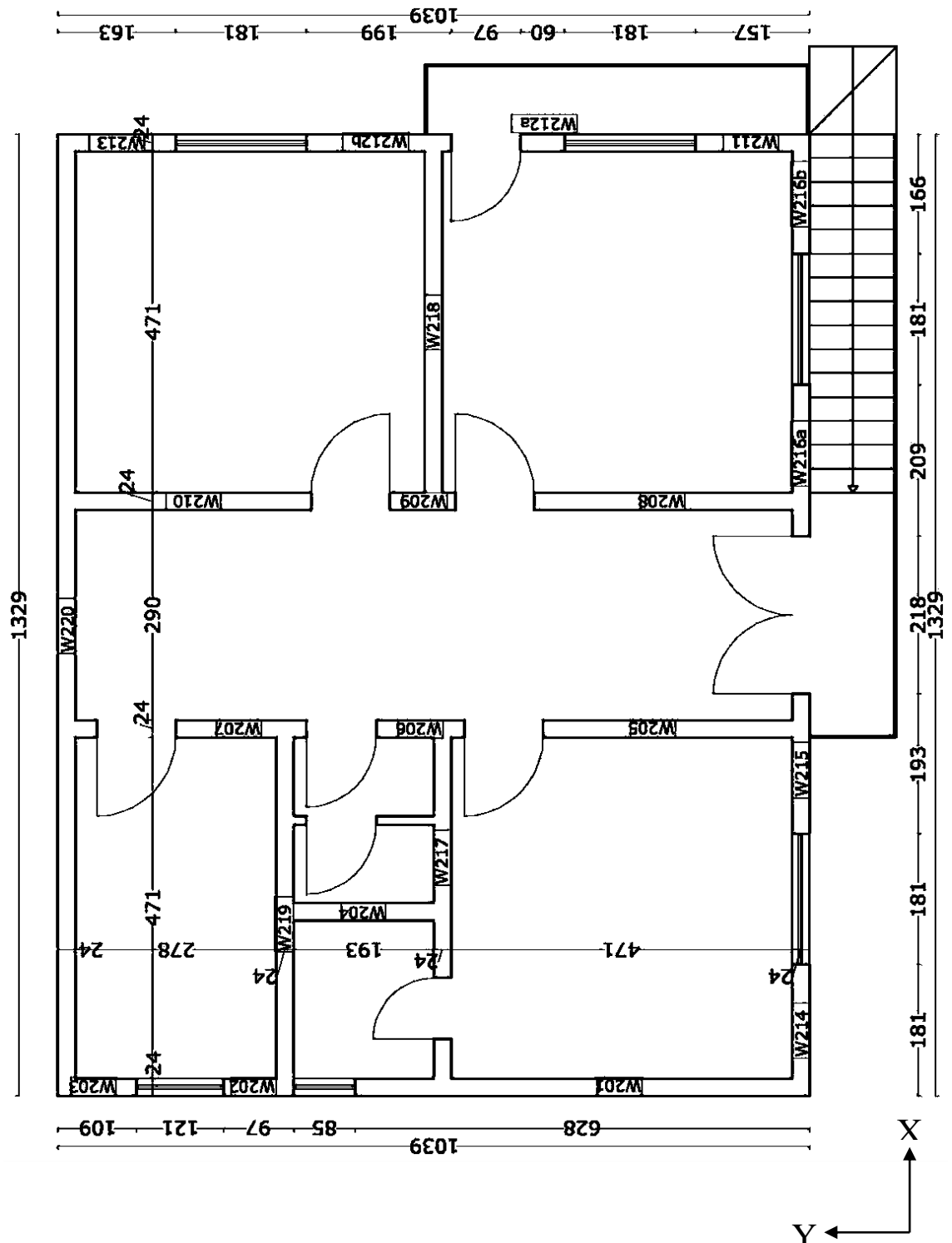
**Figure D.2** Plan View of CSB No:1 – Second Floor
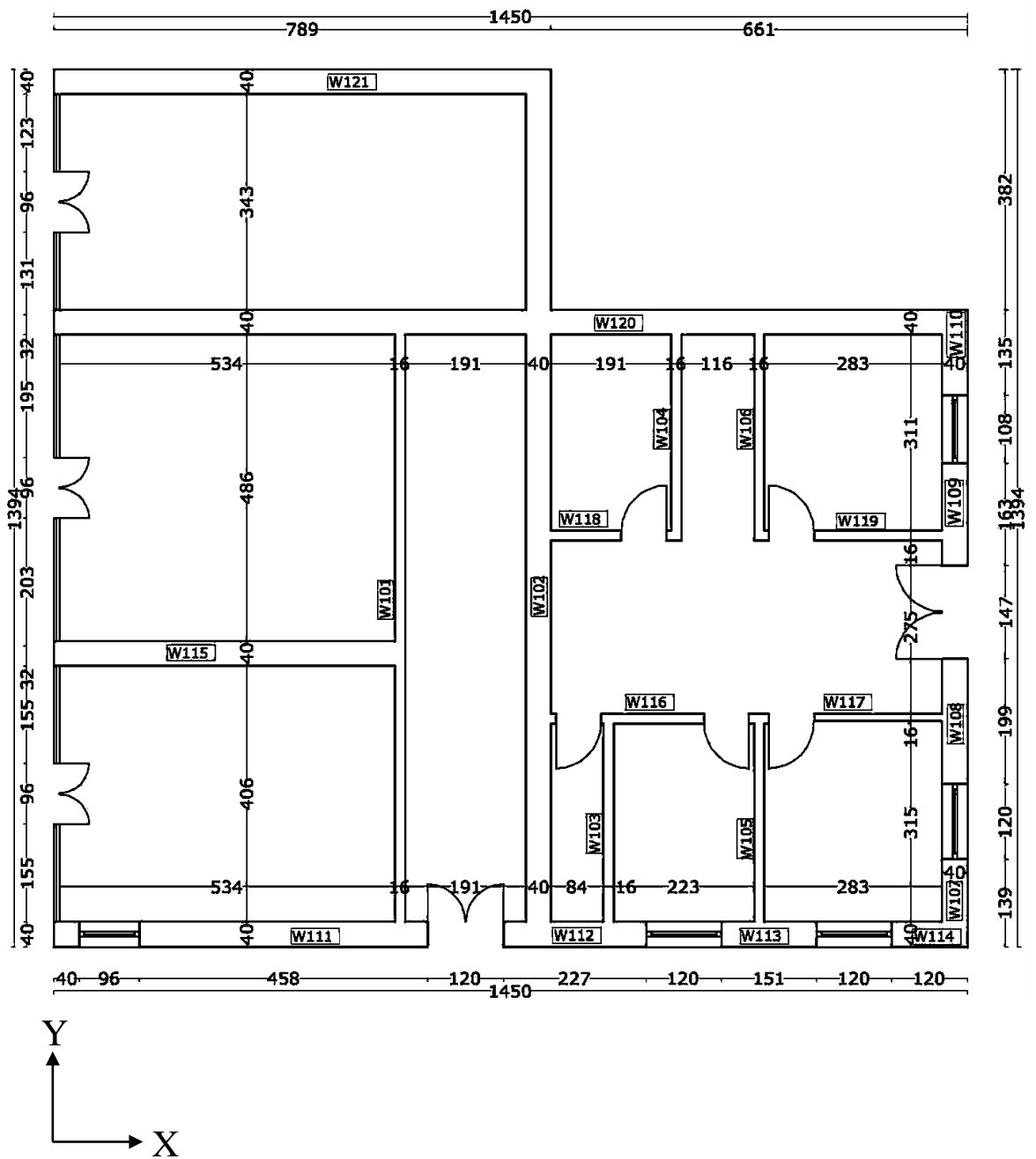
**Figure D.3** Plan View of CSB No:2 – First Floor
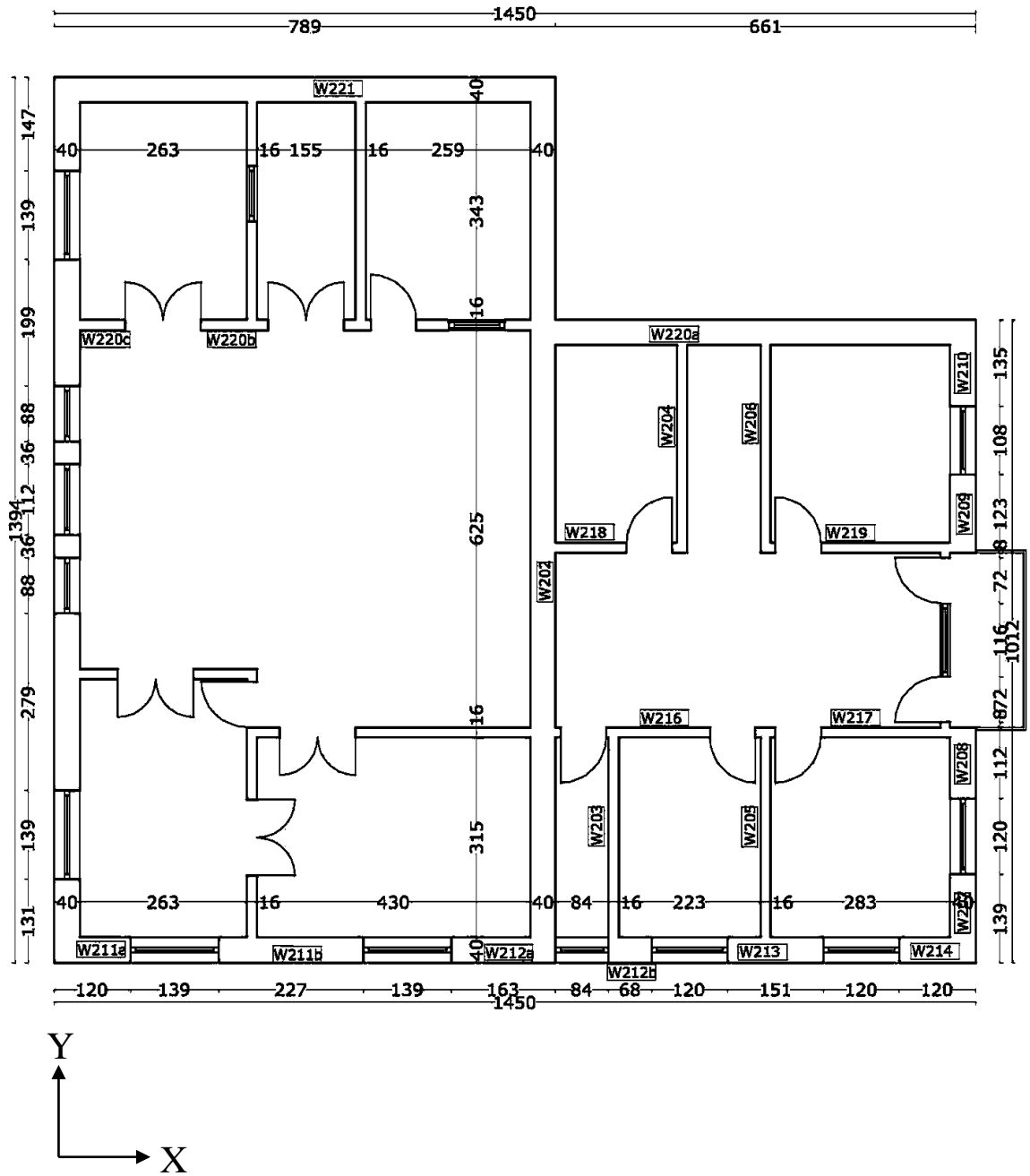
Figure D.4 Plan View of CSB No:2 – Second Floor
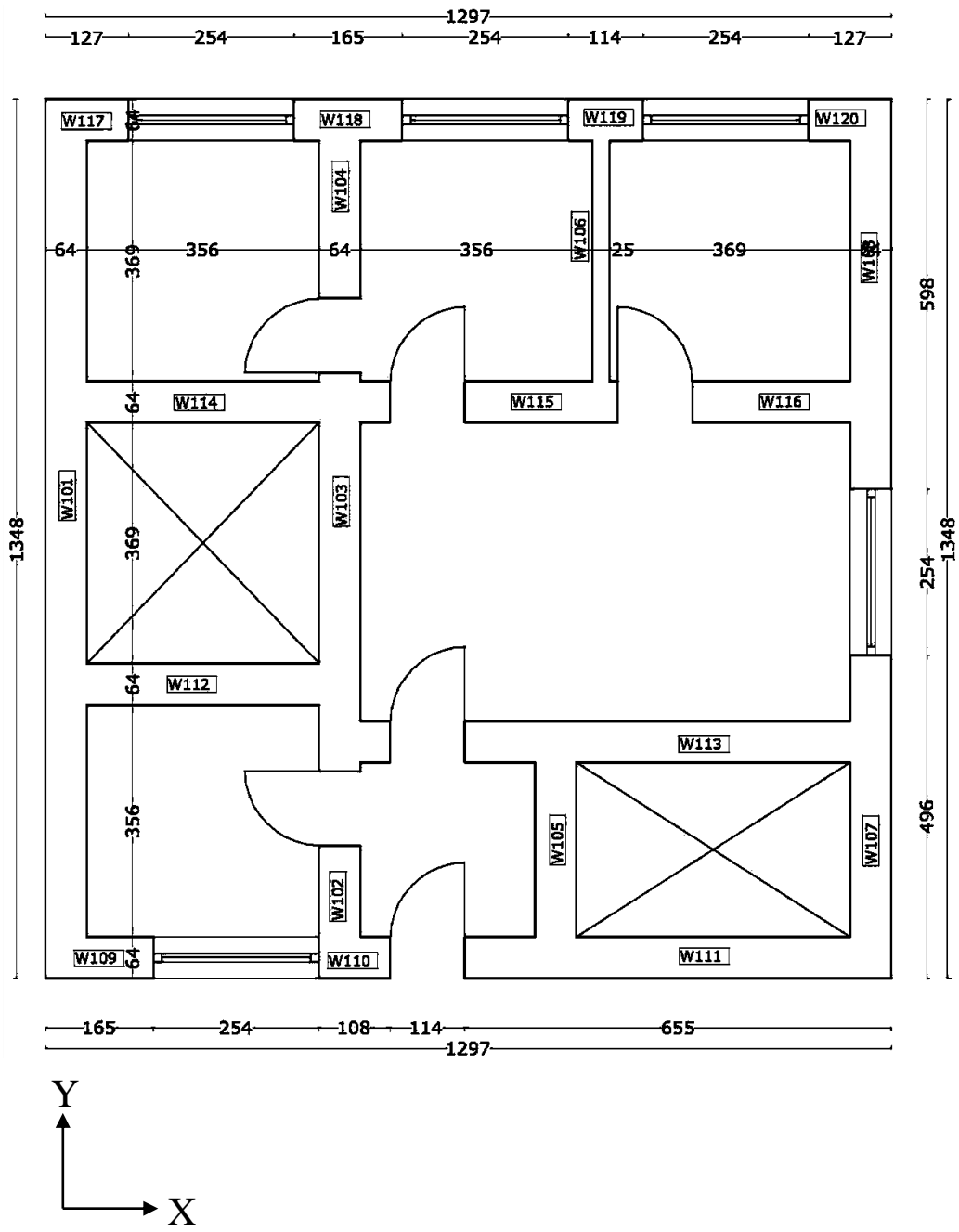
Figure D.5 Plan View of CSB No:3 – First Floor
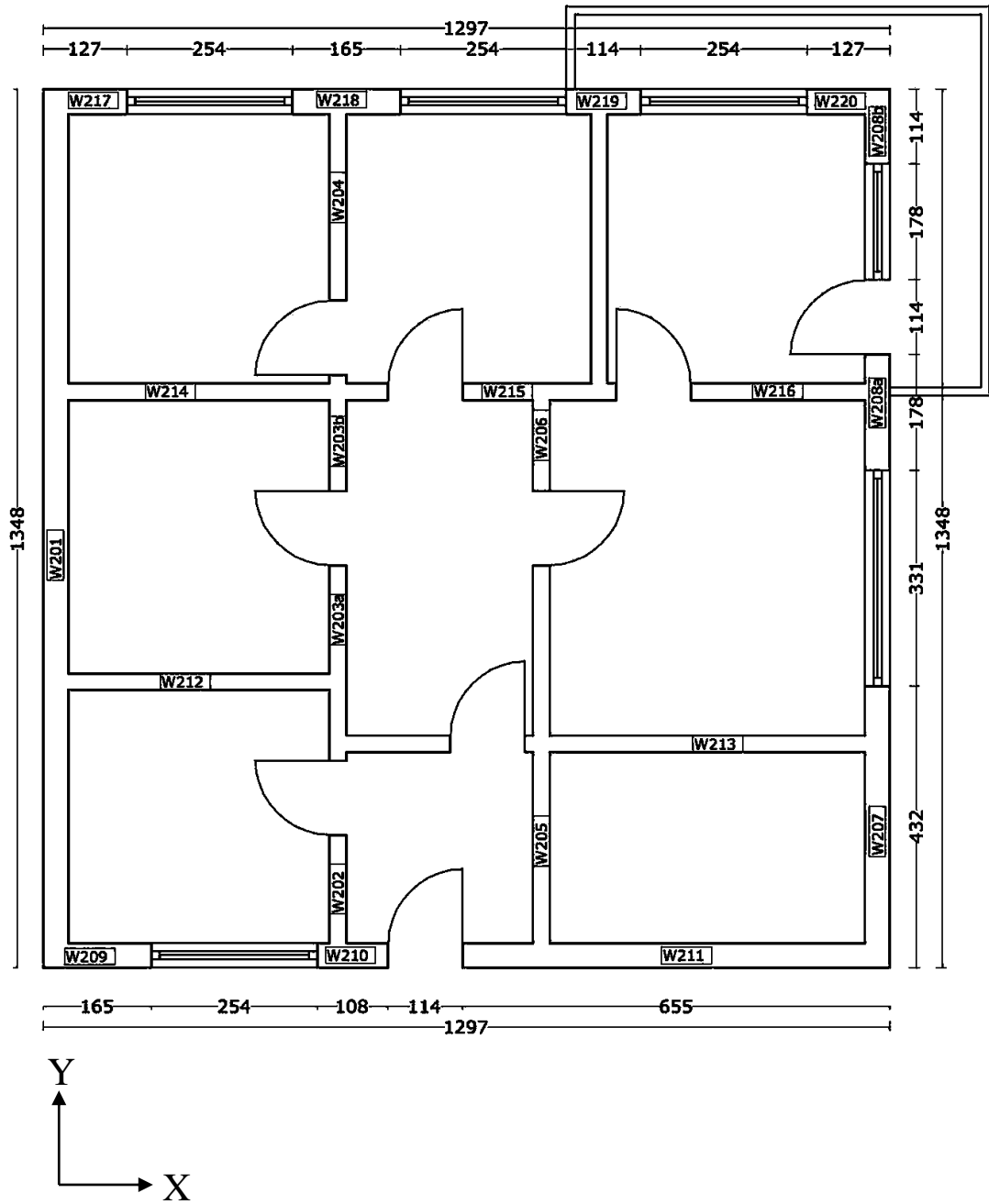
Figure D.6 Plan View of CSB No:3 – Second Floor

Figure D.7 Plan View of CSB No:3 – Third Floor